Development of a Simple Full Field Optical Coherence Tomography System and its Applications

Chen Li

Department of Electrical Engineering and Electronics

University of Liverpool

Thesis submitted in accordance with the requirements of the University of Liverpool for the degree of

Doctor of Philosophy

December 2015

I would like to dedicate this thesis to my loving husband and parents.

Declaration

The author hereby declares that this thesis is a record of work carried out in the Department of Electrical Engineering and Electronics at the University of Liverpool during the period from October 2010 to December 2015. The system developments, measurements, result analysis are my own research outcomes. I hereby declare that except where specific reference is made to the work of others, the contents of this dissertation are original and have not been submitted in whole or in part for consideration for any other degree or qualification in this, or any other university. This dissertation is my own work and contains nothing which is the outcome of work done in collaboration with others, except as specified in the text.

Chen Li
December 2015

Acknowledgements

The thesis would not have been possible without the help of many people in so many ways. First and foremost, I would like to express my sincere gratitude and gratefulness to my supervisor, Dr. Yaochun Shen, who has always been available to advise me, provided me with various aspects of research suggestions, offered continuous guidance and support on this work, and introduced me to a great industrial experience.

I also would like to thank Dr. Harm van Zalinge, who has helped me so much during the thesis revision, suggested valuable writing tips, clarified my understanding of doing an academic research and boosted my confidence in completing the revision.

Special thanks go to Dr. Philip Taddy and Dr. Robert May from Teraview Ltd., for your generous supports throughout the industrial placement.

I would like to offer my special thanks and appreciation to my parents and parents-in-law, who always have faiths in me and supported me all the time.

Last but not least, I am greatly indebted to my husband, Dr. Chenghao Wei, who always stands by me and gets me through difficulties. I would not be able to finish this work without him. I am truly grateful for his constant support and love.

Abstract

Optical coherence tomography (OCT) is a versatile and powerful imaging technique widely used in biomedical applications. It employs non-destructive radiation and performs non-contact micrometre-scale cross-sectional imaging of the sample structure. However, classic OCT systems generally apply a single-point detection scheme, which creates inefficiencies in terms of the experimental alignment of system, the point-by-point signal acquisition process and the measurement speed. One of its variants, full-field optical coherence tomography (FF-OCT) employs parallel illumination and directly acquires *en-face* images with a complementary camera, hence omitting the need of electromechanical lateral scans as in classic OCT systems. Current FF-OCT systems could offer more efficient measurement procedures as well as superior imaging performance, however, they are neither economically viable nor universally applicable to different applications. There is a need for a simplified low cost system to make such a powerful technology readily available for a wide range of applications.

In this thesis, the development of a low cost simple FF-OCT system is described from its system setup, experimental procedures, data analysis, and system performance. The system consists of only essential components including the probing lens and beam-splitter, together with a low-cost infrared LED source and CMOS camera. During the measurement, the system only requires to control the axial movement of the sample arm and the image acquisition by the camera. For the imaging of a sample with a depth of 100 µm, the FF-OCT measurement only takes less than two minutes. The time-efficient measurement with the simple system offers great advantage over the developed phase-shifting FF-OCT system, which requires lengthy measurement and excessive operations, despite the decoupling of signal strength and instantaneous phase with penetration depth. Therefore, compared to state-of-the-art systems, it has the advantage of being low-cost, fast image acquisition speed and simple experimental operations.

For the data analysis of tomographic imaging, the axial position of a structural feature is determined by that of the envelope, which is obtained by processing raw FF-OCT signal with Hilbert transform. The imaging performance of the simple system is measured to have a spatial resolution of $(3.6 \times 10.3)\,\mu m^2$ (axial $\times$ lateral) and a system sensitivity of

74 dB. The characterisation of small-size pharmaceutical pellet coatings, bovine corneal layers and paint films is to demonstrate the potential of the simple FF-OCT system for the tomographic imaging. The layered structures and internal morphology features can be revealed by analysing the measured FF-OCT B-scan images and A-scan signals. First of all, the simple FF-OCT system is capable of performing accurate and quick measurements of pellet coatings, which are validated by the XμCT technique. FF-OCT imaging can provide a spatial characterisation of coating layers, an accurate determination of coating thickness, and an estimation of coating uniformity and porosity, making the simple system a powerful tool for the coating evaluation of similar pharmaceutical pellets. Secondly, the simple system can detect corneal surfaces and the two anterior layers of bovine cornea. This could permit the prediction of the corneal oedematous state and epithelial erosions by the analysis of the FF-OCT results of the corneal structure. Thirdly, the simple system is capable of revealing the surface and subsurface of basecoat and clearcoat films. The measurement of their paint thicknesses is also verified by the reference profilometry results. FF-OCT imaging can provide further spatial evaluation of a paint film and the areal thickness map could be obtained. The study of these paint samples with the simple system might provide an indication for the FF-OCT measurement of industrial automotive paint.

For the data analysis of the surface topography, the axial position of the surface is obtained by applying interpolation and a minimum search algorithm to the raw FF-OCT signal. This allows sub-micrometre depth precision to be obtained with the simple system. In the validation of the measurement of the surface topography, a less than 10 nm deviation of the FF-OCT measurement is found compared to the AFM measurement of a nanostructured step-like surface. The capability of the simple system for the surface topography is further illustrated by the determination of the electrode thickness of semiconductor microelectronics. By analysing the phase change upon reflections and the optical path lengths during the measurement, the step-like structure and the sandwich configuration can be revealed from the measured FF-OCT surface maps. The usefulness of the simple system is presented in the surface topography of PMMA models. It is demonstrated that the areal refractive power can be obtained by analysing the 2-D curvature of the FF-OCT measured surface map, which is useful in the identification of surface irregularity.

Table of contents

List of figures

List of tables

Chapter 1

Introduction

The thesis is dedicated to the development of the simple full-field optical coherence tomography (FF-OCT) system and the evaluation of its potential for the characterisation of biomedical, pharmaceutical and other industrial applications. The overview of this research is introduced firstly in this chapter, followed by the motivation and the objectives of this thesis. The thesis outline is also presented to give a clear view of the entire contents.

1.1 Research Overview

Optical coherence tomography (OCT) is a non-contact, non-invasive technique that uses light waves to take high resolution cross-sectional images from within optical scattering media (e.g. biological tissue) [1]. It features micrometre-scale resolution and millimetre-scale penetration depth, which makes it a perfect analytical tool for the diagnosis of retinal diseases and the examination of coronary arteries [2]. As an interferometry technique, OCT detects interference signals whenever there is a variation of the refractive index. As an imaging technique, OCT acquires a stack of images regarding the visible and invisible aspects of a sample, such as internal or covered parts. Cross-sectional images are analysed to study structural performance and to reveal possible internal defects within a sample.

As a powerful modality in medical imaging, OCT has achieved sub-micrometre resolution along the light propagation direction, depending on the low (temporal-) coherence properties of the light source [3]. The use of relatively long wavelength radiation in OCT allows it to penetrate the scattering medium with millimetre-scale depth of penetration. Broadband near-infrared (NIR) light and white light are typically employed in most OCT systems and exhibit much smaller photon energy, compared to the ionising electromagnetic waves in radiographic imaging techniques, such as X-ray computed tomography (CT). In addition,

OCT is a practical technique with high imaging resolution and excellent imaging sensitivity. Because of these superiorities, recent years have seen rapid developments and research into OCT-based imaging techniques in ophthalmology, cardiology, dermatology studies [4] and non-biomedical applications, such as art conservation [5], electronics production [6] and the pharmaceutical industry [7], etc.

One of the derivatives of OCT is the FF-OCT technique, which enables parallel (full-field) illumination of the sample with similar imaging quality [8]. It permits easier experimental operations, while achieving quicker three-dimensional (3-D) structural evaluation, compared to the classic OCT system.

This work is concentrated on the development of a low-cost FF-OCT system and the evaluation of its imaging performance for different applications. The FF-OCT system is assembled with inexpensive systematic elements including optical components and controlling devices, while it features a simple configuration, a fast image acquisition speed, simple experimental operations, and ease of use. The potential of the developed FF-OCT system is explored in terms of both tomographic imaging and surface topography for several applications.

The thesis is going to describe the development of the FF-OCT system, and demonstrate the usefulness of the built system in ophthalmological, pharmaceutical and industrial applications.

1.2 Thesis Motivation and Objectives

1.2.1 Development of the FF-OCT System

OCT is technically versatile for many applications, as it performs non-contact, non-invasive measurements, delivers spatially resolved information about internal structures, and provides images with micrometre-scale resolution.

However, OCT systems employing single-point schemes generally require rigorous alignments of the system elements and perform a lot of scans (transversely and longitudinally) during measurement. In terms of cost and ease of use, FF-OCT is considered more appropriate than other OCT variants, as it uses parallel detection and performs quick measurements of 3-D volumetric images. Additionally, it inherits all the technical properties of OCT, such as performing non-destructive imaging with a micrometre-scale depth resolution, evaluating the internal structure by cross-sectional images, etc.

Measurement with the FF-OCT system should be designed to have fast data acquisition and superior imaging performance, while the system itself is expected to be easy to use, low-cost, experimentally convenient and adaptable. A commercial FF-OCT system could be an option, yet, it is neither economically friendly nor universal for unspecified applications. There could also be some limitations with commercial systems, e.g. the maximum allowed field of view, which could induce problems for large or varied shaped samples to be properly positioned.

1.2.2 Tomographic Imaging

1.2.2.1 Characterisation of Pellet Coatings

Pharmaceutical dosage forms typically contain active drug components for the diagnosis, cure, treatment, or prevention of disease during drug therapy [9]. The use of coatings or shells for many modern solid dosage forms (tablets and nonpareil seeds) enables the extension or control of the drug release, as needed in order to safely achieve the desired therapeutic effect. Ideally, designated coatings are dissolved over a period of time in a controlled manner until the active substances reach the target area of the body. As the drug dissolution profile is closely related to the physical properties of coatings, various techniques are used to assess the coating quality in accordance with manufacturer specifications.

Pharmaceutical manufacturers traditionally determine the coating process endpoint by taking samples in-process, weighing a known sample size and determining the theoretical amount of polymer added. NIR spectroscopy is a more rapid method gaining acceptance in industry and has been used to non-destructively evaluate the coating quality [10]. However, both methods lead to a conservative estimation of the coating thickness, on the basis of gained weight and calibration models, respectively. In addition, the mean coating thickness obtained from these empirical measurements is not likely to provide detailed information about the coating characteristics (e.g. coating layer uniformity, porosity). Their abilities to predict the coating quality and imply the drug release profile are thus limited. These issues also apply to the small-size pellets that are described in this thesis; besides this, the pellet samples are additionally difficult to be measured experimentally due to their small size.

Therefore, the developed FF-OCT system is employed for the characterisation of the coating structure of small-size pellets, in order to demonstrate the potential of the system for the tomographic imaging of pharmaceutical applications.

1.2.2.2 Imaging of the Ultra-fine Corneal Layers

The cornea is the transparent front part of the eye that contributes to most of the eye's focusing power. The diagnosis of the human cornea is of great importance as regards corneal condition, symptoms and treatment [11]. Both the central corneal thickness (CCT) and the properties of corneal layers are essential in the analysis of new corneal transplantation techniques, diagnosis of ocular disorders, observation of surgical incisions, etc. In order to evaluate the extent of corneal disorders, such as corneal oedema and erosion, it is necessary to explore the ultra-fine corneal layer structure.

Prior to corneal surgery, such as the laser-assisted in situ keratomileusis (LASIK) surgery, corneal pachymetry is performed to measure CCT for ensuring sufficient thickness to prevent abnormal bulging of the cornea. It is also considered an important test in the early detection of glaucoma. The established ultrasonic pachymeter can measure single-point CCT when the ultrasound transducer touches the cornea. The non-contact ultrasound biomicroscopy (UBM) creates real-time cross-sectional images in a very cost-effective manner. It uses higher frequency transducers hence a finer resolution (e.g. 25 µm), to identify more superficial structures in the qualitative and quantitative assessment of the cornea [12]. However, the imaging operation requires water immersion of the UBM transducer, leading to discomfort for patients [13].

OCT is the most promising imaging technique used in ophthalmology today [14]. Compared to the UBM technique, OCT offers new diagnostic options with higher definition images upon multiple meridians across the cornea surface. The non-invasive and non-contact properties make OCT a better choice in the pre-surgical and post-surgical evaluation of the cornea. OCT techniques have been used as an analytical tool for the study of the layer structure and diagnosis of corneal disorders. However, the imaging of ultra-fine layer boundaries is always challenging when using commercially available OCT systems. Thus, to reveal the fine structure of the cornea, OCT resolution or precision can be improved by developing OCT systems.

Therefore, the developed FF-OCT system is used to measure cornea samples to determine whether it can detect the fine corneal structure. This could illustrate the potential of the system for the tomographic imaging of ophthalmological applications.

1.2.2.3 Inspection of Paints

Painting on metal or glass fibre or rigid plastic panels is an essential step during automotive manufacturing. It is favoured to give a sparkling appearance and provide protection to

vehicles [15]. Inspection of paint films is required during the coating process in order to ensure adequate protective coverage and at the same time to control coating costs. In the field of forensic science, the examination of paint chips can also be of evidential value in a variety of vehicle-related crimes [16].

Non-destructive methods including magnetic gauges, the eddy-current principle and ultrasonic gauges are used upon the completion of each layering work, making it possible to monitor the individual layer thicknesses in accordance with project specifications. However, all these methods require physical contact with the paint surface and only the single-point total paint thickness can be measured at any one time. In addition, the first two gauges only apply to paints on metal substrates.

Although these methods can provide a precise finish thickness, they require complicated monitoring procedures in order to meet industry standards, coating quality, and/or customer requirements. There's a need for an inspecting system to enable non-contact and direct measurement of all paint layer structures. On the other hand, spatial assessment of the paints is also considered beneficial for the control and verification of paint quality.

Therefore, the supplied panels with paint coated on mirror surfaces are measured by the developed FF-OCT system, in order to determine whether FF-OCT radiation can penetrate the paint material. This could indicate the potential of the system for the tomographic imaging of automotive paint applications.

1.2.3 Surface Measurements

Surface profilometry is significant in determining surface physical characteristics [17], including surface shape, roughness, curvature, etc. It can be used to identify artefacts and estimate the fabrication quality of the sample. It is also a useful predictor for the calibration of instrument performance.

Contact profilometers such as stylus profilometer and atomic force microscopy (AFM) are surface-profiling instruments that require physical contact with the sample [18]. The pseudo-contact method of scanning tunnelling microscopy (STM) employs quantum tunnelling to eliminate physical contact between the tip and the substrate. It can measure very tiny surface variations in vertical probe (stylus or tip) displacements as a function of position. However, it is protracted to do 3-D scanning and there could be surface wear by the probe. Moreover, it cannot normally measure steep walls or overhangs owing to the nature of the probe. On the other hand, the optical profilometer employs non-contact measurement using direct interferometry techniques [19], such as coherence scanning interferometry (CSI)and

vertical scanning interferometry (VSI), of which the systems have a lower cost and an easier data acquisition for 3-D scans.

For the semiconductor microelectronics and the polymethyl-methacrylate (PMMA) models in this thesis, an optical profilometer is expected to be used for 3-D representation due to its non-contact profiling scheme and the relatively large area of the surface region of interest (ROI). Regarding the specific requirements of both applications, it is needed for the profilometer to be able to differentiate nanometre-scale height difference; 3-D surface topography is also required to be produced for the evaluation of surface variation and curvature.

Therefore, their surfaces are measured by the developed FF-OCT system, in order to determine whether the system can obtain their surface topography to evaluate electrode thickness and refractive power. This could suggest the potential of the system for the surface profiling.

1.2.4 Thesis Objective

As stated in the preceding sections, FF-OCT is an imaging modality that offers a few advantages: performing non-contact measurements, utilising non-invasive radiations, spatially evaluating internal structures, producing cross-sectional images with micrometre-scale resolution, and operating fast data acquisition.

This thesis is devoted to the development of a simple FF-OCT system for the tomographic imaging and surface topography of various applications. The developed FF-OCT system is desired to have a low cost, simple configuration, fast image acquisition speed, simple experimental operations and ease of use. The system is also expected to have good imaging and profiling capabilities, in order to be readily available for a wide range of applications.

In addition, the system should allow for high-precision imaging and surface profiling. To evaluate the system's potential for tomographic imaging, the small-size pellet coating, the cornea and the paint panels are measured, in order to evaluate whether the system is precise and sensitive enough to detect internal structural features. To evaluate the system's potential for tomographic imaging, the semiconductor microelectronics and the PMMA model are measured, in order to assess whether the system can profile the nanometre-scale surface variations.

1.3 Thesis Outline

The written thesis is composed of six chapters.

Chapter 2 begins by introducing the OCT technique and conventional techniques for the 3-D imaging and surface metrology. Then, the OCT technique is further explored as regards OCT development and major findings described in ophthalmology, cardiology, etc. The principle of OCT is explained and discriminated from similar techniques in terms of tomography and interferometry. Three OCT variants including time-domain OCT, Fourier-domain OCT and FF-OCT are described with respect to their system layout, operational scheme, etc.

Chapter 3 systematically presents the development of the simple FF-OCT system. This chapter first introduces the principle of imaging and surface profiling by using the FF-OCT technique. System development is described in terms of the system setup, experimental procedures and data analysis for both imaging and surface profiling. The robustness of the simple system is demonstrated by the performance parameters including micrometre-scale spatial resolution and system sensitivity. The simple system is compared with the phase-shifting FF-OCT system, which is developed for the purpose of enhanced system sensitivity. Experimental efficiency, system performance, adaptability to different applications, etc. of the simple FF-OCT system is evaluated.

Chapter 4 illustrates tomographic imaging studies by using the simple FF-OCT system.

Section 4.1 delivers the evaluation of pharmaceutical coatings of small-size pellets using the simple FF-OCT system, which detects refractive variations to indicate structural changes. It starts by an overview of analytical techniques for assessing pellet coating quality, such as weight gain and NIR spectroscopy. Then, a brief description of each small-size pellet is given first, followed by the described coating characterisation using the simple system. With the reconstructed cross-sectional images, these pellets are discriminated with different coating structures; the thickness of each coating layer can be measured precisely down to micrometre scale, allowing for the presentation of coating structures and an accurate evaluation of coating quality. The X-ray micro-CT technique is used to validate the simple FF-OCT system for the imaging of pellet coatings.

Section 4.2 first briefly describes the fine corneal structures. Both the corneal layers and possible corneal disorders that could result in corneal structure change

are introduced. Then, measurements of the cornea using state-of-the-art OCT techniques are reviewed. Subsequently, the characterisation of internal layers of a healthy bovine cornea using the simple FF-OCT system is presented with clear layer boundaries and measurable corneal thickness. Based on the obtained corneal structural results, the potential of the simple FF-OCT system for the diagnosis of mentioned corneal disorders is discussed.

Section 4.3 gives a presentation of the characterisation of paint films coated on a mirror surface by using the simple FF-OCT system. It begins by giving brief background information including the function and configuration of automotive paints. Conventional paint quality assessment methods are described and evaluated. The characterisations of these panels with the simple system are reported in detail, with the paint surface and subsurface identified using FF-OCT images and signals. The measured paint thicknesses are compared with that obtained from the reference method, in order to determine whether the simple FF-OCT system is capable of providing accurate spatial evaluation of paint films. After that, there is a discussion regarding the potential of the FF-OCT technique for the assessment of the actual automotive paint during the manufacturing process.

Chapter 5 reports surface topography studies by using the simple FF-OCT system. The analysis of phase change upon reflections in interferometric profilometry is first briefly introduced, and then the FF-OCT technique for surface topography is validated by the AFM method in the measurement of the surface step of a semiconductor sample. Subsequently, the simple FF-OCT system is used in the surface topography of two microelectronics to determine electrode thickness. PMMA models are also measured with the simple system. The FF-OCT measured surface map is used to compute the refractive power for each PMMA model.

Chapter 6 concludes this thesis by giving a summary of the results obtained.

Appendix A provides a list of symbols and abbreviations appearing in each chapter.

1.4 Contribution of Research

The major contributions of this thesis are:

- The development of a low-cost FF-OCT system with apparent simplicity, improved practicality, and retained good imaging performance;

- The structural evaluation of pharmaceutical coatings of small-size pellets using the FF-OCT system.

This thesis describes, for the first time, an original work on the coating characterisation of the pharmaceutical pellet using presented methods, including the quantitative evaluation of coating structures with measurable spatial thicknesses using the simple FF-OCT system, the analysis of coating uniformity with identified structural changes, and the qualitative assessment of the coating's physical characteristics. It also covers the verification of the FF-OCT measurement utilising the X-rays micro-CT (XμCT) method, which produces consistent coating structures of the pellet.

The simple system has also been used for the identification of ultra-fine corneal structures and the non-contact revealing of paint layer structures. The obtained results confirm that the proposed method provides accurate descriptions of sample subsurface formation, from the layer structures and material uniformity. Agreement with literature or results which are based on reference methods have shown that the simple FF-OCT system is powerful with regard to the structural characterisations of both biomedical and industrial applications.

This thesis also proposes that the FF-OCT technique can be used to spatially assess refractive power based on measured actual surface shape. With the interferometric technique, the surface height can be accurately measured with sub-micrometre-scale precision. Consequently, the simple FF-OCT system is competent to resolve nanostructured surface variations of semiconductor microelectronics, providing comparable surface topography with that of the reference method. Hence, the simple FF-OCT system offers great convenience and precision to evaluate surface characteristics, allowing for further investigations such as the refraction analysis of PMMA models and the electrode thickness of microelectronics.

1.5 Auto-bibliography

List of the publications produced from this work:

1. **C. Li**, J. A. Zeitler, Y. Dong, and Y. C. Shen, "Non-destructive Evaluation of Polymer Coating Structures on Pharmaceutical Pellets using Full-Field Optical Coherence Tomography," J. Pharm. Sci., 103, 1, 161-166, Jan. 2014.

2. H. Shen, L. Gan, N. Newman, Y. Dong, **C. Li**, Y. Huang, and Y. C. Shen, "Spinning disk for compressive imaging," Opt. Lett., 37, 1, 46-48, Jan. 2012.

3. **C. Li**, Y. Dong, Y. C. Shen, "Characterisation of tablet coatings using infrared optical coherence tomography," Poster session presented at Photon 12 conference, 3-6 Sep. 2012, Durham, United Kingdom.

4. H. Shen, V. Abolghasemi, L. Gan, **C. Li**, Y. C. Shen, "Compressive three-dimensional (3D) terahertz imaging," Poster session presented at Photon 12 conference, 3-6 Sep. 2012, Durham, United Kingdom.

5. **C. Li**, Y. C. Shen, "Characterisation and surface topography of tablet coatings using optical coherence tomography", Oral presentation session at Mass Spectrometry, Surface Tomography and Sensing workshop, 21 Mar. 2012, Liverpool, United Kingdom.

Chapter 2

Overview of Optical Coherence Tomography

2.1 Introduction

This chapter begins by introducing the OCT technique and presents its utilisation in the non-destructive imaging of the internal structure and the surface metrology. Then, it presents its key technical advantages over conventional methods, including radiography, profilometry and microscopy techniques, on the basis of their imaging and profiling characteristics. Subsequently, the development of the OCT-based imaging techniques is demonstrated with major findings described in ophthalmology, cardiology and other biomedical areas. The fundamental principle of OCT is explained and discriminated from similar techniques in terms of tomography and interferometry. OCT variants including time-domain OCT, and Fourier-domain OCT are described in details with respect to their system configuration, mathematical treatment, operational schemes, performance characteristics, and so on. The subsequent section overviews the FF-OCT technique from its configuration and operations. The high spatial resolution, fast imaging speed and good sensitivity are acquired using FF-OCT. It is thus beneficial to develop custom-built FF-OCT systems to achieve further experimental efficiency and system performance.

2.2 Background

2.2.1 Imaging

Imaging is a technique of creating a visual representation of an object for diagnostic analysis or performance evaluation. In the biomedical context, analysis of specimen's internal structures is of great importance for the understanding of the form and functioning of living organisms, as well as studying of the formation and development of possible disease. In the industrial context, structural monitoring is a key procedure for the assessment of the manufactured product to specification and the control of the usage of raw materials. Imaging systems employ electromagnetic (EM) waves to penetrate though the sample surface, while either reflecting or transmitting waves are detected as indications of internal structures covered by media and surface. A set of methods is designated as imaging techniques that seek to noninvasively produce images of internal structures, in order to identify abnormalities, such as diseases and defects.

Medical imaging has long been using X-rays (30 PHz to 30 EHz) for the detection of pathology of the skeletal system [20] and processes of lung disease [21], as the bone exhibits much higher X-rays absorptions than tissue types and trapped gas or lungs. X-rays CT enables the production of volumetric data to demonstrate various bodily structures [22]. Ultrasonography is an ultrasound-based (1 MHz to 18 MHz) diagnostic imaging technique that detects sound echoes for the representation of internal body structures [23]. It has been widely used to examine the fetus inside a pregnant woman's uterus [24]. In case of nuclear medicine, magnetic resonance imaging (MRI) is a complementary imaging technique to X-rays CT in many applications, e.g. cardiovascular [25], liver [26] and gastrointestinal imaging [27]. It is more sensitive for small tumours [28] and offers better contrast of the central nervous system in neuroimaging [29]. Recent years have seen rapid developments of imaging techniques in the infrared frequency range (0.3 THz to 300 THz). These analytical techniques including NIR spectroscopy and imaging (NIRSI), terahertz pulsed imaging (TPI) and OCT allow more precise measurements of specific parts, such as biomedical tissues [30–32]. Besides biomedical applications, they have been utilised for studies spanning a number of disciplines.

2.2.2 Surface Topography

Surface metrology refers to measuring the surface topography (or surface roughness), conceptually including surface shape, surface finish, surface texture, step height measurement,

asperity and structural characterisation. The surface topography is essential to determine the suitability of a surface for a particular function, for example, the nanometre scale electrode thickness has great impact on the efficiency of the solar cells [33]. For a precision fabricated component, the low performance or the component failure is often traced back to a surface that was not manufactured to its specification, either due to an improperly set up machine or use of a process that is not capable of repeatedly producing the quality of surface needed.

To enable quantitative examination of the surface, two parallel branches of instrumentation were developed: one follows the contact method (tactile measurement) with a stylus and the other makes use of optical light to perform non-contact measurements. The past few decades have seen rapid development for surface measurement techniques. Both contact and non-contact methods are converging to satisfy linear and areal measurement requirements. The contact instruments have progressed from the conventional stylus profilometer to modern AFM systems, which can operate at sub-nanometre scale along the vertical direction. With the invention of STM, non-contact surface imaging at true atomic-level is available under near real-time scanning. Optical profilometers operate much quicker for an areal measurements as they do not contact the surface. Neither do wears occur to the surface nor are there stylus damages by the rough surface, which could potentially lead to a change in resolution [34]. Commercial non-contact instrument based on white light interferometry (e.g. NT9080, Veeco Instruments, Inc.) can effectively measure vertical distance in sub-nanometre level. Other interferometric techniques including CSI, VSI and OCT are also widely used for the surface topography studies. Despite of the lack of calibration standard for non-contact measurements, optical profilometers are gaining acceptance by standardisation committees.

2.3 Optical Coherence Tomography

OCT is an established medical imaging technique that uses low (temporal-) coherence optical light to investigate the physical structure of specimen (e.g. biological tissue) at near-microscopic resolution. It has been used as an analytical tool for characterising interior structures and surface texture from within optical scattering media. It relies on optical tomography that performs optical sectioning and creates a digital volumetric model of the sample. Evaluation of sample structures are based on the analysis of OCT cross-sectional images and reconstructed volumetric representations. However, interferometry is also a key aspect of OCT to enable precise measurements of structural features, variations of internal refractive index and superficial irregularities. High resolution OCT imaging of internal microstructures is permitted by employing low-coherence light source for illumination of

the sample in an OCT system, owing to corresponding interference occurrence over a short distance of micrometres.

Since its proposal in ophthalmic studies, OCT has been attracting interest within the medical community because of its non-invasive imaging property. However, OCT's capability to offer superb characterisation of sample internal structure with micrometre spatial resolution makes it stand out among other medical imaging systems. An overview of the imaging resolution and the penetration depth among the most common imaging techniques is provided in Fig. 2.1. As illustrated in this figure, X-ray CT, MRI and conventional ultrasonography can penetrate through the whole body but have low resolution imaging capability (typically a fraction of a millimetre) [35]. Confocal microscopy is advantageous to deliver micrograph of cells or tissues with sub-cellular imaging resolution. However, it is only able to probe up to 100 μm in depth and usually requires fluorescent staining during specimen preparation [36]. The prevalent NIRSI and TPI techniques provide more balanced spatial resolution ($>$20 μm) and penetration depths ($<$10 mm) that are adequate for many applications [37, 38]. Nevertheless, better spatial resolution are still required, e.g. to delineate the internal structures of retina and coronary arteries. OCT is capable of imaging features at a relatively high resolution (better than 10 μm) with millimetre scale probing depth, as shown in Fig. 2.1. It also provides a competitive imaging contrast based on the principle of interferometry. Hence, OCT acts as a complement to those conventional imaging techniques, providing better imaging and more detailed characterisation, especially for ophthalmic applications and biomedical tissues which demands micrometre resolution and millimetre penetration depth.

In addition to interior structure imaging, OCT has been adapted for surface measurements in order to quantify surface roughness, to measure step height, and to detect surface defects. These surface properties are traditionally measured with standardised methods [39], such as stylus profilometer, AFM, and STM. The former two require physical contact with the surface and usually take long for a typical areal scan. The latter can only scan conductive surfaces or thin nonconductive films and small objects deposited on conductive substrates [40], though the surface measurement is non-contact with achievable atomic level resolution. Optical profilometers generally perform surface profiling in a non-contact manner to eliminate abrasion on both surface and instrument stylus. Their scanning speeds are hence much quicker than contact methods. Confocal microscopy features high spatial resolution, but surface positions are indirectly derived based on the detected response (i.e. intensity) at the corresponding transverse location along the axial direction [41]. OCT and other interferometric profilometers based on white light interferometry (WLI), phase-shifting interferometry (PSI) and VSI can also achieve comparable nanometre precision [42] (limited

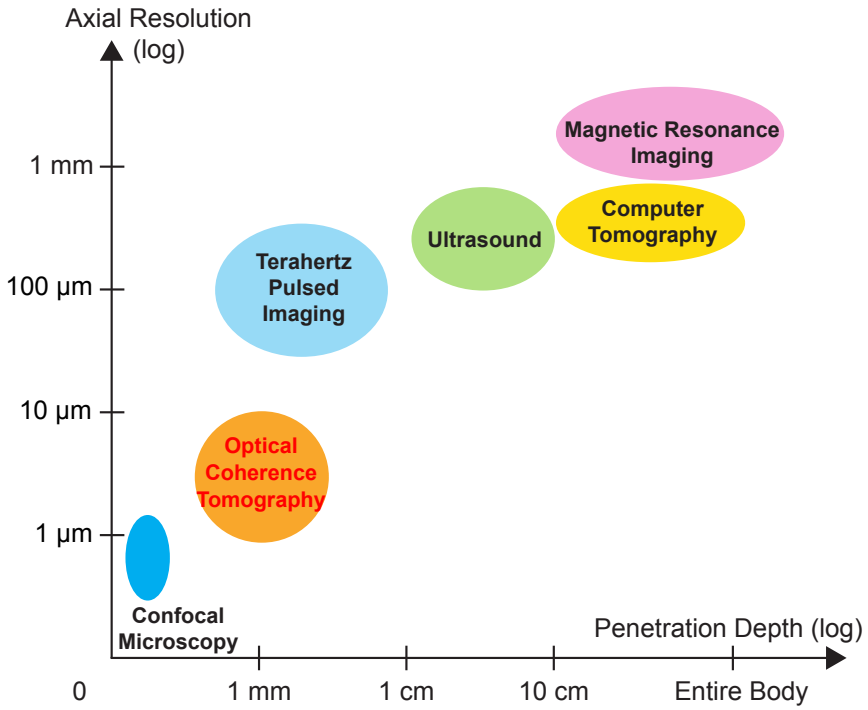

Fig. 2.1 An overview of the axial resolution and the penetration depth for imaging modalities including X-ray CT, MRI, ultrasonography, TPI, OCT and confocal microscopy.

by the system noise level [43]) on a smooth and reflective surface. However, they record interference waves instead and the surface position is directly measured by the peak position of the corresponding interference wave. In addition, large scale areal measurement is practical by using optical interferometric profilometry as they provide fast profiling. The large scale field of view can be easily acquired by adjusting the bulk-optics system.

Therefore, OCT is a great imaging modality, allowing both high resolution imaging of internal structure and high-precision profiling of superficial features.

2.3.1 Development of OCT

OCT is based on low-coherence interferometry (LCI), which has been used for non-contact depth ranging measurements with micrometre spatial resolution and superb sensitivities [44], such as non-destructively determination of the eye-length [45] and mapping of the surface contour of integrated circuits [46].

The concept of OCT to enable 3-D tomographic imaging with high precision and sensitivity was first pioneered by Huang *et al.* in 1991 for the retina analysis, which demonstrates OCT's potential to deliver a few micrometres spatial resolution and to detect

reflected signal as small as 10^{-10} of the incident optical power [1]. With the proposed time-domain OCT, it is possible to synthesise a cross-sectional image from a series of adjacent LCI depth scan signals by a photodetector; hence a 3-D image can be reconstructed by combining a series of adjacent cross-sectional images. Since then, a large amount of research was conducted regarding OCT development and applications covering various areas such as ophthalmology [3], cardiology [47], etc. Low (temporal-) coherent light sources, optical fibres, longitudinal and lateral translation devices are normally used in a standard OCT system. The most popular superluminescent semiconductor diodes (SLDs) and femtosecond lasers light sources have yielded 4.5 µm [48] and approximately 1 µm [49] depth resolution in OCT, respectively.

Fourier-domain (frequency-domain) OCT was proposed in 1995 by Fercher *et al* [50], following the generation of Fourier-domain OCT images in 1997 and 1998 [51–53]. The frequency-domain method broke the routine of time-domain OCT as the only method of OCT. The time-domain depth scans were replaced by spectroscopic measurements using a spectrometer (spectral-domain OCT) [54, 55] or by scanning the wavelength of a tuneable laser (swept-source OCT) [56, 57]. In terms of the imaging performance, Fourier-domain OCT exhibit same spatial resolution and faster scanning speed [58]. Moreover, it enhances the system sensitivity by, e.g. an improvement of 21.7 dB, over time-domain OCT [59] and is hence able to deal with more turbid sample structures [60].

Nevertheless, full-field OCT was proposed by Beaurepaire *et al* in 1998 [8] to produce tomographic images in the *en-face* orientation (orthogonal to the optical axis) without scanning a light beam laterally on a sample. It has become a prevalent OCT variant owing to the rapid development of high speed high definition cameras, which are capable of a shortened measurement time and an improved imaging performance. This powerful technique employs a parallel detection scheme, allowing an even faster scanning speed than the conventional point-scan time-domain and Fourier-domain OCT for a 3-D imaging. Besides, high spatial resolution, e.g. <1 µm, is allowed if the system is coupled with high numerical aperture (NA) optics and sufficient camera pixel size [61]. However, in contrast to single point detection schemes, the entire field of image is illuminated by low temporal and low spatial coherent light [62–64]. Tungsten halogen lamps and infrared light-emitting diodes (LED) are thus frequently adopted [61, 65] due to their spatially low coherence and low cost. While performing quicker and simpler measurement [66], FF-OCT systems employing these thermal light sources can deliver comparable depth resolutions with the standard OCT systems using sophisticated femtosecond lasers.

2.3.2 Applications of OCT

Since the introduction of OCT, the non-invasive technique has been mainly applied for imaging in ophthalmology and optometry [67, 68]. Advances in OCT technology have made it possible to be used in a wide variety of applications during the past decade. The micrometre spatial resolution allows high precision investigations of both interior imaging and surface topography of specimen. The superior interferometric detection sensitivity enables optical radiation to penetrate reasonably deep into biomedical tissues and industrial materials [4, 69]. This section only presents a brief overview of some OCT applications, covering the main biomedical and non-biomedical applications.

a. Biomedical Applications

Ophthalmology is still the dominating field of the biomedical OCT. The ocular media generally exhibit high transmittance and low scattering in the visible and NIR region, which allows effective interferometric sensitivity and precision in the OCT imaging [3]. Furthermore, imaging of the fundus of the eye, especially the retinal structure can be perfectly fulfilled by OCT with high depth resolution at a lower beam NA. [4] (i.e. better penetration depth). Retinal OCT has been reigning in ophthalmology studies for the measurement of details of retinal pathologies [14, 56, 67, 70] and diagnosis of retinal disorders, such as macular degeneration [71–74] and macular oedema [75–79]. The evaluation of retinal nerve fibre layer, optic nerve head and macular thickness using OCT helps the detection and management of glaucoma [80–84]. Recently, the OCT technology is enhanced to be able to penetrate into the choroid [85–88] and measure choroidal thickness in normal eyes [89, 90].

In addition, OCT is helpful to investigate anterior segment [14, 91, 92], i.e. to image and measure corneal pathologies and structural changes of the chamber angle and iris. Anterior segment OCT provides comparable results with the conventional ultrasound biomicroscopy (UBM) method, but OCT is featured with a higher spatial resolution [93, 94]. Furthermore, OCT has also been applied to monitor the corneal laser ablation [95, 96] and cataract surgery [97].

OCT is also an important analytical tool for other biomedical disciplines such as cardiology [47, 98] and gastroenterology [98]. Both of the two subjects require intraluminal imaging into the small coronary arteries and the gastrointestinal (GI) tract, respectively. These conditions are accessible to endoscopic OCT, which uses a catheter integrated with fibre optics to detect disorders at the innermost layer [4].

Intracoronary OCT has been demonstrated as a safe and effective modality for characterising coronary atherosclerosis and vulnerable plaques [99–102], which are primary indications of acute coronary events including acute myocardial infarction (AMI) [103] and acute coronary syndromes (ACS) [104]. OCT delivers consistent image features with intravascular ultrasound (IVUS), which is the conventional standard for intracoronary imaging [99, 103]. However, OCT images turn out to have much better depth resolution than high frequency IVUS [105–107].

Likewise, endoscopic OCT with a catheter probe is applied to investigate GI track with several millimetres penetration depth and micrometre-scale spatial resolution. The GI wall structure is of a multiple layer architecture. OCT characterisation of the GI wall permits an accurate evaluation of the mucosa, lamina propria, muscularis mucosae, and part of the submucosa [4, 108, 109]. OCT has been used to predict the presence of many disorders of the GI tract, including dysplasia [110–114], metaplasia [115, 116], Barrett's esophagus [111, 112, 117, 118], intramucosal carcinoma [112], adenocarcinoma [113, 117], malignancy [114, 119, 120], etc. Furthermore, the pancreatico-biliary ductal system can be explored by a side-view endoscopic OCT catheter probe [113]. The OCT resolution can be 10 times better (about 10 μm) than with the emerging catheter-probe endoscopic ultrasonography (CPEUS), but OCT's depth of penetration is up to 3 mm [113]. Hence, it is potential that OCT and CPEUS can become complementary techniques for high-resolution endoscopic imaging of the GI tract [121].

Further biomedical applications using OCT techniques are in developmental biology, dermatology, dentistry, laryngology, pulmonary medicine, etc. [122–124]. Their histological architectures are evaluated by OCT, functioning as the optical biopsy to make an instant diagnosis at endoscopy. Previously, this was only possible by using histological or cytological analysis, which requires removal of a tissue specimen and processing for microscopic examination [2, 32, 125, 126].

b. Non-biomedical Applications

OCT enables a non-contact, non-invasive, and high-resolution imaging of subsurface features. It is already a well-established diagnostics technique in biomedical areas. However, OCT has been receiving attention as a non-destructive testing (NDT) tool for non-biomedical applications, with more and more research groups being engaged in further exploring possible applications of OCT [127, 128].

First, the use of OCT technique has grown in art and cultural heritage artefacts studies, e.g. non-destructive investigations of varnish layer, paint layer and underdrawings in oil

paintings [5, 129, 130]. Second, layer structures (or thicknesses) of moving plastic foils can be monitored with an in-line OCT system along with the foil production [131], which is applicable in the food packaging industry. Third, the potential of OCT has been demonstrated to non-destructively monitor coating structures of pharmaceutical tablets [7, 132, 133]. This helps control the manufacturing procedure and maintain the drug effectiveness in a more precise manner than the conventional ways, such as the weight-gain method.

Besides, OCT has also been used for contactless and faster measurements of textile roughness or surface topography, e.g. in printed electronics products quality [6] and in paper industry [134, 135]. Furthermore, OCT has been introduced for the characterisation of laser-drilled holes and micro-machined devices [136], organic solar cells [137], aerospace materials [138, 139], etc. Hence, OCT techniques help NDT of a wide variety of material systems and processes. The use of faster and more robust OCT devices in industrial environments is desired to enable the *in situ* and real-time monitoring of industrial processes [127].

2.4 Principle of OCT

OCT is one of the optical interferometric techniques, which use superimposed EM waves or light beams to extract information about surface irregularities, subsurface structures [140, 141], and refractive indices [142]. Interferometry makes use of the principle of superposition to combine EM waves with same frequency in a way that the resulting pattern is determined by the phase difference between the two waves; constructive interference occurs when two waves are in phase, while destructive interference occurs if two waves are out of phase.

Conventional interferometry with temporal-coherence light source (e.g. narrow-linewidth laser) tends to have interference occurrence over a distance of meters. OCT and other interferometric techniques such as WLI, VSI (or CSI), PSI can be used in the context of LCI and typically configured in Michelson interferometers. These techniques all essentially apply the time-of-flight measurements [44], which measure the difference in the flight times of signals to travel a distance through a medium. The distance measurements are associated with interference events.

Despite that these techniques have been applied in surface profile measurements according to the localisation of interference fringes [143, 144], they are used to serve different purposes. WLI generally uses a broad optical bandwidth (usually 100 nm or more) light source for distance measurements and the measurement of chromatic dispersion [145]; while laser

sources (or monochromatic radiation) can be used in PSI and VSI for laser beam wavelength measurements and measurement of the moving speed of an interferometer arm [146]. OCT employs a low (temporal-) coherence light source in a Michelson interferometer, although the linewidth of the radiation does not need to be broadband like WLI. In terms of signal acquisition, VSI moves a sample along the optical axis over the full depth range of the sample and measures the position of maximum fringe contrast (i.e. the fringe centre) to determine the sample surface profile [147]; while PSI performs phase shifts by using a piezoelectric transducer (PT) or modulating the source central frequency, and records multiple interference signals with fixed phase intervals (a precise fraction of the source central wavelength between each exposure) to derive structural information [42].

OCT is also one of the tomographic techniques, which perform optical sectioning of a sample with EM or light waves. Other tomographic techniques like X-rays CT, MRI, positron emission tomography (PET), ultrasound-modulated optical tomography (UMOT), confocal laser scanning microscopy (CLSM) enable frontal plane or transverse plane sectioning in medical diagnosis and industrial inspections. Consequently, volumetric imaging can be realised by combining a series of adjacent optical sections, allowing a 3-D evaluation of internal structures. For single point scanning scheme, a cross-sectional image is synthesised from a series of adjacent depth or transverse profiles. Unlike these mentioned tomographic techniques, OCT features micrometre resolution, millimetre scale penetration depth and high detection sensitivity, allowing more precise characterisation of the fine structures. Hence it is adequate and advantageous for microstructure samples, such as biomedical tissues, small industrial components etc.

2.4.1 Basic OCT Configuration

a. Michelson Interferometer

From the invention of OCT technology, the majority of OCT interferometers are Michelson configurations implemented in fibre-optics or in bulk-optics [1, 69, 148]. The Michelson interferometer is the heart of a typical OCT system.

The design of Michelson interferometer is based on two-beam interferometer with amplitude division. It is of simple form to make measurement of sample structure using interferometry. A beamsplitter is contained in the configuration to divide (the intensity) an incoming beam into two equal (intensity) beams that travel along separate arms. After being reflected from mirrors on the two arms, the two beams are recombined at the beamsplitter. A condition is created until which interference can take place. This is largely dependent on the

relative phase or the difference between the optical path lengths (OPL) of the two recombined beams. Here, OPL is the product of the geometric length of the path light follows through the system, and the index of refraction of the medium through which it propagates. If the difference in OPL between the two beams, i.e. optical path difference (OPD), is within half a coherence length, interference between the beams can occur. Under above condition, the output interference beam intensity can be varied along with the changes of the OPD. The variations can thus be measured with a detector as a function of the OPD.

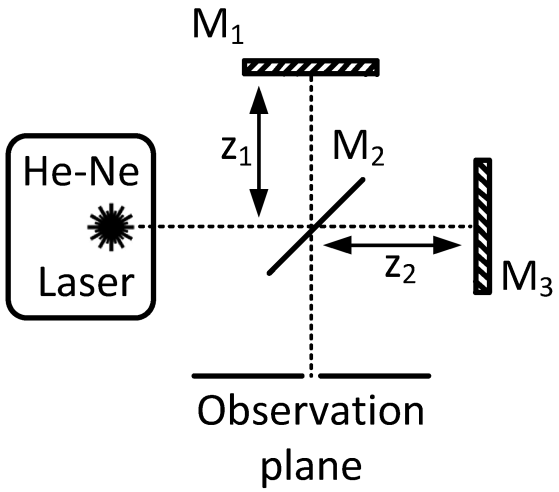

Fig. 2.2 Schematic diagram of a Michelson interferometer. M_2: 50 % beam-splitter, M_1, M_3: dielectric mirrors. Adapted from Lucki *et al* [149].

b. Basic OCT Components

Fig. 2.3 presents general components integrated with the Michelson configuration in a typical OCT systems. A low-coherence light source is used to illuminate the interferometer. The light beam is divided into two separate arms by the beamsplitter. Reflections or scattering would occur at both arms when beam wavefronts encounter the reference mirror and the sample. The two returned beams are reunited and combine their intensities at the beam-splitter. The resulting beam is typically directed to a photoelectric detector with the instantaneous light intensity recorded. To make measurements of the optical interference event, the returning sample and reference beams are made to interfere on condition that their OPD is within half the coherence length, where the output intensity is recorded by the detector.

The ideal OCT light source would yield strong enough (high power) radiation with temporally low coherence or incoherence [69]. Generally, a low coherent light source is required in an OCT system mainly to promote the depth resolution. However, the choices of

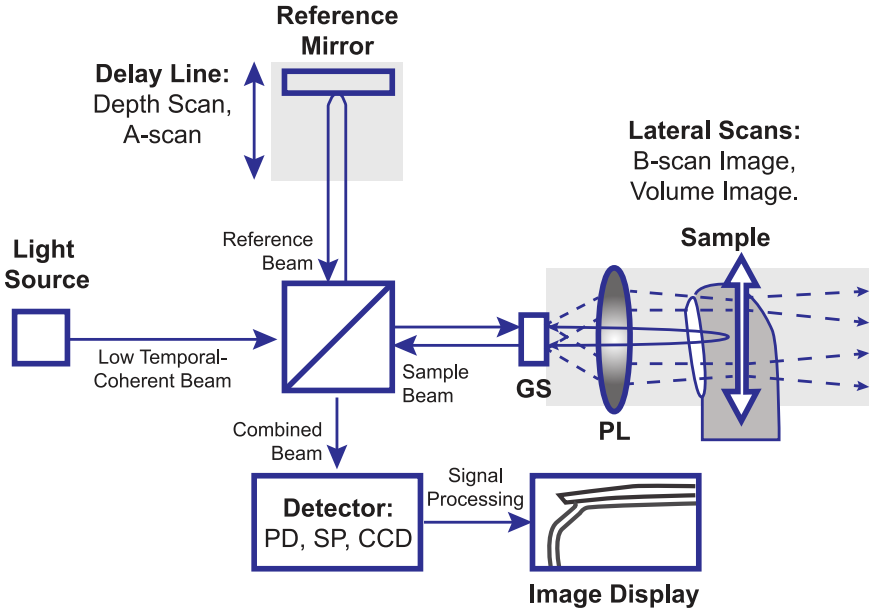

Fig. 2.3 Basic configuration and components of an OCT system. Light source: a low temporal-coherence light source. BS: beam-splitter to split source radiation into two arms with equal intensity. Reference Mirror: a plain mirror or window on the reference arm (it usually has similar reflectivity with the sample). Sample: the sample under test on the sample arm. GS: galvo scanner; PL: probing lens; PD: photo-detector; SP: spectrometer; CCD: charge coupled device;

source central wavelength and spectral width are crucial to the OCT imaging performance. According to the Beer-Lambert law, optical penetration depth is related to the material absorbance [150], which is strongly wavelength dependent [151]. Hence, OCT employing different spectral ranges leads to various OCT probing depths, for example, OCT applying NIR radiation can penetrate deeper than that with the white light in biomedical tissues. Besides, OCT depth resolution is defined by the temporal coherence of the light source, which is proportional to the central wavelength, and inverse proportional to the spectral width. Popular light sources in OCT include SLD [1], femtosecond Titanium-sapphire laser [49], photonic crystal fibre based light source [152, 153] and thermal source [154], etc. Note that, all optical components including the beam-splitter and detector should have a corresponding spectral range to the chosen light source.

The OCT detector is required to have superior performance characteristics including fast data acquisition speed and excellent sensitivity, noise and homogeneity [4]. Photodetectors equipped with charge coupled device (CCD) sensors and complementary metal-oxide-semiconductor (CMOS) sensors are used for high quality imaging performance [155]. Modern progresses made in CCD and CMOS technologies has led to faster acquisition speed and enable real-time imaging [156, 157].

OCT operating single-point scheme requires to perform depth scanning whilst laterally scanning the beam in either one or two orthogonal directions, in order to obtain a 2-D or 3-D image [158]. A control module should be included to operate all mechanical scans and trigger the data acquisition of the photodetector. A process module is also required to perform on-line or off-line data processing for the purpose of further characterisation, analysis and presentation of the OCT images.

In addition, OCT systems are generally composed of either bulk-optics or fibre-optics or a mixture of both setups. Traditional bulk-optics comprise discrete optical elements, which offers high flexibility and convenience in development, testing and maintenance, as one can easily remove or replace optical components and access optical powers or beam profiles [159]. However, fibre-based OCT systems are particularly adaptable to industrial environments [160]. They can access interiors of hard-to-reach spaces [161], and operate in hostile environments - whether radioactive, cryogenic, or very hot [162].

c. OCT Optics

The time-domain OCT and Fourier-domain OCT are two physical alternatives that exist for the OCT technique.

In time-domain OCT, sample depth structures are recorded as a sequence of partial temporal coherence interference signals [163]. These interference signals are generated by modulating the OPL of either one interferometer beam using optical delay lines, while their signal intensities are based on the complex of the back scattered sample beam and the back reflected reference beam. With this detection scheme, the weak structural signal from the sample is dramatically amplified by interfering with a strong coherent carrier wave [164].

Unlike the time-domain OCT with an OPL modulated beam, Fourier-domain OCT is operated in the frequency domain [50]. It can be implemented either based on a spectrometer detector (spectral-domain OCT) or on a tuneable laser source (swept-source OCT) [4]. While both interferometer arms remain fixed OPLs, the sample depth structural information can be derived by the inverse Fourier transform (FT) of the output spectrum of the interferometer. Both time-domain OCT and Fourier-domain OCT have been shown to be equivalent in terms of depth resolution [165].

Standard A-scan signals are derived from OCT interference signals after a depth scan in time-domain OCT, otherwise, they are obtained from the FT of OCT spectrums in Fourier-domain OCT. For both cases, A-scan signals convey single point structural information along the depth direction. OCT B-scan images are cross-sectional images synthesised from laterally adjacent OCT A-scans, analogous to ultrasound A-scans and B-scan images [4]. B-scan images present depth oriented 2-D structural distributions, which provide important information regarding the layer structure (or thickness) and media distribution, etc. OCT volume image is thus the combination of a series of laterally adjacent B-scan images, offering a straightforward presentation of the spatial or 3-D structural distribution. The spatial structure variations over time are also assessable with OCT.

To obtain A-scan signals and B-scan images, the depth scan is implemented with the linear translation stage in time-domain OCT. Fourier-domain OCT eliminates the needs of depth scanning, but requires inversely Fourier transformed spectrum to derive the A-scan signals. Lateral scans in single-point OCT systems are usually performed by laterally moving the sample under test or moving focus of the probing beam with the help of, e.g. a galvanometer scanner or a laterally scanning mirror [3]. Parallel OCT systems adopt a 2-D detector array, thus avoiding the needs of lateral scanning for the spatial evaluation of the sample, but it still requires OPL modulated depth-scan to record longitudinally distributed OCT signals.

d. Other OCT Configurations

OCT systems are commonly set up by using Michelson interferometers, which use a beam-splitter to divide the source light into separate paths and combine intensities of back reflected

light interferometrically. Other configurations based OCT systems, e.g. Fizeau [166], Mach–Zehnder [155], Fabry-Perot [68], and Linnik interferometers [8], have been proposed to serve performance enhancement and specific requirements. In addition, different beam probes have been incorporated to standard OCT systems for macroscopic, microscopic and endoscopic imaging purposes [69].

Optical coherence microscopy (OCM) aims at tomographic imaging with high transverse resolution [167]. It is generally implemented in a Linnik interferometer [8], which is essentially equipped with high NA lenses (such as microscopy objectives) in both interferometer arms to focus the probe beam at the sample or reference. Extremely high transverse resolution is achievable with the adoption of water / oil immersed objectives. As the depth resolution is decoupled of the transverse resolution, high depth resolution can be achieved simultaneously in OCM by the use of broadband light sources, like femtosecond lasers, photonic crystal fibre based or thermal light sources, etc.. Besides, OCM presents more effective optical sectioning over the conventional confocal scanning microscopy (CSM) in highly scattered samples, by providing improved rejection of scattering light at defocused planes [69]. It is potential to be used for real-time optical biopsy [32].

Endoscopic OCT is proposed for its superior spatial resolution and higher sensitivity compared to CPEUS for diagnosis of intra-abdominal organs [125]. By integrating a catheter with fibre-optic sample probe arm, the OCT instrument can enable imaging of intraluminal disorders and optical biopsy into organs for cancer diagnosis. The technique has been applied for imaging in GI tract and vascular systems clinically, while there remains a wide range of promising clinical applications, such as the respiratory tract, the ovary, the breast duct and the liver, where OCT endoscopes can have significant impact [168].

2.4.2 Time-Domain OCT

Typical time-domain OCT is based on the reflectometry LCI [1, 169], which is carried out in a Michelson interferometer by moving the reference mirror continuously along the beam axis. This is to perform a depth scanning to detect depth positions of back scattering sites in the sample. However, in addition to the LCI depth scans, time-domain OCT also needs the lateral scans to address laterally adjacent sample positions. Fig. 2.4 shows a time-domain OCT system and its representative outputs.

Essential system components include a translating motor stage for depth scanning, a galvo scanner for lateral scanning, and a photodetector (e.g. photodiode) for recording interference signals. Other common components of a standard OCT system are already considered, i.e. a

low-coherent light source, beam-splitter, a reference mirror, bulk optics. The control module is needed to operate the translating stage and the galvano scanner as well as the triggering of the photodetector. The processing module needs to be involved with low-pass filters and band-pass filters to process the recorded interference signals into the A-scan signals and display the resultant B-scan image for further analysis as shown in Fig. 2.4.

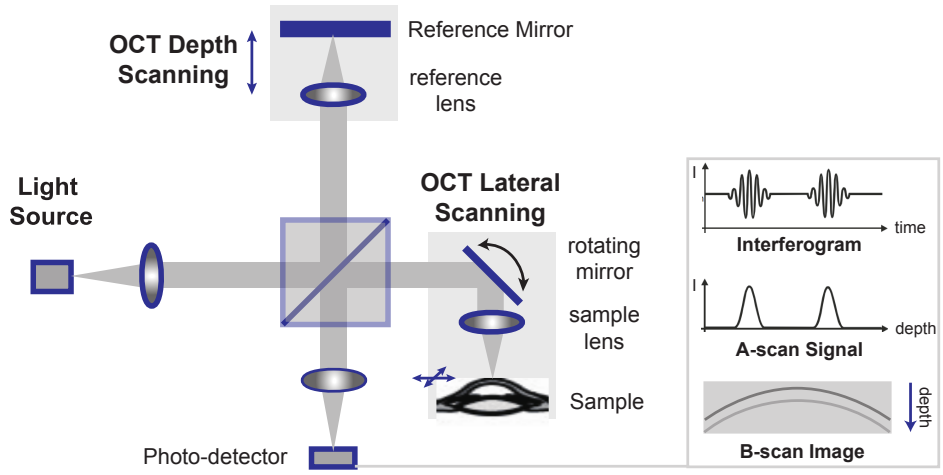

Fig. 2.4 Schematic diagram of time-domain OCT in free-space optics configuration. An interferogram is generated for each OCT depth scan. The A-scan signal is its real envelope, which can be extracted through a low-pass filter or band-pass filter. B-scan image is the combination of a series of depth scans performed after each OCT lateral scan.

To display a series of cross-section or B-scan images over time, conventional point-scan OCT also performs lateral scans either by laterally moving the sample or by moving the probe beam. It must scan the sample in two lateral dimensions to reconstruct a 3-D image of the sample volume by using depth information obtained by coherence-gating through an axially scanning reference arm. 2-D lateral scanning can be electromechanically implemented by moving the sample using a translation stage, or using a novel micro-electro-mechanical system scanner in a raster scanning style.

a. Theoretical Formulae

During the depth scanning of the reference mirror, the sample back scattering combines interferometrically with the reference reflections at the beam-splitter; the interferometric combination (namely, the interference phenomena) can be described as a second-order cross-correlation function of the sample scattering and the reference reflecting waves.

Considering $E_s(t)$ and $E_r(t,\tau)$ as the time-dependent electric fields from the sample and the reference, the recombined electric field $E_{out}(t,\tau)$ at the beam-splitter can be given by:

$$E_{out}(t,\tau) = E_s(t) + E_r(t,\tau) \tag{2.1}$$

However, the mutual coherence function between the two beams is expressed as:

$$\begin{aligned}\Gamma_{sr}(\tau) &= (E_s \star E_r)(\tau) \\ &= \langle E_s(t) E_r(t+\tau) \rangle \qquad (2.2) \\ &= \lim_{T\to\infty} \frac{1}{2T} \int_{-T}^{T} E_s(t) E_r(t+\tau) dt \qquad (2.3)\end{aligned}$$

In equations 2.1 - 2.3, τ is the time delay between two beams, denoting as $\tau = \Delta z/\upsilon$, where Δz is the OPD between the two beams and υ is the speed of light in vacuum; $\star$ indicates the cross-correlation of two terms; the angled brackets $\langle ... \rangle$ denote a time-average, suggesting an average amount of the enclosed term integrating over time (see equation 2.3).

The interferogram term $G_{sr}(\tau)$ given by twice the real part (indicated by $\Re[...]$) of the mutual coherence function $\Gamma_{sr}(\tau)$ can be specifically expanded as [3]:

$$\begin{aligned}G_{sr}(\tau) &= 2\Re\{\Gamma_{sr}(\tau)\} \\ &= 2\Re\{\frac{1}{2}\sqrt{I_s(t) I_r(t)}\, |\gamma_{sr}(\tau)|\, e^{i\Phi(\tau)}\} \\ &= \sqrt{I_s(t) I_r(t)}\, |\gamma_{sr}(\tau)| \cos\Phi(\tau) \qquad (2.4)\end{aligned}$$

Here, $I_s(t)$ and $I_r(t)$ are respective time-average intensities of sample and reference beams; $\gamma_{sr}(\tau)$ is the degree of coherence; the instantaneous phase $\Phi(\tau)$ is computed by $\alpha_0 - 2\pi\nu_0\tau$, where $2\pi\nu_0\tau$ is the phase delay between the sample and the reference beam, ν_0 is the source central frequency and α_0 is a constant phase.

The photo-detectors of time-domain OCT are square law detection devices, where the recorded intensity is a time-average intensity over the electric field multiplied by its complex conjugate [158]:

$$\begin{aligned}I_{PD}(\tau) &= \langle I_{out}(\tau) \rangle \\ &= \langle E_{out}(t,\tau) E^*_{out}(t,\tau) \rangle \qquad (2.5)\end{aligned}$$

Substituting equations 2.1, 2.2 and 2.4 into Equation 2.5, the photo-detector recorded intensity can be found as the sum of two beam intensities and their interferogram intensity:

$$\begin{aligned} I_{PD}(\tau) &= \langle E_s(t)E_s^*(t)\rangle + \langle E_r(t,\tau)E_r^*(t,\tau)\rangle + G_{sr}(\tau) \\ &= I_s(t) + I_r(t) + G_{sr}(\tau) \end{aligned} \tag{2.6}$$

The time delay τ is the corresponding optical time-of-flight difference, which is proportional to the OPD Δz induced by moving reference mirror by a geometric displacement $z = \tau c$. Hence, a single point time domain signal can be expressed in a more compact version as a function of z,

$$\begin{aligned} I_{PD}(z) &= I_s(t) + I_r(t) + G_{sr}(z) \\ &= I_{DC}(t) + M(z)\cos[\Phi(z)] \end{aligned} \tag{2.7}$$

where $I_{DC}(t) = I_s(t) + I_r(t)$ representing the *DC* intensity term from two interferometer arms, $G_{sr}(z) = M(z)\cos\Phi(z)$ is the displacement dependent interferogram term; and $M(z) = \sqrt{I_s(t)I_r(t)}\,|\gamma_{sr}(z)|$ stands for the envelope of the interferogram or the OCT A-scan signal, corresponding to sample structural variations along the depth direction; the instantaneous phase $\Phi(z) = \alpha_0 - 2\pi\nu_0 z/c$ is also depth dependent. However, the A-scan signal $M(z)$ can also be regarded as the analytical signal of the interferogram $G_{sr}(z)$. Hence, both the A-scan signal $M(z)$ and phase information $\Phi(z)$ can be obtained by $G_{sr}(z)$ and its Hilbert transform (HT) using Equations 2.8 and 2.9:

$$M(z) = \frac{1}{2}\sqrt{(G_{sr}(z))^2 + (HT\{G_{sr}(z)\})^2} \tag{2.8}$$

$$\Phi(z) = \arctan\left[\frac{HT\{G_{sr}(z)\}}{G_{sr}(z)}\right] \tag{2.9}$$

b. Depth Scanning with Heterodyne Detection

OCT configures in a Michelson interferometer, which splits source beam into sample and reference arms. The recombination of a sample wave and a reference wave at the beam-splitter creates a condition of an interference event, which requires OPLs of both wavefronts to be matched within half a coherence length. However, it is possible to observe only the intensity of an optical interference pattern at a specific depth, rather than provide a measure of structural information within the sample.

To measure the sample structure with optical radiation, the sample reflected electric waves need to be modulated from the optical band to an electronically tractable frequency range. Heterodyne detection can be used for shifting an input signal into a new frequency range [170]. It involves the mixing of a weak input signal with some strong local oscillator waves, resulting in a strong interference signal as the mixing product. Optical heterodyne detection is the implementation of heterodyne detection in optical communication. After a nonlinear combination, the detectable mixing product generally consists only the DC component and a low frequency component, which is the difference of the frequencies of the signal and the local oscillator, since all high frequency components are all filtered out by the electronic photodetector. Thereby, the photodetector enables background light rejection and the detection of weak input signal.

The local oscillator wave should be set at a close-by frequency ν_{LO} to that of the sample waves (ν_0), so that their frequency difference is low enough to be perceived by the detector. The mixer is commonly a photodetector (e.g. photodiode), which has a non-linear response of the input electric fields. Typically, the resulting photocurrent i_d is proportional to the combined optical intensity, thus the square of the combined electric field amplitude (i.e. square-law detection):

$$i_d \propto [E_s \cos(2\pi\nu_0 t + \varphi) + E_{LO}\cos(2\pi\nu_{LO}t)]^2 \tag{2.10}$$

$$= E_s^2 + E_{LO}^2 + E_s E_{LO} + E_s E_{LO}\cos[2\pi(\nu_0 - \nu_{LO})t + \varphi], \tag{2.11}$$

where the three constant terms involve the original DC component and high frequency components which are usually filtered out as DC components. The last term indicates the photodetector measurable heterodyne beat component ν_{beat} at $\nu_0 - \nu_{LO}$.

In time-domain OCT, the non-linear heterodyne mixing takes place at the photodetector which is illuminated by the superimposed local oscillator wave and sample wave at the same time. The local oscillator wave is experimentally generated by moving the sample or reference along the longitudinal direction (i.e. depth scanning). This can be accomplished by moving either one interferometric arm towards the sample/reference matching point under a fixed slow speed υ_{ref}, while the photodetector records the interference signal with a sufficient sampling rate. Following the Doppler effect, the Doppler or beat frequency ν_{beat} can be expressed by the source central wavelength λ_0 and the movement speed υ_{ref}:

$$\nu_{beat} = \frac{2\upsilon_{ref}}{\lambda_0}, \tag{2.12}$$

The oscillating beat cycle T and length λ_{beat} of the interference signal is then given by:

$$T = \frac{1}{\nu_{beat}} = \frac{\lambda_0}{2\upsilon_{ref}}, \tag{2.13}$$

$$\lambda_{beat} = \frac{2\upsilon_{ref}}{\nu_{beat}} = \frac{\lambda_0}{2}. \tag{2.14}$$

From the above equations, the oscillating cycle length is only dependent on the source central wavelength. However, to ensure sufficient sampling points to reconstruct the interference signal, the photodetector sampling rate should be at least twice the beat rate, in other words, it is proportional to the movement speed υ_{ref}. Alternatively, the interference signal can be recorded via the triggering the movement and recording at intervals, with a moving step size Δd enough to reconstruct the interference signal, hence $\Delta d < \lambda_0/4$.

A single point interferogram resulted from a uniformly moved sample arm under speed υ_s and a fixed reference arm is shown in Fig. 2.5.

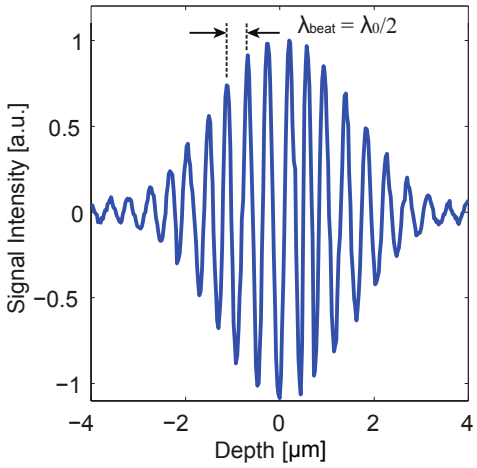

Fig. 2.5 A time-domain OCT interferogram with cycle length λ_{beat} equal to half the source central wavelength λ_0.

Therefore, depth scanning provides sufficient heterodyne beat frequency to modulate the sample backscattered signals which convey the sample structural information. Considering time-domain OCT operating on a broadband radiation, the central cycle length in an interferogram is half the central wavelength of the light beam, while the cycles away from the centre tend to have slightly larger cycle lengths which closely relates to the source spectral width. It is noticeable that optical heterodyne detection features amplifying a weak input signal. As enough optical local oscillator power could always be applied to the detector, the noise contributions are mainly due to the shot noise from the optical local oscillator induced current [171, 172].

c. Other Schemes

The reflectometry LCI scheme provides direct access to the sample structure along the depth direction, since the sample features at probing depths are directly associated with the moving displacements of the reference. However, there are other different implementations of time-domain OCT systems, which consist of dual beam, *en-face*, and parallel OCT. They all conduce to non-destructive 3-D imaging as alternatives of reflectometry scheme.

In the dual beam scheme, the sample is placed outside the LCI interferometer and illustrated by both beams exiting the interferometer (see Fig. 2.6). The splitting light beams travel through different interferometer arms, join their path at interferometer exit, and propagate until being emitted into detector by different sites within the sample. As depicted in Fig. 2.6, the interference occurs when the OPD between the two interferometer arms, i.e. $|r_1 - r_2|$, matches with the OPD between two re-emitting sample sites, i.e. depth $\cdot\, n_s$, where n_s is the refractive index of the sample site. Hence, the scheme facilitates high-precision depth measurement even in the presence of longitudinal sample movement [69], e.g. in *in vivo* diagnosis. However, under this scheme, depth scan signals might eventually deliver an ambiguous image if more than one interfaces (other than the sample surface) are dominating within the sample [3]. This scheme has been used for intraocular distance measurement in ophthalmology [68] and many applications in physiologic studies [173].

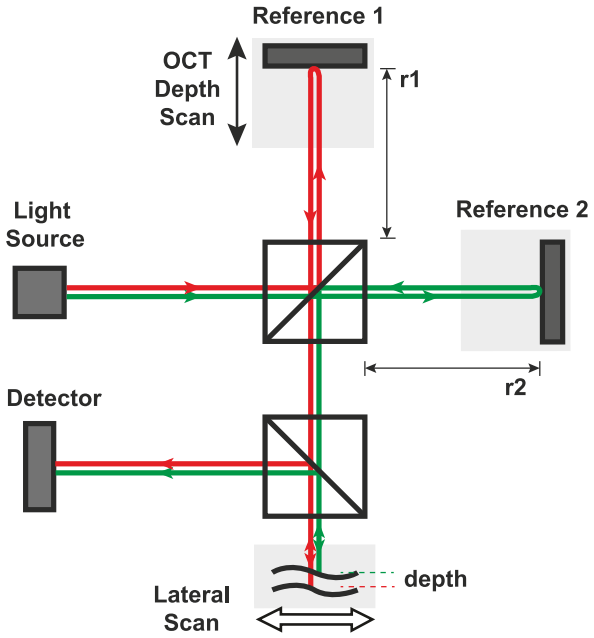

Fig. 2.6 Time-domain OCT in dual beam scheme. The splitting beam paths are highlighted with different colours. The dual beam configuration offers a stable measurement which is not sensitive to the relative longitudinal movements between sample and interferometer.

The *en-face* scheme was introduced by Izatt *et al* to enhance the probing depth of microscopy [167]. By using this scheme, an *en-face* image (i.e. transversal section that is perpendicular to the optical axis) of the sample is directly generated after a fast lateral scanning. Unlike the reflectometry scheme, no delay line is operated in the *en-face* scheme, as shown in Fig. 2.7. The reference mirror is moving longitudinally only to adjust the probing depth for lateral scans. Instead, a separate phase modulation is created for the generation of the heterodyne frequency [4]. This can be fulfilled by using a phase modulator (e.g. photoelastic modulators, electro-optic modulators) or performing a small movement in the axial direction (with e.g. a PT) at one of the interferometer arms [167].

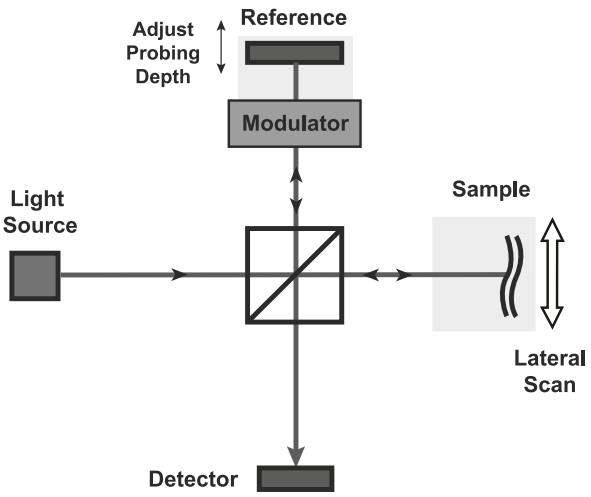

Fig. 2.7 Time-domain OCT in *en-face* scheme. A fast lateral scanning is performed. A separate modulator on either one interferometer arm can be used to yield the carrier frequency.

Standard time-domain OCT, dual beam OCT and *en-face* OCT are single-point detection techniques. However, there's a tradeoff between high frame rate and high sensitivity for such techniques. In the parallel OCT systems, detector array or cameras are used as detectors, eliminating the need for lateral scanning. Hence, the parallel scheme can dramatically increase the OCT measurement speed and enable *in situ* near real-time optical biopsy. It is also known as full-field OCT or wide-field OCT, which is the main technique used in this thesis. More details on the mechanism and experimental aspects of this technique are described in Section 2.5 and Chapter 3.

2.4.3 Fourier-Domain OCT

The Fourier-domain OCT technique was first presented in 1995 by Fercher [50]. It provides equivalent imaging of structural information as time-domain OCT with the same spatial

resolution [165]; it also features improved sensitivity and elimination of depth scanning of both interferometer arms. Instead of time-dependent interferograms acquired in time-domain OCT, the signal data obtained in a Fourier domain system are spectra, in which the spectral density intensity is plotted as a function of wavelength or frequency. Whereas in standard OCT both depth and lateral scans have to be performed, only the lateral-scan is necessary in the Fourier-domain techniques [3].

Based on the channelled spectra technique (spectral modulation), Fourier-domain OCT has been implemented into mainly two schemes; one is called spectral domain OCT with a spectrometer to detect spectrum; the other is called swept-source OCT with a tuneable laser source and a photodetector to extract spectral information over a wide bandwidth. Both methods are based on spectrums (spectral A-scan signals) acquired at the interferometer exit [50, 165]. The depth-dependent A-scan signals can be obtained by an inverse FT of the path difference modulation of OCT spectrums [4].

a. Theoretical Formulae

Considering the Wiener-Khintchine theorem [174], the spectral density (power spectrum) function of a light wave can be represented by the FT (FT$\{...\}$) of its autocorrelation (self-correlation) denoted by $\Gamma(\tau)$:

$$S(\nu) = \mathrm{FT}\{\Gamma(\tau)\}. \tag{2.15}$$

$E_s(t)$ and $E_r(t,\tau)$ are still defined the wave fields of sample and reference beams (τ is the time delay between the two waves), the power spectrum at the interferometer exit can be expressed as [174]:

$$S_{out}(\nu,\tau) = S_s(\nu) + S_r(\nu) + 2\sqrt{S_s(\nu)S_r(\nu)}\Re[\mu_{sr}(\nu)e^{-i\phi(\nu,\tau)}] \tag{2.16}$$

$$= S_s(\nu) + S_r(\nu) + 2\Re[W_{sr}(\nu)]\cos(\phi(\nu,\tau)) \tag{2.17}$$

In Equation 2.16, $S_s(\nu)$ and $S_r(\nu)$ are the spectral densities at frequency ν of sample and reference beams respectively; $\mu_{sr}(\nu)$ denotes the spectral degree of coherence at frequency ν; the spectral phase is computed by $\phi(\nu,\tau) = 2\pi\nu\tau$. In Equation 2.17, the spectral density function of two waves is obtained as:

$$W_{sr}(\nu) = \sqrt{S_s(\nu)S_r(\nu)}\mu_{sr}(\nu). \tag{2.18}$$

However, following the Wiener-Khintchine theorem in Equation 2.15, the spectral density function $W_{sr}(\nu)$ is also in relation of the mutual coherence function $\Gamma_{sr}(\tau)$ by:

$$W_{sr}(\nu) = \mathrm{FT}\{\Gamma_{sr}(\tau)\}. \tag{2.19}$$

The depth-dependent interferogram and the cross-spectral intensity are FT pairs of each other [175]. Hence the depth-dependent A-scan signal can be obtained from the path difference modulated part of the interferometer exit spectrum:

$$G_{sr}(z) = 2\Re\{\mathrm{FT}^{-1}\{W_{sr}(\nu)\}\}. \tag{2.20}$$

where FT^{-1} is the inverse FT. The spectral density $W_{sr}(\nu)$ plays essential role of a spectral A-scan signal [4].

b. Spectral Interferometry Fourier-domain OCT

This technique is known as spectral-domain OCT, in which spectra of the backscattered light are obtained at the exit of the interferometer using a spectrometer. As explained in equation 2.19 to 2.20, the inverse FT of the spectral density intensity yields the same depth-scan signal as obtained by time-domain OCT [176], since a given path difference generates a unique wavelength-dependent signature of phase difference [4]. Hence, the time-consuming mechanical OCT depth-scan is replaced by a spectrometric measurement. A typical spectral-domain OCT scheme using a spectrometer at the interferometer exit is shown in Fig. 2.8.

A broadband light source and the lateral scanning are common with the standard OCT system. Lateral scans are performed to acquire sequential depth signals along the lateral direction, allowing cross-sectional images of sample sections to be obtained. Simultaneously, all spectral components are captured at the output of a spectrometer [50, 53, 56]. The spectral information can also be extracted by distributing different optical frequencies onto a photo detector array via a diffraction grating component.

A phase modulator in the reference arm is used for the introduction of a variable single-pass phase delay. Then a set of spectral interferograms may be acquired with different phase delays, and combined in signal processing to eliminate the undesired artefacts [177]. The phase shifting technique has been important to resolve the A-scan signal for both time-domain OCT and Fourier-domain OCT. The 4-step phase shifting approach is the most common way to remove artefacts and oscillations.

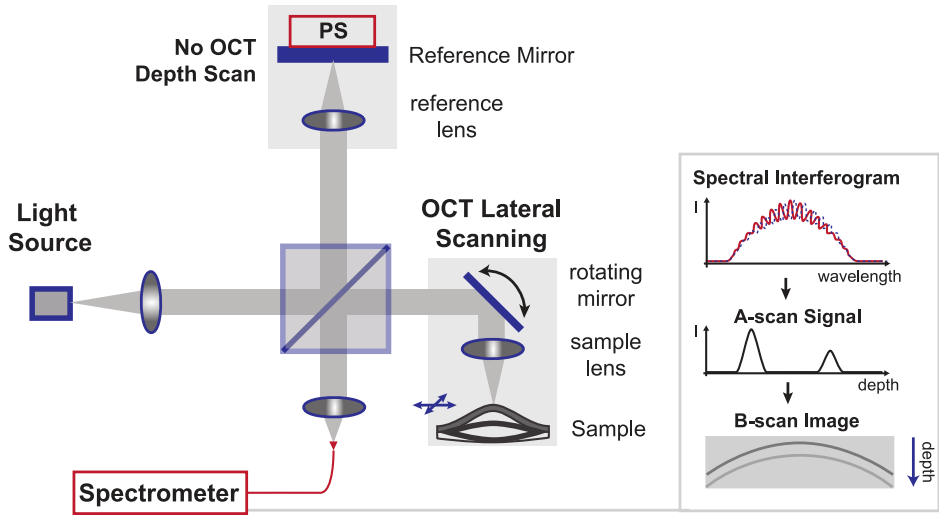

Fig. 2.8 Schematic diagram of spectral interferometry Fourier-domain OCT. PS: Phase Shifter. Spectral interferogram can be recorded instantaneously with no OCT depth scans. The A-scan signal is extracted from inverse FT of combined spectral interferograms, which are acquired under different phase delays. The B-scan image is the combination of a series of A-scan signals acquired after each OCT lateral scan.

c. Wavelength Tuning Fourier Domain OCT

Fourier-domain OCT can also be performed using a tuneable light source and detecting the intensity due to component frequencies [51]. This technique is known as optical frequency domain reflectometry, it has only recently been applied in tomography. This type of Fourier-domain OCT is called wavelength tuning Fourier-domain OCT or swept-source OCT. Whereas spectral-domain scheme simultaneously records the spectrum at the interferometer exit by a spectrometer, the wavelength-resolved intensity components are captured sequentially by a single detector during the synchronous wavelength sweeping of a narrowband swept-laser source [52, 178, 179]. However, both Fourier-domain OCT schemes are based on the same fundamental principle of optical interferometric imaging.

As shown in Fig. 2.9, a time encoded (square-law) photodetector is used at the interferometer exit in common with the time-domain OCT. Both arm path lengths are held constant as no depth scan is required, similar with the spectral-domain OCT. A tuneable light source is the key system component, the wavelength sweeping allows successive registration of all spectral components at once with short exposure time [180]. In addition, there is no further phase shifting measurements required to eliminate OCT artefacts as in spectral-domain OCT. Together with superior sensitivity over time-domain OCT [58, 60],

swept-source OCT enables high speed imaging, which is important for real-time acquisition and reduces image-blurring motion artefacts [156].

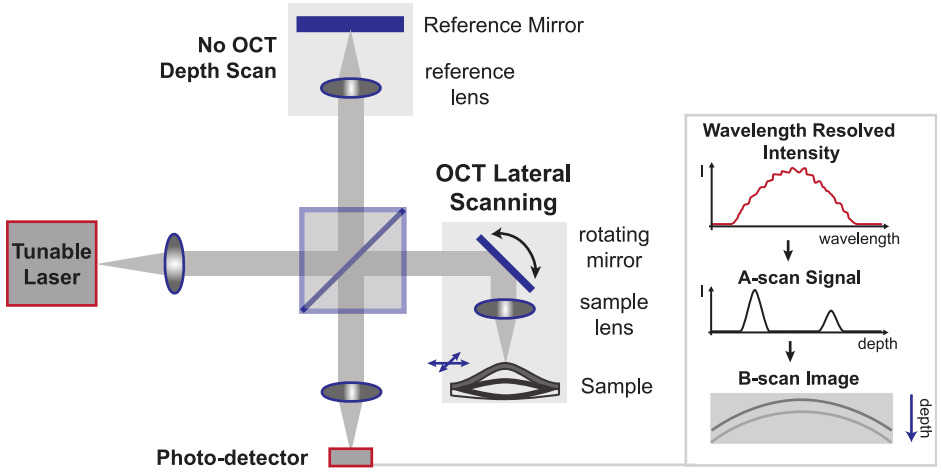

Fig. 2.9 Schematic diagram of wavelength tuning Fourier-domain OCT. Wavelength resolved intensities are recorded sequentially by a photodetector during the wavelength sweeping of a tuneable laser source. The A-scan signal is extracted through the inverse FT of the integrated spectral intensity. The B-scan image is the combination of a series of A-scan signals performed after each OCT lateral scan.

The key advantages of Fourier-domain OCT include its high sensitivity and the detection scheme does not require depth scans. It also inherits time-domain OCT's properties of the depth and the transverse resolutions (dependent on coherence length and probe beam NA). The spectral-domain OCT scheme features high speed data acquisition, whereas the swept-source OCT scheme features high speed imaging, comparing to the conventional time-domain OCT. However, the use of phase shifting method could result in the artefact reduction at the cost of increased acquisition time in spectral-domain OCT. There has been many studies on the sensitivity advantage of Fourier-domain OCT approaches over the time-domain OCT [58, 60, 181, 182].

2.4.4 Practical Aspect of OCT System Design

The image quality is a characteristic that measures the perceived image degradation. It could be affected in terms of the image contrast, the distortion, the noise, the sharpness, etc. The assessment of the image quality is hence crucial to an imaging system. The main aspects relating to the imaging performance of an OCT system consist of its imaging resolution, imaging sensitivity and imaging depth. There are also factors such as the optical power,

the light spectral range, and the image acquisition rate, whereas these parameters might be determined by specific requirements, such as the nature of the test sample.

a. Spatial Resolution

Image resolution is a measure of the shortest (spatial) distance distinguishable between two points on a specimen. Spatial resolution is an important specification of an imaging system. In many biomedical applications higher resolution is required to identify cellular boundaries and types [183]. The spatial resolution of an image system is generally evaluated by means of the spatial point spread function (PSF), which describes the spatial response to a point object. In OCT, it is advantageous that the spatial resolution along the depth and the lateral directions are decoupled; the depth resolution is defined by half the coherence length, whereas the transverse resolution depends on the waist radius of the focused Gaussian probe beam similar with classic microscopy techniques.

Depth Resolution The OCT PSF along the depth direction can be described as the functional dependence of the OCT signal of a point scatterer scanning throughout the focal space [184]. In other words, the moving reference mirror transmits the “coherence gate" to scan along the whole imaging depth of the sample site, resulting in time-dependent interference signals. The gate is of the size of the coherence length, within which OPLs of the two beams coincide. The coherence length is an explicit function of the light source spectrum [177]. The OCT theoretical depth resolution Δz is defined as half the coherence length in air l_c:

$$\Delta z = \frac{l_c}{2} = 2\ln 2 \frac{\lambda_0^2}{\pi \Delta\lambda} \tag{2.21}$$

where λ_0 is the centre wavelength, and $\Delta\lambda$ is the spectral bandwidth of the OCT light source. Experimental determination of the longitudinal PSF profile is given by the envelope of each interferogram (in Fig. 2.4), where the full-width at half maximum (FWHM) of the envelope is regarded as the experimental measured depth resolution. This is because the impulse response of OCT system in the depth direction, i.e. the longitudinal PSF, is the OCT response to the variation of refractive index. Both time-domain and Fourier-domain OCT have the same depth resolution, depending only on the power spectrum of the light source [3].

Transverse Resolution The OCT PSF along the transverse direction (in the plane perpendicular to the optical axis) is analogue to the concept in many other imaging systems (e.g. microscopes, telescopes), where the imaging quality is assessed by the degree of

spreading of a point object to form a finite area in the image plane. Mathematically the transverse PSF could be described as the impulse response profile of the point object. OCT transverse PSF shares all these properties. However, OCT transverse resolution is also limited either by an insufficient transversal sampling rate and/or the size of the probe beam spot diameter [3]. Considering an OCT imaging system with enough sampling points along the transverse direction, the transverse resolution is determined by the focused spot size as in conventional microscopy. The transverse resolution Δx is defined as twice the beam waist w_0:

$$\Delta x = 2w_0 = \frac{2\lambda_0}{\pi\theta_s} = \frac{2\lambda_0}{\pi NA} \tag{2.22}$$

Equation 2.22 is based on the Gaussian beam relationship in the far field: $\theta_s = \frac{\lambda_0}{\pi w_0}$ [185], where θ_s is the beam divergence half-angle. NA is the beam numeric aperture or $\sin\theta_s$, which is established because of the paraxial approximation: $\sin\theta_s \approx \theta_s$. High transverse resolution Δx can be obtained by using a large NA and focusing the beam to a small spot size [2]. Low NA focusing limits the transverse resolution because the focused spot sizes are large [186]. Experimental determination of the transverse resolution requires sub-resolution (point-like) radiating object to be imaged and analysed, as the object image can be seen as a convolution of the true object and the transverse PSF of the system.

b. Depth of Field

In an imaging system, the depth of field (DOF) is the distance by which the sample may be shifted before an unacceptable blur is produced. Considering a Gaussian probe beam incident on the sample, the DOF (in the absence of dispersion and absorption) can be quantified by the confocal parameter b or twice the Rayleigh length z_R [187]:

$$DOF = b = 2z_R \tag{2.23}$$

$$= 2\frac{\lambda_0}{\pi\theta_s^2} = 2\frac{\lambda_0}{\pi NA^2} \tag{2.24}$$

Equation 2.24 suggests that the use of relatively longer wavelength light allows an OCT signal to penetrate into the scattering medium. Moreover, it shows that the DOF is inversely proportional to the square of NA, the higher the NA is, the smaller the distance is that the light can penetrate into the sample. By substituting Equation 2.22 into Equation 2.24, the

relationship between DOF and the OCT transverse resolution can be expressed by:

$$DOF = \frac{\pi \Delta x^2}{2\lambda_0}. \tag{2.25}$$

Thus, the transverse resolution can be improved by increasing the NA of the objective, but at the price of a decreasing DOF. In the limiting case of very high NA in confocal microscopy, DOF can be comparable to, or shorter than the coherence length. Hence, OCT axial scan range might be restricted due to the high transverse resolution required in optical coherence microscopy [158]. There has been research looking at how to compensate for this, such as by incorporating dynamic focusing into the sample arm optics or by adjusting the focus further into the sample [48, 167, 188].

Though DOF is determined only by the light wavelength and the beam NA, the actual OCT achievable imaging depth is also limited by optical attenuation from sample scattering and absorption [2]. Factors such as distributions and refractive indices of scattering media [3] and radiation wavelength should be considered for the estimation of the attenuation of OCT signals.

On the other hand, the spectral interferogram data in Fourier-domain OCT is typically acquired by a sampling operation and inverse FT [4]. Except the previous NA and attenuation consideration, imaging depth in Fourier-domain OCT is also limited by the depth-dependent falloff in sensitivity. Note that the depth-dependent falloff in sensitivity is directly related to the spectral resolution, which is dominated by the source linewidth in swept-source OCT and the spectrometer resolution in spectral-domain OCT [177].

c. Sensitivity

Interferometry measures the field rather than the intensity of the light, it mixes a weak sample field with a strong reference field to produce heterodyne gain and very high, shot-noise-limited sensitivities can be achieved [186].

An important feature of an OCT system which relates directly to the DOF and the image quality is the imaging sensitivity. Sensitivity, signal-to-noise ratio (SNR), and dynamic range are often used interchangeably in OCT literature to denote the minimum detectable reflected optical power compared to a perfect reflector, usually expressed in decibel units [177]. However, the SNR is generally defined as time integrated OCT signal (power) divided by the square of the noise variance; the sensitivity Σ of OCT devices is defined by the minimal resolvable sample arm reflectivity $R_{s,min}$, at which the system SNR equals one [181]. The

sensitivity is generally calculated using the mathematical SNR formula:

$$\text{SNR} = \frac{\langle I_{OCT} \rangle^2}{\sigma^2_{noise}}. \tag{2.26}$$

SNR analysis for time-domain OCT For an OCT imaging performed in time domain, the desired OCT signal I_{OCT} of equation 2.26 resides in the interferogram term $G_{sr}(z)$, whose mean-square peak signal power occurs when the reference arm is matched with sample arm, i.e. $|\gamma_{sr}(z)| = 1$ and $\cos\Phi(z) = 1$ in Equation 2.7, thus,

$$\langle I_{TDOCT} \rangle^2 = \langle G_{sr}(z) \rangle^2 = 2I_r I_s. \tag{2.27}$$

The dominating noise sources for an OCT system are shot noise, excess noise and receiver noise. The receiver noise is related to the manufacturer's specification of the detector [3]; the shot noise and the excess noise are both broadband light photocurrent noise, the shot noise is due to photocurrent variance and the excess noise is due to self-beating of light waves [189]. A complete SNR analysis requires consideration of these noise sources, however, the shot noise limited regime is usually realised in OCT systems and can be regarded as optimum, since receiver noise limits the sensitivity at lower source power, and excess noise limits the sensitivity at higher power [3]. For shot-noise-limited performance, the shot noise variance in an optical receiver is given by [177]:

$$\sigma^2_{TDOCT} = 2e\bar{I}B = 2eI_r B_{TDOCT}, \tag{2.28}$$

where e is the electronic charge, $\bar{I}$ is the mean detector photocurrent, and B or B_{TDOCT} is the optimal detection bandwidth of OCT device. Assuming the light intensity backscattered from the sample is much smaller than that reflected from the reference, the mean detector photocurrent is dominated by the power returning from reference arm $\bar{I} = I_r$. As described in Section 2.4.2, the reference light frequency is Doppler shifted by ν_{beat}, resulting from a uniform scan of the reference with a velocity of υ_{ref}. The Doppler frequency is $\nu_{beat} = 2\frac{\upsilon_{ref}}{\lambda_0} = \frac{k_0 \upsilon_{ref}}{\pi}$, the FWHM signal power bandwidth of the signal $\Delta\nu_{beat}$ can be obtained via $\Delta\nu_{beat} = \frac{\Delta k_{FWHM} \upsilon_{ref}}{\pi}$ (in Hz) [190]. The optimal detection bandwidth B_{TDOCT} is approximately twice this bandwidth $\Delta\nu_{beat}$, or $B_{TDOCT} \simeq 2\Delta\nu_{beat} = \frac{2\Delta k_{FWHM} \upsilon_{ref}}{\pi}$ [177].

Thus, substituting Equations 2.27 and 2.28 into equation 2.26, the well-known expression for the SNR of a time-domain OCT system is given by:

$$\mathrm{SNR}_{TDOCT} = \frac{I_s}{eB_{TDOCT}}. \tag{2.29}$$

Hence, if the detector efficiency is not considered, the SNR of the time-domain OCT is proportional to the power returning from the sample I_s, but is independent of the reference arm power level I_r.

SNR analysis for Fourier-domain OCT Fourier-domain OCT has a significant SNR advantage both theoretically and experimentally over time-domain OCT [60, 181, 182]. To obtain comparable expressions for SNR of the Fourier-domain OCT, both signal and noise propagation through the spectral sampling and inverse FT processes should be considered. In the case of spectral-domain OCT with M detector pixels, the SNR can be expressed as [177]:

$$\langle I_{SDOCT}\rangle^2 = \langle\sqrt{S_s S_r}M\rangle^2 = S_s S_r M^2 \tag{2.30}$$

$$\sigma^2_{SDOCT} = 2e\bar{I}B_{SDOCT} = 2eS_r B_{SDOCT} M \tag{2.31}$$

$$\mathrm{SNR}_{SDOCT} = \frac{S_s M}{2eB_{SDOCT}} \tag{2.32}$$

In the case of swept-source OCT with M spectral channels, the SNR can be expressed as [177]:

$$\langle I_{SSOCT}\rangle^2 = \langle\sqrt{S_s S_r}\rangle^2 = S_s S_r \tag{2.33}$$

$$\sigma^2_{SSOCT} = 2e\bar{I}B_{SSOCT} = 2eS_r B_{SSOCT}/M \tag{2.34}$$

$$\mathrm{SNR}_{SSOCT} = \frac{S_s M}{2eB_{SSOCT}} \tag{2.35}$$

Here, the same source output power and sample reflectivity are assumed for time-domain and Fourier-domain OCT systems. For an spectral-domain OCT system, as all spectral channels are illuminated simultaneously, the illumination power for all detector pixels is the same as the total power in time-domain OCT, then $S_s = I_s/M$; since the signal from each spectral channel are integrated over the entire A-scan time, the spectral-domain detection bandwidth can be given by $B_{SDOCT} = B_{TDOCT}/M$.

For a swept-source OCT system, only one spectral channel is illuminated at a time and hence the allowable sample illumination power for each channel is the same as

the total power in time-domain OCT, $S_s = I_s$; the swept-source detection bandwidth is limited by the analogue-to-digital sampling frequency, where it is given by $f_s = M/\Delta t = 2 \cdot 2\Delta k_{FWHM} z_m/(\pi\Delta t)$, assuming a maximum imaging depth of z_m, an A-scan acquisition time of Δt (equivalent with $\upsilon_{ref} = z_m/\Delta t$ in time-domain OCT) and a scanning range of $2k_{FWHM}$ are chosen; then the swept-source detection bandwidth can be limited to half the sampling frequency f_s, hence $B_{SSOCT} = f_s/2 = B_{TDOCT}$. Therefore, the SNR relationships among the three cases can be acquired as [177]:

$$\mathrm{SNR}_{SDOCT} = \mathrm{SNR}_{SSOCT} = \mathrm{SNR}_{TDOCT}\frac{M}{2}. \tag{2.36}$$

The $M/2$ times improvement in Fourier-domain OCT schemes over time-domain OCT can be understandable by their simultaneous scanning of all depths information. However, the SNR improvement is based upon the fact that the system employs a shot-noise limited detection, which requires sufficient reference arm power to assure the domination of shot noise [60].

Experimental verification of the system sensitivity is performed by first placing a neutral density (ND) filter (of D optical density) followed by the sample mirror in the sample arm optics to attenuate the returning sample arm signal by $20D$ in dB [190]. (An identical mirror is placed in the reference arm.) This facilitates the estimation of the weakest sample reflectivity that an OCT system can detect. The sensitivity in dB can be measured according to Equation 2.37, where the square of the measured A-scan peak height is taken as the value of $\langle I_{OCT}\rangle^2$ and the standard deviation (STD) of the noise floor at the location of A-scan peak by removing the sample mirror is taken as σ_{noise} [60]. The increased factor $20D$ accounts for the attenuation of the sample arm by the ND filter.

$$\Sigma = \mathrm{SNR}_{dB} = 10\log_{10}\frac{\langle I_{OCT}\rangle^2}{\sigma^2_{noise}} + 20D \tag{2.37}$$

Dynamic range The dynamic range (DR), however, defines the range of observable OCT signals or the maximum signal over the noise floor that OCT can measure without, e.g. saturating a detector, overloading an amplifier, or exceeding a digitisation range [191]. Imaging of biomedical applications demands OCT systems with high resolution and high sensitivity as well as high DR. The DC background and the detector photoelectron capacity are two factors limiting the OCT DR.

The time-domain OCT features direct removal of the DC component by using a filter and passing the rest OCT signal to the image sensor, in a way that the system DR is optimised (to the sensor DR). Fourier-domain OCT do not easily permit the removal of a DC component

[191]. The same sensor will be required to capture Fourier-domain OCT signal on top of the DC components, which limits the DR of the OCT signal.

Besides the DC background, the DR is also limited by the full well capacity (FWC) of the image sensor [181]. The FWC can be virtually increased by pixel binning and image accumulation, which is an advantage for parallel OCT schemes [66]. In practice, no time-domain or Fourier-domain OCT system realises a DR equal to the sensitivity, which can be easily above 100 dB. A system DR of 40 dB to 60 dB suffices in most cases [191].

2.4.5 Comparison between Time-Domain OCT and Fourier-Domain OCT

Time-domain OCT provides direct access to the sample structure, as the sample depth is directly associated with the axial position of the reference. It produces depth oriented cross-sections, illustrating the in-depth sample structure with micrometre scale resolution. There are many other implementations of time-domain systems in their uniqueness, such as dual beam OCT and *en-face* OCT. However, the main disadvantage is that it requires mechanical movements for both axial and lateral scans, which demand static sample fixture and takes a long time before obtaining a volumetric image.

As described previously, the Fourier-domain OCT schemes requires fewer moving parts to obtain entire depth scans in a single exposure [158]. It also features an $M/2$ factor SNR improvement over the time-domain OCT. Despite the high sensitivity and fast imaging or fast acquisition advantages, the indispensable DC background acquired by Fourier-domain OCT limits the dynamic range of the OCT signals. Furthermore, since no mechanical scanning is operated, the DOF of Fourier-domain OCT is limited by the swept source linewidth or the spectrometer resolution. In addition, there is a significant loss of sensitivity and dynamic range as a function of depth. A sensitivity drop of 5 dB over a 2 mm depth range has been observed at 850 nm [192].

2.5 Full-Field OCT

FF-OCT is a recently emerging technology for non-destructive imaging of biological samples. It employs parallel illumination and captures frontal plane sections, which allows direct analysis of *en-face* images in a way that is similar with most standard medical imaging schemes (e.g. microscopy). It has been used to perform histology in a non-invasive manner, hence no manual preparation of sample slices, staining and other delicate procedure (i.e.

fixation, dehydration, clearing, infiltration, and embedding) are needed [66]. Sample structures can be evaluated from the processed *en-face* and cross-sectional images, as well as the 3-D representation of the sample morphology. The FF-OCT technique has been used in various applications, demonstrating faster acquisition speed and comparable spatial resolution to standard OCT.

2.5.1 System Configuration

Similar to the time-domain and the Fourier-domain OCT system, the central part of the FF-OCT scheme is a Michelson interferometer which splits the beam into the reference and sample arms (as shown in Fig. 2.10). Note, that for single point OCT scheme, a partial coherent light source is generally used with high spatial but low temporal coherence. However, both low spatial and low temporal coherence is required in parallel OCT (to eliminate mutual coherence as in Young's double slit experiment). Instead of scanning the sample in two lateral dimensions, FF-OCT employs full-field illumination and the backscattered signals are *en-face* imaged by using a 2-D detector array, such as a CCD or CMOS camera at the exit of the interferometer. No electromechanical scans along the lateral directions is needed, whereas a depth scanning or stepping is required in the reference or the sample arm to record successive *en-face* images for the reconstruction of 3-D representation of sample structure. Likewise, this is either done by a simple translation stage or by a rapid scanning optical delay line.

2.5.2 Operational Schemes

Axial Movement Most current FF-OCT measurements are operated with continuous stepping of one arm. A motorised stepper is generally used to fulfil the stepping procedure. Accordingly, a camera is commanded to grab images at these stepped positions, in a way that the interference event can be digitalised. To ensure effective reconstruction of the interference signal, the stepping increment should be at most $\frac{\lambda_0}{4}$ since the interferogram oscillation cycle length is half the source central wavelength.

Alternatively, depth scanning of FF-OCT can be operated by a single axial movement of the reference (or sample) arm under a fixed velocity, similar with time-domain OCT. As described in Section 2.4.2, the mechanism is essentially based on the optical heterodyne detection, which mixes a weak sample signal with some strong local oscillator waves, resulting in a strong interference signal as the mixing product. The resultant interferogram have oscillating beat frequency and cycle length expressed respectively in equation 2.12 and

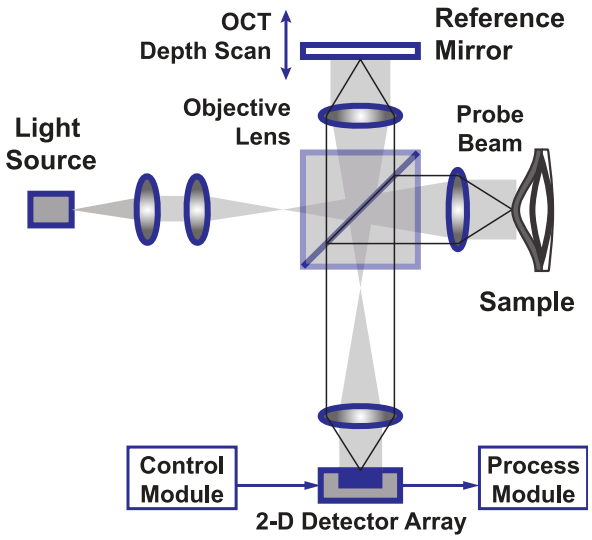

Fig. 2.10 Schematic diagram of the parallel or full-field OCT system. The sample is under parallel illumination, which is reflected back to a 2-D detector array. A series of *en-face* images are continuously grabbed during the depth scanning. No time-consuming 2-D OCT lateral scans (e.g. raster scanning) are required.

2.14. During the steady moving of one arm, the passing of fringes is observable on the 2-D detector array.

For both movement cases, the detector should grab the images at a frame rate which allows at least half the source central wavelength separation to be obtained between adjacent sampling points within the interferogram. More sampling points are desired in an interference signal to greatly enhance the imaging sensitivity, however, this would increase the measurement time.

Phase-Shifting Phase-shifting based on phase-stepping and other methods are applicable to a FF-OCT system for retrieving *en-face* images with better sensitivity achievable and less storage requirement [147, 193–197].

The phase modulator (e.g. PT, photoelastic modulator) is used along with the continuous stepping of one arm to prevent varying stepping increments from affecting the imaging quality. It can also be used in FF-OCT for on-line acquisition of fringe-free *en-face* image. Generally, the method shifts the phase by a known amount between each intensity measurement. The phase-shifting algorithm makes use of recorded intensities at each of these steps to extract the peak position of the corresponding interference signal. Table 2.1 provides example phase-shift algorithms employing a constant $\Delta\phi$ phase shift between P intensity samples. While only intensity measurements of three stepping phases are required, generally more

than three measurements are made to reduce the errors due to phase steps being incorrect, detector non-linearity, electronic noise, air turbulence, vibration, etc [42]. A least-squares fit approach is useful in the derivations of these phase-shift algorithms.

Table 2.1 Example phase-shift algorithms with uniform phase shift

P	$\Delta\phi$	$\tan(\theta)$	I_{int}
3	$\frac{\pi}{2}$	$\frac{I_1-I_3}{-I_1+2I_2-I_3}$	$(I_1-I_3)^2+(-I_1+2I_2-I_3)^2$
4	$\frac{\pi}{2}$	$\frac{I_4-I_2}{I_1-I_3}$	$(I_1-I_3)^2+(I_4-I_2)^2$
5	$\frac{\pi}{2}$	$\frac{2I_2-2I_4}{-I_1+2I_3-I_5}$	$4(I_2-I_4)^2+(-I_1+2I_3-I_5)^2$
8	$\frac{\pi}{4}$	$\frac{I_7-I_3}{I_1-I_5}$	$(I_1-I_5)^2+(I_2-I_6)^2+(I_3-I_7)^2+(I_4-I_8)^2$

2.5.3 Performance Characteristics

Inherited from the standard time-domain OCT, the axial resolution of FF-OCT is determined by the spectral property of the illumination source; the achievable DOF and system sensitivity are measurable following the routines described in Section 2.4.4. Unlike the single point detection scheme relating the transverse resolution to the actual beam spot size upon the sample, the transverse resolution of FF-OCT is only limited by the optics and the camera pixel size (similar to that of a classic microscope). In comparison with the conventional OCT, the technique provides more convenient and efficient imaging, especially for the evaluation of samples which are difficult to be positioned or imaged (e.g. small-size samples) by point detection schemes.

The FF-OCT system was first implemented to facilitate high-resolution imaging within a commercial microscopy body [8]. Recently, thermal sources such as halogen light source have been used with FF-OCT in many studies [64, 65], due to their relative low price, broad spectrum (i.e. high axial resolution), and low spatial coherence (reducing image speckles). The reported ultrahigh-resolution FF-OCT system has achieved one of the best spatial resolution ($0.7\,\mu m \times 0.9\,\mu m$) with 80 dB shot-noise limited detection sensitivity during a near real-time acquisition (1 sec per image) [63]. Indeed, the FF-OCT system has also been frequently used for topographic purposes [198]. It has been applied for imaging and surface profiling in a number of areas, including biology [61], histology [199], ophthalmology [200], and industrial applications [198].

FF-OCT is beneficial to yield 3-D imaging with a faster acquisition speed and less operations than conventional OCT techniques. Mechanical lateral scans are eliminated by the

use of full-field illumination and 2-D detector array, which facilitate experimental simplicity and convenience. An inexpensive thermal light source is perfectly appropriate to obtain full-field illumination and high spatial resolution. Parallel detection enables fast acquisition of the OCT signals with millions of pixels captured at video rates. Nevertheless, the number of photons that can be acquired at each pixel of a camera sensor is much less than that of a single photodetector, the shot-noise limited SNR is directly related to the light intensity available to the imaging field [66]. Hence a high power illumination source might be used to compensate the imaging sensitivity. However, small-unexpected object motions during the image acquisition time could induce effective changes in optical phases, which leads to undesired tomographic images and reduced image contrast [201].

Current FF-OCT systems generally perform the measurement with the phase-shifting method to acquire fringe-free *en-face* images. The depth scanning is operated with a motorised axial stepper and a phase modulator positioned at either the sample or the reference arm. Typically the motorised stepper is still used to carry out probing at incremental depths within the sample for the depth scanning. During the interval of axial stepping, the phase modulator is used to modulate the OPD between the two interferometric arms. The corresponding phase shifts should be strictly implemented according to the selected phase shifting method as illustrated in Table 2.1 before the measurement of each modulated intensity. To prevent measurements from being time inefficient, the modulation of the phase needs to be synchronous with the image acquisition of the camera [65], which is executed at a certain rate. As a consequence, an external synchronisation module is needed to handle simultaneously the phase modulation and image acquisition. The system control module thus needs to operate the depth scanning and the phase shifting to be synchronous with the image acquisition. Meanwhile, the acquired images need to be immediately saved to a PC and follow subsequent processing with the selected phase-shifting algorithms. High performance PC and system components are essential in these systems to ensure that these control and processing operations won't hold up the measurement procedures. Each tomographic image takes 4 s acquisition time during the FF-OCT measurement [64].

There's a need for a simplified low cost system to be implemented in a much more convenient manner for a wide range of applications. This could be accomplished by using the classic depth scanning scheme, using a uniformly moved interferometer arm to modulate the sample signal. Chapter 3 will explore further details with regards to the construction of the efficient FF-OCT systems.

2.6 Summary

OCT is an established imaging modality permitting cross-section and 3-D imaging at sub-micrometre resolution. It has been used for characterisation of internal structures as well as surface textures in many disciplines. It offers non-invasive imaging with high spatial resolution, high sensitivity with millimetre penetration depth, allowing for OCT investigations into biomedical and industrial areas, such as ophthalmology, cardiology, gastroenterology, cultural heritage and food packaging industry.

Time-domain OCT and Fourier-domain OCT are two main OCT variants. Their technical details and mathematical treatments have been included in this chapter. Fourier-domain OCT features elimination of depth-scan, fast imaging speed and superb sensitivity, making it the mainstream of OCT technology. However, time-domain OCT is still advantageous because of its simplicity and straightforward operations. It has been implemented in dual beam, *en-face* and parallel schemes, in their own uniqueness.

FF-OCT employs parallel detection scheme using a camera, permitting 3-D imaging without 2-D lateral-scan. It is a powerful technique to perform fast histology in a non-invasive manner without lengthy and delicate sample preparations. In particular, it provides extreme experimental convenience for samples which are difficult to be positioned in point detection schemes. The imaging performance is comparable with time-domain OCT, but allows much faster acquisition speed. Current FF-OCT systems perform 3-D imaging with high resolution and high sensitivity. However, they demand high performance system components as well as complex measuring processes. A simple FF-OCT system with a uniformly moving sample arm is more efficient in terms of both cost and complexity. It is considered to promote the use of the powerful FF-OCT technique to a variety of areas. The construction of the FF-OCT systems will be presented in the next chapter.

Chapter 3

Development of two FF-OCT System

3.1 Introduction

OCT is an emerging imaging technique allowing non-destructive characterisation of surface textures and subsurface structures with micrometre resolution. It was first discovered as time-domain OCT, which drives a probing beam to scan all over the sample structure, both transversely and longitudinally. The probing depth within the sample is directly associated with the OPD between two interferometric arms, however, this scheme involves mechanical movement, which inherently leads to relatively slow measurements. Back then, the time-domain OCT was mainly used in biomedical applications, especially in ophthalmology [3]. The Fourier-domain OCT was proposed subsequently, and it has been the most prevalent of OCT techniques thereafter in both academia and industry. It can be implemented in two different detection schemes: one utilises a spectrometer as the detector (spectral-domain OCT) and one requires the sweeping of the source wavelength (swept-source OCT). Either way, the power spectrum is the output used to generate the A-scan signal after inverse FT. The main features of the Fourier-domain schemes are the elimination of depth scanning facilitating near real-time imaging and the great improvement in the imaging sensitivity. The sensitivity advantage and the adaptation of OCT technology has broadened its use in many more applications including cardiology, gastroenterology, dermatology, cultural heritage artefacts' studies, etc., although ophthalmology remains the dominant area of OCT application.

FF-OCT is an OCT variant performing parallel illumination and detection. It inherits many properties from the standard OCT including carrying out a time-of-flight measurement, implementing optical heterodyne detection, etc. However, FF-OCT requires full-field illumination throughout the interferometer with optical light of low temporal coherence

and low spatial coherence. The main advantage over time-domain and Fourier-domain OCT is that there are no transverse mechanical movements operated in the measurement. In particular, it provides simplicity and convenience for applications that are difficult to be probed with point-scan OCT systems. Recent FF-OCT studies have already demonstrated the imaging performance of this technique to be comparable with standard OCT [66], although current FF-OCT systems demand high-performance system components as well as on-line measuring processes.

This chapter focuses on the development of FF-OCT systems during this PhD. Following this introduction, a short section provides a brief description of the FF-OCT system principle. Subsequently, the developments of two low-cost FF-OCT systems are presented respectively in two individual sections, containing detailed characterisation of the system setups, experimental procedures, and data analysis as well as the measurements of the system's performance. System constructions are based on incorporating only the essential OCT components, such as low coherent light source, motorised stages, and camera. Imaging performance is evaluated based on the imaging resolution and the sensitivity. A thorough discussion is included afterwards on the FF-OCT technique and the two developed FF-OCT systems.

3.2 Principle of the FF-OCT Technique

FF-OCT is an OCT technique that is different from both time-domain and Fourier-domain OCT. Instead of the point scanning, an FF-OCT system employs full-field illumination of a specific area on the sample and produces frontal plane tomographic images in parallel using an image detector.

According to Equation 2.7 for describing a time-domain OCT signal, the FF-OCT *en-face* image or the FF-OCT signal at a camera pixel (p_x, p_y) is expressed as a function of depth z by:

$$I_{cam}(p_x, p_y, z) = I_{DC}(p_x, p_y) + M(p_x, p_y, z)\cos[\Phi(p_x, p_y, z)]. \tag{3.1}$$

The DC term represents the background image, $M(p_x, p_y, z)$ is the *en-face* tomographic image at a depth of z, and $\Phi(p_x, p_y, z)$ is the instantaneous phase map at a depth of z.

Inheritance from Time-domain OCT FF-OCT inherits the fundamental imaging properties from the standard time-domain OCT. Firstly, it performs the same time-of-flight measurements, in order to measure the time delay between two FF-OCT signals that are

backscattered from the sample media. Secondly, it also implements depth-scanning according to the optical heterodyne detection, so that a sufficient beat frequency can be generated to modulate the sample backscattered signals. With respect to the system configuration, the core of an FF-OCT system is also based on the Michelson interferometer, with light beams split into reference and sample arms.

Despite that, FF-OCT is a more advanced technique by using the Michelson configuration coupled with a 2-D array detector to acquire images over an entire field of view (FOV). Besides, the sample is illuminated with low temporal and low spatial coherence light [62–66].

Full-field Illumination Time-domain OCT systems employ single-point scanning (transversely and longitudinally) over the volume of interest. However, 2-D lateral scanning generally increases the system's complexity and the acquisition time. FF-OCT targets the illumination of a sample over a specified area. Successive tomographic images in the *en-face* orientation are obtained using a 2-D detector array during the depth-scanning. Considering system scanning operations, FF-OCT combines 3-D mechanical movements (as required in time-domain OCT) into a single 1-D movement along the depth direction. In terms of system control, fewer controlling commands are required as there is no need for additional transverse scanning. Measurements with the FF-OCT technique are hence time-saving and electromechanically more efficient, compared to time-domain OCT. Without additional devices, the 2-D detector of an FF-OCT system, such as a real-time camera, can also facilitate the monitoring of the system alignment and small adjustment of the sample arm after a specimen is inserted.

Low Spatial Coherence Radiation Temporal coherence means that a strong correlation is exhibited between the light waves at one location but at different times. Spatial coherence means that a strong correlation (a fixed-phase relationship) is exhibited between the light waves at one time but at different locations across the light-beam profile.

The depth resolution of OCT images is governed by the temporal coherence length of the illumination source. Time-domain OCT usually employs a light source emitting low temporal but high spatial coherence radiation, allowing an increased number of photons per spatial mode [174, 202], i.e. an improved SNR. However, speckle noise arises in OCT images as a natural consequence of the limited spatial-frequency bandwidth of the OCT interference signals [203]. The speckle noise can be suppressed by employing a low temporal and low spatial coherent light source in these point-scan OCT systems, despite an SNR degradation resulting [204].

For the FF-OCT system, spatially coherent illumination generates coherent cross talk, leading to a significant image degradation. Spatially incoherent illumination, on the other hand, allows the suppression of coherent cross talk [205]. The use of thermal light sources is of great interest because of their spatially low-coherence radiation and the extremely short temporal coherence length at a very low price. Only femtosecond lasers in conventional OCT systems can achieve a comparable depth-resolution. In addition, thermal light sources have a smoother spectrum and more stable optical power [63].

3.3 Development of a Simple FF-OCT System

FF-OCT is an emerging OCT technique that allows the parallel detection of *en-face* images as a function of the probing depth. It eliminates the 2-D lateral scanning and its feasibility has been demonstrated in the area of biology [61], histology [199], ophthalmology [200], etc.

Many FF-OCT systems use a phase-shifting technique to acquire fringe-free *en-face* images directly from the measurements. The phase-shifting is required to be synchronised with the image acquisition to improve the time efficiency and to lock the phases. However, the phase-shifting method complicates the system control by the phase-shifting and the synchronisation of operations. High performance PC and system components are needed to ensure that these system control commands are not delayed by the transfer of acquired images and the ongoing processing with the corresponding phase-shifting algorithm. Several phase-shift images are acquired at a given depth to generate the corresponding fringe-free image. The acquisition of these phase-shift images neither contributes to an increase in the imaging sampling rate, nor promotes the imaging sensitivity. Moreover, these phase-shift images are susceptible to external disturbances like vibrations and turbulence. The FF-OCT systems employing the phase-shifting method may therefore not be simple or straightforward in terms of the system's complexity.

There is a need for a simplified low-cost FF-OCT system to provide great ease and flexibility to be used in different industrial environments as an alternative to current FF-OCT systems.

3.3.1 System Setup

The simple FF-OCT system described in this section is based on the time-domain OCT operating with optical heterodyne detection. It is equipped with the essential FF-OCT

components and constructed on an optical breadboard. Fig. 3.1 (see below) illustrates a schematic diagram and a photo of the developed table-top FF-OCT system which consists of a bulk Michelson interferometer, an infrared LED source for system illumination, a motorised stage for axial translation of the sample with a speed υ_s, a window as the reference mirror, and a CMOS camera at the interferometer exit.

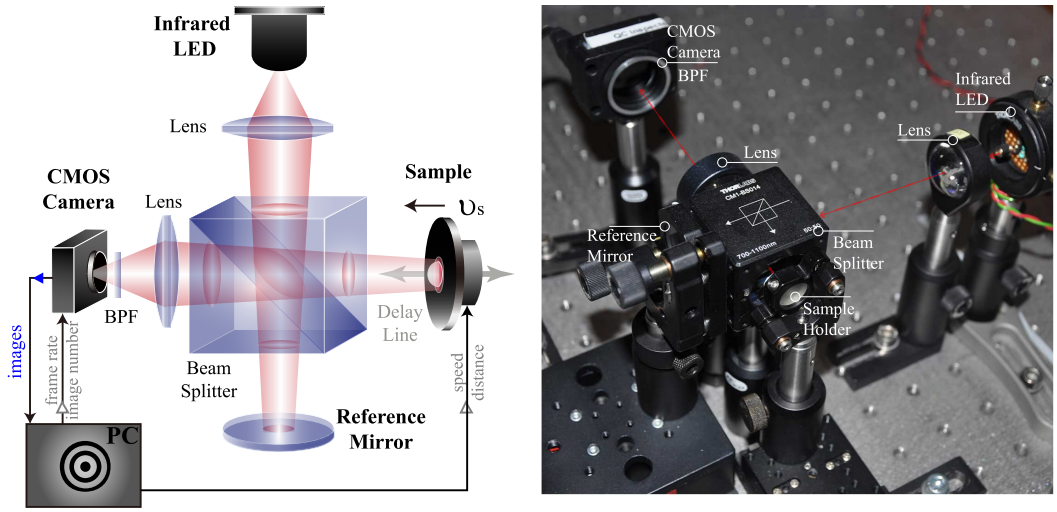

Fig. 3.1 (a) Schematic diagram and photo of the developed simple FF-OCT system with an infrared LED source. BPF, band-pass filter; (b) photo of the Table-top FF-OCT System.

The infrared LED source was charged in series with a 5 Ω resistor in a simple electric circuit powered by a 3 V voltage and a 0.15 A current, providing an irradiance on the sample of 0.3 mW cm^{-2} typically. The optical spectrum of the infrared LED source has a central wavelength $\lambda_0 = 880$ nm and a spectral width $\Delta\lambda = 110$ nm. The best focused spot of the light from the infrared LED source has a square shape. However, the LED does not have a uniformly-illuminated square aperture, as there is a loop-shaped electrode on top of the semiconductor chip to link to the anode lead of the LED. The focused spot on a sample and the formed image on the image sensor exhibited weaker illumination strength at the location of the electrode.

The CMOS camera (FMVU-03MTM-CS, Point Grey) is a high-speed camera recording 16-bit monochromatic digital data (10-bit valid grey levels, i.e. a 60 dB dynamic range). It grabs a typical raster image containing a fixed number of rows and columns of picture elements or pixels. Each pixel holds a quantized value that represents a shade of gray (varying from black at the weakest intensity to white at the strongest) at any specific point. The maximum frame rate allowed by the CMOS camera is 120 fps for an image size of

376×240 pixels, of which the corresponding pixel size is equivalent to $12\,\mu m \times 12\,\mu m$ after 2×2 pixel binning.

The motorised translation stage is controlled electronically and has a 50 mm linear travel along a well-defined axis. It can be operated to achieve an incremental movement as small as $0.1\,\mu m$. It can provide a smooth and constant friction movement under a slow, steady speed of $1\,\mu m\,s^{-1}$. Both the camera and the stage are connected via USB to the PC, in which a control module is used to handle the operations in an OCT measurement, and a process module is used to process the acquired OCT data.

a. Interferometry Mechanism

Considering the light propagation within the designed FF-OCT system, the low-coherence light from the infrared LED source is first split into a reference beam and a sample beam by a non-polarising 50/50 beam-splitter. Light backscattered by the sample is recombined with the light reflected by the reference mirror at the beam-splitter and finally captured with a CMOS camera. Interference occurs only if the OPD between the reference and sample arms is within the coherence length of the light source. An on-screen interference pattern (see Fig. 3.1 (a)) indicates the matching point for the two interferometer arms.

b. System Alignment

An accurate optical alignment was carried out to assemble these system elements, i.e. aligning the reference arm with the light source and the beam-splitter and then aligning the CMOS camera with the beam-splitter and the sample arm. A laser beam, e.g. from a laser diode was used to assist the alignment of the optical axis to be parallel to the horizontal plane. Meanwhile, the positions of both lenses, the light source and the camera were roughly adjusted according to the calculated distances, which were derived from the required magnification and imaging FOV of the sample.

Further precise adjustments were made by the use of both the infrared LED source and the camera. A distance calibrator (R1L3S2P, Thorlabs) with horizontally sputtered micrometre divisions on a glass substrate was frequently used as the sample to calibrate the FOV and assist the alignment process. With an aligned and fixed reference mirror, first the position of the calibrator was adjusted along the optical axis until the strongest interference pattern was formed in the camera screen; then, with the reference beam covered up, the camera and the lens were adjusted to have the desired FOV identified by a sharp image of the micrometre divisions. Finally, with the reference beam uncovered and the sample beam shielded, the

light source and the lens were adjusted so that the luminous pattern within the LED occupied the full screen of the camera and was displayed as a sharp image.

c. Depth-Scanning Preparation

After the alignment process, the sample under test can be attached to the sample arm, replacing the distance calibrator. The depth-scan parameters, including the movement speed of the sample and the frame rate of the camera, need to comply with the requirement of the sample measurement.

Following the optical heterodyne detection in time-domain OCT (see Section 2.4.2 above), the modulation of the OCT signal is carried out by mixing with a strong local oscillator wave, which is experimentally generated by moving the sample or reference arm along the longitudinal direction. To digitise the interferogram using a photodetector with a fixed sampling rate, the depth-scanning can be accomplished by translating either arm towards the sample/reference matching point under a fixed slow speed υ_s. An effective digitalisation in FF-OCT is guaranteed by grabbing images at a frame rate ν_{cam} larger than twice the heterodyne beat frequency ν_{beat} (see Equation 2.12 above) according to the Nyquist rate:

$$\nu_{cam} \geq 2\nu_{beat} = \frac{4\upsilon_s}{\lambda_0}, \tag{3.2}$$

in which λ_0 is the central wavelength of the source spectrum. The sensitivity-enhancement of the OCT signal can be fulfilled by sampling more points in an oscillating beat cycle. Hence, a slower translation speed and/or a faster camera frame rate are desired to increase the sampling rate of the OCT signal. However, the increased measurement time and/or data storage should also be considered according to the specific requirements in the actual measurements.

For most measurements using the simple FF-OCT systems, the CMOS camera was operated to successively grab 16-bit 240 px × 240 px mono images with a pre-set frame rate of 120 fps. The stage in the sample arm could be moved at a steady speed towards the beam-splitter, such as 1 µm s^{-1}, 3 µm s^{-1}, or 5 µm s^{-1}. It involved a trade-off between high axial precision and less data storage. Normally an overall measurement time of less than 1 minute can be achieved for probing the depth of a sample of less than 100 µm.

3.3.2 Experimental Procedures

During the system alignment and preparation, the manufacturer-supplied software of the camera (FlyCapture Viewer, Point Grey) was used to monitor the image sharpness and

interference events. It also provided a straightforward interface for editing camera settings. The automatic gain and brightness options of the CMOS camera were often disabled to avoid image degradation. The shutter time of the camera was manually adjusted to ensure that no OCT images exceeded the saturation during a measurement. The built-in timestamp register was sometimes activated to encode a timestamp in the first two pixels of each image. The starting point of the sample translation towards the beam-splitter was usually at least 10 µm away from the matching point of the sample arm.

It was necessary that the control module within the PC was triggered at the same time of the image acquisition using the camera and the steady movement of the sample in the depth direction (along the optical axis). A home-made user program in C++ was created to send commands to the camera, including the pre-set number of images that needed to be acquired and a selected frame rate. The user can also define the filename of a binary file that is created to store all acquired images on the PC. A graphic user interface (GUI) in Matlab (see Fig. 3.2) was created to start the sample movement, and monitor the movement across the whole imaging depth of the sample. Note that all of the system setup and software programming, e.g. control and processing, were my own work.

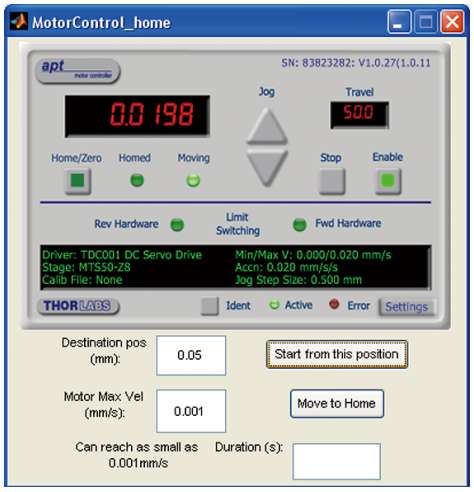

Fig. 3.2 GUI for the motorised translation stage. The type-in text boxes are for inputting user-specified travel distance (in mm) and velocity (in mm/s) before an OCT measurement; the overall travelling time of an OCT measurement would be returned in the bottom text box after the translation was accomplished.

During the measurement with the simple FF-OCT system, the reference mirror was stationary, while the sample was moving at a constant speed towards the beam-splitter. The instantaneous displacement was displayed in the GUI on the PC. Meanwhile, the CMOS camera was acquiring images at a fast frame rate and immediately transferred these images

to the PC. Acquired images were temporarily stacked in the PC buffer, before they were saved as a single binary data file at the end of the measurement. This binary data file was an integrated OCT image volume, containing useful OCT signals that were related to the sample structures.

The movement of the sample and the image acquiring by the camera were parallel operations during the measurement, as illustrated in the flowchart of Fig. 3.3 (see below). However, the two processes were generally running on separated PCs, as the transfer of acquired images into the PC buffer tended to congest the computer buses; the interplay between the two processes could lead to abnormal performances, such as the slowdown of the sample movement and the delay of the image-grabbing.

To give an example of a complete FF-OCT measurement: 6000 images with 240×240 pixels were acquired successively at 120 fps, while a sample was moved at a constant speed of $3\,\mu\mathrm{m\,s}^{-1}$. This resulted in an image stack with $240 \times 240 \times 6000$ data points equivalent to a physical volume of $(3 \times 3 \times 0.15)\,\mathrm{mm}^3$, assuming that the image of a camera pixel corresponded to an area of $(12.5 \times 12.5)\,\mu\mathrm{m}^2$ on the sample. The FF-OCT measurement took only 50 seconds to acquire a 3-D data cube with an effective probing depth of 150 µm in air. A fixed depth interval of 25 nm between sequential images could be derived as the thickness of each slice of the volumetric data cube. More than 16 images were acquired within a single-beat cycle. The sampling rate exceeded the Nyquist rate by at least a factor of 8 to deliver better precision to the imaging performance. A single binary file was used to store the stack of images.

The file was read as the original OCT data that had undergone processing in a Matlab environment in the process module. The 3-D data cube is composed of a stack of *en-face* images, or it can be regarded as a set of single-point OCT signals, similar to those acquired in time-domain OCT. However, an OCT signal in FF-OCT represents the intensity changes for a pixel over multiple *en-face* images. It contains interference events that result from the matching of OPLs between the reference and sample structures. By analysing the position of these interference events, the structure of the sample can be quantitatively evaluated.

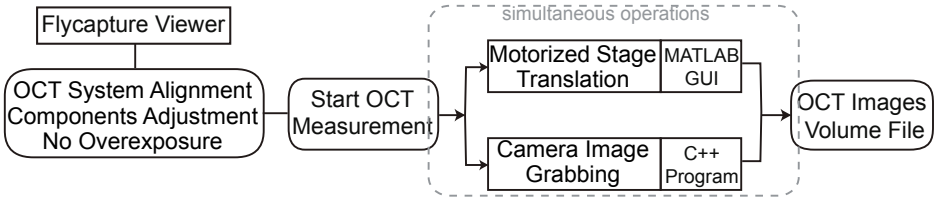

Fig. 3.3 Flowchart of the experimental procedures for the simple FF-OCT system.

3.3.3 Data Analysis for Tomographic Imaging

As a tomography technique, OCT enables optical sectioning to obtain virtual slices, i.e. B-scan images, with a great depth resolution. This resolution is determined by the power spectrum of the light source. Moreover, it is fundamentally presented by the width of the axial PSF of the imaging system. The OCT response to a sample interface (between two media of different refractive indices) is the system's impulse response, i.e. the axial PSF. The axial PSF is experimentally obtained as the envelope of an OCT interference signal.

In an FF-OCT measurement, to ensure no actual information is lost in the OCT A-scan signal during the sampling process — image acquisition by using a camera — the system must utilise a sampling interval (axial step size) that is no greater than half the size of the smallest resolvable feature, i.e. half of the depth-resolution, according to the Nyquist criterion or Shannon's sampling theorem. The depth resolution is in the order of a micrometre in state-of-the-art OCT systems employing low coherent light sources. A micrometre (or submicrometre) scale axial step size is theoretically sufficient to guarantee a micrometre accuracy in the tomographic imaging with clear discrimination by using the FF-OCT technique. An A-scan signal should thus have at least four intensity points to reconstruct an OCT response, i.e. PSF, of a sample interface. Conventionally, the highest intensity point is regarded as the peak of the A-scan signal, with which the corresponding depth position is taken as the physical position of an interface.

The simple FF-OCT setup, however, cannot be used to directly obtain the PSF intensity points from measurements. They are envelope points generally derived from the envelope detection of a discrete interferogram in an original FF-OCT signal. Critical sampling of an interferogram with an axial step size of half the depth-resolution will lead to aliasing problems for the reconstructed envelope. The precision of the envelope peak position can be greatly improved by increasing the sampling rate of the FF-OCT signal. This is implemented by utilising a slower translation speed and/or a faster camera frame rate, as mentioned in Section 3.3.1 (see above). More discrete points in the interferogram allow a more accurate reconstruction of the envelope signal. In the meantime, a smaller axial step size results in a higher imaging precision. Although 3-D data sets with a higher sampling rate need larger memory storage capacities, the cost of memory is rapidly becoming less significant in digital implementation [206].

In this study, the FF-OCT data analysis for tomographic imaging is a process of smoothing and envelope detection of the original FF-OCT signals with the goal of discovering sample internal structures from the reconstructed A-scan signals, B-scan images, etc.

a. Signal-Smoothing

A Savitzky-Golay filter was applied to the original FF-OCT signals for the signal-smoothing, i.e. to increase the SNR without greatly distorting the signals. Smoothing with this filter can slightly reduce the deviation of some intensity points while preserving the width and height of peaks in the signal [207, 208]. It was used as the first step of the signal-processing to produce smoothed FF-OCT signals for an effective envelope detection.

b. Envelope Detection

The objective of the envelope detection in the processing of FF-OCT data is to ascertain the position of the peak of an interference signal. There have been many algorithms for the fringe analysis and the envelope detection in interferometry using the least-squares fit method [206], the FT method [209], and the PSI algorithms [42, 210] as noted in Section 2.5.2 (see above). Unfortunately, calculations for the former two methods are computationally intensive [206]. The latter requires measurements of intensities at multiple fixed-phase steps to derive an envelope intensity point at a depth location within the sample, which cannot be implemented using the current simple FF-OCT system.

Many studies employed a Hilbert transform (HT) kernel to extract the envelopes [211] and analyse the fringe-patterns [212]. It has recently been utilised in the FF-OCT technique [213] because of the computational efficiency and the ease of use. The perfect HT algorithm can be considered as a phase-shifter which gives every sinusoidal function a phase shift of $-90°$ [212] and is capable of obtaining the envelope corresponding to the original interference signal.

Hilbert Transform: The HT of a real-valued function $f(t)$ is defined by:

$$h(u)(t) = HT\{f(t)\} = \frac{1}{\pi} PV \int_{-\infty}^{+\infty} \frac{f(t)}{u-t} dt, \tag{3.3}$$

in which PV is the Cauchy principal value taken in the integral. Computationally, $h(u)(t)$ can also be regarded as the convolution ($\star$) of $\frac{1}{\pi u} PV$ and $f(t)$:

$$h(u)(t) = \frac{1}{\pi u} PV \star f(t). \tag{3.4}$$

As mentioned, the HT can be considered to be a filter that simply shifts the phase of its input by $-\frac{\pi}{2}$ radians. The analytic representation of an input signal is an analytic signal. The real

and imaginary parts of an analytic signal $F(t)$ are the input signal $f(t)$ and its HT $h(t)$:

$$F(t) = f(t) + jh(t). \tag{3.5}$$

The analytic signal $F(t)$ can also be expressed in terms of its time-variant magnitude $A(t)$ and phase $\phi(t)$ in polar coordinates:

$$F(t) = A(t)e^{j\phi(t)}. \tag{3.6}$$

$A(t)$ can be regarded as a slow-varying envelope of $f(t)$, while the phase derivative $\frac{\partial\phi(t)}{\partial t}$ is an instantaneous frequency [214]. Then, the magnitude $A(t)$ and phase $\phi(t)$ can simply be determined by the input signal $f(t)$ and its HT $h(t)$:

$$A(t) = |F(t)| = \sqrt{f(t)^2 + h(t)^2}, \tag{3.7}$$

$$\phi(t) = \tan^{-1}(\frac{f(t)}{h(t)}). \tag{3.8}$$

Thus, the HT method can be interpreted as a way to represent the boundary value in the upper half-plane of a real-valued function [215]. In this study, the HT method was used for the extraction of the envelope of each interference signal.

In the following analysis of the envelope detection, explicit camera pixel (p_x, p_y) variation in Equation 3.1 can be ignored, as long as it is remembered that the calculations are performed over a matrix of pixels (p_x, p_y) in the sample data. Then, the FF-OCT signal of a random pixel on the camera sensor may be expressed in a simplified form by:

$$I_{px}(z) = I_0 + M(z)\cos[\Phi(z)]. \tag{3.9}$$

By deducting the background image, i.e. the *en-face* image free of any interference events, the DC term can be removed from the acquired FF-OCT signal, resulting only in the interference signal.

As the camera was operated at a constant frame rate ν_{cam} during the movement of a sample at a speed of υ_s, a discrete interference signal as a function of sampling point number n is denoted as:

$$z = \frac{n}{\nu_{cam}} \cdot \upsilon_s, \tag{3.10}$$

$$I_{re}[n] = I_{re}(z) = M(z)\cos[\Phi(z)],\ n \in \mathbb{Z}(\text{integer}). \tag{3.11}$$

in which the square brackets [.] indicate that the signal is sampled in discrete time. The HT signal $I_{im}[n]$ and the analytic signal $I_a[n]$ of the interference signal $I_{re}[n]$ are then given by:

$$I_{im}[n] = I_{im}(z) = M(z)\sin[\Phi(z)], \tag{3.12}$$

$$I_a[n] = I_{re}[n] + jI_{im}[n]. \tag{3.13}$$

Thus, referring to Equation 3.7 (see above), the envelope intensity sequence $M[n]$ can be obtained as the magnitude of the analytic signal with removed phase terms:

$$M[n] = M(z) = |I_a[n]| = \sqrt{I_{re}^2[n] + I_{im}^2[n]}. \tag{3.14}$$

In the actual data analysis, the calculation of the sequence $M[n]$ was performed in Matlab using a "Hilbert" command to directly compute the discrete-time analytic signal $I_a[n]$ and an "abs" command to compute the complex magnitude $|I_a[n]|$. The HT method is advantageous as it is computationally more efficient because the final algorithm requires only two multiplications per interferogram point to produce the corresponding envelope squared at each point [206].

After the envelope detection, depending on the envelope strength, a low-pass filter might be used for the reduction of residual signal noise. In the FF-OCT system, OCT signals are shot-noise-limited, and speckle noise is suppressed because of the use of light source of low spatial coherence. However, noise could still exist as a result of degradation of the quality of OCT images. This could be caused by the abnormality of the camera and the translation stage. Another noise source could be due to optical aberration and dispersion inhomogeneity [64].

c. Displaying

Following the above procedures, all interference signals within the original 3-D data cube were removed and replaced by clear distinct envelope signals. Fig. 3.4 (a) (see below) illustrates the power of the envelope detection using the HT method. It is shown that the computed envelope signal in blue can approximate the boundary of the grey interference signal in the upper half-plane. The envelope signal also corresponds to the axial profile of the PSF of the FF-OCT system. Although a slight fringe structure is still visible in the envelope, the overall shape is close to a Gaussian profile, the envelope outline is smooth and the peak position is unambiguous. Fig. 3.4 (a) also identifies that more than 16 discrete interferogram points are sampled in a single beat-cycle, allowing a complete digitalisation of

the interferogram signal and a smooth reconstruction of the envelope with no information lost. Note that each sampling point can be clearly distinguished from another, indicating that the imaging system has a submicrometre precision in the depth direction.

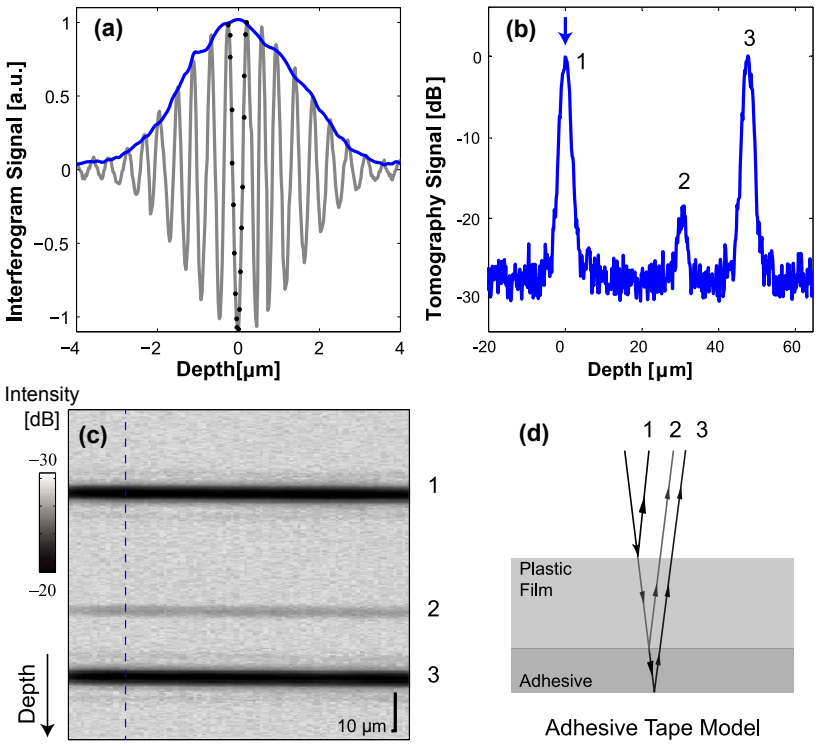

Fig. 3.4 (a) Interferogram signal and the derived envelope signal (b) A-scan signal or tomography signal in logarithmic scale, the main (first) peak (c) B-scan image presented in logarithmic scale with intensity and dimension scale bars (d) OCT light reflections within an adhesive tape model in correspondence with (b) and (c)

Fig. 3.4 (b) and (c) (see below) shows an A-scan signal or tomographic signal and a B-scan image in a logarithmic scale for an FF-OCT measurement of a piece of adhesive tape. As mentioned before, A-scan signals are envelope signals that are free from interference signal. B-scan images are cross-sectional images, presenting depth oriented 2-D structural distributions. The A-scan signal in (b) is the intensity variations along the dashed line of the B-scan image in (c). The surface peak of the A-scan signal corresponds to the reconstructed envelope in (a). The double-layer (three interfaces) structure of the sample can be identified from these two figures. The layer thickness d_L is evaluated by the displacement of adjacent peak positions $z_2 - z_1$. Since the A-scan signal and the B-scan image are both presented with depth in air, the layer refractive index n_L is also necessarily considered during the calculation:

$$d_L = \frac{z_2 - z_1}{n_L}. \tag{3.15}$$

This is because the OPL in a medium of constant refractive index, n_m, for a path of physical length d_m is:

$$OPL = n_m d_m. \tag{3.16}$$

The OCT signal is generally presented in dB as twenty times the base 10 logarithm of the signal that is normalised to a scale of 0 to 1. The use of the logarithmic scale for signal or image presentations in Fig. 3.4 (b) and (c) is for the compression of relative variations in signal or image, in order to obtain a well-contrasted image and to highlight the weak signal, such as the peak 2, in both the A-scan signal and the B-scan image. In Fig. 3.4 (c), an intensity scale bar in dB indicates the intensity range of the B-scan image from -30 dB to -20 dB. A dimension bar is also included. Fig. 3.4 (d) displays an adhesive tape model to demonstrate the light reflections incident upon the three interfaces. The second interface exhibits the weakest signal strength among the three interfaces, due to the lowest variation of refractive indices from the plastic film to the adhesive. Results in (b) and (c) have good agreement with the structure of the adhesive tape model in (d) and the real sample.

It is also needed to review images and signals to trace their structural changes, which may involve repetitive processing and data analysis. To facilitate convenient processing and displaying of B-scan images, a simple GUI was created and shown in Fig 3.5 (see below). It was designed to browse a series of processed B-scan images with optional commands and constraints to be specified by the user.

3.3.4 Data Analysis for the Surface Topography

a. Imaging Precision

The internal structures of a sample are distinguishable with the FF-OCT tomographic imaging. The locations of internal interfaces can be clearly revealed by the envelope signal in the A-scan signals or B-scan images. The layers distribution underneath the sample surface can be evaluated.

The OCT depth-resolution was measured as the FWHM width of a main envelope signal (at sample surface) or the OCT axial PSF profile. This is based on the fact that the spatial resolution of an imaging system is characterised by the PSF, which describes the response of the imaging system to a point object. An envelope signals representing the axial PSF in the simple FF-OCT system is derived from the acquired interferogram with well-separated

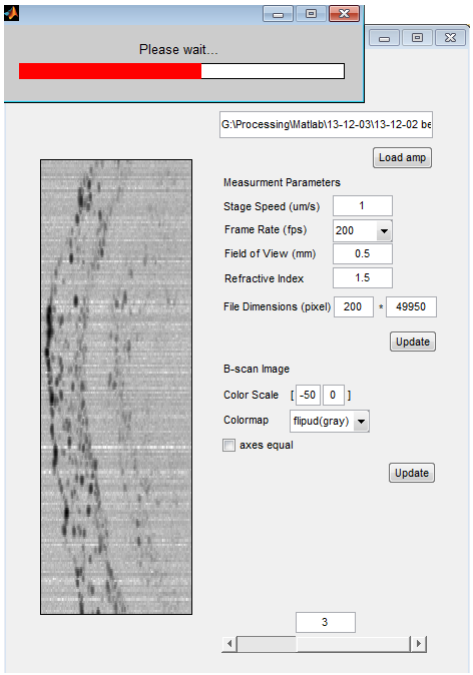

Fig. 3.5 GUI for browsing the FF-OCT B-scan images.

over-sampling points. They have a perfect fidelity and their peak positions can reach a sub-micrometre precision. The axial resolution is one of the inherent characteristics of an imaging system. It is determined only by the width of the axial PSF, which stays at the micrometre scale in this simple FF-OCT system.

For the OCT tomographic imaging, the location of a sample interface is measured by the position of the highest sampling point of the axial PSF (envelope). Alternatively, the position of the strongest sampling point of the zero-order beat cycle of the interferogram can be taken as the location of the interface, as shown in Fig. 3.6. Since the sampling points in the originally acquired interference signal are distinct in terms of the axial position and the intensity, the position deviation of the strongest sampling point from the true peak point (best-focus or highest contrast position) should be within the sampling depth interval. In the case of more than 16 sampling points per beat cycle in the interferogram, the theoretical depth interval is less than 25 nm, which indicates the theoretical imaging precision in the axial direction. Moreover, interpolation between sample points can be used to further increase the imaging precision beyond the sampling interval [146]. In practice, the imaging precision is limited by the systematic noise and sampling spacing (or step size) errors of instruments.

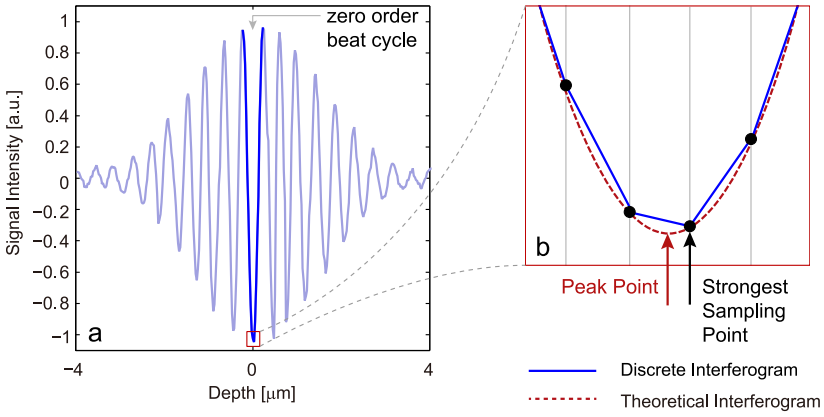

Fig. 3.6 (a) Zero-order beat cycle in a typical measured interferogram, (b) the zoomed-in central interferogram with the highlighted strongest sampling point and true peak point.

b. Determination of true peak position

The data analysis with the envelope detection for tomographic imaging may neither have sufficient precision to detect nanometre scale structural elements, nor be able to differentiate interfaces of optically thin layers, as the resultant A-scan signal could have connected / combined envelopes, of which the maxima are not well separated. By searching for the maxima positions of the central beat cycles, both the determination of the areal surface topography and the investigation of optically thin layers with nanometre scale precision are allowed. The same FF-OCT experimental procedures were followed to acquire a 3-D data cube. The number of sampling points per beat cycle was sufficient to permit a good fidelity in the reconstruction of an interference signal. Low noise is required in the measured OCT signals, so that the assumption of local linearity of the sampling interferogram is valid.

By using this method, the surface height was obtained, based on the true peak separation of the measured and the reference signals. Usually the highest contrast interference signal extracted from the acquired 3-D data cube was chosen as the reference signal.

Interpolation is a method of constructing new data points based on a discrete set of known data points. With the spline interpolation and a value a, a new interferogram can be reconstructed (interpolated) with a displacement of a from the old interferogram. This is equivalent to the shift of the interferogram from its initial axial position z_s to a new position $z_s - a$ (Fig. 3.7 (a) see below). It is also possible to derive the displacement with known raw and shifted interference signals.

A minimum search algorithm was used with the spline interpolation to find displacement a, so that the new interpolated interferogram and the reference signal can be approximate. The searched minimum displacement a is obtained by using the Nelder-Mead simplex algorithm

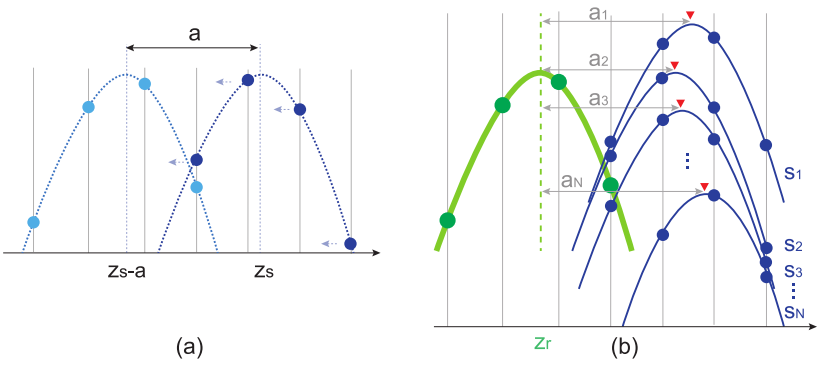

Fig. 3.7 Schematic diagram of position search with interpolation. (a) A zero-order interferogram cycle in dark blue with the peak at z_s and its interpolated interferogram cycle in light blue with the peak at $z_s - a$ (their peak displacement is a); (b) a reference zero-order cycle in green with the peak at z_r, N measured cycles s_1, s_2, s_3... s_N with respective peak displacements of a_1, a_2, a_3... a_N from the reference peak

[216, 217]. This algorithm is a direct search optimisation method which works by minimising an objective function:

$$\Delta^2 = \sum_{i=0}^{n} [I_0(z_s[i]) - b \cdot I_{OCT}(z_s[i] - a)]^2, \, i = 0, 1, 2, ..., n. \tag{3.17}$$

in which Δ^2 is the error metric that is minimised in the minimum search algorithm, I_{ref} is the selected reference interference, I_{OCT} is the OCT measured signal at pixel (p_x, p_y), n denotes the number of sampling points in the interferogram, $z_s[i]$ is the axial position at point number i, and the coefficients a and b represent respectively the axial shifting and the magnification of the OCT sample signal. Note that a is the searched displacement value as well as the desired surface height. Two commands "interp1" and "fminsearch" were used to implement the interpolation technique and the minimum search algorithm.

All interference signals of the measured 3-D data cube were processed with this method to find the displacements a_1, a_2, a_3... a_N for cycles s_1, s_2, s_3... s_N from the reference signal, as demonstrated in Fig. 3.7 (b). The resultant displacement values were taken as surface heights of measured interference signals relative to the reference peak position. They were stored as a 2-D topographic image, in which the surface height of a pixel was indicated by the scale of colour. The image can be used to interpret the surface topography by the colour variations. It is also possible to depict a 3-D representation of the surface on which superficial characteristics can be directly distinguished.

c. Phase-Unwrapping

The phases of the measured sampling points are inherently ambiguous outside of a 2π range; the variations of surface heights acquired from the minimum search algorithm lie within a range of $\frac{\lambda_0}{2}$ corresponding to a single beat-cycle [210]. To measure height variation larger than this limited range, the fractional phases of measured sampling points have to be unwrapped to retrieve height information.

The wrapped phase can be corrected (unwrapped) by adding or subtracting 2π to the phase of one of the data points so that the phase difference is less than π. The unwrapping of phases needs to be repeated for all data points until the phase difference between all adjacent data points is less than π [218]. It is more complicated to fix the wrapped phases for a 2-D topographic image.

A 2-D phase-unwrapper based on a region-merging principle [219, 220] was adopted in the 2-D phase-unwrapping process and corrected surface heights were obtained with wrapped phases eliminated. Fig. 3.8 demonstrates the phase-unwrapping of an example topographic image in Fig. 3.8 (a) with wrapped phases. Note that there still exists a residual wrapped phase shift in the topographic images in Fig. 3.8 (b) and (c), suggesting that a more robust unwrapping algorithm might be needed for more accurate measurements.

A flowchart presented in Fig. 3.9 summarises the data analysis with both tomographic imaging and surface topography of a 3-D data cube acquired with the simple FF-OCT system. In tomographic imaging, the FF-OCT data analysis is to illustrate sample internal structures. B-scan images and A-scan signals are obtained by the determination of peak positions of envelopes of FF-OCT signals. In surface topography, the FF-OCT data analysis is to describe surface characteristics. Surface maps are obtained by the determination of peak positions of zero-order interferogram cycles.

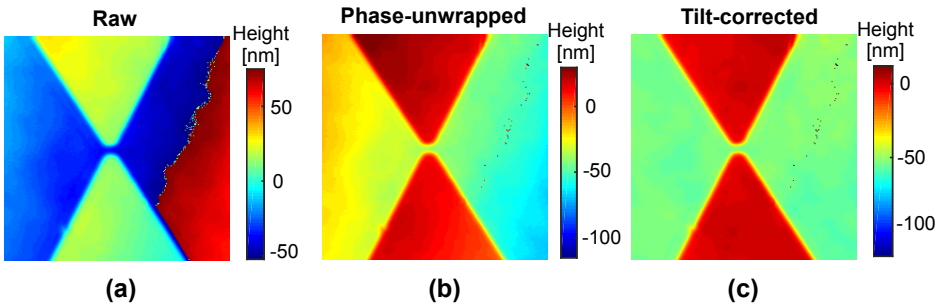

Fig. 3.8 (a) An example topographic image with wrapped phases, (b) the phase-unwrapped topographic image, (c) the tilt-corrected topographic image.

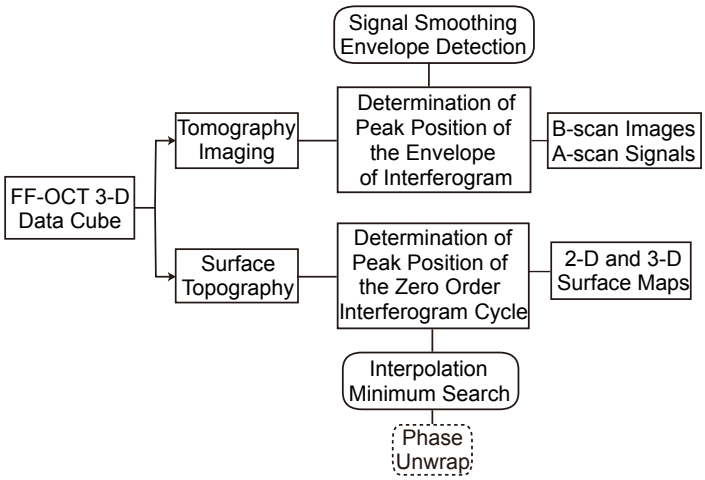

Fig. 3.9 Flowchart of FF-OCT data analysis with tomographic imaging and surface topography.

3.3.5 System Performance

FF-OCT is beneficial to yield 3-D imaging with a faster acquisition speed and less operations than conventional OCT techniques. However, some of the imaging characteristics of FF-OCT are inherited from the conventional OCT. Micrometre-scale spatial resolution and shot-noise-limited detection sensitivity are also achievable using the FF-OCT systems. This section focuses on the evaluation of the spatial resolution and the detection sensitivity of the simple FF-OCT system, based on the OCT imaging performance discussed in Section 2.4.4 (see above).

3.3.5.1 Depth-Resolution

The depth-resolution of the simple FF-OCT is determined by the spectral property of the illumination source, i.e. the infrared LED source with a central wavelength $\lambda_0 = 880\,\text{nm}$ and a spectral width $\Delta\lambda = 110\,\text{nm}$. According to Equation 2.21 (see above), the theoretical depth-resolution of the simple FF-OCT system is 3.1 µm.

However, the resolving capability of an imaging system is fundamentally presented by its impulse response, i.e. the PSF. For all OCT variants, the depth-resolution can be alternatively verified by the FWHM of the main OCT envelope, which is the OCT PSF profile along the axial direction. For the simple FF-OCT system, the depth-resolution was thereby measured as 3.6 µm, resulting from an obtained main envelope signal, as described in Fig. 3.10. The measured resolution is slightly larger than the theoretical value, which can be explained by the presence of systematic noise.

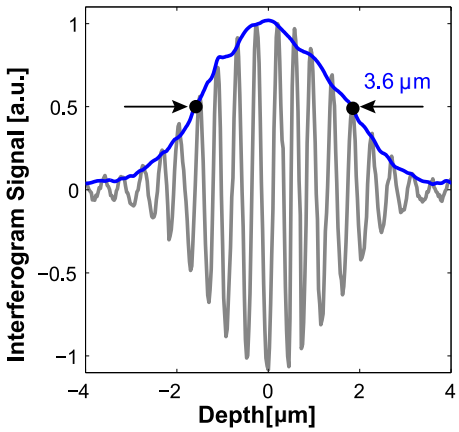

Fig. 3.10 The envelope of a main interferogram with the identified depth-resolution of 3.6 µm.

3.3.5.2 Transverse Resolution

The transverse resolution is determined by the focused spot size in a point-scan OCT system. A small spot size results in a high transverse resolution with a high NA-focused beam, if the transverse scanning step size is smaller than the spot size. For a full-field illuminated OCT system, beams are not focused as a spot of light. Despite that, point sources of light from a sample appear as spots at the FF-OCT camera sensor. Considering Equation 2.22, the transverse resolution of FF-OCT is dependent upon the beam NA. The higher the NA of the total system, the better the transverse resolution.

However, for a camera-acquired *en-face* FF-OCT image, the transverse sampling interval or the dimension of sample for a camera pixel must also be considered. In situations when the calculated value with Equation 2.22 (see above) is smaller than the sampling interval, the transverse resolution of the resulting digital image is limited only by the sampling interval.

The transverse PSF profile can be used to describe the transverse resolution. The image formed through the optical system is the convolution of the object's irradiance with the transverse PSF of system [221]. In other words, the transverse profile of the FF-OCT image w is the convolution ($\star$) of the transverse profile of the object v with the transverse profile of the system PSF u, given by:

$$w = v \star u. \tag{3.18}$$

The PSF profile can then be derived through a deconvolution process [222], once both w and v are acquired.

A micrometre division line of a distance calibrator was taken as a sub-resolution radiating object. The division line was first imaged at the focal plane of the FF-OCT system to acquire the profile w from an acquired *en-face* image (Fig. 3.11 (a) and (b)), and then imaged with a

high resolution optical microscope to acquire a precise object profile v (Fig. 3.11 (c) and (d)). The transverse PSF profile u was computed by the deconvolution of w and v, and it is displayed in Fig. 3.11 (e). From these figures, the width of the object profile is found to be 7.6 µm, the width of the OCT image profile is found to be 11.5 µm, the width of the transverse PSF profile, i.e. the transverse resolution is measured as 10.3 µm.

Fig. 3.11 (f) (see below) further describes a PSF calculated from ideal object and image profiles with the same widths, i.e. 7.6 µm and 11.5 µm, and a slightly smaller PSF width of 10 µm is obtained, which may indicate a more accurate determination of the OCT transverse resolution. On the other hand, there are sufficient sampling points (camera pixels) within the PSF profile, suggesting that the transverse resolution is not limited by the sampling interval.

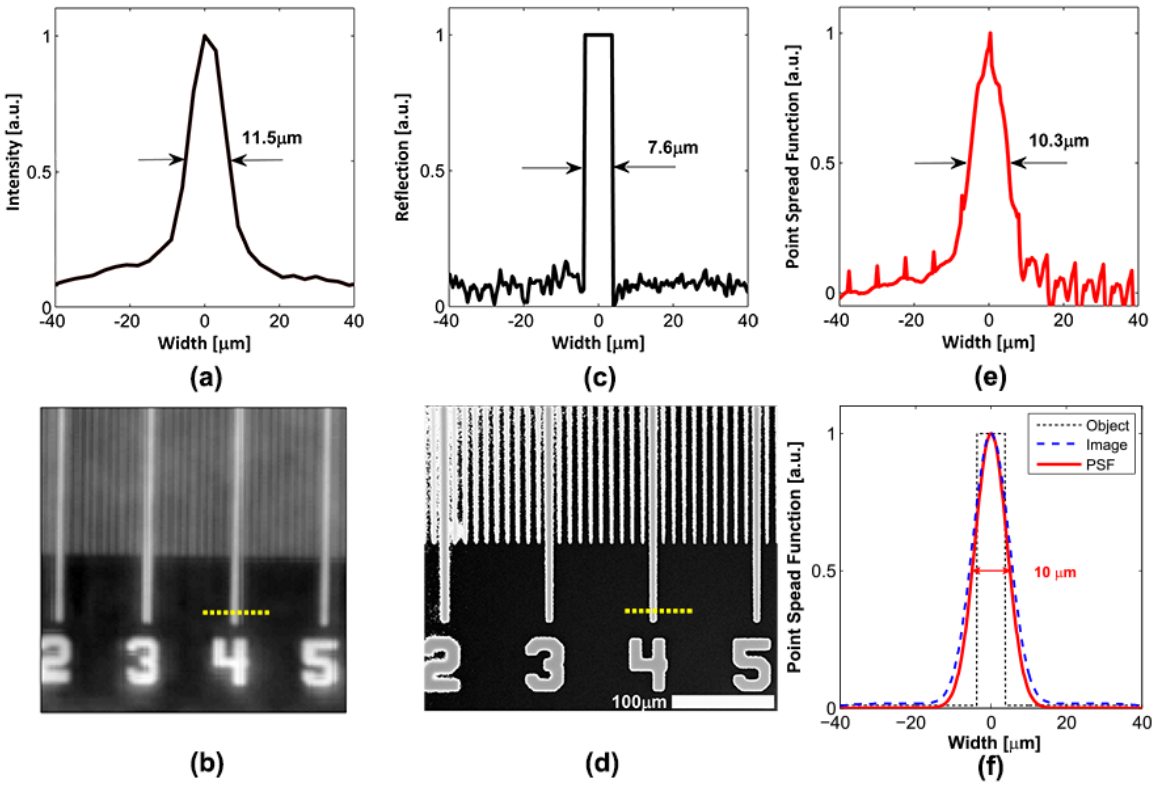

Fig. 3.11 (a) An OCT profile of the test scale line with a width of 11.5 µm; (b) an OCT image of the test scale line; (c) an object profile of the test scale line with a width of 7.6 µm; (d) a microscopy image of the test scale line; (e) a transverse PSF profile of the OCT system with a width of 10.3 µm; and (f) a PSF profile computed from the simulated dashed OCT profile and dotted object profile — the resultant width of the PSF is 10 µm.

3.3.5.3 System Sensitivity

Sensitivity is an important feature of an OCT system to denote the minimum detectable reflected optical power. It is generally calculated using the mathematical SNR formula in Equation 2.26 (see above), which can be expanded into Equation 2.29 for a time-domain OCT system. The latter SNR formula indicates that the system sensitivity is proportional to the power returning from the sample. To calculate a minimum resolvable reflectivity or the imaging sensitivity, an ND filter (with an optical density of D) followed by a mirror is normally used to attenuate the sample reflection, so that a sample with a reflectivity of $-20D$ in dB can be created. As mentioned before, the experimental verification of the system sensitivity is performed by measuring the OCT A-scan peak height and the noise floor, following Equation 2.37 (see above).

For the simple FF-OCT system, a window sample was used to generate a reflectivity at -28 dB (as $R_{win} = 0.04$). With a mirror reference, an A-scan signal was obtained in the FF-OCT measurement of the window. In Fig. 3.12 (a) (see below), the acquired envelope signal was adjusted to present the variation of the reflectivity within the range of 0 to 0.04 as a function of the penetration depth. The smallest resolvable reflectivity is identified below -60 dB in the logarithmic profile of the envelope for the window measurement, as shown in Fig. 3.12 (b). This indicates the imaging sensitivity for measurement of this window sample. The DR for this measurement can be also obtained within the range of -60 dB to -28 dB.

According to Equation 2.37 (see above), the expression of the system achievable sensitivity in dB can be rewritten as the reflectivity attenuation plus ten times the base-10 logarithm of the ratio of the square of the A-scan peak intensity to the standard deviation of the reference arm noise floor, given by:

$$\Sigma = \mathrm{SNR}_{dB} = 10\log_{10}\frac{I_{FFOCT}^2}{\sigma_{noise}^2} + 28. \tag{3.19}$$

in which I_{FFOCT} represents the FF-OCT A-scan peak intensity, σ_{noise} stands for the STD of the reference arm noise floor, and 28 dB is the sample arm attenuation. As the reference mirror contribute $\frac{1}{1.04}$ of the total reflection power of both interferometric arms, the reference arm noise power accounts for a same proportion of the A-scan noise power. The STD of the reference noise was calculated as 1.98×10^{-4} by using 140 intensity points in the A-scan noise floor within the depth range highlighted in Fig. 3.12 (a). By substituting the envelope peak reflectivity 0.04 and the reference noise variance 1.98×10^{-4} into Equation 3.19 (see above), the sensitivity of the simple FF-OCT system can achieve as large as 74 dB.

Fig. 3.13 (a) and (b) demonstrates the reflectivity variation of a mirror sample in the FF-OCT measurement of the mirror / mirror envelope signal. In Fig. 3.13 (b), the weakest resolvable reflectivity is just below -40 dB, indicating that the imaging sensitivity for the measurement of the mirror sample is below -40 dB. It is also noted that the system DR for this measurement covers a range from -40 dB to 0 in Fig. 3.13 (b). The side lobes are echoes that are due to the non-Gaussian spectral shape of the light source. They are more distinct in the measurement of the sample with a higher reflectivity than the window sample. The reference noise variance was calculated as 9.37×10^{-4}, according to A-scan noise intensity points as marked in Fig. 3.13 (a). The achievable sensitivity of the system was estimated to be 60 dB by Equation 3.19, while the sample attenuated reflectivity was zero.

Hence, the attenuation of the sample arm reflectivity can facilitate the estimation of the achievable system sensitivity of the simple FF-OCT system. The DR of the system can also be measured in terms of samples with different reflectivity.

Therefore, by using a cheap LED for the illumination of the sample at a power of 40 µW in the simple FF-OCT system, the achievable system sensitivity was obtained as 74 dB by the use of a window sample. For the imaging of the window sample, the smallest resolvable reflectivity was measured below -60 dB and a DR was acquired from -60 dB to -28 dB. For the imaging of the mirror sample, the smallest resolvable reflectivity was measured below -40 dB and a DR was acquired from -40 dB to 0.

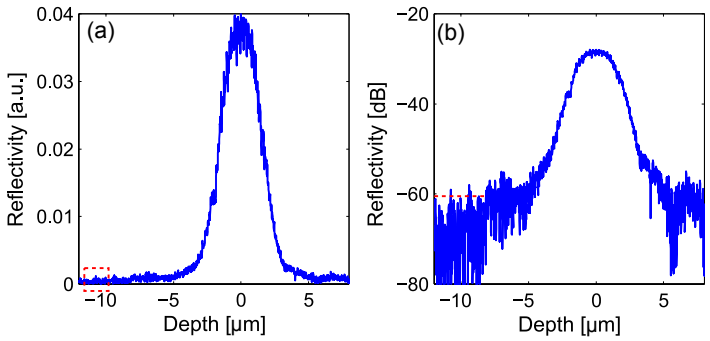

Fig. 3.12 Determination of the system sensitivity with a window sample; (a) an A-scan signal in a range of 0 to 0.04 to describe the window reflectivity as a function of depth; (b) the logarithmic scale of the A-scan signal in (a) with minimum identifiable reflectivity below -60 dB.

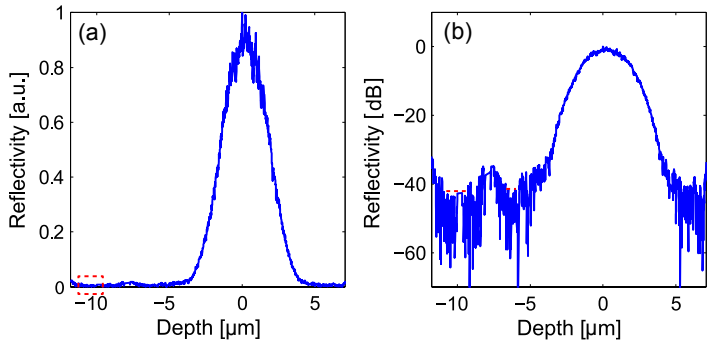

Fig. 3.13 Determination of the system sensitivity with a mirror sample; (a) an A-scan signal to describe the mirror reflectivity as a function of depth; (b) the logarithmic scale of the A-scan signal in (a) with minimum identifiable reflectivity below -40 dB.

3.4 Development of a Phase-Shifting FF-OCT System

The simple FF-OCT system utilises a steady-speed movement of the sample arm to produce a heterodyne beat frequency to modulate the OCT signals. A high frame-rate image acquisition and a low-speed sample movement are applied to ensure sufficient sampling points for the reconstruction of OCT interference signals. Good imaging precision can be obtained with the sampling rate of a beat cycle exceeding the Nyquist rate, which allows the determination of the envelope peak position. However, having more sampling points requires the occupation of a larger amount of storage space of the FF-OCT data in the computer. A general case of a depth-scanning of 200 µm with a movement speed of $3\,\mu\mathrm{m\,s^{-1}}$ and a camera frame rate of 120 fps, i.e. more than 16 sampling points per beat cycle, results in 8000 images being acquired, in which the file size of the images can reach 860 MB if a normal image setting with 240 px $\times$ 240 px per image and 16-bit unsigned integer data type is considered.

To determine the envelope peak position with less sampling points, the envelopes may be retrieved without recovering the interference patterns. The PSI technique has been performed with interferometry systems through the use of different algorithms [206, 223–228] to extract a phase map from several intensity fringe patterns [229]. The phase-shift is applied by shifting the phase by a known amount, e.g. $\frac{\pi}{2}$, between each intensity measurement. The envelope intensity point can be obtained by analysing the point-by-point intensity of three or more interference signals [230].

Many FF-OCT systems use the phase-shifting technique to acquire fringe-free *en-face* images directly from the measurements. The synchronisation between the phase-shifting and the image acquisition is required to improve the time efficiency and to lock the phases.

Nevertheless, this method requires high-performance system components in order to achieve a good sensitivity with such a small sampling rate.

The purpose is to modify the established simple FF-OCT system with minor modification and to aim for less image acquisition with the new system. The phase-shifting technique is employed in the development of the new system without synchronised operations. A phase-shifting method/algorithm is chosen to minimise the phase error caused by external disturbances such as vibrations and turbulence. In this section, the development of a phase-shifting FF-OCT system is described to illustrate the retrieval of envelope signals with fewer sampling points.

3.4.1 Experimental Arrangement

The phase-shifting FF-OCT system is based on the PSI technique. It was developed as an add-on to the simple FF-OCT system, in which the fixed reference arm was replaced by a phase-shifting module. Only minor modifications were made to construct the phase-shifting FF-OCT system. As illustrated in Fig. 3.14 (see below), the core of the system remained as a Michelson interferometer with the same infrared LED source for system illumination and the CMOS camera as detector. Instead of a steady speed movement of the sample arm, a motorised stepper was used to move the sample step by step with a submicrometre or micrometre-scale step size. A piezoelectric transducer (PT) was used to generate phase shifts to the grabbed *en-face* images and to modulate the OPD.

In this study, the five-step phase-shifting algorithm was used to retrieve the envelope. It requires a fixed phase-shift of $\frac{\pi}{2}$ between adjacent steps. A quarter phase change corresponds to a depth interval of $\frac{\lambda_0}{8}$. The sequence of values of phase-shift steps at which phase-shift images are grabbed is determined by the sequence of positions of the PT [206]. A PT displacement of $\frac{\lambda_0}{8}$ was achieved by a voltage step (drop or rise) of 0.61 V. Phase-shift images of five steps at $-\pi$, $-\frac{\pi}{2}$, 0, $\frac{\pi}{2}$, π relative phases can be obtained by four voltage increments of 0.61 V and used in the five-step phase-shifting algorithm.

Both the interferometry mechanism and the system alignment are similar to the simple FF-OCT system. A sampling rate above the Nyquist rate, i.e. at least four sampling points, is sufficient to retrieve the envelope signal and obtain the envelope peak position. The minimum step size of the envelope signal in the depth direction should be half the depth resolution, which is about 2 µm.

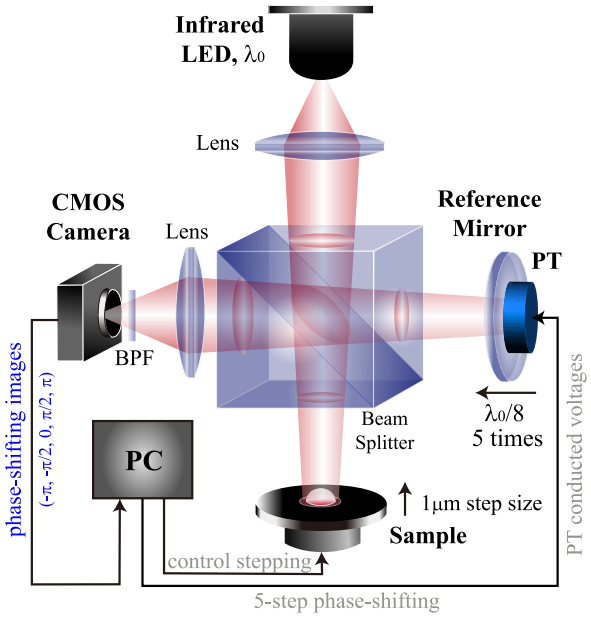

Fig. 3.14 Schematic diagram of a phase-shifting FF-OCT system with a PT to generate phase shifts to the grabbed images.

3.4.2 Experimental Procedures

a. Mechanism of the five-step phase-shifting algorithm

To retrieve the envelope and obtain the envelope peak position, the interference pattern, represented by $\cos[\Phi(p_x, p_y), z]$ in Equation 3.1 (see above), have to be removed. In the simple FF-OCT system, the HT method was used to shift the phase of an interferogram by -90°. The interference pattern was removed using the shifted signal, resulting in only the reconstructed envelope signal.

As mentioned before, the system must utilise a sampling depth interval that is no greater than the one half of the size of the depth-resolution, i.e. the FWHM of the envelope. At least four envelope sampling points thus are needed for the reconstruction and peak determination of the envelope. The simple FF-OCT system requires at least two sampling points per beat cycle to perfectly retrieve the envelope. Hence, the phase-shifting method allows for a large reduction of the number of images required in the FF-OCT imaging, compared to the simple system.

Some basic phase-shifting algorithms with three to eight phase steps are illustrated in Table 2.1 (see above). The five-step phase-shifting method was employed in the developed phase-shifting FF-OCT system for its advantage of lower phase error and better reliability, because the phase shift images are susceptible to external disturbances. Like most of the

algorithms, it utilises a phase step of $\frac{\pi}{2}$, as a result, its first phase $(-\pi)$ is overlapped with the last one (π), offering a phase-shifter calibration. It is also suggested by Larkin that both phase and envelope calculations with the algorithm are insensitive to sampling spacing or step-size error [206].

The five-step phase-shifting algorithm requires five sequentially sampled *en-face* images, in which adjacent images are separated by a $\frac{\pi}{2}$ phase interval. Referring to Hariharan equations, these five images can be theoretically expressed by:

$$\begin{aligned}
I_1(p_x, p_y) &= I_{DC}(p_x, p_y) + M(p_x, p_y)\cos[\Phi(p_x, p_y) - \pi], \\
I_2(p_x, p_y) &= I_{DC}(p_x, p_y) + M(p_x, p_y)\cos[\Phi(p_x, p_y) - \frac{\pi}{2}], \\
I_3(p_x, p_y) &= I_{DC}(p_x, p_y) + M(p_x, p_y)\cos[\Phi(p_x, p_y)], \\
I_4(p_x, p_y) &= I_{DC}(p_x, p_y) + M(p_x, p_y)\cos[\Phi(p_x, p_y) + \frac{\pi}{2}], \\
I_5(p_x, p_y) &= I_{DC}(p_x, p_y) + M(p_x, p_y)\cos[\Phi(p_x, p_y) + \pi].
\end{aligned} \tag{3.20}$$

At a pixel location (p_x, p_y) in the tomography *en-face* image, one combines all five intensity values to extract the envelope amplitude $M(p_x, p_y)$ and the instantaneous phase $\Phi(p_x, p_y)$, which are expressed as:

$$M(p_x, p_y) = \frac{1}{4}\sqrt{4(I_2 - I_4)^2 + (-I_1 + 2I_3 - I_5)^2}, \tag{3.21}$$

$$\Phi(p_x, p_y) = \tan^{-1}\{\frac{2[I_2(p_x, p_y) - I_4(p_x, p_y)]}{-I_1(p_x, p_y) + 2I_3(p_x, p_y) - I_5(p_x, p_y)}\}. \tag{3.22}$$

Both the envelope amplitude and the instantaneous phase are calculated from the five intensity values corresponding to five phase steps. The correlation of the envelope amplitude or the instantaneous phase with the penetration depth are decoupled.

Fig. 3.15 (see below) demonstrates the mechanism of the five-step phase-shifting algorithm to retrieve the envelope signal of an interference signal, which was simulated by the multiplication of a cosine signal and a Gaussian function. The cosine signal represents the Doppler-shifted optical carrier and the Gaussian function represents the FF-OCT envelope. In Fig. 3.15 (a), the interference signal illustrated by the solid blue line was mathematically expressed by $y = a \cdot e^{-\frac{x^2}{2b^2}} \cdot cos(cx)$, for which $a = 1$, $b = 10.25$, $c = 1$ and x denotes the depth in arbitrary unit.

The interference signal is sampled by nine points with a depth interval of five. Assuming θ as the phase of an arbitrary sampling point at x, the five coloured points at x denote the

signal intensities (I_1,I_2,I_3,I_4 and I_5) at $\theta-\pi$, $\theta-\frac{\pi}{2}$, θ, $\theta+\frac{\pi}{2}$ and $\theta+\pi$, after the applied corresponding phase shifts to the sampling point. The black diamond identifies the envelope intensity of the sampling point after the interference term $cos(cx)$ is removed via the five-step phase-shift algorithm in Equation 3.21 (see above). Fig. 3.15 (b) illustrates the consistency of the retrieved envelope intensities with the simulated Gaussian function.

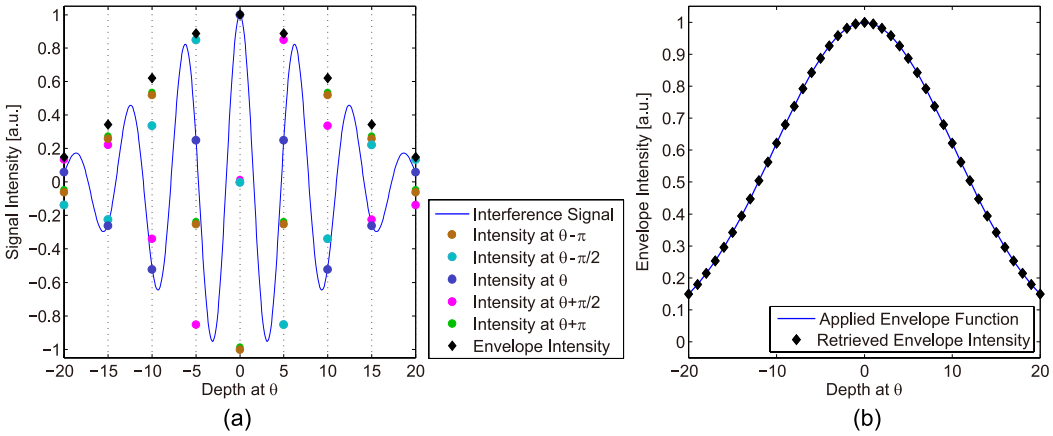

Fig. 3.15 Illustration of the five-step phase-shifting algorithm for envelope retrieval. (a) The coloured points on a grid line are the phase shift points after applying respective phase shifts to the sampling points of the simulated interference signal on the grid line. The black diamond point is the resultant envelope intensity point calculated from the five-step phase-shifting algorithm with the phase shift points. (b) The retrieved envelope intensity points are overlapped with the applied envelope function.

b. Experimental Operations

Before the measurement, a system alignment procedure was followed, i.e. aligning the reference arm with the beam-splitter and the CMOS camera and aligning the sample arm with the beam-splitter and the infrared light source. Further systematic adjustment to the elements was carried out until a sharp image of the sample with a desired FOV was identified on the camera screen.

The CMOS camera and the infrared LED light source retained the same settings as for the simple FF-OCT system. However, the control module needed to consecutively control the axial stepping of the sample arm, the phase-shifting of the reference arm, the image acquisition and processing. No parallel operations and no interplay or delay problems arose in the actual measurements. A home-made GUI in Matlab was programmed to include a stepping control module, a PT voltage (displacement) control module, and a camera screen to display the grabbed *en-face* images with the user input settings, as shown in Fig. 3.16.

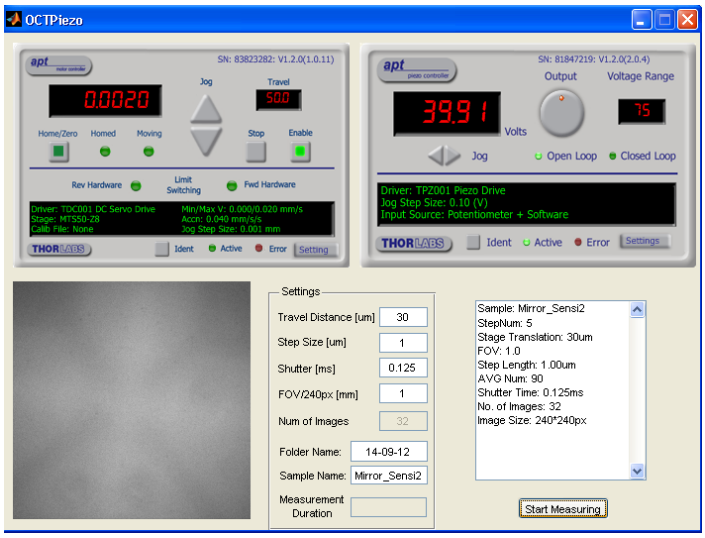

Fig. 3.16 GUI of the control module of the phase-shifting FF-OCT system

The phase-shifting of the reference arm relies on the voltage variation of the PT. To introduce a phase shift of $\frac{\pi}{2}$ (or a displacement of $\frac{\lambda_0}{8}$) to the sampling points, the PT is driven with a voltage increment of 0.61 V. According to the requirement of the sample, the total travel distance and the step size were pre-set for the stepping of the sample arm.

After each shifting of the phase, i.e. shifting by $\frac{\pi}{2}$, a pre-set number of images was acquired by the camera at this step for the purpose of the signal averaging. At each axial travel step of the sample, the reference arm was phase-shifted five times and images of the five different phase shifts were temporarily stored in the PC buffer. Once all the five times of phase-shifting were complete, the five-step algorithm was used to remove the interference pattern and resulted in a fringe-free image. This unique image was saved to the image stack in the PC to represent the FF-OCT *en-face* tomography at a step of the sample movement. Other phase-shift images were immediately deleted from the PC buffer.

Subsequently, the control module was ready to start a new cycle of sequential operations, including moving the sample by the pre-set step size, performing five steps of phase-shifting, acquiring a pre-set number of images after each phase-shafting and computing a fringe-free image to be saved to the image stack. These cycles and sub cycles of operations are characterised in Fig. 3.17.

The total number of tomographic images is determined by the total step number of the sample movement, given by the ceiling integer of the travel distance divided by the travelling step size. For a case of a 200 µm travel depth into a sample, the simple FF-OCT system has to acquire 8000 images to make sure there are enough sampling points to reconstruct the

envelope signal. However, for the phase-shifting system only 200 images will be saved onto the PC if a step size of 1 µm is taken.

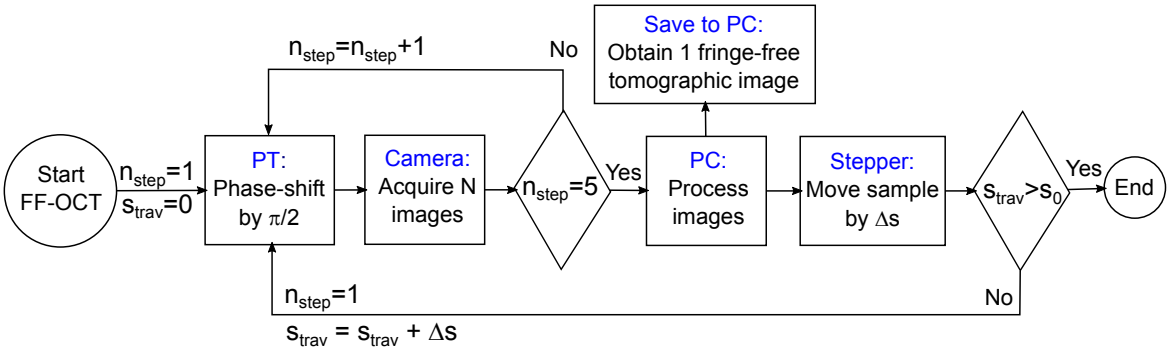

Fig. 3.17 Flowchart of the measurement with the phase-shifting FF-OCT system to generate the tomographic image at a given depth. n_{step} is the number of times that the phase has been shifted. s_{trav} is the distance travelled by the sample. Δs is the step size of the stepper for the movement of the sample. s_0 is the pre-set travel distance of the sample. N is the number of images acquired after each phase-shifting for the purpose of image averaging.

After the measurement, the image stack saved in the PC contained all fringe-free *en-face* tomographic images. A-scan signals and B-scan images can be directly reconstructed from the image stack for further data analysis.

3.4.3 System Characteristics

The phase-shifting FF-OCT system is beneficial into directly obtaining fringe-free tomographic images during the measurement. The resultant image volume occupies a much smaller storage space in the PC than the simple system for the investigation of the same sample with the same imaging depth.

The depth-resolution and transverse resolution of the phase-shifting system is identical to that of the simple system. This is because the phase-shifting system was developed based upon the simple system and there were no modifications to the light source, the CMOS camera, and the beam spread. According to Equations 2.21 and 2.22 (see above), the imaging resolution stays the same with the fixed source central wavelength λ_0, the spectral bandwidth $\Delta\lambda$, the NA and the pixel size. As described in Section 3.3.5 (see above), the depth-resolution was measured as 3.6 µm and the transverse resolution was measured as 10.3 µm.

The sensitivity of the simple FF-OCT system is determined by the high sampling rate of the interference patterns. For the phase-shifting system, the sensitivity is enhanced by the averaging of a large number of acquired phase-shift images.

During the measurement, a pre-set number N of images at each step of phase-shifting was acquired and stored temporarily in the PC buffer. By averaging these images, the system sensitivity in dB can be enhanced by $10\log_{10}N$:

$$\Sigma_{avg} = 10\log_{10}\frac{\langle NI_{OCT}\rangle^2}{\sqrt{N}\sigma^2_{noise}} = 10\log_{10}\frac{\langle I_{OCT}\rangle^2}{\sigma^2_{noise}} + 10\log_{10}N. \tag{3.23}$$

To compare the sensitivity between the two developed systems, the same window sample was measured by the phase-shifting system with a mirror reference. Each resultant fringe-free image was averaged by 90 phase-shift images. Fig. 3.18 (see below) shows both the measurements of the window sample by using the phase-shifting system and the simple system, respectively. The reflectivity variation obtained from the phase-shifting system is described by the dark blue dots; the background light blue signals are taken from Fig. 3.12 (see above) for the sensitivity evaluation of the simple system.

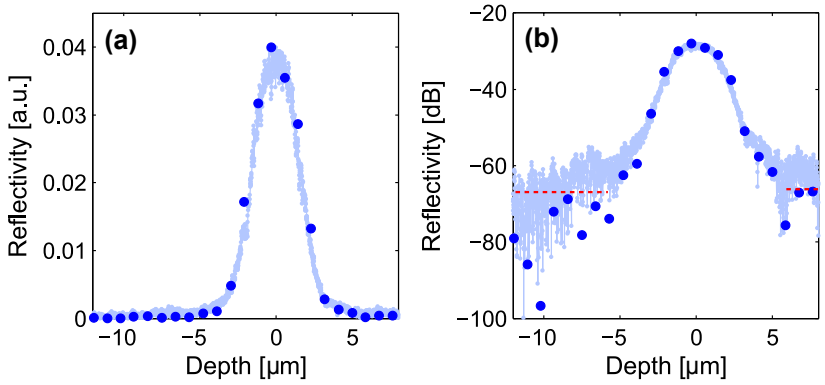

Fig. 3.18 Sensitivity comparison between the phase-shifting system and the simple system by measuring a window sample; the dark blue dots were obtained from the phase-shifting system and the background light blue signals were obtained from the simple system; (a) A-scan signals in a range of 0 to 0.04 to describe the window reflectivity as a function of depth; (b) the A-scan signals in dB obtained by using the phase-shifting system with a minimum identifiable reflectivity approaching -70 dB.

As the window has a reflectivity of 0.04 or -28 dB, Fig. 3.18 (a) demonstrates the variation of the reflectivity within the range of 0 to 0.04 as a function of the penetration depth. The retrieved envelope points from the phase-shifting system agree with the envelope signal obtained from the simple system, but the number of envelope points is largely reduced in the phase-shifting system, as there are only 32 sampling points within a 20 μm depth range. Fig. 3.18 (b) identifies the smallest resolvable reflectivity approaching -70 dB for the phase-shifting measurement. Compared to the minimum identifiable reflectivity below -60 dB of the background signal, the imaging sensitivity for the measurement of the same

window sample has a 10 dB advantage over the simple system. The DR is also obtained to have a wider range from -70 dB to -28 dB.

As mentioned in Section 3.3.5.3 (see above), the system's achievable sensitivity can be calculated by the reflectivity attenuation plus ten times the base 10 logarithm of the ratio of the square of the A-scan peak intensity to the STD of the reference arm noise floor. The STD of the reference noise was calculated as 3.4×10^{-5} based on the reference arm contribution to the A-scan noise floor. By substituting the envelope peak reflectivity 0.04 and the reference noise variance 3.4×10^{-5} into Equation 3.19 (see above), the achievable sensitivity of the phase-shifting FF-OCT system was obtained as 89 dB, which has a 15 dB advantage over the simple system.

The superiority of the phase-shifting FF-OCT system thus is that it directly retrieves fringe-free *en-face* images during the measurement and envelope signals are reconstructed with fewer sampling points. The total space in the PC for storing the image volume is hence greatly reduced. It is also found that the imaging sensitivity of the phase-shifting system can be better than the simple system, if the averaging over a large number of phase-shift images are applied during the phase-shifting. The averaging enhances the system sensitivity, but also prolongs the measurement duration. A larger depth step-size, e.g. 5 µm between adjacent acquired images, would lead to the loss of image precision. It could be unrealistic to measure a 3-D data cube on biological samples, as the sample would dry out during the measurement. The system can permit a single *en-face* tomographic image to be acquired in real-time, in a similar manner to the histology (biopsy), which would definitely require more sophisticated processing and more efficient system components.

3.5 Discussion

a. FF-OCT

FF-OCT is an advantageous OCT variant to provide faster and simpler experimental operations. It shares same derivations of imaging resolution with point-scan OCT techniques. However, for a beam spread with a similar NA, it is easy to achieve a better transverse resolution with FF-OCT than with the point-scan systems, as it is difficult for the probe beam to have a fixed, accurate, small interval of transverse movement. Like the standard OCT, the sensitivity of FF-OCT is also shot-noise-limited.

Despite that, the SNR actually gets worse in FF-OCT systems compared to time-domain OCT systems. Firstly, this is because the energy of the light source is spreading into a 2-D

area instead of focusing on a point and hence the recorded intensity for each camera pixel is degraded. Secondly it is because the thermal light sources used in most FF-OCT systems are essentially low-power light sources and the low irradiance incident on the sample results in a degraded signal intensity. High-power light sources with low temporal coherence and low spatial coherence are desired in FF-OCT systems to effectively improve the SNR and suppress the speckle noise, although they are usually very expensive light sources. Note that the high-power light sources of the point-scan OCT, e.g. SLD and femtosecond laser, would cause speckle noise in FF-OCT images if they were used in an FF-OCT system because of their spatial coherence property.

In general, FF-OCT is a good imaging technique in terms of the simple experimental operations and good imaging performance. The two developed low-cost FF-OCT systems have confirmed comparable imaging resolution to point-scan OCT systems and good system sensitivity of above 74 dB.

b. Phase-shifting FF-OCT system

The phase-shifting FF-OCT system is demonstrated as directly obtaining fringe-free tomographic images during the measurement procedures. The resultant image volume occupies a much smaller amount of space on the PC compared to the simple system for the investigation of the same sample with the same imaging penetration depth. The system is also beneficial for the decoupling of the envelope amplitude and the instantaneous phase with the imaging penetration depth.

However, apart from the lengthy measurement time and the excessive measurement procedures, there could be some issues arising in actual operations, such as the non-uniform step size driven by the stepper, the hysteresis in the load voltage of the PT and varied PT displacements of the same voltage increment. The phase-shifting itself is susceptible to external disturbances.

c. Simple FF-OCT system

The simple FF-OCT system is advantageous for 3-D imaging with a faster acquisition speed and fewer operations than conventional OCT techniques and the phase-shifting system. Good imaging precision can be delivered with the sampling rate of a beat cycle exceeding the Nyquist rate. Both tomographic and topographic investigations are allowed with precisely reconstructed envelopes and interference signals. The only weaknesses are the relatively low sensitivity and the occupation of a large storage space for the image volume.

The low sensitivity mainly originates with the FF-OCT system itself, because of the 2-D spreading of the light beam and the low power of the low-cost thermal source. Other factors are due to the slowdown of the sample movement by the motorised stage and the hysteresis of the image acquisition by the CMOS camera. These do have effects on the reconstruction of the interference signals, e.g. the deformation of an interferogram fragment within a beat cycle could be caused. However, the overall shape of the retrieved envelope stays the same. The large number of acquired images is an issue of the simple FF-OCT and yet it permits high fidelity in the reconstruction of interference signals, which lead to a high imaging precision to enable both tomographic imaging and surface topography studies. In addition, the system sensitivity would be degraded if fewer images were acquired. The great easiness and flexibility of the simple system allow the use of the FF-OCT technique in different industrial environments.

The following chapters highlight a couple of applications where the simple FF-OCT system can be employed effectively to study the subsurface and superficial structures.

3.6 Summary

This chapter has given a deep characterisation of the developments of the two FF-OCT systems. The two systems were both explored from their system setups, the experimental procedures, the data analysis, and the system performance.

The simple FF-OCT system has the advantage of a fast acquisition speed and simple experimental operations. The HT method is used for the envelope detection in the data analysis for the tomographic imaging. The interpolation technique and a minimum search algorithm is used for the peak position determination of the interferogram in the data analysis for the surface topography. The phase-shifting FF-OCT system in effect requires much less image storage than the simple system. A 5-step phase-shifting algorithm is used as one of the experimental operations to derive the fringe-free images during the measurement.

The imaging resolutions of the two systems are identical, measured as 3.6 µm for the depth-resolution and 10.3 µm for the transverse resolution. The sensitivities of the two systems are calculated by using a window sample. The achievable system sensitivities are obtained as 74 dB for the simple system and 89 dB for the phase-shifting system. However, compared to the developed phase-shifting FF-OCT system, the simple FF-OCT system has been demonstrated to be more efficient in terms of cost, easiness to use, experimental simplicity and adaptability to different applications.

Chapter 4

Tomographic Imaging Studies using the Simple FF-OCT System

4.1 Evaluation of Pharmaceutical Pellet Coating

4.1.1 Introduction

Pharmaceutical products are produced for use in drug therapy to prevent, control and cure diseases and to treat symptoms [231]. They typically involve a mixture of drug components and non-drug components such as excipients, along with other non-reusable material that may not be considered either ingredient or packaging e.g. a capsule shell [232]. The active pharmaceutical ingredient (API) is the active or central ingredient of a drug component which causes the direct effect on the disease treatment [233]. The excipients are usually included as binders and coating materials to protect and enhance the function of a dosage form. They may also assist in product identification and patient acceptability [234].

Pharmaceutical Coating

Drug delivery refers to technologies for transporting a drug component in the body to safely achieve its desired therapeutic effect [235]. Most common routes of administration include the preferred oral (GI tract), topical (skin) and injection approaches [236]. Tablet and pellet are the two most common types of solid dosage forms for oral administration. To ensure an even disintegration of dosage forms inside the human body, the drug components are usually mixed with excipients and/or binders. By applying additional polymer coatings, the release of the drug components can be delayed or sustained in a predetermined manner [237, 238].

Additional benefits of polymer coatings include reducing the breakage and chipping of the dosage forms during product packaging, providing a protection from light, moisture and environmental gases, improving the taste and the appearance, etc.

Polymer coatings are usually achieved by spraying polymer materials at the tablet or pellet cores in a coating pan until a desired polymer coating thickness is achieved. In particular, enteric polymers are used as coating materials to resist stomach acid and break down rapidly at a less acidic pH [239]. For example, enteric coated aspirin tablets dissolve only in the alkaline environment present in the small intestine and prevent irritation in the stomach caused by aspirin. A desired drug release profile can be attained by applying sophisticated coating structures and particular polymer materials as illustrated in many controlled-release systems [240].

The coating quality is directly related to the drug release performance and the therapeutic efficiency of a dosage form inside human body [10]. Coating structure and layer uniformity are key coating attributes affecting the drug dissolution [241]. Effective monitoring and controlling of the coating process is important to maintain coating capability and efficiency. It is also critical to evaluate the coating quality in terms of the coating structure and uniformity in order to predict the drug release of a final coated product.

Pharmaceutical Pellet

Pharmaceutical pellets are important components in many controlled-release drug delivery systems [242]. Small-size pellets of sub-millimetre diameter provide a higher degree of flexibility during the design and development of oral dosage forms. They are designed to be coated and filled into capsules or compressed into other dosage forms, such as tablets, in order to control the drug release. The use of small-size pellets avoids dose-dumping problems because of local defects in the coating structure which are much more severe in a monolith as opposed to a multi-particulate release system. It also allows a more even spread of the drug after the dissolution of the tablet excipient or the capsule shell, and thus the drug absorption within the gastrointestinal tract can be ensured [243].

In the following subsections, conventional analytical techniques for the evaluation of the pharmaceutical coating quality are first reviewed. Then the coatings of the small-size pellets are studied by using the developed simple FF-OCT system. These samples include single-layer and multi-layer coated pellets.

4.1.2 Overview of Analytical Techniques for Coatings Analysis

4.1.2.1 Pharmaceutical Coating Characteristics

Controlled-release technologies include immediate-release, delayed-release, and sustained-release of the drug components, which can be obtained by using various coatings [244]. Depending on the desired dissolution profile, the API can be mixed with excipient powders prior to being compressed into solid dosage forms. In addition, the API can exist within the matrix core of a tablet or a pellet possibly encapsulated by a polymer coating. The API can also be absorbed onto the surface of the core or within the polymer coating to form a drug-loaded coating layer [245].

The pharmaceutical coatings are of great importance in determining the dissolution profile of the solid dosage forms. Small changes in coating properties such as, layer thickness, uniformity, and porosity have direct implication on product performance. Haddish-Berhane *et al.* [241] demonstrated that the drug release profile was predominately affected by the coating thickness; Ho *et al.* [243] reported the effect of layer uniformity on in vitro drug release; Shivanand and Sprockel [246] investigated the relationship between the physicochemical properties of porosity and the drug release rate. It is hence of great interest for these coating characteristics to be monitored and controlled during the production process [247].

4.1.2.2 Analytical Techniques

The coating characteristics of solid dosage forms have so far been studied by using a number of analytical techniques.

Weight Gain

Most common in the pharmaceutical industry is to evaluate the coating quality by taking tablets or pellets during the manufacture, weighing a known size and determining the average amount of polymer added [10]. The measurement is a rapid and non-destructive method that typically detects the weight gain [248] and gives an indication of the final product characteristics, such as average coating thickness and dissolution rate.

The weight-gain method has been employed profitably as a quantitative tool [10]. However, coating quality cannot be determined based solely upon an average value of the coating weight gain without considering the distribution and the uniformity of coating layers [249].

Microscopy

Microscopy is a common technique in histology to study the sample morphology. To study pharmaceutical coatings with microscopy, the standard approach involves mounting, microtome cutting and slicing or staining of a dosage form to be viewed under a microscope [250]. The cross-sectional cuts of tablets or pellets are generally captured in a microscopy image, from which the coating characteristics can be determined. For example, the thickness of a specific coating layer can be obtained by measuring the distance between manually marked points on the borders of the coating layer [250].

Conventional optical microscopy and scanning electron microscopy (SEM) have been used to investigate the structural characteristics of pharmaceutical coatings [243, 251]. However, they are destructive techniques and consequently difficult to apply as an in-process quality control [252]. The lengthy and delicate procedures during the preparation of cross-sections require time-consuming and complicated manual preparations. It might also introduce artefacts, e.g. plastic deformation of the coating layers [253]. Moreover, the 3-D volumetric visualisation will require realignment and reconstruction of the acquired microscopic images [66].

NIR spectroscopic imaging

Unlike microscopy techniques, NIR spectroscopic imaging (NIRSI) is a fast and non-destructive analytical technique. It is established in the pharmaceutical industry to provide qualitative and quantitative pharmaceutical analysis [254]. Pharmaceutical materials can be measured in diffuse transmittance, diffuse reflectance or transflectance depending on their absorption and scattering characteristics [255]. Acquired NIR spectra allow for the identification and assessment of the physical and biopharmaceutical parameters, such as hardness, coating thickness and dissolution rate of intact dosage forms [255]. Many studies also conduct process monitoring using NIRSI in in-line and on-line measurements for the determination of these characteristics [238, 256–258].

Yet, NIRSI is an inherently indirect and highly empirical method [10, 258] for the analysis of pharmaceutical coatings. It requires both the NIR spectral signatures and the calibration model of a certain coating material for the prediction of its coating properties [238]. Chemometric procedures for data modelling are heavily relied on, with sample selection and data pretreatment being the most critical issues regarding calibration [255, 259].

It is even more difficult to resolve the coating characteristics from the NIR spectra of multi-layer coatings, as exhaustive calibration models are needed to be built by sophisticated

mathematical techniques with the properties of the involved coating materials and/or drug substance [255].

These are the most commonly used methods to study the coating. However, apart from these methods, many other techniques have been used to analyse coating characteristics.

Raman spectroscopy has been employed to analyse pharmaceutical coating qualities by using Raman scattering of a laser light in the visible, NIR or near ultraviolet range [260]. It yields similar and complementary information with respect to NIR analysis [247]. However, it suffers the same issue in that chemometric models are needed during the analysis of Raman spectra.

Electron paramagnetic resonance spectroscopy (EPRS) has been used to illustrate the influence of coating thickness on the solubilisation speed of pellets [261], although it still requires the development of mathematical models for the prediction of coating compositions and drug-release profile.

MRI has been used to monitor the dissolution process and their capabilities are demonstrated to study drug release *in situ* [262]. However, coating thicknesses are analysed indirectly from the acquired dissolution profile in MRI [247, 263]. The structural information of pharmaceutical coatings cannot be evaluated.

AFM and SEM have been used to investigate polymer coating surfaces in the study of the controlled-release mechanism [248]. These techniques are useful for the analysis of the porosity and roughness of the coating surface in order to predict their effects on the eventual dissolution profile. However, the layer distribution and the uniformity beneath the tablet or pellet surface cannot be assessed.

Confocal laser scanning microscopy (CLSM), TPI and OCT have recently been used as high-resolution imaging techniques for pharmaceutical coating analysis. Their capability of direct quantification of the coating structure has been demonstrated with a better than micrometre scale precision. Hence, a more accurate determination of coating characteristics is enabled with these techniques.

CLSM

CLSM is an imaging technique combining a laser scanning method with confocal microscopy to obtain high-resolution optical images with depth selectivity [36]. It has been used for the physicochemical characterisation of pharmaceutical systems [264]. It is beneficial for exposing the coating structures non-invasively by optical sectioning [265], allowing for an accurate prediction of coating characteristics.

TPI

TPI is an imaging technique using terahertz radiation, which is broadly applied to sub-millimetre electromagnetic waves between the high frequency edge of the microwave band 0.3 THz and the long-wavelength edge of far-infrared light 3 THz.

Similar to NIR radiation, terahertz radiation permits non-ionising and non-destructive investigation into pharmaceutical products. In particular, numerous amorphous pharmaceutical excipients are transparent or semi-transparent to terahertz radiation, whilst plentiful pharmaceutical crystalline constituents have spectral signatures within the terahertz frequency range [266]. An unparalleled penetration depth into pharmaceutical tablet of approximately 5 mm can be achieved with terahertz radiation [267]. High resolution imaging is allowed with TPI due to the relatively ultra-short width pulses of terahertz radiation [268].

TPI has been demonstrated as a powerful method for the determination of coating structures of tablets and pellets [269, 270]. It is capable of characterising coating structures (thickness) and coating uniformity [38]. It has been recently developed as an in-line measurement tool for tablets with coating thicknesses ranging from 40 µm to 1 mm [271].

Point-scan OCT

Together with other groups we have recently demonstrated that OCT can be used for the characterisation of tablet coatings [7, 132, 133]. The tablet coatings with a layer thickness range of 10 µm to 60 µm were measured quantitatively [132]. An in-line monitoring of a pharmaceutical film-coating process was also successfully implemented with OCT [272].

4.1.2.3 Characterisation of Pellet Coating

As stated in the previous part, the weight gain method only determines an average amount of the coating added to the core, which is insufficient to predict either coating structures (thicknesses) or coating uniformity; NIRSI, Raman and EPRS require the use of mathematical models to analyse coating characteristics; MRI are indirect methods to assess coating quality by the monitored dissolution profile; microscopy approaches need lengthy preparations of

the cross-sectional cuts of tablets or pellets, and thus they are destructive techniques; AFM and SEM can be used to study the drug release caused by the porosity of the coating surface; however, coating structure and uniformity cannot be assessed.

CLSM, TPI and OCT are all high-resolution imaging techniques for the pharmaceutical coating analysis. They allow a non-destructive imaging of coating structures as well as a direct quantification of coating characteristics.

However, there is only a small amount of literatures on the coating characterisation of small-size pellets using non-destructive imaging techniques because of the difficulties associated with the measurements of these small pellets.

TPI is a powerful technique, but it does not work for such small pellets owing to its large probe spot size, which is fundamentally limited by the wavelength of the terahertz radiation (i.e. 0.15 mm to 1.50 mm), resulting in strong scattering from sub-millimetre size pellets. CLSM shares an imaging precision of confocal microscopy. However, the imaging performance with CLSM for pharmaceutical coatings is limited by its low imaging contrast. OCT offers advantages over TPI and CLSM in terms of imaging resolution and imaging sensitivity, respectively. OCT generally provides a spatial resolution of several micrometres and adopts an interferometric sensitivity; the coating boundaries are unambiguously identified by the peak positions of OCT A-scan signals.

In previous OCT studies on pharmaceutical coatings, the single-point spectral-domain OCT systems were used for the measurement of pharmaceutical tablets. Each time the probe beam was shifted and focused onto a different (transverse) position on the tablet surface, an OCT spectrum was measured as a function of the wavelength(frequency). The A-scan signals were derived from these OCT spectra; the B-scan images and the volumetric representation would require the reconstruction from the A-scan signals acquired at different transverse locations. Therefore, for these point-scan systems, a full OCT measurement involves electromechanically moving either the tablet or the OCT probe beam along at least two transverse directions.

For small-size pellets, the point-scan approach is difficult and inefficient to perform OCT measurements. In the following section, the investigation of the coating characteristics of small-size pellets using the constructed simple FF-OCT system is described.

4.1.3 Characterisation of Pellet Coating using FF-OCT

4.1.3.1 Measurement Procedures

Prior to each FF-OCT measurement, the system optics were aligned and adjusted to obtain the required imaging FOV on the surface of a pellet. Blu-tack was used to attach a pellet to the sample arm with its front surface perpendicular to the optical axis. The position of the pellet on the optical axis was adjusted to reach the optimal position to start the depth-scan. The image-grabbing and the stage moving programs were prepared with all the required settings and parameters ready to be run.

During the FF-OCT measurement of a small-size pellet, the pellet or the sample arm was triggered to travel at a constant slow speed towards the beam-splitter. At the same time, the CMOS camera was operated to successively acquire images at a fast-frame rate. Sufficient phase shifts can be induced for the extraction of OCT features corresponding to the pellet coating structures. The pre-set travelling distance should cover the required imaging depth within the pellet, in order to ensure that the air/coating, coating/coating, and coating/core interfaces were retrieved from the FF-OCT measurement.

After the measurement, the FF-OCT system was reset to its original state. The 3-D image file was read and processed in Matlab following the data analysis procedures for tomographic imaging as described in Chapter 3. The processed data could be interpreted in A-scan signals, B-scan images or even 3-D volumetric representation for the assessment of the coating quality of the pellet sample.

Fig. 4.1 (a) and (b) show the photos of two example types of small-size pellets of up to 1 mm diameter. Fig. 4.1 (c) shows a microscopy image of the cross-section of a double layers coated pellet by using a normal optical microscope, which also suggests that microscopy is not always an effective imaging technique to distinguish coating structure.

The following subsections describe the FF-OCT characterisation of several pellets of different coating structures. These small-size pellets have diameters of approximately 0.85 mm to 1 mm. The coating thicknesses and coating structures are demonstrated with the A-scan and B-scan representations. Because of the curved surfaces and coating layers of these pellets, the layer thicknesses are manually measured by the widths between the upper and lower layer boundaries. Note that for all coating thickness calculations, a common refractive index of 1.5 was used even if there were slight variations of refractive indices between adjacent coating layers. The evaluation of coating quality rely on analysis of the A-scan signals and the B-scan images.

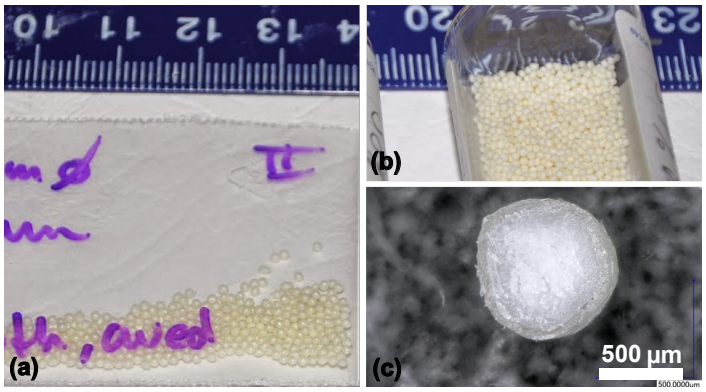

Fig. 4.1 (a) and (b) Photos of two example types of coated pellets; (c) a microscopy image of the cross-section of a double-layer coated pellet.

4.1.3.2 Single-Layer Coated Pellets

This part describes the characterisation of the single-layer coated pellets by using FF-OCT.

Measurements

The pellets in this study had a smooth surface morphology and a mean diameter of 1 mm. They were manufactured to have a drug-loaded coating layer; thus, active substance was contained in the single-layer coating. Four batches of pellets were classified in accordance with the thicknesses of the drug-loaded coating layers, which were estimated as 100 µm, 80 µm, 60 µm and 40 µm respectively for the four batches by weight-gain measurements. Three pellets per batch were randomly selected and measured by the simple FF-OCT system.

These single layer coated pellets were measured with a 3 µm s^{-1} sample arm movement speed, and a 120 fps camera frame rate. A total of 10,000 *en-face* images were acquired for the measurement of each pellet, covering a physical volume of $(800 \times 800 \times 250)$ µm^3. The data cubes were subsequently analysed with the aforementioned procedures for tomographic imaging.

Data Analysis

The resultant B-scan images and A-scan signals are presented in Fig. 4.2. Each combination of image and signal was extracted from a processed FF-OCT data cube of the corresponding batch of pellets. The B-scan images are used to illustrate the coating structures of pellets with coating thicknesses of 100 µm, 80 µm, 60 µm and 40 µm. The A-scan signals correspond to the intensity variations of the central depth profiles of the B-scan images. The peak in the A-scan signal and the particle-like feature in the B-scan image indicate an interference event due to a variation of refractive index in the actual pellet structure.

As shown in Fig. 4.2, single-layer structures are distinguished by the localisation of the particle-like features in B-scan images and the multiple peaks in A-scan signals. They could be the drug-loaded coating layer, which was applied to achieve a required drug release profile i.e. to dissolve the active substance under a fixed release rate. As mentioned in literatures [263, 270, 273], a drug-loaded coating of small pellet is usually obtained by spray an aqueous drug-binder solution onto inert pellet cores, such as commercial available sugar and microcrystalline spheres.

FF-OCT responses of pellet coating could only be introduced at pellet surface, coating/core interface and refractive index variation events inside a drug-loaded coating layer. Features on upper and lower borders of single-layer structure of each B-scan image in Fig. 4.2 may be due to pellet surface and coating/core interface, respectively. Inside a drug-loaded coating layer, drug molecules cannot be differentiated from the binders by FF-OCT signals, because their dimensions are far beyond the ability for OCT imaging to resolve. However, there could exist pores inside drug-loaded coating layers caused by inefficient coating and drying processes during pellet manufacture. The porosity within the drug-loaded coating can also lead to an acceleration of pellet disintegration and a modification of drug dissolution profile. Localised features in FF-OCT results may be caused by porosity of drug-loaded coating layers. This is because of the refractive index variation between the coating and the air (in pores) can effectively result in an OCT feature. However, features in B-scan image may not be completely caused by the porous structure. The possibility of the presence of other substances e.g. drug in crystalline form [263] to cause the variation of refractive index cannot be excluded.

The porosity distribution of drug-loaded coating layer is an important factor to affect the drug dissolution performance. The images and the signals in Fig. 4.2 demonstrate dense distributions of FF-OCT features for all batches of pellets, which may imply that most of the detectable pores have a diameter ranging from 4 µm to 10 µm and they are densely located inside drug-loaded coating layers. Presence of pores with a lower diameter than the current depth resolution cannot be determined with the simple FF-OCT system. The effect of the porosity on the drug dissolution should be evaluated by analysing cross-sectional cuts of these pellets with a high-resolution microscopy technique e.g. SEM [265, 270].

Coating Thickness

For this particular type of pellets, the drug-loaded coating layer can be distinguished by the localised features. About 20 pairs of points were manually marked on the inner and outer borders of the coating layer in the central B-scan image of each pellet measured in each

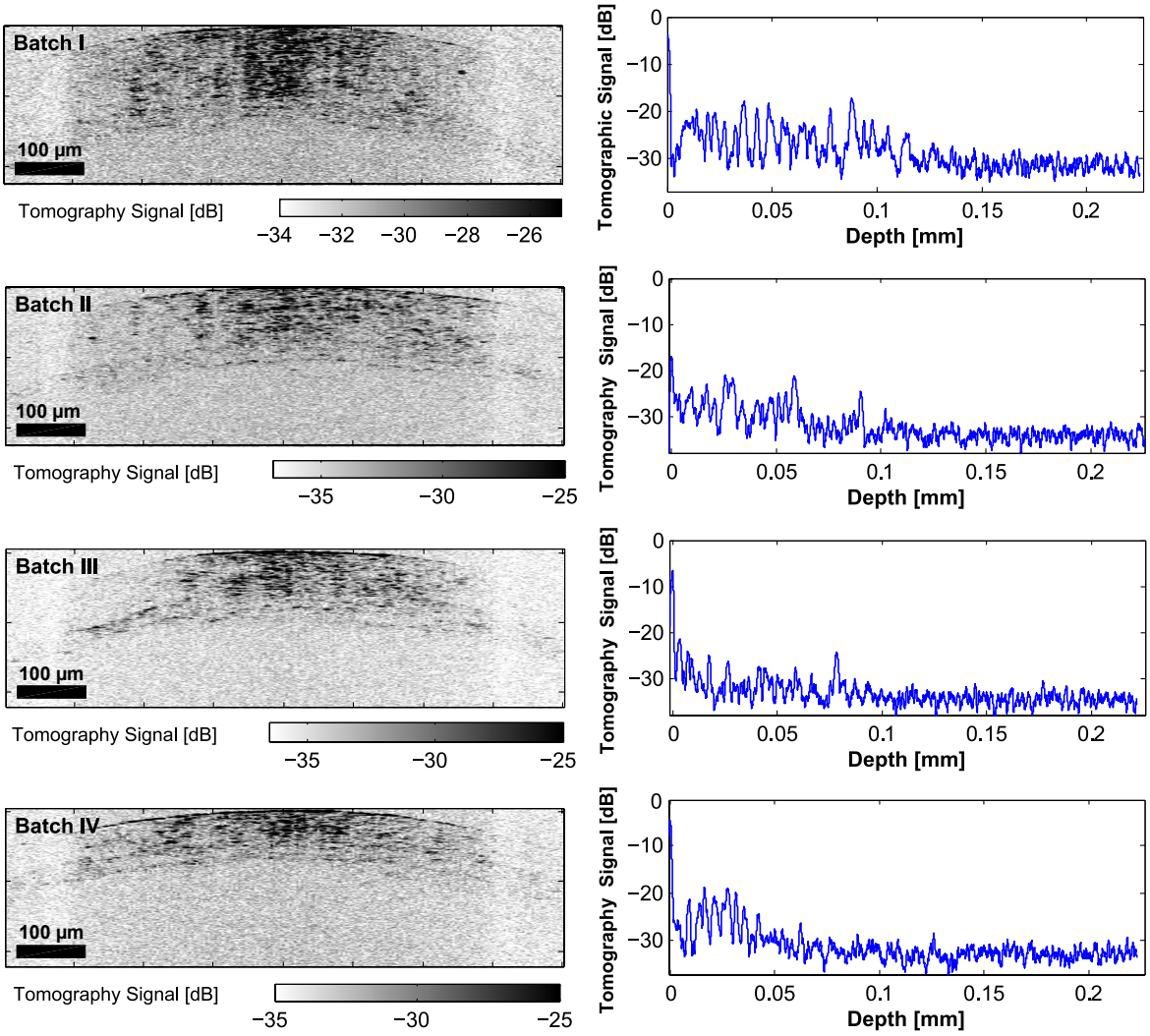

Fig. 4.2 B-scan images and A-scan signals of single layer coated pellets with varying coating thicknesses of 100 µm, 80 µm, 60 µm and 40 µm for Batch I, II, III, IV respectively. The 100 µm bar is used to scale B-scan images in both horizontal and vertical directions.

batch. Fig. 4.3 shows an example Batch IV pellet B-scan image, in which layer borders are marked by several pairs of points. The distance between each pair of points was measured as the coating thickness at this specific transverse position. A mean thickness value and a thickness variance were obtained for each batch by quantifying coating thicknesses of all three pellets in this batch.

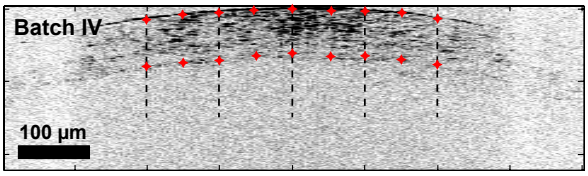

Fig. 4.3 An example Batch IV B-scan image showing manually marked points on the layer borders for the determination of coating layer thickness.

The nearly linear correlation between the FF-OCT measured mean coating thicknesses and the weight gain estimations for the four batches is exhibited in Fig. 4.4. The FF-OCT measured thickness is expressed by $\bar{x} \pm$ std, where $\bar{x}$ is the mean coating thickness, and std is the standard derivation of the coating thicknesses.

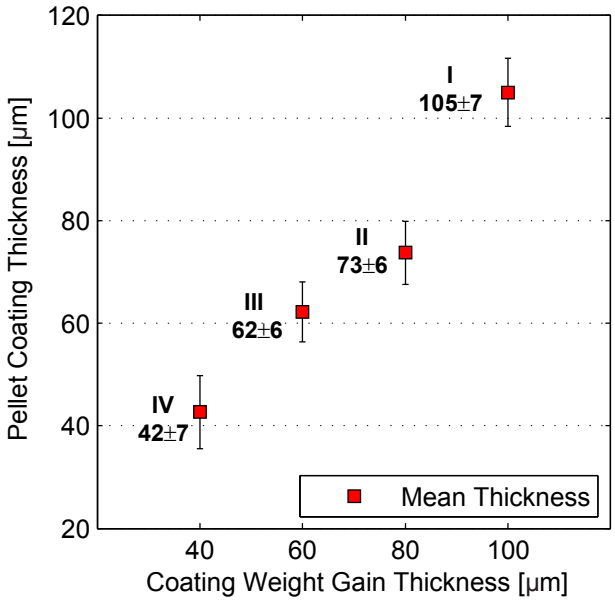

Fig. 4.4 Linear correlations between the OCT measured pellet coating thicknesses and estimated weight gain thicknesses for four batches.

It is in agreement with the weight gain estimations that the pellet coating thicknesses are decreasing from Batch I to Batch IV. However, there are varying discrepancies between

the quantified mean coating thicknesses and the weight gain estimation for the four batches. The FF-OCT quantified mean thicknesses (105 µm, 62 µm and 42 µm) of batch I, III and IV have less than 5 % thickness deviations from the weight gain estimations, while the thickness deviation of the mean coating thickness of Batch II (73 µm) exceeds 10 % from the weight gain estimation.

Coating Uniformity

Coating uniformity can be assessed from two aspects of the coating layer. Firstly, the B-scan images in Fig. 4.2 show dispersed particle-like features in single-layer coating, suggesting non-uniform distribution inside drug-loaded coating due to the localisation of other substances. If the particle-like features in the coating are mainly caused by pores, the rate of drug release may still be constant, however, it could be boosted to be faster. Secondly, coating uniformity is related to the coating thickness variation. Fig. 4.4 shows the calculated STD of the coating thickness for each batch to be 7 % to 17 % of the mean thickness. This gives qualitative and quantitative data for an indication of the coating uniformity, which is one of the coating characteristics for the evaluation of coating efficiency.

Although there were no reference measurements to verify the FF-OCT results of the mean thickness, thickness variance and layer uniformity in this study, it shows that FF-OCT can non-destructively provide B-scan images similar to microscopy images from cross-section cuts; FF-OCT can differentiate two media whenever there is a change in the refractive index; FF-OCT permits quantitative analysis of coating structures, which gives additional indications of the coating thickness and coating uniformity.

4.1.3.3 Double-Layer Coated Pellets

This part presents published work [274] during my PhD on the characterisation of a double-layer coated pellet by FF-OCT.

Measurements

The pellet in this study had a mean diameter of 0.85 mm and was coated with two coating layers. The core is a pharmaceutical excipient, microcrystalline cellulose (MCC) sphere (CP-507). The inner coating layer is a drug-loaded layer containing 10 % API and 90 % hydroxypropyl methylcellulose (HPMC). The outer coating formulation contains a combination of ethyl cellulose (EC) and hydroxypropyl cellulose (HPC). All EC, HPC, HPMC and MCC are commonly used drug excipients. Table 4.1 shows their refractive

indices as used in the data analysis. The API substance has a refractive index larger than these excipients.

Table 4.1 Refractive Indices of the Coating and Core Materials

Excipient	Refractive Index
EC	1.47 [275]
HPC	1.53 [276, 277]
HPMC	1.52 [278]
MCC	1.50 [279]

For a full FF-OCT measurement, a series of *en-face* images was acquired at a rate of 120 fps frame rate while the reference mirror was moving at a constant speed of $3\,\mu m\,s^{-1}$. Each *en-face* image was composed of 180×180 pixels (about $(4 \times 4)\,\mu m^2$ per pixel) covering a sample area of $(700 \times 700)\,\mu m^2$. The stage was scanned over a depth of 166 µm, thus a full OCT data cube covering a volume of $(700 \times 700 \times 166)\,\mu m^3$ was acquired. The data cube was subsequently processed with the data analysis for tomographic imaging.

To validate the FF-OCT measurement of the structure of the double-layer coating, a high-resolution X-ray micro-computed tomography (XµCT) scanner (SkyScan1172, Bruker-microCT) was used to measure the same pellet. It took a total measurement time of about 5 hours and a subsequent image reconstruction time of about 4 hours. The obtained XµCT images had an isotropic voxel resolution of 1.2 µm.

Data Analysis

For the FF-OCT measurement of the double-layer coating, the resultant A-scan signal and B-scan image are presented in Fig. 4.5 and Fig. 4.6, respectively. Fig. 4.5 (a) shows a typical OCT interference signal that is extracted from the raw OCT data cube. Several interference events were recorded at the pellet surface and within the coatings. The A-scan signal in Fig. 4.5 (b) is obtained from the data processing of the raw signal in Fig. 4.5 (a). Compared to the interference signal, it provides a more intuitive and better representation of the depth profile of the pellet coatings.

The positions of the signal peaks illustrate the double-layer coating structure of the investigated pellet. The first major feature at z = 0 corresponds to the OCT response of the pellet surface. The subsequent features could be due to the scattering from internal interfaces and dispersed API substance in the inner coating layer. The inset in Fig. 4.5 (a) also confirms the minimum resolvable feature (in the depth direction) as identified by the FWHM of the main peak.

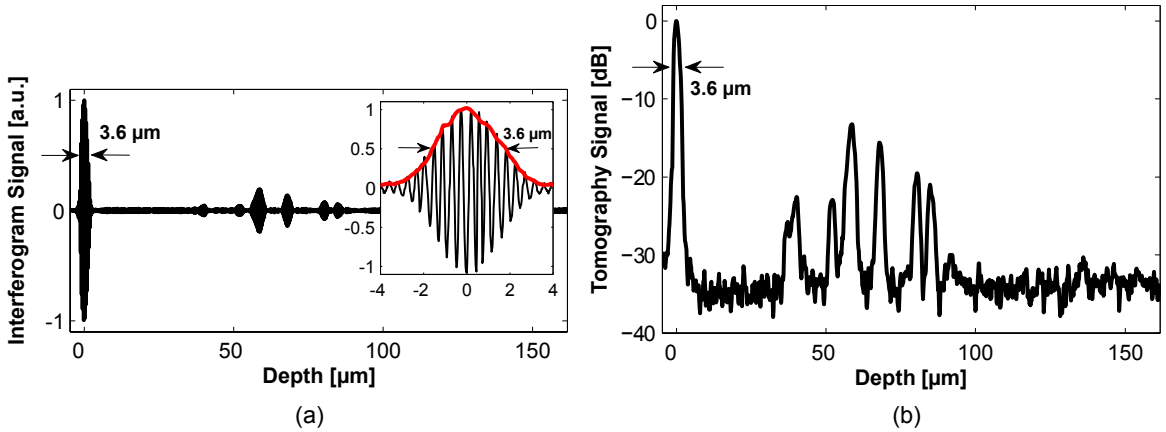

Fig. 4.5 An FF-OCT interference signal in (a) and the corresponding A-scan signal (or tomography signal) in decibel in (b) of the double-layer coated pellet; the inset in (a) shows an enlarged view of the first main peak, with the envelope (in red) showing the demodulated tomography signal and the determination of the depth resolution of 3.6 µm.

A B-scan image of the double-layer coating structure is shown in Fig. 4.6 (a). As shown in this figure, the pellet surface are distinguished by the connected dark features. Beneath the pellet surface, there are dispersed particle-like features localised within a curved band. Two yellow dashed lines are used to indicate the upper and lower boundaries of the band. This band is estimated as the drug-loaded inner coating layer, because it exhibits different structure from the outer coating layer and the pellet core. By manually marking points on the band borders, the thickness of the inner coating layer was determined as (50 ± 3) µm. The outer coating layer was evaluated similarly by the gap between the pellet surface and the upper boundary of the inner coating layer and the coating thickness was measured as (40 ± 5) µm.

It is also shown that the first 40 µm region is relatively "clean", that is no peaks in the tomography signal in Fig. 4.5 (b) and no particle-like features in the B-scan image can be observed in the first 40 µm below the surface in Fig. 4.6 (a), indicating that the outer coating layer is uniform. In contrast, the region of 40 µm to 90 µm below the pellet surface is dominated by multiple peaks in the tomography signal and particle-like features in the B-scan image, suggesting that the inner coating layer is non-uniform. The particle-like features have a smallest transverse length of approximately 12 µm and a smallest axial height of approximately 4 µm. They could be API particles that are dispersed in an HPMC matrix. The porosity of the inner coating layer is also likely to result in the particle-like features observed here. Note that the discrete particle-like features on the edge of the band could indicate OCT response at the coating/coating and coating/core interfaces.

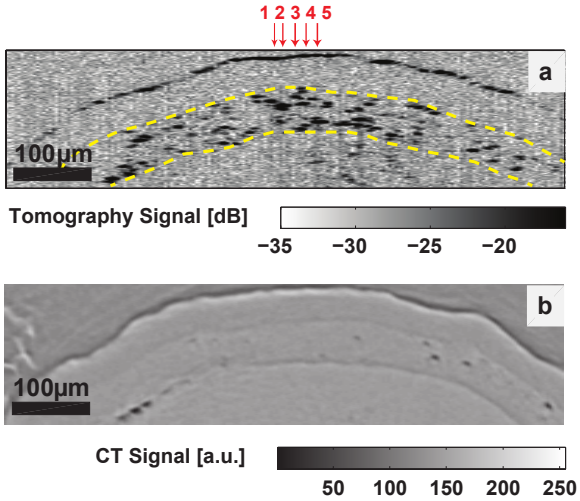

Fig. 4.6 B-scan images of the double-layer coated pellet by FF-OCT in (a) and XµCT in (b); two dashed yellow lines in (a) are to indicate the upper and lower interfaces of the inner coating layer; The red arrows mark the transverse position of the five signal traces in Fig. 4.7 (a); note that the images do not correspond to the exact same location in each sample, but are representative of the morphology in each case.

The inner coating layer of the pellet is identified by the localisation of particle-like features in Fig. 4.6 (a). Unlike the connected OCT features of the pellet surface, the coating/coating interface and the coating/core interface are detected as discrete features. The refractive index of the outer coating layer is close to the averaged value of EC and HPC, which is 1.50 according to Table 4.1. Hence, both the coating/coating and coating/core interfaces have a common refractive index variation of 0.02, which is much smaller compared to the refractive index variation of 0.50 at the pellet surface ($n_{air} = 1$); therefore weaker OCT responses are expected at these interfaces. The discreteness of these boundary features in Fig. 4.6 (a) could be due to the limited imaging sensitivity that is unable to resolve all OCT responses at these interfaces.

To validate the OCT results, Fig. 4.6 (b) shows the XµCT B-scan image of the same pellet. For comparison, both B-scan images of Fig. 4.6 (a) and (b) cover approximately an area of $(700 \times 166)\,\mu m^2$ (transverse $\times$ axial). It confirms the double-layer coating structure of the pellet and the presence of many particle-like features within the inner coating layer. These features have a transversal dimension of approximately 9 µm. The thickness of each layer was quantified by manually measuring the width of the band at 40 points on the boundaries of the two layers in Fig. 4.6 (a). The mean thicknesses of the outer coating layer and the inner coating layer were calculated as 40 µm and 50 µm, respectively. The FF-OCT results were confirmed to be consistent with those of XµCT.

Coating Thickness

One of the key metrics to characterise the coating structure of the pellet is the mean thickness of the respective coating layers. It is noted that for this specific type of pellet the boundaries between neighbouring coating layers are not always clearly visible in the B-scan image (Fig. 4.6 (a)), let alone in the optical microscope image (Fig. 4.1 (c)). For a general coating samples containing only excipients, the coating thickness is determined by the peak to peak distance in an A-scan signal. As further illustrated in Fig. 4.7 (a), the coating thickness of the drug-loaded layer cannot be precisely determined from a single A-scan signal.

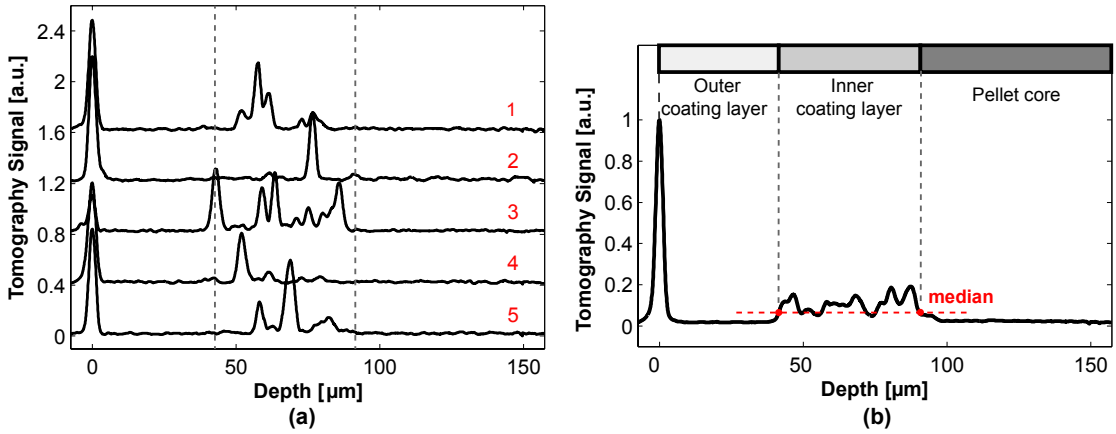

Fig. 4.7 (a) Five randomly selected signals from the region of interest (ROI), showing the inhomogeneity of the inner coating layer. The position of these pixels is also identified using red arrows in Fig. 4.6 (a). (b) The mean signal obtained by averaging 200 signals within the ROI. The median values of the OCT signal in the depth range of the inner coating layer are marked with two red dots, which indicate the starting and ending positions of the coating layer.

To determine the coating thickness in a robust and automatic way, it is proposed that the coating thickness can be evaluated from a mean A-scan signal in Fig. 4.6 (b) that is averaged over a set of A-scan signals acquired within a wide central volume. The ROI of this volume is illustrated in Fig. 4.8 (a). About 200 neighbouring A-scan signals within this region (here of a diameter of 68 µm) were used to calculate a mean A-scan signal. This region was chosen to provide a sufficient number of tomography signals, whilst the measurement error (i.e. the deviation between the measured thickness AC or D and the true thickness AB or d in Fig. 4.8 (b)) introduced by the surface curvature is still within an acceptable range. For example, the thickness error is theoretically smaller than 0.2 µm for a 40 µm thick coating layer, as shown in Fig. 4.8 (b).

Fig. 4.7 (a) shows five randomly selected A-scan signals within the ROI, revealing that particle-like features appear randomly distributed in the range of approximately 40 µm to

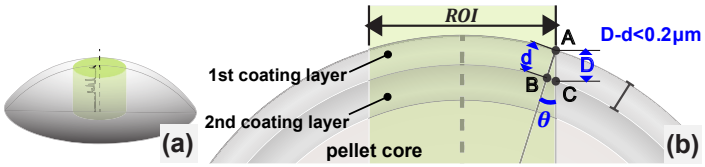

Fig. 4.8 (a) A model covers a partial surface of the double-layer coated pellet with a diameter of 0.85 mm. The central cylinder volume illustrates the ROI, in which a set of A-scan signals were used for calculating the mean A-scan signal in Fig. 4.7 (b); (b) a cross-section model of the pellet with a diameter of 850 µm. A central ROI with a diameter of 68 µm was cropped from an FF-OCT measured area. D and d are the measured thickness (AC) and the true thickness (AB) at the edge of ROI, respectively.

90 µm. Fig. 4.7 (b) shows the mean A-scan signal averaged over about 200 neighbouring A-scan signals within this region. It has non-zero values in the range of approximately 40 µm to 90 µm. The starting and end positions of the inner coating layer were subsequently determined by the depths of the mean A-scan signal at its median value, i.e. 41 µm and 90 µm as indicated by the two red dots in Fig. 4.7 (b). Consequently, the mean coating thickness can easily be determined to be 41 µm and 50 µm for the outer and inner coating layers, respectively.

It should be pointed out that for samples with an uneven coating layer, such as the drug-loaded layers in the pellet studied in this study, the proposed method can be used for calculating the mean coating thickness, although it is not possible to obtain a coating thickness map of the sample.

As a further illustration of the microstructure of the pellet coatings, Fig. 4.9 (a) shows a set of *en-face* images at progressive depths reconstructed from the FF-OCT 3-D volume data. The dark features again indicate the events of changing of refractive indices induced by the pellet surface, the internal interfaces, the presence of API substance and/or pores, etc. Because of the surface curvature of the spherical pellet sample, one can see clearly the annular shape (in dark) in image A to F. In image G, a dark dot reappears at the centre, indicating that the inner coating layer has started to appear. The thickness of the outer coating layer could then be estimated as 40 µm (image A-G). In a similar manner, the thickness of the inner coating layer can also be estimated as 47 µm (image G-N). As a comparison, Fig. 4.9 (b) displays seven XµCT *en-face* images of the same pellet sample at corresponding depths. Again, there is a general agreement between the FF-OCT and the XµCT results.

In this study, the capability of the FF-OCT technique is confirmed for the imaging of the double-layer coated pellet. Consistent coating structures and thicknesses are obtained by FF-OCT and XµCT. The accuracy of the FF-OCT results is verified by XµCT. Although

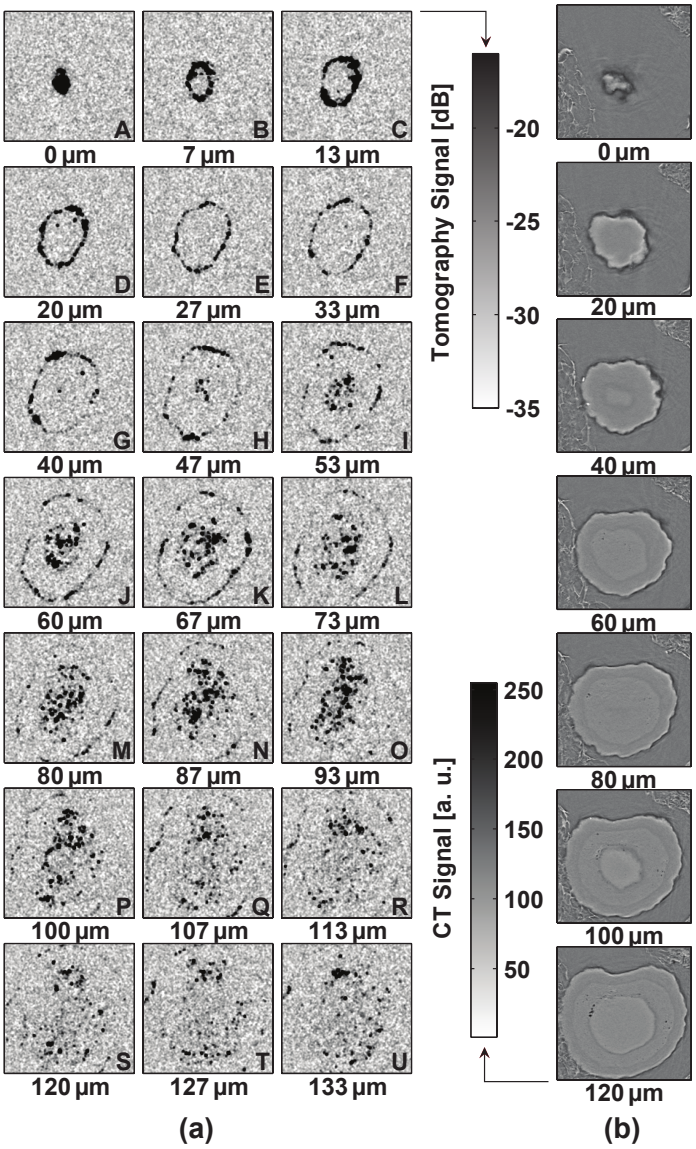

Fig. 4.9 (a)*En-face* FF-OCT images with 6.7 µm depth interval between successive images; (b) XµCT depth-resolved *en-face* images with 20 µm depth interval (through a slightly different plane of the pellet); all images cover an FOV of $(700 \times 700)\,\mu m^2$.

the boundaries of the drug-loaded layer are not completely resolved by the simple FF-OCT system, the coating layer distribution and the layer thicknesses obtained by such a low cost fast system are comparable with that obtained by the expensive, lengthy, but reliable XμCT instrument. Thus the simple FF-OCT system can be used to provide quick structural estimation and evaluation of pharmaceutical pellet coatings.

4.1.3.4 Triple-Layer Coated Pellets

This part describes the characterisation of triple-layer coated pellets by using FF-OCT.

Measurements

The two batches of pellets in this study were coated with three layers. Above the pellet sugar core, there exists one layer of polymer excipient in between two drug-loaded coating layers. The total coating thickness of these pellets was in the range of 80 μm to 110 μm. The final coating of the pellets had a smooth surface morphology and a mean diameter of 1 mm.

Three pellets per batch were measured by using the simple FF-OCT system under the same operational settings as with the previous pellet studies (i.e. $3\,\mu m\,s^{-1}$ translation and 120 fps frame rate). The total axial scanning distance was 0.2 mm to cover all of the pellet coatings. Each FF-OCT data cube contains $240 \times 240 \times 12\,000$ data points and corresponds to a $(900 \times 900 \times 200)\,\mu m^3$ volume. The data cubes were subsequently analysed with the processing procedures for tomographic imaging mentioned before.

Data Analysis

The B-scan images and the A-scan signals of two pellets of the respective batches are shown in Fig. 4.10. Three coating layers are clearly revealed by the B-scan images. As a drug-loaded layer, the outer coating layer is shown to have many particle-like features, which could be due to API substances and/or porous structure. In addition, distinct and continuous FF-OCT responses are identified at the pellet surface and the lower coating/coating interface of the outer coating layer. Similar particle-like features are exhibited in the innermost coating layers, while they suffer strong absorptions and hence the upper and lower boundaries are less likely to be distinguished. The middle coating layer is shown to have no FF-OCT responses, hence it is fairly uniform. The A-scan signals all confirm the coating structures depicted in the B-scan images.

The coating thicknesses of each coating layer can be quantified from the given signals and images. However, as these pellets have irregular spherical shapes, the coating layers are also affected with inhomogeneous thicknesses of each layer. For the Batch I pellets,

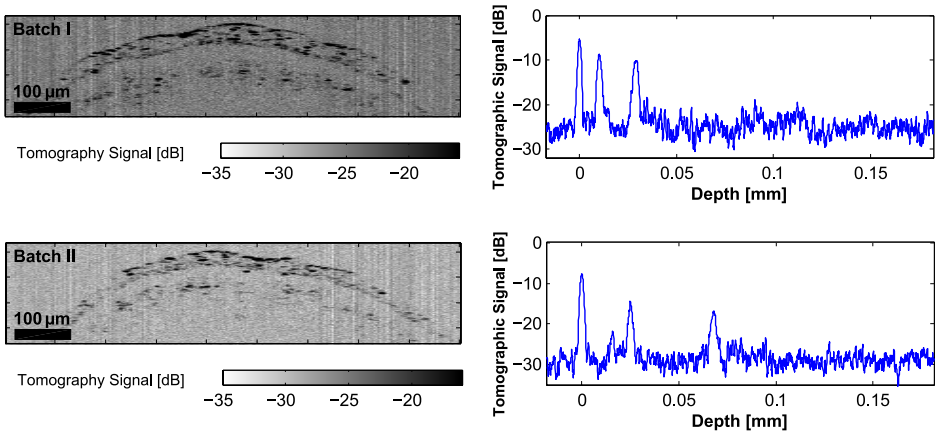

Fig. 4.10 B-scan images (left) and A-scan signals (right) of two batches of triple layers coated pellets in decibels.

the outer coating layer has a mean thickness of 35 µm with a STD of 5 µm and the middle layer thickness is measured as (33 ± 5) µm. For the Batch II pellets, the thickness of the outer coating layer is (24 ± 3) µm and the middle layer thickness is measured as (27 ± 6) µm. The innermost coating thicknesses are ambiguous to be detected in both pellet samples with roughly 35 µm and 30 µm respectively.

Dissolution Study with FF-OCT

The structural differences of the pellet coatings could effectively result in variations of their dissolution profiles, which directly concern the quality of the pharmaceutical design and fabrication. The dissolution rate indicates the speed of dissolving the solid dosage form into a solution. The FF-OCT technique can be used to illustrate that the structural difference of pellet coatings could lead to the extension or shortening of the dissolution process.

A further four batches of triple-layer coated pellets were investigated by FF-OCT. Each batch had a different dissolution rate. Three B-scan images per batch are shown in Fig. 4.11 and the triple-layer coating structures are illustrated to be similar to the previous study. As shown in these images, one uniform coating layer in between two non-uniform coating layers is distinguished from coating structures. The two non-uniform coating layers contain particle-like features which confirm the presence of API substance and/or pores.

The dissolution rates of the four batches are labelled on the respective B-scan images. Fig. 4.11 (a) shows the pellet coatings with a relatively higher dissolution rate (76 % and 78 %) and Fig. 4.11 (b) shows the pellet coatings with a lower dissolution rate (57 % and 58 %).

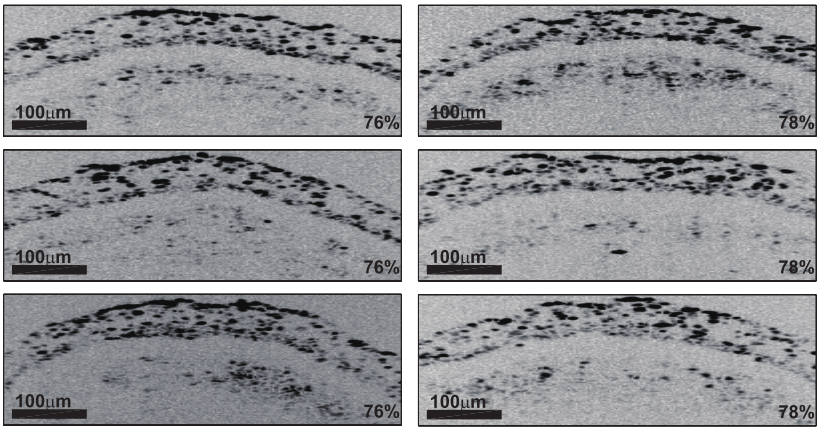

(a) pellet samples with higher disolution rates

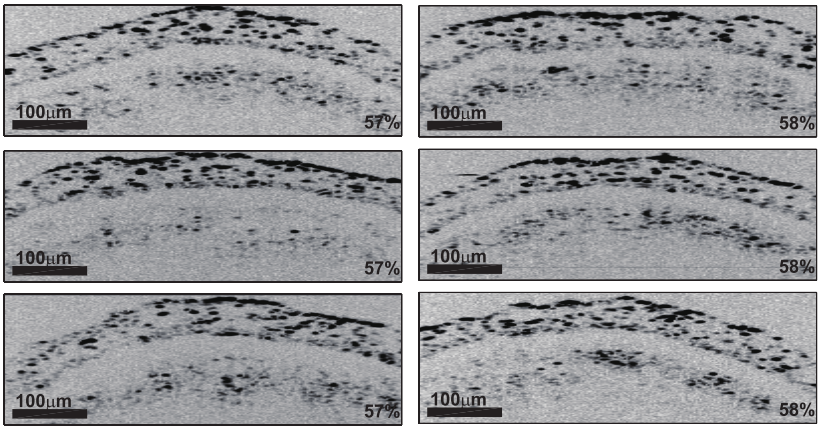

(b) pellet samples with lower disolution rates

Fig. 4.11 B-scan images in logarithmic scale obtained by FF-OCT for the four batches (three pellet samples per batch) of triple layer coated pellets, with their dissolution rates stated. Images in (a) display coating structures for pellets with relatively high dissolution rates, and images in (b) show coating structures for pellets with relatively low dissolution rates.

As shown in these B-scan images, there are no significant structural differences between pellets with higher and lower dissolution rates. The outer coating layers are shown to have strong FF-OCT responses of dispersed particle-like features and boundary features. The coating thicknesses of the outer coating layers range from 40 µm to 43 µm for all batches, except for the first image of the 78 % rate (37 µm) and the second image of the 58 % rate (38 µm). The middle coating layers have no OCT responses and could be an excipient-based coating. Their thicknesses are mainly in the range of 27 µm to 32 µm. However, thicknesses of approximately 15 µm and 38 µm are detected for the first image of 58 % rate and the second image of 78 % rate, respectively. The innermost coating layers are also shown to have particle-like features, although layer boundaries are not clearly resolved for all batches.

Nevertheless, denser particle-like features are localised in the outermost coating of pellets with higher dissolution rates in Fig. 4.11 (a) than that of pellet with lower rates in Fig. 4.11 (b). This might be due to a higher concentration of drug particles and/or pores, either would lead to a higher dissolution rate. Unlike the outermost coating, the innermost coating does not exhibit strong enough FF-OCT response for the evaluation of coating structural discrepancies. It is hence uncertain to predict the effect of the innermost coating on the drug dissolution with FF-OCT results. Further studies on the thickness of the innermost coating, distribution of other substances and what these particle-like features in FF-OCT results are should be conducted using a ultrahigh resolution microscope.

4.1.4 Discussion

The simple FF-OCT system has been used to deliver accurate, reliable and quick evaluations of pharmaceutical pellet coatings. The micrometre-scale FF-OCT imaging permits a high precision, qualitative and quantitative analysis of pellet coatings. Instead of a mean coating thickness that is normally obtained in the weight-gain and the NIRSI method, the FF-OCT method enables acquisition of detailed coating structural information. With the B-scan images and the A-scan signals, FF-OCT is demonstrated as a useful analytical tool for the characterisation of pellet coatings and the evaluation of the coating characteristics that are related to the final release rate and the dissolution profile of the pellet.

Porosity

As stated in previous sections, the presence of particle-like features in the FF-OCT B-scan images can differentiate a coating layer from ambient coating structure. However, the FF-OCT technique essentially detects variations of refractive indices, which could also be caused by pores inside the coating layer. However, it is difficult to determine the distribution of

drugs and pores within the coating layer, as the general dimensions of the API substances and the pores are unknown. Further analysis of the distribution of the API substance and the porosity within a coating layer should be carried out by using a high resolution microscopy technique [265] to determine what is happening inside the layer.

Coating Thickness

As illustrated in Section 4.1.3.3, the coating thickness of the drug-loaded coating layer in the pellets is evaluated from a mean A-scan signal that is averaged over a set of A-scan signals. Through the averaging process, the FF-OCT responses at the depth range of the drug-loaded layer are enhanced in the mean A-scan signal, which enables the localisation of the layer and the determination of the layer's mean thickness.

For tablets with uniform coating and core structures, the measured OCT signals show distinct peaks and the resultant B-scan maps show uniform coatings with clear boundaries, as reported in previous studies [7, 132]. These distinct peaks correspond to the change in refractive index at the air/surface and the coating/core interface of a tablet. Consequently, the coating thickness at each transverse position of the tablet surface (rather than the mean coating thickness) can be directly determined as the peak position difference, in a similar way as in the coating analysis by using TPI [269, 280]. This also allows the coating thickness map to be subsequently constructed. Note that the proposed method in this study can be used for calculating the mean coating thickness, although it is not possible to obtain a coating thickness map of the sample.

Comparison of FF-OCT with other techniques

Pygall *et al.* [264] and Laksmana *et al.* [265] evaluated pellet coatings using CLSM. As a microscopy technique, CLSM detects the variation of optical intensity of reflected or scattered light, whereas FF-OCT detects interference patterns, i.e. the electric field of the light reflected or scattered from the reference and sample arms [177]. Thus FF-OCT has a better imaging depth and is more sensitive to small changes in the inner structures of a sample.

TPI has also been used for directly measuring the layer thickness of film coatings [269, 270]. As most pharmaceutical excipients used in film coating are either transparent or semi-transparent in the terahertz frequency range [249], TPI can be used to quantify thick pharmaceutical coatings in the range of 40 µm to 140 µm and beyond [132]. However, because of the relatively long wavelength of terahertz radiation (300 µm at 1 THz), TPI has limited spatial resolution in the transverse direction and thus is not suitable to investigate the

Table 4.2 Comparison of Analytical Techniques

	TPI	FF-OCT	XμCT	CLSM
Radiation	THz	NIR	X-rays	Laser
Transverse Resolution	150 μm [269]	10.3 μm	0.5 μm [281]	0.16 μm [282]
Depth Resolution	30 μm [269]	3.6 μm	0.5 μm [281]	0.5 μm [282]
Penetration Depth	5 mm	2 mm	Large	1 mm [283]
Measurement Time	1 hour	2 mins	5 hour	real-time
Cost	High	Low	High	High

fine structure of small-size pellets such as the ones studied here. In contrast, the FF-OCT system presented in this study achieves a spatial resolution of $(10.3 \times 3.6)\,\mu m^2$ (lateral $\times$ axial) allowing a more precise analysis of the coating thickness and revealing more detailed features beneath the surface.

It is also demonstrated in this work that XμCT has an excellent capability in obtaining high-resolution 3-D coating structures non-destructively. However, currently the XμCT measurement and the required subsequent image reconstruction are a time-consuming process. Furthermore, the ionising nature of X-ray radiation also makes it extremely difficult, if not impossible, to be used for online monitoring applications. Table 4.2 illustrates further comparisons of TPI, FF-OCT, XμCT and CLSM in terms of their imaging resolutions, penetration depths, measurement time and instrument costs. In this sense, the FF-OCT method proposed here is advantageous as it is fast, compact and safe (it uses low power NIR light).

4.1.5 Summary

In this section, pharmaceutical pellets of up to 1 mm in diameter with three different coating structures have been investigated by using the simple FF-OCT system. The FF-OCT technique has been demonstrated as an analytical tool for the characterisation of small size pellet coatings. The simple FF-OCT system is also confirmed to provide accurate, reliable and quick evaluations of pharmaceutical coatings. The coating layer boundaries and internal morphology features more than 100 μm beneath the pellet surfaces have been characterised by the B-scan images and the A-scan signals. Coating characteristics such as the layer thickness, uniformity and porosity have been evaluated by data analysis of the FF-OCT results. The high spatial resolution, the imaging accuracy, the quick measurement and the low-cost attributes make the simple FF-OCT system an attractive tool for the non-destructive evaluation of small pharmaceutical pellets.

4.2 Characterisation of Corneal Structure

4.2.1 Introduction

Current clinical practice aims for the development of techniques to diagnose a disease in its early stage, when treatment is most effective and irreversible damage can be prevented or delayed. In ophthalmology, the precise visualisation of pathology is especially critical for the diagnosis of ocular diseases [14]. Therefore, many imaging techniques have been used to characterise ophthalmic pathology to estimate ocular conditions. Optical techniques such as conventional fundoscopy and slit-lamp biomicroscopy are of interest because they often enable *in vivo* and *in situ* diagnosis. Among other imaging techniques, OCT has recently become a widespread tool in ophthalmology to provide high-resolution cross-sectional images for the characterisation of the key structure of the retina and anterior segment of the eye.

Corneal conditions are among the targets in ophthalmic pathology. The corneal structure can be imaged by OCT imaging for the diagnosis of corneal disorders, such as keratoconus [284] and conjunctival pathology [285]. OCT is also used in the pre-operative planning of e.g. laser-assisted lamellar keratoplasty [286] and the post-operative evaluation of e.g. cataract surgery [287] and Descemet's stripping automated endothelial keratoplasty [288]. The micrometre-scale depth resolution of OCT allows the precise measurement of the central corneal thickness (CCT), which is an important factor in the diagnosis of glaucoma [289] and monitoring of keratoconus and Fuchs' dystrophy [290].

There are various methods for the imaging of corneal structures, such as slit-lamp illumination [291], UBM [12], scanning-slit confocal microscopy [292], and specular microscopy [293]. Ultrasound pachymetry is currently the most commonly used for the measurement of CCT in ophthalmology [289], but it requires physical contact with the cornea. In UBM, the ultrasound probe does not come into contact with the eye directly but via an immersion bath (i.e. an immersion shell placed on the ocular surface and filled with e.g. sterile water) [294]. For the imaging of anterior eye structures, high-frequency ultrasound is often employed in UBM to enable high-resolution imaging with an axial resolution of approximately 25 µm [12, 295].

OCT has had a significant impact on ophthalmic diagnostics through its ability to elucidate morphological correlations of disease processes by allowing the qualitative imaging of gross anatomical changes as well as the quantitative measurement of corneal and retinal layer thicknesses [289, 296, 297]. OCT performs non-contact, non-invasive measurement and provides high-resolution, cross-sectional images with the image resolution that is 1-2 orders

of magnitude higher than that of conventional ultrasound [14]. From the earliest introduction of ophthalmic OCT, it has been utilised as an effective technique for the imaging of corneal structure and the general assessment of corneal thickness [298]. Dada *et al.* [94] presented a good agreement of the measured CCTs by OCT and UBM, respectively. OCT variants, e.g. spectral-domain OCT and FF-OCT, have also been applied to analyse corneal structure and corneal pathology [200, 299].

This section first describes the corneal structure and illustrates structural variations of corneal disorders. Corneal structures of bovine corneas are subsequently investigated by using the simple FF-OCT system. The potential of the FF-OCT system is discussed regarding the diagnosis of corneal disorders.

4.2.2 Ultra-fine Corneal Structure

The cornea is the transparent front part of the eye, providing two-thirds of the eye's focusing power. It also helps to shield the rest of the eye from germs, dust, and other harmful matter. Although it is clear and seems to lack substance, it is actually a highly organised group of cells and proteins. The human cornea is composed of five layers [300], including epithelium, Bowman's membrane, central stroma, Descemet's membrane, and endothelium from the anterior to posterior, as shown in the histological cross-section in Fig. 4.12.

The corneal epithelium is the first layer of the cornea and protects the eye. It consists of several layers of cells and has a thickness of approximately 52 µm [302]. The endothelium is an 8 µm-thick cell monolayer whose main role is to maintain the cornea in a slightly dehydrated state that is required for optical transparency [303]. The Bowman's and the Descemet's membranes are smooth acellular layers with thicknesses of roughly 10 µm and composed of randomly disposed collagen fibrils [304]. The stroma is composed of about 200 flattened collagen lamellas and represents around 90 % of the total thickness of the cornea [305].

Kaushik *et al.* [306] reported the imaging of human cornea by UBM. Fig. 4.13 reveals the upper and lower surfaces of the cornea and the interface between the Bowman's membrane and the central stroma. The corneal epithelium and the Bowman's membrane are contained in the thin outer layer. The Descemet's membrane and the endothelium are detected as a single ultrasound echo signal.

Casadessus *et al.* [304] investigated the micrometric-scale structure of a human corneal graft by an FF-OCT instrument. As shown in Fig. 4.14, OCT imaging reveals the presence of all five layers of a 670 µm-thick cornea. The upper right image discloses some dispersed

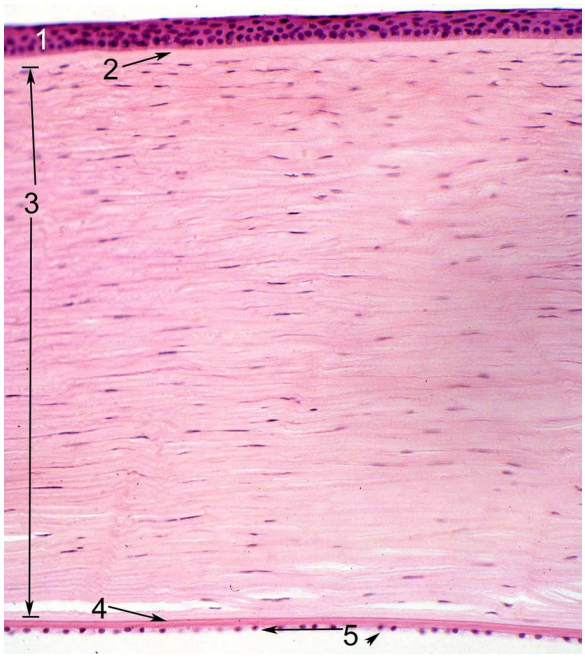

Fig. 4.12 Histological section of a healthy human cornea. Layers 1 to 5 are epithelium, Bowman's membrane, central stroma, Descemet's membrane and endothelium, respectively. Figure adapted from Mission for Vision [301].

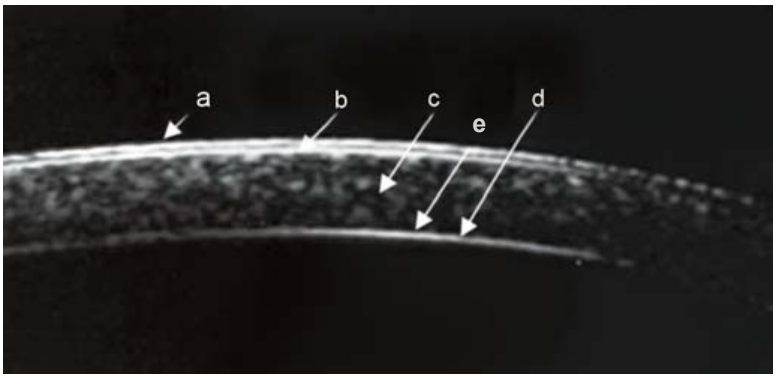

Fig. 4.13 A UBM image of corneal structure; labels a to e correspond to the locations of the epithelium, Bowman's membrane, central stroma, Descemet's membrane and endothelium, respectively. Figure adapted from Kaushik *et al.* [306].

dark features within the epithelium, which could be the epithelial cell nuclei. The stroma is shown to have many superimposed internal features in the lower right image, which could be the existence of flattened collagen lamellas. The Bowman's membrane (in the upper right image) and the Descemet's membrane (in the lower right image) are shown to be very uniform corneal layers. The endothelium is quite thin and has an uneven layer outline. Both the UBM image in Fig. 4.13 and the OCT images in Fig. 4.14 of the corneal structure are consistent with the histological cross-section shown in Fig. 4.12.

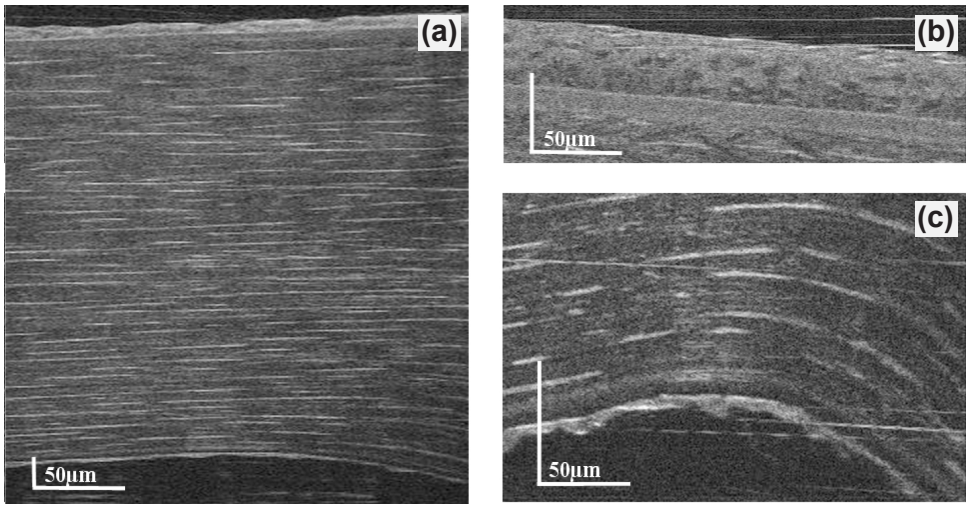

Fig. 4.14 OCT images of corneal structure of a 670 µm-thick cornea; the depth-scan along the whole depth in (a), details of the anterior part with epithelium and Bowman's membrane in (b) and the posterior part with stroma, Descemet's layer and endothelium in (c). Figures adapted from Casadessus *et al.* [304].

A well-known refractive index of 1.376 is always used for the human cornea, when the cornea is considered as a single transparent tissue. However, the refractive index of the cornea is not uniform and varies from one corneal layer to another. The mean refractive indices of the epithelium (or the endothelium), the Bowman's membrane (or the Descemet's membrane) and the stroma are reported as 1.401, 1.380, and 1.373, respectively [307]. The reflectivity of internal corneal interfaces is hence very weak due to low reflection coefficients (less than 0.008) at these interfaces. It is therefore challenging to resolve all corneal layers, as a high imaging sensitivity is required to differentiate one layer from another with a similar refractive index.

4.2.3 Characterisation of Corneal Disorders by OCT

There are a number of corneal disorders which include various corneal dystrophies, keratoconus and conjunctivitis, etc. Patients suffering from these disorders probably experience itching and swelling of the cornea. However, these disorders might cause corneal inflammation, corneal erosion, severe pain and a loss of vision [308]. Some of the symptoms may lead to structural changes in the cornea, such as corneal oedema and corneal erosion.

In this section, the characterisation of corneal oedema and corneal erosion by using the OCT technique is described to illustrate the structural variations of the cornea due to corneal disorders.

4.2.3.1 Corneal Oedema

Corneal oedema is the swelling of the cornea following corneal surgery, infection or inflammation. Various ocular diseases can lead to corneal swelling such as Fuchs' endothelial dystrophy [309], iridocorneal endothelial (ICE) syndrome [310] and keratoconus [311].

For most diseases, corneal oedema manifests itself as an increase in the thickness of the stroma. The swelling mainly occurs in the posterior stroma and is lowest in the most anterior stroma [312, 313]. In addition, there usually exist collagen-free regions (i.e. 'lakes') within oedematous corneas such as corneas affected by Fuchs' dystrophy [314].

Casadessus *et al.* [304] reported the variation of the stroma when the cornea swelled. As shown in the top three images in Fig. 4.15, lakes appear as darker areas within the stroma and develop first from the posterior stroma. Then, they grow with the corneal thickness and the oedematous state of the cornea. Such structural evolution is illustrated in the top three images in Fig. 4.15 where lamellar gaps extend while the tissue swells. The bottom two images in Fig. 4.15 show the presence of long and thin lakes (with a length of up to 50 µm) sparsely distributed in the stroma.

Apart from the thickening of the cornea, the corneal oedema can also lead to the impairment of corneal transparency. Disturbances such as mechanical strains or hydration trouble may lead to tissue clouding. Corneal oedema is a manifestation of such disturbances and may be consecutive to scarring or endothelial dysfunction, causing haziness (opacification) in the cornea [304]. Corneal oedema also results in reduced contrast sensitivity and an increased susceptibility to glare [315, 316].

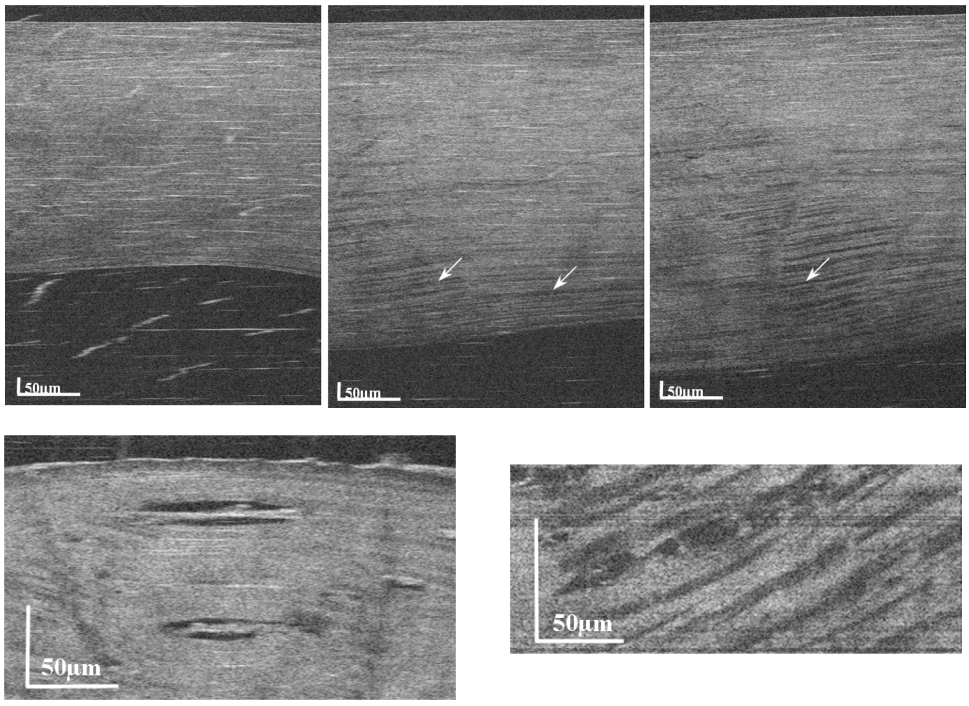

Fig. 4.15 OCT images of a cornea of three different oedematous states; thicknesses are from left to right of 730 µm, 795 µm and 815 µm; arrows point out lakes appearing when the corneal swells; long and thin lakes are sparsely disposed. Figures adapted from Casadessus *et al.* [304].

4.2.3.2 Corneal Erosion

Corneal erosion is a corneal disorder characterised by the failure of the outermost cellular layer of the epithelium to attach to the underlying Bowman's membrane [317]. It is often caused by a previous corneal injury, i.e. corneal abrasion or ulcer. More commonly, it is developed as a result of severe corneal dystrophy, such as epithelial basement membrane dystrophy (EBMD) [318]. The condition exposes the nerves that line the cornea, causing severe pain; it also alters the cornea's normal curvature, resulting in temporary vision problems [308].

El Sanharawi *et al.* [318] reported the structural analysis of the corneal EBMD with spectral-domain OCT. Corneal structural changes due to epithelial erosion in eyes were characterised as the protrusion of an abnormal basement membrane into the epithelium, as shown in the OCT images in Fig. 4.16.

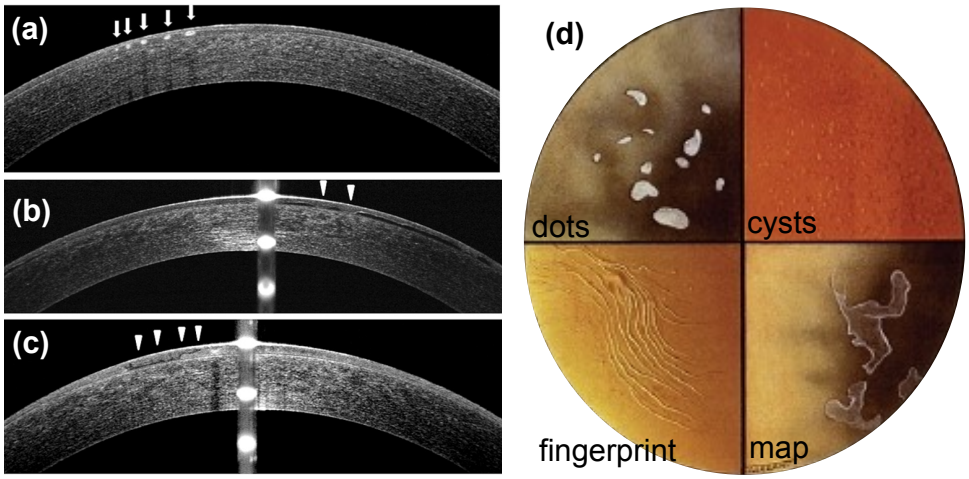

Fig. 4.16 OCT images of dots or cysts in (a), corneal epithelial detachment in (b) and splitting of the corneal epithelial layer in (c) as typical epithelial erosions in eyes with corneal EBMD. Figures adapted from El Sanharawi *et al.* [318]. Slit-lamp images in (d) show the characterisation of EBMD [319].

Fig. 4.16 (a) shows the presence of hyperreflective dots, with or without posterior shadow cones, in the middle of the corneal epithelium (arrows), corresponding to dots or cysts observed via a slit-lamp examination. In Fig. 4.16 (b), there are extensive corneal epithelial detachment areas separated by regions of normal adhesion between the corneal epithelium and Bowman's membrane (arrowheads). The corneal epithelial detachments correspond to map-like lesions observed through a slit-lamp examination. Fig. 4.16 (c) shows the presence of a separation between the corneal epithelium and Bowman's membrane and a cleavage of a stair-step appearance inside the corneal epithelium. On a slit-lamp examination, these

patients had fingerprint-like lesions in both eyes. These mentioned slit-lamp images are all included in Fig. 4.16 (d), where EBMD is characterised by dots, cysts, geographic map-like lines and greyish epithelial fingerprint lines.

4.2.4 Imaging of Corneal Structure by FF-OCT

Measurement

A number of researchers have reported the optical properties of ocular tissues of various species such as bovine and porcine [320–324]. A bovine cornea was demonstrated to have similar corneal structure and transparency to a human cornea [313, 325].

Two bovine cornea samples were investigated with the simple FF-OCT system. The samples had corneal thicknesses larger than those of *in vivo* conditions: this was caused by the immersion solution used for the preservation of the samples that induced them to swell. Before the FF-OCT measurement, a cornea sample was fixed in a cornea gauge holder and inflated by water. It was mounted vertically onto the motorised stage and positioned facing the optical axis of the FF-OCT system.

The FF-OCT beam was focused onto a $(400 \times 400)\,\mu m^2$ FOV of the corneal surface. The depth-scan was performed in the measurement over a distance in air of approximately 1.40 mm, which was equivalent to a distance in the cornea of approximately 1.00 mm. A fixed refractive index 1.37 was adopted for the calculations of depth and thickness measurements. After a measurement by FF-OCT, a binary file containing the structural data within a volume of approximately $(400 \times 400 \times 1000)\,\mu m^3$ was created and subsequently processed.

Data Analysis

The following Figs. 4.17 and 4.18 show B-scan images and A-scan signals for the two corneal measurements. Both the CCT and corneal structure can be evaluated quantitatively. The corneal surfaces and internal interfaces are identified by the dark features in the B-scan images and the peaks in the A-scan signals. The frontal and rear features (or peaks) are most significant and were estimated as the corneal surfaces. This enables the measurement of the CCT as the distance between these surface features. The CCTs were measured as 0.91 mm for the first sample in Fig. 4.17 and 0.92 mm for the second sample in Fig. 4.18. The obtained two CCT values are very close to each other. Both of them agree with the thicknesses of oedematous corneas in the literature [290, 326, 327].

For the internal corneal structure, two interfaces at depths of around 0.1 mm beneath the surface are exposed in B-scan images and A-scan signals of the two cornea samples. They exhibit much weaker OCT signal strength compared to the surface features due to their

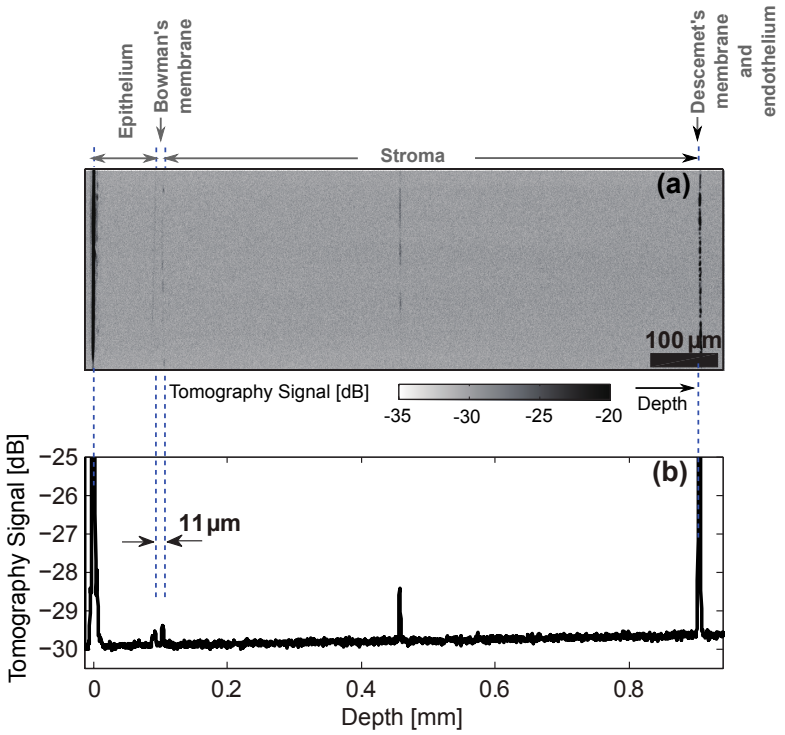

Fig. 4.17 The FF-OCT B-scan image in (a) and the A-scan signal in (b) of the first cornea sample. The thickness of the Bowman's membrane is marked as 11 µm.

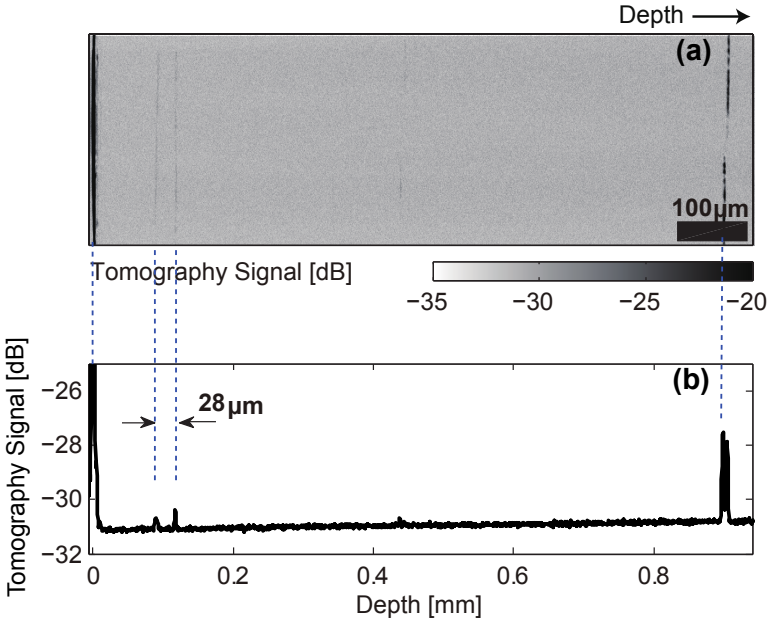

Fig. 4.18 The FF-OCT B-scan image in (a) and the A-scan signal in (b) of the second cornea sample. The thickness of the Bowman's membrane is marked as 28 µm.

relatively low reflectivity. Note that there is an additional feature at a depth of approximately 0.45 mm beneath the surface for both corneal measurements. In spite of its appearance in FF-OCT results, its presence in the actual corneal structure is not confirmed by literature. It was thus considered as an unknown structural component or a measurement artefact.

Three corneal layers are clearly differentiated in both Fig. 4.17 and Fig. 4.18, with the unknown features left out of the corneal structure. The thickness of each corneal layer is calculated as the displacement between two consecutive peaks of the upper and lower interfaces of the layer in the A-scan signal. The thicknesses of the three layers are summarised as 85 µm, 11 µm, 810 µm in Fig. 4.17 and 86 µm, 28 µm, 805 µm in Fig. 4.18. The first two layers were estimated to be the epithelium and the Bowman's membrane, respectively, because the very thin second layer matched the Bowman's membrane described in Section 5.2. The third detected layer occupying most of the cornea may contain the stroma, the Descemet's membrane and the endothelium, despite the fact that the latter two would be much thinner compared to the stroma. The composition ratios of the thicknesses of the epithelium and the Bowman's membrane to the total corneal thickness are calculated as 9.3 % and 1.2 % to 3 %, respectively. The rest of the corneal layers including the stroma, Descemet's membrane and endothelium, account for 87.5 % to 89 % of corneal thickness. These values concur with the work on bovine corneas by Hoeltzel *et al.* [327].

The Descemet's membrane and the endothelium were not resolved in either measurements. Possible explanations are: firstly, the OCT signal strength was already largely attenuated before reaching the two layers at the rear of the cornea; secondly, the related interfaces exhibited very low reflectivity (theoretically less than -84 dB, although this value may vary with the swelling of the stroma); thirdly, they were both very thin layers (less than 10 µm). The back surface was essentially the interface of cornea and water, which exhibited a reflectivity of about -54 dB, higher than the minimum detectable reflectivity of the simple FF-OCT system.

4.2.5 Discussion

Characterisation of corneal structure

In Section 4.2.2, the five-layer corneal structure (of a normal cornea) has been fully characterised by a state-of-the-art OCT instrument. Features of all layer interfaces, epithelial cells and stromal lamellas have been detected with high spatial resolution and image contrast. Imaging of bovine corneas by the simple FF-OCT system has been described in Section 4.2.4, where the corneal surfaces, the epithelium and the Bowman's membrane were measured

Table 4.3 Characterisation of corneal structure with the state-of-the-art OCT instrument and the simple FF-OCT system

	State-of-the-art OCT [304, 328]	Simple FF-OCT system
Imaging resolution	$(1 \times 1.5)\,\mu m^2$	$(3.6 \times 10.3)\,\mu m^2$
Imaging sensitivity	93 dB	76 dB
CCT	YES	YES
Epithelium	YES	YES
Bowman's membrane	YES	YES
Stroma	YES	Not completely
Descemet's membrane	YES	NO
Endothelium	YES	NO
Epithelial cells	YES	NO
Stroma lamellas	YES	NO

quantitatively. However, no layer boundary has been discovered in between the stroma and the Descemet's membrane. The endothelium also has not been resolved. Table 4.3 summarises the capability of the simple FF-OCT system for characterising the corneal structure compared to the state-of-the-art OCT instrument [304, 328].

The rear two corneal layers and intra-layer cellular structures have not been detected by the simple FF-OCT system. This is mainly due to the fact that the simple system does not offer a sufficient imaging sensitivity for clear illustration of small refractive index variations. Despite this, the simple system is advantageous for low cost, ease of use, and much quicker image acquisition speed (at about 8.3×10^{-3} seconds per *en-face* image). The mentioned state-of-the-art OCT instrument took around three seconds for the acquisition of an *en-face* tomographic image [328].

Diagnosis of corneal disorders

In Section 4.2.3, the investigation of corneal disorders by using OCT techniques has been reviewed. The feasibility and reliability of OCT has been illustrated in the characterisation of structural variations of the cornea due to corneal oedema and corneal erosion, respectively. The increasing of the total corneal thickness and the existence of collagen-free regions or lakes as a result of corneal oedema has been depicted in the OCT images. The morphologic changes of corneal erosions due to corneal EBMD have been exposed in the corneal epithelium and the Bowman's membrane. The presence of hyperreflective dot features or the cleavage within the epithelium layer or the detachment of the epithelium layer from the Bowman's membrane in the OCT images are all typical symptoms of corneal EBMD.

The simple FF-OCT system is also likely to provide useful information for the analysis of these corneal disorders. The system has been demonstrated to quantitatively measure corneal frontal and rear surfaces. It may permit the prediction of the oedematous state of a cornea by the variation of the total corneal thickness. An improvement of the detection sensitivity of the simple FF-OCT system is required for the imaging of the intrastromal lakes. On the other hand, the simple system has demonstrated the ability to distinguish the epithelium and the Bowman's membrane. Epithelial erosions often develop among these two layers as a result of corneal EBMD. It is possible to detect the hyperreflective dot features by the simple FF-OCT system, as it exhibits higher reflectivity (see Fig. 4.16) than any other corneal interfaces, such as the one in between the epithelium and the Bowman's membrane, which is detectable by the simple system. The cleavage within the epithelium layer and the detachment of the epithelium layer from the Bowman's membrane might also be resolved if the detection sensitivity of the system is large enough.

The feature at a depth of approximately 0.45 mm beneath the surface was observed in the FF-OCT results. Further investigation (such as measuring in vivo bovine cornea with the simple system) should be undertaken to determine whether it is caused by a measurement artefact which could present a major limitation of the simple FF-OCT system.

Evaluation of the simple FF-OCT system

The simple FF-OCT system might not deliver a comparable imaging performance with the state-of-the-art OCT instrument; however, the current spatial resolution and detection sensitivity permit the identification of the anterior two corneal layers and a precise determination of the CCT. The low-cost system also offers an easier and quicker structural evaluation of the cornea.

Nevertheless, current imaging sensitivity is not sufficient for an effective characterisation of all five corneal layers or detailed analysis of corneal disorders. The Descemet's membrane and the endothelium have been measured as a single OCT feature or peak reflected by the corneal back surface; the superimposition structure of the epithelial cells and the intrastromal collagen lamellas have not been resolved. The imaging sensitivity of the simple FF-OCT system can be improved by, for example, increasing the radiation power, which will result in the saturation of the frontal surface and measurement artefacts.

4.2.6 Summary

In this section, bovine corneas have been investigated by using the simple FF-OCT system. The simple FF-OCT system has been demonstrated as an analytical tool for the

characterisation of the corneal front and rear surfaces, the epithelium and the Bowman's membrane. Both the CCT and the structure of the front two corneal layers are in agreement with previous works. The simple FF-OCT system is hence likely to provide useful information for the prediction of the corneal oedematous state and the indication of epithelial erosions. However, the remaining three corneal layers cannot be differentiated from the FF-OCT results and a possible measurement artefact has been discovered inside the stroma, which could limit the imaging potential for corneal structure and the possibility for analysing corneal disorders with the simple FF-OCT system.

4.3 Assessment of Paint Quality

4.3.1 Introduction

In the manufacturing of industrial products such as aircraft, automobiles and boats, it is an essential step to paint on metal, fibre-glass or rigid plastic. The painting is important to provide not only a superior gloss finish with a distinct colour effect, e.g. metallic and pearlescent, but also forms a tough and durable protection from water, ultra-violet radiation, corrosion, scratches and harmful chemicals. Strict quality control of the paint film by monitoring the paint thickness is required to maintain these functions during manufacturing.

Commercially available thickness meters, including magnetic gauges [329, 330], eddy current testing [331, 332] and ultrasound testing [333], are established methods to take portable measurements of the paint thickness. However, all these meters require direct contact with the paint surface, which may cause problems when the paint is still wet. The paint quality is evaluated based on thickness measurements over a limited number of sampling points; hence these methods lack the capability of identifying paint defects, monitoring drying processes and mapping the thickness distribution over a larger surface [334]. Besides, the use of magnetic gauges and eddy current testing are limited to measuring the total thickness of the paint coated on metal substrates. Ultrasound testing is useful with metal substrates as well as plastic, and can determine the individual thickness for multi-layered paint [335].

There are also some imaging techniques which allow non-contact and non-destructive measurement of the paint. For example, Carduner *et al.* [336] invented a patent involving the use of NIR spectroscopy apparatus for measuring each constituent film of multilayered automotive paint; Ying *et al.* [337] employed a second-harmonic optical scanning imaging method for the evaluation of incipient corrosion of painted metals; De Gelder *et al.* [338]

reported the use of Raman spectroscopy and Fourier transform IR spectrometry for the forensic analysis of automotive paints.

Terahertz-based methods have recently been introduced for the evaluation of paint thickness distribution and paint quality. Yasui *et al.* [339] demonstrated a terahertz "paintmeter" for non-contact mapping of the thickness of both single layer and two-layer paints with relatively thick films (above 100 µm). Su *et al.* [334] reported a terahertz approach to measure the individual thickness of paint layers on multi-layered painted panels on both metallic and non-metallic substrates.

OCT detects subsurface structures in a similar manner to those of terahertz methods, but with better spatial resolution. It has been successfully applied in art conservation projects [340, 341] for the non-contact and non-destructive examination of wall painting [342, 343]. The capability of OCT for the measurement of the paint thickness of industrial products has been mentioned in the study by Yasui *et al.* [339] to be only applicable for translucent paint films, as opaque paints cannot be assessed with the OCT methods.

In this section, the structure of typical automotive paint and the supplied single-layer paint panels are described first. Then the paint thickness of the supplied panels is measured by using the simple FF-OCT system. The FF-OCT results are described and the potential of the simple system for the determination of the paint thickness is assessed.

4.3.2 Single-Coat Paint Samples

4.3.2.1 Automotive Paint

Typical paint used in the automotive industry generally requires four paint layers to be built up on a metal substrate, as shown in Fig. 4.19. Initially at least two layers of primer are coated directly upon the substrate surface to ensure optimum adhesion and to give the best finish [344]. Alternatively, this could be a combination of an electrocoat and a primer. The second step is the layering of the pigmented basecoat over the dried out primer. This layer contains the visual properties of colour and effects, such as solid, metallic and pearlescent colours, and is usually the one referred to as the paint. Eventually, a pigment-free polymer clearcoat is coated on top of the basecoat. It is usually a transparent and glossy paint that forms the final interface with the environment, hence it must be durable enough to resist abrasion and chemically stable enough to withstand UV light [344].

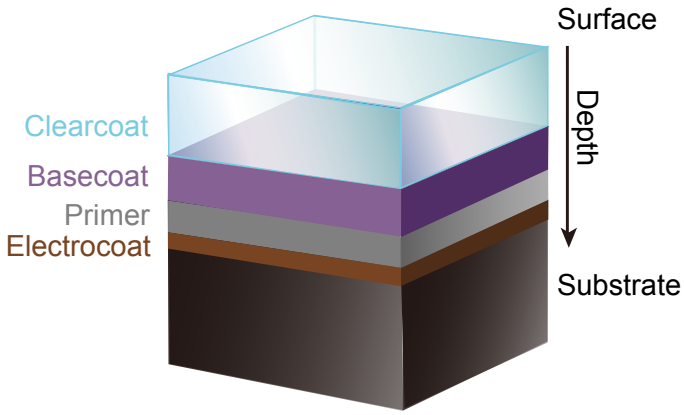

Fig. 4.19 Cross-sectional schematic of layered structure of general car paint in the automotive industry.

4.3.2.2 Single-Coat Paint Panels

The supplied paint panels were prepared by coating a layer of paint over half of the surface of the optically flat mirror (ME1S-G01, Thorlabs), as illustrated in Fig. 4.20 (a). The paint films on the panels correspond to electrocoat, primer, basecoat, and clearcoat, as shown by the photos in Fig. 4.20 (b) - (h). The external appearance of the basecoat panel has a sparkle effect due to the dispersed metallic flakes (Basecoat A) or pearlescent pigments (Basecoat B). The electrocoat and primer panels generally exhibit a solid colour with a matt finish. The clearcoat is a transparent paint film as expected. These paint films are essential components in automotive paint.

However, the use of these panels is to test the potential of the simple FF-OCT system for the characterisation of these paint films. The paint panel was supplied as a testing sample instead of a model of automotive paint, which is generally multi-layered and coated onto the actual metal body. The measurement of these panels might not be directly comparable to what happens in the automobile industry. Besides, the adhesion of paint and metal is totally different from that of a paint and mirror surface. The surface quality of the metal is also different from that of the mirror (surface roughness equal to 633 nm).

The reason why the paint was coated on one half of the mirror is because stair step topography can be determined on the paint and mirror surface. This enables the use of surface profilometry to determine the paint thickness by the measured step height. The measurement of these paint panels was conducted at the University of Cambridge by using a stylus profilometer (Talysurf i120, Taylor Hobson). A diamond stylus was employed to move vertically in contact with a sample and then move laterally across the sample for a specified distance. Small surface height variations can be measured by the vertical stylus displacement

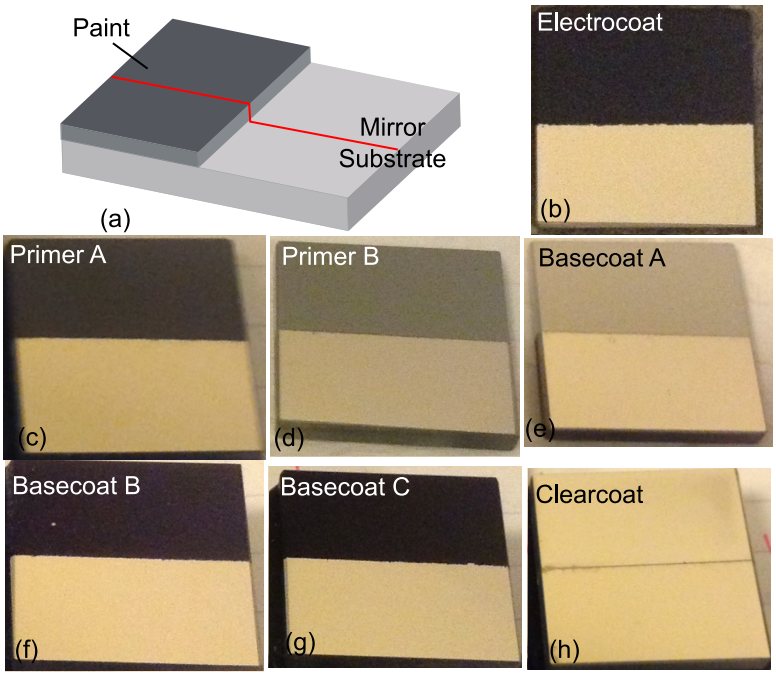

Fig. 4.20 A schematic in (a) and photos in (b) - (h) of paint panels. The paint was coated on one half of the mirror surface. The red line in (a) indicates a transverse line, along which the panel surface was profiled by the stylus profilometer.

as a function of the lateral position. During the measurement of the paint thickness, the paint panel surface was profiled along three transverse lines across the mirror and the paint, as depicted by the red line in Fig. 4.20 (a). The paint thickness was quantified by its mean and STD values of the surface step height. Table 4.4 lists the paint thickness measured by the profilometry together with that estimated by the supplier based on weight gain.

There are discrepancies between the measured and estimated thicknesses of the electrocoat and primer, as shown in Table 4.4. The stylus profilometry is a reliable surface measurement technique and has much greater precision than the weight gain estimation. Hence, the measured thicknesses are considered correct and used as the reference for the subsequent FF-OCT measurement. It helps the evaluation of the simple FF-OCT system in the characterisation of paint thicknesses of the electrocoat, primer, basecoat and clearcoat panels.

Table 4.4 also includes the optical properties, i.e. the refractive index n and the extinction coefficient k, of all paints. These refractive indices of paint films are going to be used in the determination of paint thicknesses with the simple FF-OCT system in the next section.

Table 4.4 Optical properties, i.e. refractive index n and extinction coefficient k (adapted from [334]) and paint thicknesses measured by profilometry and estimated based on the weight gain.

Paints	n	k	Measured [µm]	Estimated [µm]
Electrocoat	1.72	84	15.4 ± 1.0	10 - 14
Primer A	2.31	991	36.0 ± 2.0	20 - 30
Primer B	2.11	55	28.0 ± 2.0	30 - 50
Basecoat A	8.22	3880	14.4 ± 2.0	10 - 20
Basecoat B	1.73	140	11.8 ± 1.0	10 - 20
Basecoat C	1.64	78	14.0 ± 2.0	10 - 20
Clearcoat	1.56	30	58.0 ± 3.0	50 - 70

4.3.3 Results and Discussion

FF-OCT measurement

Prior to each FF-OCT measurement, the system optics were aligned and adjusted to obtain the required imaging FOV on the paint panel. The focal area of $(900 \times 900)\,\mu m^2$ of the FF-OCT imaging was used for all panels. The paint panel was fixed onto the sample arm of the simple FF-OCT system. The position of the panel on the optical axis was adjusted to reach the optimal position to start the depth-scan.

Each FF-OCT measurement was conducted by acquiring *en-face* images at a camera frame rate of 120 fps and moving the paint panel at a constant speed of $3\,\mu m\,s^{-1}$ for the depth-scan. An axial movement of the stage of 100 µm was operated for all electrocoat, primer and basecoat panels, while a displacement of 200 µm was applied for the measurement of the clearcoat panel. Each measurement only took less than two minutes. Thus an OCT 3-D data cube was obtained covering a volume of $(900 \times 900 \times 100)\,\mu m^3$ or $(900 \times 900 \times 200)\,\mu m^3$ for the clearcoat panel. An image file containing the data cube was created and subsequently processed.

The processed data was interpreted in B-scan images and A-scan signals for the determination of the paint thickness. Note that the refractive indices of paint films are not taken into account for the axial distance in any images and signals in this section; in other words, the scale bar in images and the horizontal ordinate in signals represent the propagation depth of the OCT signal in air (or the vacuum) instead of in the paint. However, the refractive index needs to be considered in the calculation of the paint thickness.

4.3.3.1 Determination of Paint Thickness

Electrocoat and Primer

The B-scan images of the FF-OCT measurements of the electrocoat, Primer A and Primer B panels are shown in Fig. 4.21 (a) - (c). Only the response of the paint surface is resolved by the simple system. It is also observed that there exist some weak responses just beneath the paint surface in the image of the two primer panels. Their measured thicknesses listed in Table 4.4 suggest that for a thinnest 26 µm-thick primer film, a layer structure of 55 µm thickness (i.e. (26×2.11) µm) should have been revealed in the B-scan image, which is not the case.

Therefore, the simple FF-OCT system is not capable of measuring the film thickness of the electrocoat, Primer A and Primer B panels in this study. This could be due to the high extinction coefficient k of the electrocoat and primer films (especially Primer A: k = 991), leading to a quick decay of the incident FF-OCT electric field. This could result in a significant reduction of the OCT signal along the penetration depth, which is consistent with the averaged A-scan signal as shown in Fig. 4.21 (d).

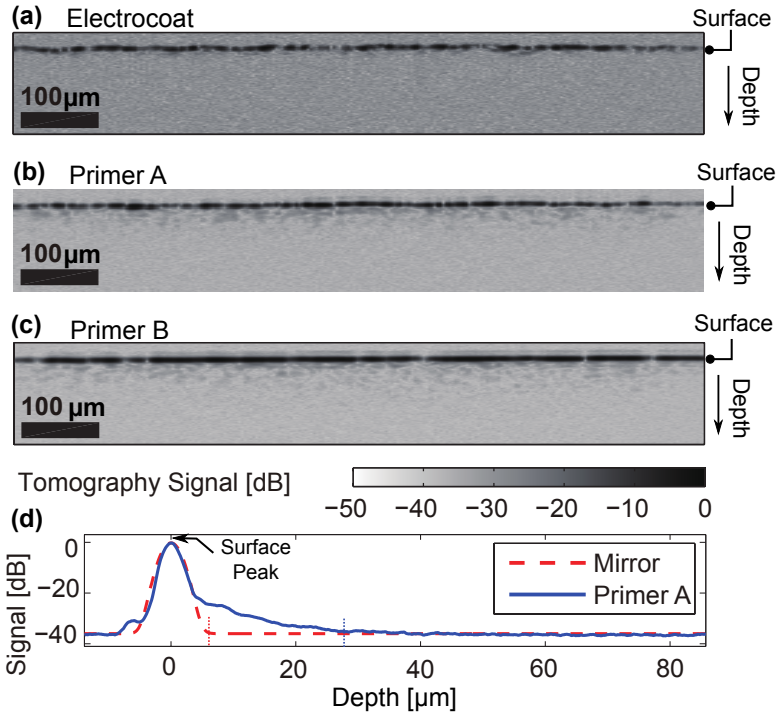

Fig. 4.21 (a) - (c) B-scan image of (900×100) µm^2 of the electrocoat, Primer A and Primer B panels. The grey scale bar applies to all three images. (d) the A-scan signal (blue line) of Primer A after applying averaging on all axial signals in (b) and the A-scan profile of a bare mirror (red dashed line) under the same measuring conditions.

Basecoat

The supplied basecoat panels have different visual effects. Basecoat A is coated with a metallic paint, in which small metal flakes are contained inside the paint layer to create a sparkling and metallic look; Basecoat B is coated with a pearlescent paint, in which special iridescent pigments are included to create a subtle colour effect; Basecoat C is coated with a solid paint, which is the most common type of basecoat and just provides a solid colour [345].

These basecoat panels exhibit a better response in the simple FF-OCT system than the electrocoat and primers, since the subsurface structure of the basecoat can be characterised as shown in Figs. 4.22 to 4.24. The B-scan images as shown in Figs. 4.22 (a) - 4.24 (a) reveal the FF-OCT response within the basecoat. The A-scan signals as shown in Figs. 4.22 (b) to 4.24 (b) are used to highlight these internal responses by averaging all axial signals in these B-scan images. The main peak of an averaged A-scan signal represents the averaged response of the front surface at a depth of zero. The minor peaks are found to be 2.4 µm, 10.4 µm and 12.5 µm away from the front surface responses of Basecoats A, B and C, considering the respective refractive index of 8.22, 1.73 and 1.64 that are listed in Table 4.4.

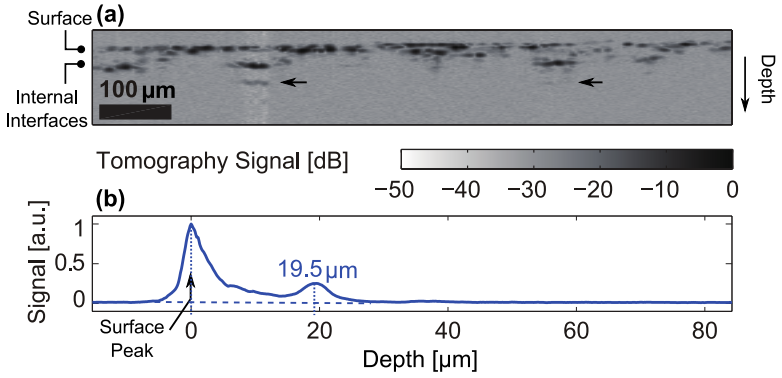

Fig. 4.22 (a) B-scan image of $(900 \times 100)\,\mu m^2$ and (b) linear depth profile of Basecoat A (metallic) after averaging all axial signals in (a).

The depth separations of the minor peaks and the main peaks of Basecoat B (10.4 µm) and Basecoat C (12.5 µm) approach the measured paint thicknesses listed in Table 4.4. Hence, the minor peaks could be the averaged FF-OCT responses of the back surfaces of Basecoats B and C. Both the B-scan images and the A-scan signals as shown in Figs. 4.23 and 4.24 suggest the resolving of well separated frontal and back surface responses for Basecoat B and C. The paint back surface is also the front surface of the mirror, of which the surface roughness is equal to 633 nm, compared to a depth resolution of 3.6 µm. This is the reason why the back surface features in the B-scan images as shown in Figs. 4.23 (a) and 4.24 (a)

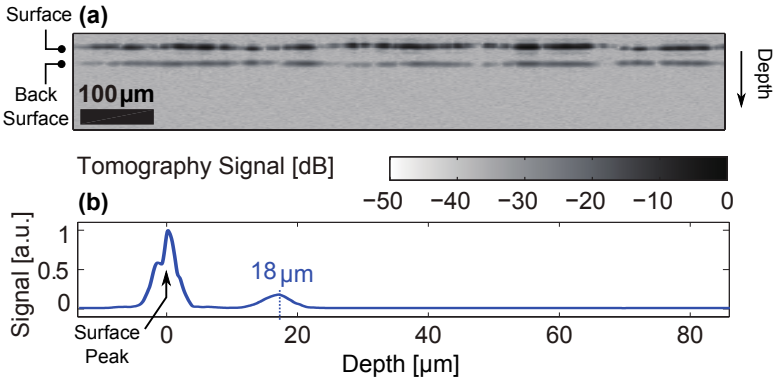

Fig. 4.23 (a) B-scan image of $(900 \times 100)\,\mu m^2$ and (b) linear averaged depth profile of Basecoat B (pearlescent).

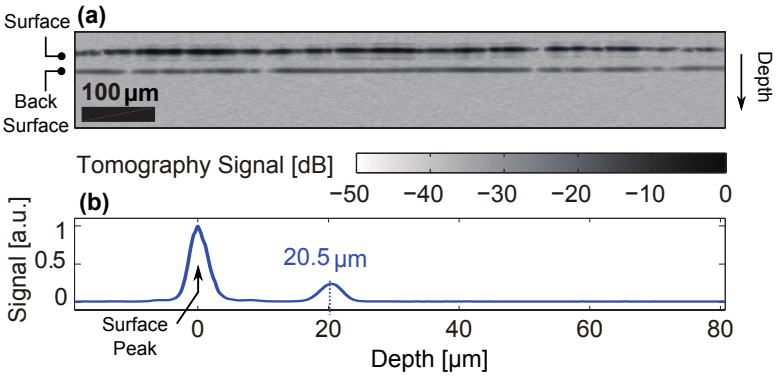

Fig. 4.24 (a) B-scan image of $(900 \times 100)\,\mu m^2$ and (b) linear averaged depth profile of Basecoat C (plain).

are along a line. Nevertheless, the averaged front surface peaks are not a standard Gaussian function and suffer some defects, especially for Basecoat B. This indicates the locations of the front surface responses could have a small variation in the depth direction, which is less than or close to the depth resolution of 3.6 µm. The spatially distributed paint thickness could also have variations and is thus uneven for Basecoats B and C.

Basecoat A is a metallic paint containing a suspension of fine metallic flakes. A random distribution of the flakes is expected in the basecoat. The flakes would essentially obstruct the injected light from transmitting further. The simple FF-OCT system employs NIR radiation, which cannot propagate through the metallic flake. Before the encounter with the flake, the FF-OCT signal should travel inside the basecoat in a similar way to that in a normal solid basecoat (such as Basecoat C). A more adequate refractive index could be close to the one of 1.64 for Basecoat C, rather than the listed 8.22 for Basecoat A in Table 4.4, which is the refractive index of the mixture including the metallic flakes and the bare basecoat.

By using 1.64 as the refractive index, scattered features are distributed from the surface to a depth of about 14 µm, as revealed in the B-scan image in Fig. 4.22 (a). This depth value approaches the measured paint thicknesses listed in Table 4.4. The minor peak in the A-scan signal has a peak position of 11.9 µm. The averaged A-scan signal also presents a depth range of 0 µm to 11.9 µm in which the signal intensity is always above zero (Fig. 4.22 (b)). This indicates that there are successive FF-OCT responses within this depth range, which could be caused by the flakes, internal pores as well as the paint back surface. There are no connecting features found to demonstrate the detection of the paint back surface, the simple FF-OCT system is thus not capable of measuring paint thickness for Basecoat A.

The deepest detectable FF-OCT responses at about 23.0 µm beneath the surface, as identified in the B-scan image in Fig. 4.22 (a), cannot represent the location of either the metallic flake or the paint back surface. If the response at 11.9 µm is caused by metallic flakes or the paint back surface, which do not allow the transmission of FF-OCT radiation, the response at about 23.0 µm cannot be detected. If the response at 11.9 µm is caused by pores, the response at about 23.0 µm should have a much stronger signal strength, instead of the contrary. Hence, the presence of these response could be due to the measurement artefact.

Clearcoat

Clearcoat is a glossy and transparent coating that is used to form the final interface of the industrial automotive paint with the environment. The clearcoat panel was measured to have two well separated responses of interface in the B-scan image and the averaged A-scan signal as shown in Fig. 4.25. The two interfaces could be the clearcoat front and back surface (or the

mirror surface). The back surface exhibits a stronger response than that of the paint surface, because the paint surface (air/clearcoat interface) only reflects about 4 % of the incident signal intensity, while the mirror surface reflects all the rest of the signal intensity theoretically. The thickness of the clearcoat can be determined by the peak separation computed as 56 µm using a refractive index of 1.56 as listed in Table 4.4. The FF-OCT measured clearcoat thickness is consistent with the measured thickness of (58.0 ± 3.0) µm as listed in Table 4.4.

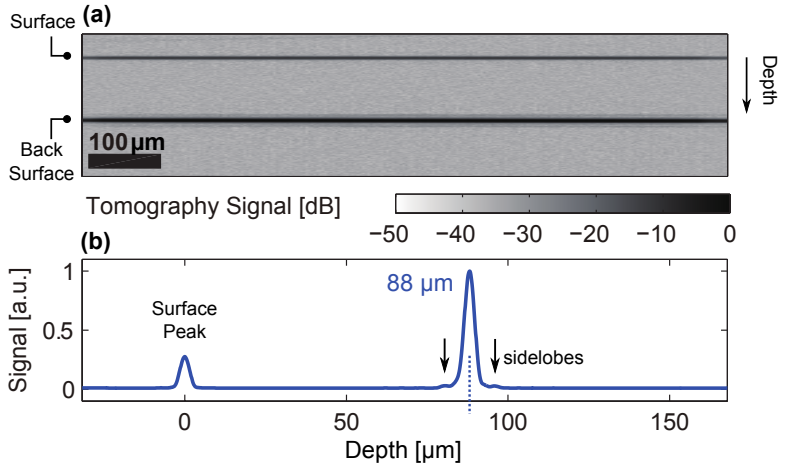

Fig. 4.25 (a) B-scan image of (900×200) µm^2 and (b) linear depth profile of the clearcoat layer after applying averaging on all axial signals in (a).

Note that in Fig. 4.25, there are noticeable sidelobes on both sides of the mirror surface response in the A-scan signal and B-scan image. They are caused by the non-Gaussian or non-smooth spectrum of the OCT light source [346–348]. Generally the intensity of the sidelobes are much less than that of the main OCT interferogram; however, it is usually sufficiently strong to produce artefacts when the OCT light reflects off a highly reflected surface, e.g. a mirror.

4.3.3.2 Evaluation of Thickness Distribution

In the previous section, the capability of the simple FF-OCT system has been demonstrated to measure the paint thickness of Basecoat B, Basecoat C and the clearcoat based on the depth separation between the FF-OCT responses of the frontal and back surfaces of the corresponding paint. By computing the paint thickness at each transverse position inside the FF-OCT measured area of (900×900) µm^2, the thickness map can be obtained and the spatial distribution of the paint thickness can be assessed.

Fig. 4.26 shows the thickness maps and histograms of the FF-OCT measurements of Basecoat B, Basecoat C and the clearcoat, respectively. The paint thickness at a transverse

position is represented by the colour level in the thickness map. The mean thickness and the thickness STD are also computed based on the obtained thickness map for each paint panel. The measured paint thicknesses in the previous section are in good agreement with the computed paint thickness range. The thickness maps in Fig. 4.26 (a), (c) and (e) show that Basecoats B and C have a more variable paint thickness (about 1 µm thickness STD) than that of the clearcoat (about 0.5 µm thickness STD).

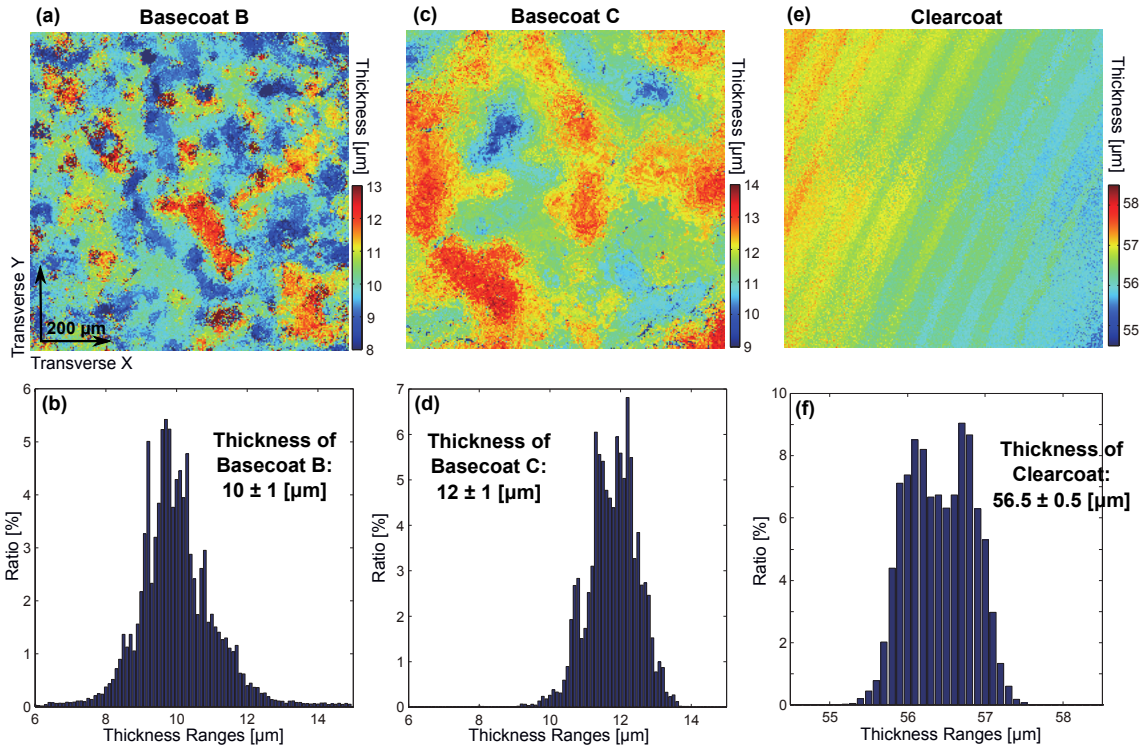

Fig. 4.26 Thickness maps covering an area of $(900 \times 900)\ \mu m^2$ in (a), (c), (e) and histograms in (b), (d), (f) of Basecoat B, Basecoat C and the clearcoat, respectively. The bin width is 0.1 µm for all histograms.

The histograms in Fig. 4.26 (b), (d) and (f) are plotted based on the spatial thickness data of Basecoat B, Basecoat C and the clearcoat. They illustrate the thickness probability distributions by dividing the entire range of thickness values into a series of thickness intervals (bin width) of 0.1 µm and calculating the percentage of the thickness values that fall into each thickness interval. The coverage ratio of a paint thickness range in the map is specified by the height of the corresponding bin. The thickness of Basecoat B and C exhibits a near normal distribution, of which the highest probability lies in a thickness of about 10 µm and 12 µm, respectively. The histogram of the clearcoat shows a near bimodal distribution, which might suggest the ambiguity in the differentiation of sub-micrometre variation of the clearcoat thickness.

The measured thickness (mean ± STD) of Basecoat B, Basecoat C and the clearcoat by the simple FF-OCT system are summarised in Table 4.5 together with the profilometry results. Consistency is found between the results of the FF-OCT and the profilometry measurements. There are small deviations of the FF-OCT measured thickness from the profilometry ones, which could be due to the fact that FF-OCT measures paint thickness over a small square, while the stylus profilometer measures that along three transverse lines.

Table 4.5 Thicknesses (mean ± STD) of Basecoat B, Basecoat C and the clearcoat measured by the profilometry and the simple FF-OCT system

Thickness	Profilometry [µm]	FF-OCT [µm]
Basecoat B	11.8 ± 1.0	10.0 ± 1.0
Basecoat C	14.0 ± 2.0	12.0 ± 1.0
Clearcoat	58.0 ± 3.0	56.5 ± 0.5

4.3.4 Discussion

Industrial relevance The paint panels in this study are a layer of paint coated onto the mirror surface. They are not industrial automotive paint, which is generally multilayered and coated onto an actual metal body. The use of these panels is only to investigate the capability of the simple FF-OCT system to resolve the paint film and its ability to measure the paint thickness.

The measurement of these panels might not be directly comparable to what happens in the industry. Firstly, metals, fibre-glass and plastics that are common substrates used in the industry have different levels of surface roughness and paint adhesion compared to the optical flat mirror. Secondly, the multilayered paint applied in the industry is a combination of clearcoat, basecoat, primer and electrocoat, as depicted in Fig. 4.19. It is hence different from the single coated paint panels in this study. Differentiation of surface and internal structures cannot be guaranteed with the simple FF-OCT system. Table 4.6 compares the desired capability of a measurement tool for the industrial automotive paint with those that the simple FF-OCT can achieve. Note that the capability that is achievable by the simple system only applies to the non-metallic basecoat and clearcoat.

Artefacts in industry There are many paint defects that may arise during the production of automotive paint, such as solvent popping, blisters and pinholes, etc. It is thus important

Table 4.6 Capabilities desired in the automotive industry and achievable with the simple FF-OCT system

Desired Capability	FF-OCT
Single-layer single point thickness	Yes
Single-layer areal thickness	Yes
Multi-layer single point thickness	No
Multi-layer areal thickness	No

to diagnose and remedy the defect before entering the market. The applicability of the simple FF-OCT system is estimated for the identification of blisters and solvent pops.

Blistering appears as a swollen area of the paint. It could be situated between the primer and the basecoat. This defect might be detected by the simple FF-OCT system, because it is demonstrated to be able to characterise non-metallic basecoats, and FF-OCT might detect the refractive index variation between the basecoat and the contaminant air.

Solvent popping is a blister-like surface defect mostly caused by solvent or air trapped in the clearcoat. This defect might be identified by using the simple FF-OCT system, because the employed FF-OCT radiation can propagate inside the clearcoat and FF-OCT could detect the refractive index variation between the clearcoat and the trapped air or solvent.

4.3.5 Summary

This section investigates the potential of the simple FF-OCT system for the characterisation of various paint films coated on identical mirror surfaces. The simple system is able to resolve the surface and the subsurface structure for basecoat and clearcoat. In addition, it is demonstrated to be capable of not only measuring the single-point thickness but also obtaining the areal thickness map for Basecoat B, Basecoat C and the clearcoat. The thickness ranges obtained by using the simple FF-OCT system are shown to be consistent with that of profilometry results. However, the study of the paint panels may have slight relevance to industrial automotive paint.

4.4 Conclusions

In this chapter, the capability of the simple FF-OCT system have been explored for the tomographic imaging of pharmaceutical coating of small-size pellets, corneal structures and

paint films coated upon mirrors. The layer boundaries and internal morphology features have been characterised in the acquired FF-OCT B-scan images and A-scan signals.

For the imaging of small-size pellet coating, the simple FF-OCT system allows a spatial characterisation of coating layers, accurate determination of coating thickness, estimation of coating uniformity and porosity. The FF-OCT results are validated by the XμCT measurement, indicating that the FF-OCT measurement could provide accurate, reliable and quick evaluations of pellet coatings. Because of the high spatial resolution, the imaging accuracy, the quick measurement and the low-cost attributes, the simple FF-OCT system could be a powerful tool for the evaluation of the coating structure of similar pharmaceutical pellets.

For the corneal structure, the simple system has been demonstrated to be useful for the detection of corneal surfaces and the two anterior layers, and have the potential for predicting the corneal oedematous state and epithelial erosions. However, the potential for the FF-OCT imaging could be limited by the possible artefact.

For the paint panels, the simple system could reveal the paint surface and subsurface and provide an accurate measurement of paint thickness, which is consistent with that of the reference method for basecoat and clearcoat. The FF-OCT imaging also permits the spatial evaluation of a paint film and the areal thickness map could be obtained, although these paint panels might exhibit slight relevance to the measurement of industrial automotive paint.

Chapter 5

Surface Topography Studies using the Simple FF-OCT System

5.1 Introduction

OCT has traditionally served as a high precision profilometer to evaluate surface topography in addition to the imaging of a sample's structure. In this chapter, two typical surface topographic applications are studied using the simple FF-OCT system. The potential of the system is studied for the characterisation of surface analysis.

5.2 Determination of Surface Variation

Contact profilometry techniques generally employ a stylus or tip to move in contact with the sample surface and across the region of interest. The vertical displacement of the stylus is measured to directly determine the surface variation as a function of the transverse position. For non-contact profilometry techniques based on the interferometry, the surface variation is evaluated by the displacement of the peak position of the measured interference signal. As described in Chapter 2, the interference occurs on condition that the OPLs of sample and reference arms are matched in an OCT system. Note that, the OPL is dependent on both the geometric length and the refractive index, it can also be affected by reflections. The misunderstanding of the relationship between the OPL and the geometric length could result in a failure in the determination of the surface variation.

Hence, it is important to analyse the phase change upon reflection in order to understand the OPL variation of both the sample and reference arms in the simple FF-OCT system. The

phase change is dependent on the medium from which light originates and the new medium that light enters. For a normal case of air/glass configuration, light propagates from a lighter medium (low refractive index), i.e. air, to a denser medium (high refractive index), i.e. glass, and part of the light is reflected at the air/glass interface; the reflected light undergoes a phase change of π or 180°, compared to the incident light; a phase change of π corresponds to an additional OPL of $\frac{\lambda_0}{4}$, where λ_0 is the source central wavelength. Since the simple FF-OCT system uses a window as the reference mirror, the reference arm also has a phase change of π and an additional OPL of $\frac{\lambda_0}{4}$, similar to that of the normal air/glass case.

For light propagating from a lighter medium to a metallic or high-κ (high dielectric constant κ as compared to silicon dioxide) material of a known refractive index n_1 and extinction coefficient k_1, the reflected light undergoes a phase change of β, which is expressed by [349]:

$$\beta = \pi - \arctan\left(\frac{2k_1 n_0}{{n_1}^2 + {k_1}^2 - n_0^2}\right), \tag{5.1}$$

where n_0 is the refractive index of the light or wave incident medium (e.g. air). The additional OPL for a phase change of β is calculated by $\frac{\lambda_0}{4} \cdot \frac{\beta}{\pi}$, which should be considered if such a metallic or high-κ material is investigated by the simple FF-OCT system.

Note that, phase changes of π and β only apply to the propagation of light from a lighter medium to a denser medium. Light travelling from a denser medium to a less dense medium will have no phase change upon reflection, hence, no OPL change. By analysing the relationship of the FF-OCT measured surface map and the OPL variation, the true surface variation can be determined.

5.3 Validation of the FF-OCT System for Surface Topography

To validate the simple FF-OCT system for surface topography studies, the profiling performance has to be compared to that of a state-of-the-art instrument, which should be of industry standard to measure surface quality. AFM is a high-resolution type of microscopy, capable of investigating surfaces with atomic scale axial resolution (less than 1 nm) [350]. It has become an established tool for nanostructured surface characterisation, especially in the semiconductor industry [351, 352].

In this section, the surface characterisation of a semiconductor sample using both an AFM instrument and the simple FF-OCT system is demonstrated. The semiconductor sample

was fabricated by depositing a thin film of gold mask onto a substrate of silicon, forming a dot-patterned nanostructured surface. The cross-sectional schematic and the photo of the sample as shown in Fig. 5.1 identify the sample structure.

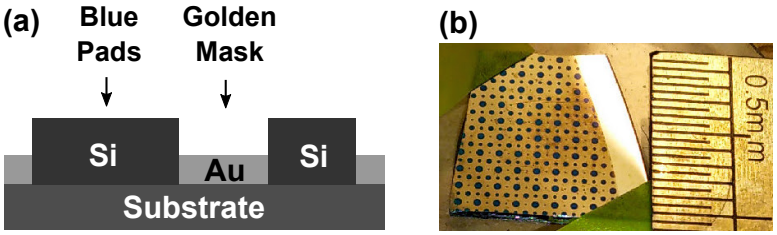

Fig. 5.1 (a) Schematic of the cross-sectional view and (b) photo of the dot-patterned semiconductor sample.

5.3.1 Surface Characterisation by AFM and FF-OCT

Both methods measured the nanostructured surface of smallest dots (or pad) and their surrounding gold film.

5.3.1.1 AFM Measurement

The AFM measurement was undertaken at room temperature by Dr. van Zalinge of the Solid State Group using an AFM instrument (CP-II, Brücker). The cantilever of the AFM instrument allowed an axial resolution of less than 1 nm and a transverse resolution of lower than 1 nm. An area of $(40 \times 40)\,\mu m^2$ of dot and gold surface was measured. The measurement took approximately 5 minutes before the final surface map was generated.

Fig. 5.2 (a) shows the measured AFM image, in which the surface height is represented by the colour level. The brighter the colour, the higher is the surface height. A quadrant of the silicon pad surface at the upper left corner is outlined by the dotted line in Fig. 5.2 (a). The Au surface is shown to have many noisy patterns and is likely to be coated in dirt or grease from fingers. Their heights cannot be taken as the true height of the Au surface. The area of Au surface in the AFM image that is low in surface height and located near the silicon pad or at the scratch at the bottom right corner, as identified in Fig. 5.2 (a), can be used to indicate the surface height of the clean Au surface. There is a major artefact at the downward bending near the left edge of the AFM image, as pointed out in Fig. 5.2 (a); while it could be smoothed out, it doesn't affect the measurement of the surface height variation.

Fig. 5.2 (b) shows the surface height profiles along lines A and B as marked in Fig. 5.2 (a). Both lines cover the silicon pad and the clean Au surface. The two profiles are

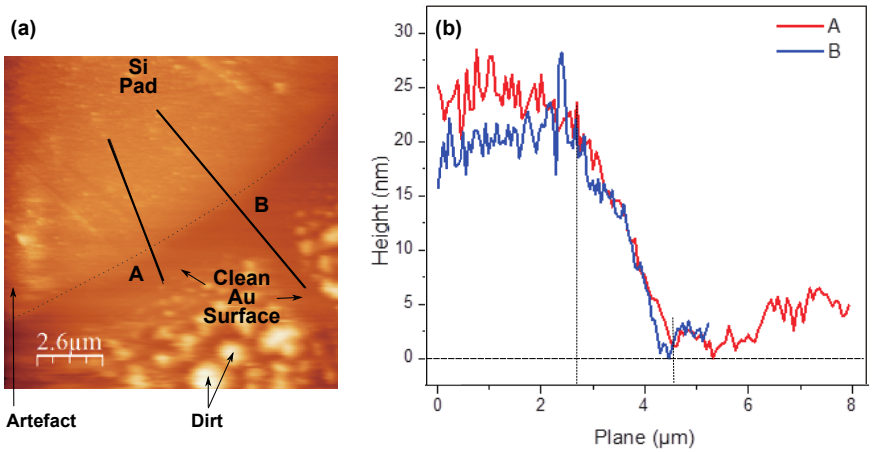

Fig. 5.2 (a) AFM image of the measured surface with the silicon pad outlined by the dotted line and (b) the height profiles along lines A and B in (a).

demonstrated to have the lowest heights of the clean Au surface at a depth of approximately zero. Their surface height at the silicon pad ranges from 18 nm to 26 nm. Based on the two height profiles, the thickness of the silicon pad over the clean Au substrate can be estimated as (22 ± 2) nm.

5.3.1.2 FF-OCT Measurement

The FF-OCT measurement was undertaken by me using the simple FF-OCT system. The central wavelength λ_0 of the FF-OCT radiation is 880 nm. The imaging system was focused onto an FOV of (250×250) µm^2 of the dot and gold surface. The sample was scanned with a steady speed of 1 µm s^{-1} of the sample arm and a normal camera frame rate of 120 fps. The stack of *en-face* image was acquired covering a total axial distance of 17 µm with a step size of about 8.3 nm between successive images. The FF-OCT measurement took less than 20 seconds before subsequent processing could be applied to the acquired final binary image file for the determination of the surface height variation.

According to the data analysis for the surface topography in Section 3.3.4, the nanoscale surface height or the true peak position of an OCT signal was obtained by using the interpolation and a minimum search algorithm. The resultant FF-OCT map reveals the surface height variation of the silicon pad and gold surface by the colour level in Fig. 5.3 (a). The step between the round pad surface and the surrounding surface can be clearly distinguished in Figs. 5.3 (a) and (c). Two height profiles along lines A and B show that the thickness of the silicon pad surface over the Au surface can be estimated as (14 ± 2) nm.

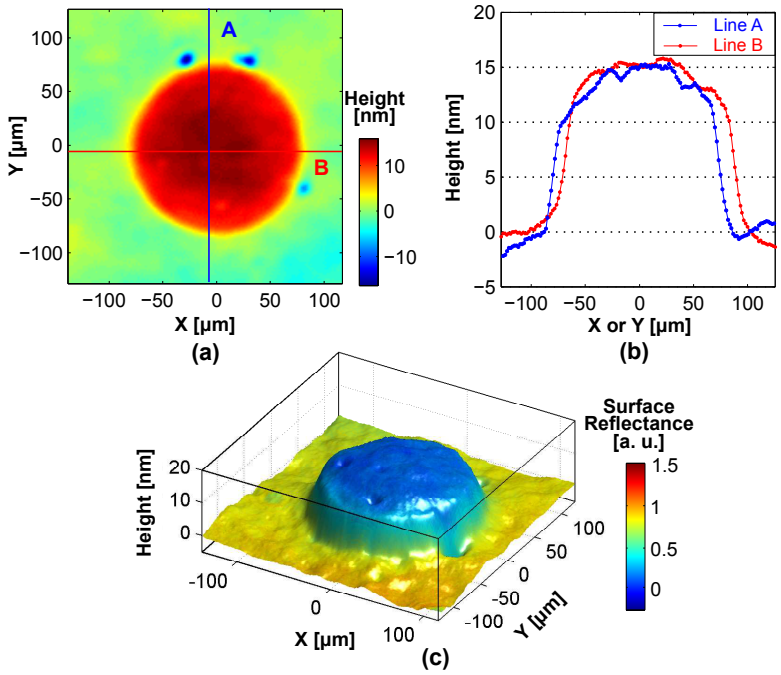

Fig. 5.3 (a) FF-OCT image of the measured surface, (b) the height profiles along lines A and B in (a), and (c) FF-OCT 3-D image of the measured surface.

Phase Change upon Reflections The sample surface consists of both silicon and Au. Since Au is metallic, the phase change upon reflections of the Au surface is different from that of the silicon pad surface, the factor of the phase change has to be analysed in the measurement of the Au surface height. The Au surface undergoes a phase change of $\beta_{\mathrm{Au}} = 0.877\pi$, which is calculated by substituting the refractive indices $n_{\mathrm{air}} = 1$, $n_{\mathrm{Au}} = 0.64$ and the extinction coefficient $k_{\mathrm{Au}} = 4.78$ [353] into Equation 5.1.

Considering the interference of reflections from the Au surface (air/Au interface) and reference surface (air/window interface) in the FF-OCT measurement, the OPLs of two arms were matched, which can be expressed as

$$\mathrm{OPL}_{\mathrm{ref}} + \frac{\lambda_0}{4} = \mathrm{OPL}_{\mathrm{Au}} + \frac{\lambda_0}{4} \cdot \frac{\beta_{\mathrm{Au}}}{\pi}. \tag{5.2}$$

Considering the interference of reflections from the silicon pad surface (air/silicon interface) and reference surface (air/window interface) in the FF-OCT measurement, the OPLs of two arms were matched, which can be expressed as

$$\mathrm{OPL}_{\mathrm{ref}} + \frac{\lambda_0}{4} = \mathrm{OPL}_{\mathrm{Si}} + \frac{\lambda_0}{4}. \tag{5.3}$$

A schematic is shown in Fig. 5.4 to explain the OPLs of the reference and sample arms for the interference events at the Au surface and the silicon pad surface. Fig. 5.4 also shows that the true thickness of the silicon pad over the Au surface can be computed by $s_1 - s_2$.

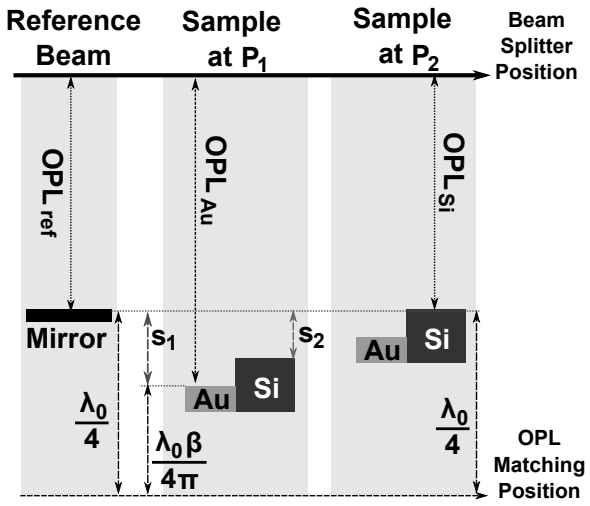

Fig. 5.4 A schematic of the OPL relationships of two interference events. When the sample was moved to axial position P_1, the reference surface interfered with the Au surface; when it was moved to position P_2, the reference surface interfered with the silicon pad surface.

From Equation 5.2, s_1 of Fig. 5.4 can be calculated by $s_1 = \mathrm{OPL_{Au}} - \mathrm{OPL_{ref}} = 27\,\mathrm{nm}$. s_2 of Fig. 5.4 is the moving distance $(P_2 - P_1)$ of the sample between two interference events, which corresponds to the estimated thickness of the silicon pad of $(14 \pm 2)\,\mathrm{nm}$ from the previous FF-OCT data analysis of the surface topography. Hence the true thickness of the silicon pad over the Au surface can be obtained as $(13 \pm 2)\,\mathrm{nm}$.

5.3.2 Performance Evaluation

The thickness of the silicon pad over the Au surface is obtained as $(22 \pm 2)\,\mathrm{nm}$ in the AFM measurement and $(13 \pm 2)\,\mathrm{nm}$ in the OCT measurement. This discrepancy could be due to the limited axial precision of the simple FF-OCT system for the surface topography. However, the simple FF-OCT system can measure the nanostructured step-like surface of the sample, which confirms that the system can achieve an axial nanoscale precision for the surface measurement. On the other hand, the data analysis of the surface topography only works on the signals that are extracted from the FF-OCT image volume. The axial accuracy can reach a nanoscale precision; however, there is no improvement in the transverse resolution of the system.

5.4 Determination of Electrode Thickness

Microelectronics relates to the study and manufacture (or microfabrication) of very small electronic designs and components. These components including transistors, capacitors, resistors and diodes are usually of micrometre-scale dimensions and are typically made from semiconductor materials together with insulators and conductors. It is essential to make a critical selection of the dielectric material and fabricate the gate dielectric and gate electrode configuration with high accuracy [354].

Some physical characteristics play a crucial role in determining the device performance. For example, the transistor can exhibit greatly decreased noise and increased reliability if atomically flat silicon is obtained [355]; the electrode thickness has an effect on the final dielectric stability and the interface quality in metal-oxide-semiconductor field-effect transistors (MOSFETs) [356]. To ensure desired device behaviour, device characteristics, e.g. thicknesses and surface roughness of the dielectric layer and electrode, require rigorous characterisation after device fabrication.

Semiconductor devices are explored at a small scale using many imaging and surface topography modalities, in order to measure physical characteristics. Spectroscopic ellipsometry (SE) has been used for the thickness characterisation of the oxide dielectric film [357]; AFM and confocal microscopy have been used to measure surface morphology of the dielectric material [358]; SEM and X-ray diffraction (XRD) have been used for the study of the structural properties of the oxide thin film [359]. A white-light optical profiler, as one of the optical interferometric techniques, has also been used for the thickness characterisation of the oxide film on patterned silicon substrate [360].

In this section, the surface topography of a photoconductive antenna and an optical rectifier is investigated by using the simple FF-OCT system. The potential of the simple system is explored for the nanometre-scale characterisation of surface structure, electrode and film thicknesses.

5.4.1 Bow-tie Photoconductive Antenna

Photoconductive antennas are fundamental and essential components for the generation of the terahertz radiation based on photoconductive sampling [361], for which the gap of the photoconductive antenna is generally irradiated with the femtosecond ultrafast laser [362]. Strip line, bow-tie, and dipole are some of the popular designs of photoconductive antenna used for the terahertz wave generation [363, 364]. These antennas employ antenna electrodes deposited on the surface of a semiconductor and an external bias field is apply

across the antenna [365]. In a photoconductive antenna, the optical laser pulse creates carriers (electron-hole pairs) in a semiconductor material. Effectively, an electric field present in the semiconductor results in a sudden current surge across biased antenna electrodes [366]. This changing current emits terahertz radiation, similar to that in the antenna of a radio transmitter.

5.4.1.1 Bow-tie Antenna

Bow-tie antennas are one of the favourite photoconductive antenna types in terahertz wave generation systems due to the small and simple planar structure and their broadband characteristics [367]. The bow-tie photoconductive antenna in this study is a bow-tie dipole of a deposition of gold with a gap of 10 µm on a gallium arsenide (GaAs) substrate, as shown in the cross-sectional schematic and the FF-OCT image in Fig. 5.5. This geometric design supports a large electric field across the antenna surface. The electrode gap is designated to avoid high voltages but to provide the required high electric fields. A modulated DC bias voltage is applied across the electrodes for the generation of a terahertz wave. Terahertz radiation is produced by the highly enhanced localised electric fields at the bow tip [368].

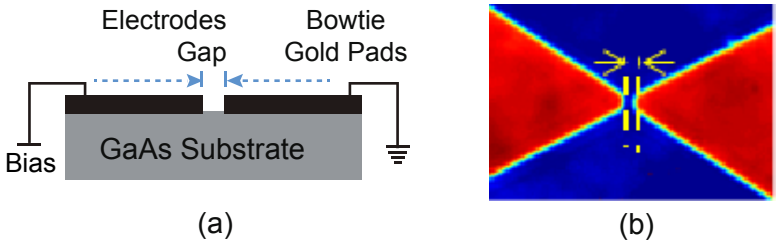

Fig. 5.5 (a) Schematic of the cross-sectional view and (b) FF-OCT *en-face* (top view) image of the bow-tie antenna.

5.4.1.2 FF-OCT Measurement

The surface measurement of the bow-tie antenna was undertaken by using the simple FF-OCT system. The imaging system was focused onto an FOV of $(350 \times 350)\,\mu m^2$ covering the bow tips. The antenna was scanned over a total axial distance of 17 µm with a steady speed of $1\,\mu m\,s^{-1}$ of the sample arm and a common camera frame rate of 120 fps. A step size of about 8.3 nm was obtained between successive images. Less than 20 seconds was taken by the FF-OCT measurement before subsequent processing was applied to the acquired final binary image file for the determination of electrode thickness.

Following the data analysis for surface topography, an FF-OCT map was obtained as shown in Fig. 5.6 (a). It reveals the surface height variation of the gold electrode and the GaAs substrate by different colour levels. A step between the electrode and the substrate surface can be clearly distinguished in Fig. 5.6 (b) and (c). Two height profiles along lines A and B show that the thickness of the gold electrode deposited upon the GaAs substrate can be estimated as (52 ± 2) nm. The electrode gap is detected by a height profile as displayed in Fig. 5.6 (b) (line A). Despite the width of the height profile at FWHM approaching the requirement of 10 µm, the width of the gap is not fully resolved by using the system, because the acquired height profile of the gap doesn't reach a minimum peak at a height of zero. This is due to the limited transverse resolution of the simple FF-OCT system being 10.3 µm.

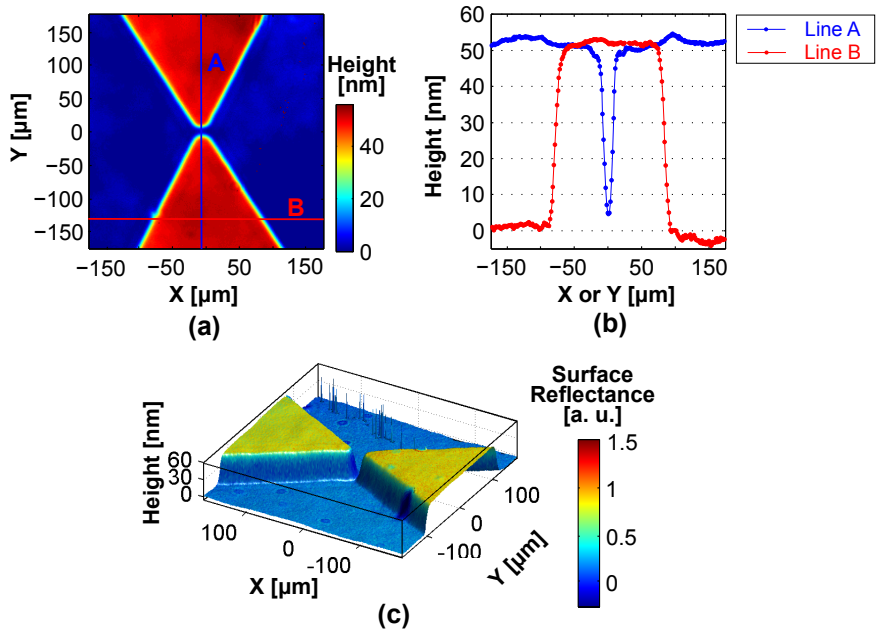

Fig. 5.6 (a) FF-OCT image of the bow-tie antenna, (b) the height profiles along lines A and B in (a), and (c) FF-OCT 3-D image of the bow-tie antenna.

5.4.1.3 Nanostructured Surface Characterisation

Phase Change upon Reflections

The bow-tie antenna employs gold electrodes deposited on the GaAs substrate. The phase change upon reflections of the gold electrode is different from that of the GaAs substrate; the factor of the phase change has to be analysed in the determination of the thickness of the gold electrode. Considering the phase changes upon reflections of both electrode and the substrate, the gold electrode undergoes a phase change of $\beta_{\text{gold}} = 0.877\pi$ of the reflection

(same as that of the Au surface in the previous section) according to Equation 5.1; the GaAs substrate undergoes a normal phase change of π or 180°, the same as the reference surface.

In the FF-OCT measurement, the reference surface (air/window interface) interfered twice with the gold electrode (air/gold interface) and the GaAs substrate (air/GaAs), respectively. While the two arms were matched, the relationship of the OPLs of the reference mirror, the gold electrode and the GaAs substrate can be expressed as:

$$\mathrm{OPL}_{\mathrm{ref}} + \frac{\lambda_0}{4} = \mathrm{OPL}_{\mathrm{gold}} + \frac{\lambda_0}{4} \cdot \frac{\beta_{\mathrm{gold}}}{\pi}, \tag{5.4}$$

$$\mathrm{OPL}_{\mathrm{ref}} + \frac{\lambda_0}{4} = \mathrm{OPL}_{\mathrm{GaAs}} + \frac{\lambda_0}{4}. \tag{5.5}$$

The OPL relationship at the interference event is the same with that of the previous study of the dot-patterned sample, as illustrated in Fig. 5.4. The true thickness of the gold electrode over the GaAs substrate can be computed by $s_2 - s_1$, as shown in Fig. 5.4.

5.4.1.4 Determination of Areal Electrode Thickness

From Equation 5.4, s_1 of Fig. 5.4 can be calculated by $s_1 = \mathrm{OPL}_{\mathrm{gold}} - \mathrm{OPL}_{\mathrm{ref}} = 27\,\mathrm{nm}$. s_2 of Fig. 5.4 is the moving distance $(P_2 - P_1)$ of the bow-tie antenna between two interference events, which corresponds to the estimated thickness of the gold electrode of (52 ± 2) nm from the previous data analysis of the FF-OCT measurement. Hence the true thickness of the gold electrode can be obtained as (25 ± 2) nm.

To quantify the areal thickness of the electrode upon the GaAs substrate, the obtained surface height map covering an area of $(350 \times 350)\,\mu\mathrm{m}^2$ of the electrode and the substrate height was analysed with their height data collected separately according to Fig. 5.7. There were 9379 height data collected inside region R_1 (enclosed with yellow dashed line in Fig. 5.7), giving the areal height of the gold electrode as (25 ± 2) nm. Each height data is measured over a area of for a camera pixel in this study. Similarly, the areal height of the GaAs substrate was obtained as (0 ± 3) nm, after the averaging 24480 height data collected inside region R_2 (enclosed with cyan dashed line in Fig. 5.7). Table 5.1 lists all the areal height data of the electrodes and GaAs substrate surface.

These surface heights could further confirm the gold electrode thickness to be 26 µm on average from both linear and areal evaluations made by the simple FF-OCT system. The STD values could give an indication of the roughness of these surfaces, which may have an effect on the device performance. However, the potential for the surface roughness measurement requires further verification using a state-of-the-art instrument, such as AFM.

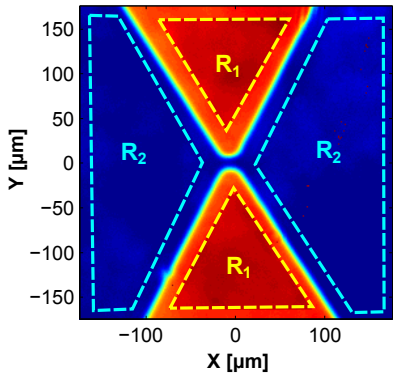

Fig. 5.7 A schematic of two regions for the collection of surface height data from the electrode and substrate.

Table 5.1 Summary of the areal height of the gold electrodes and GaAs substrate surface.

	Mean Height [nm]	STD [nm]	No. Pixels
Gold Electrodes	25	2	9379
GaAs Substrate	0	3	24480

5.4.2 Diode Rectifier

A rectifier is an electrical device (e.g. semiconductor diode) that converts alternating current (AC), which periodically reverses direction, to direct current (DC). It is often integrated with an antenna to form a rectenna, which is used for the conversion of received EM radiation (from the antenna) into a DC signal in a communication system. When considering EM waves at optical frequencies, fast response (high operating frequency) and high efficiency are desired for the direct rectification of, for example, the solar and thermal EM radiation in power harvesting devices [369].

For a diode rectifier to operate at high frequencies, it must have high conductivity; to operate efficiently, it must have a sufficiently nonlinear current-voltage characteristic [370]. Metal-insulator-metal (MIM) tunnel diodes have been potential rectifiers for use in optical frequency rectennas, as superior nonlinear characteristics can be achieved [371]. Nevertheless, the MIM diode may encounter a trade-off between nonlinearity and conductivity. A diode with two insulator layers, i.e. metal-insulator-insulator-metal (MIIM), enhances the rectification efficiency by increasing the nonlinearity of the diode characteristics [372, 373], while high conductivity may be obtained simultaneously.

To ensure the device performance, MIIM rectifiers require optimised design and fabrications. However, it is challenging for a rectifier to be fabricated to the nanometre level and have a complete impedance matching with the receiving antenna [374]. Diode rectifiers of a high frequency response are currently limited and inoperable for rectification at frequencies beyond 5 THz [375, 376]. It is hence important to monitor the fabrication process and to measure the electrode thickness of the rectifier.

5.4.2.1 MIIM Rectifier

The MIIM rectifier in this study was a test sample for the purpose of the sandwich configuration characterisation. It was fabricated on a 4 cm × 4 cm glass substrate (SiO_2). The metal aluminium (Al) was first deposited to form a bottom electrode. Then the whole surface was covered with two ultra-thin insulators: tantalum pentoxide (Ta_2O_5) and aluminium (III) oxide (Al_2O_3), with a total thickness of 9 nm by using the atomic layer deposition (ALD) technique. Eventually the metal Al was deposited to form the top electrode on the insulator surface. Fig. 5.8 shows the schematic diagram and the FF-OCT *en-face* image of the device over an area of about $(2 \times 2)\,mm^2$. As shown in Fig. 5.8 (a) and (c), the two-layer insulators are sandwiched in between two crossing Al bars of a width of about 150 µm. The MIIM diode was configured for a dielectric gating effect inside the diode.

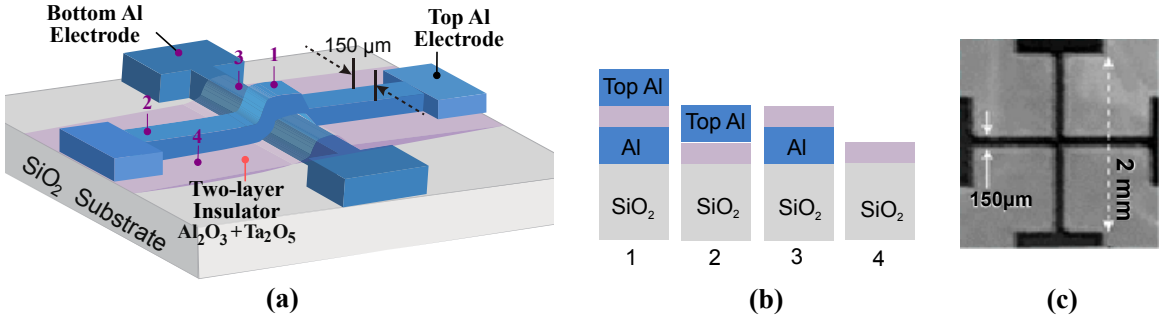

Fig. 5.8 (a) 3-D schematic diagram revealing the sandwich structure of two Al bars and insulator films, (b) side views of four different layered configurations identified by points 1 to 4 in (a), and (c) FF-OCT *en-face* image of crossing Al bars of the rectifier.

Note that there are four layered configurations of the rectifier, which are identified in Fig. 5.8 (a). These include air/Al/insulators/Al/SiO_2 at the electrode joint, air/Al/insulators/SiO_2 at the position of the top Al bar, air/insulators/Al/SiO_2 at the position of the bottom Al bar, and air/insulators/SiO_2, corresponding to the marked positions 1, 2, 3 and 4, respectively, as shown in Fig. 5.8 (b).

The rectifier was previously studied by confocal microscopy; however, the resultant 3-D representation revealed only a crossing electrodes configuration, the expected overlapping structure (Fig. 5.8 (a)) was not illustrated. In confocal microscopy, the surface height is measured by the position of focus, at which the highest intensity of the excitation light is obtained. As stated in Section 4.1.4 for the imaging of pellet coating, microscopy detects the variation of optical intensity, whereas FF-OCT detects interference events as a result of the refractive index variations, i.e. the electric field, allowing a higher sensitivity to small surface height variations. Hence, the simple FF-OCT system is used in this study to investigate the nanostructured rectifier surface. Under the NIR radiation of the simple FF-OCT system, the two ultra-thin insulator films (Al_2O_3 and Ta_2O_5) should be transparent. Their refractive indices are listed in Table 5.2, together with thickness values provided by the manufacturor. The Al electrode has a refractive index of 2.7 and an extinction coefficient of 8.27 under FF-OCT radiation. The refractive index of the silicon is 1.5.

Table 5.2 Refractive index and thickness of the two dielectric films.

Insulator	Refractive Index	Thickness
Al_2O_3	1.7529 [377]	1 nm
Ta_2O_5	2.1149 [378]	8 nm

5.4.2.2 FF-OCT Measurement

The surface topography of the MIIM rectifier was investigated by using the simple FF-OCT system. The FF-OCT measurement was carried out by focusing onto an FOV of $(600 \times 600)\,\mu m^2$ centred upon the sandwich structure of two Al bars and two insulator films. Experimental procedures similar to the previous dot-patterned and antenna samples were used with a steady movement of the sample arm under $1\,\mu m\,s^{-1}$ and a fixed rate image acquisition under 120 fps. The rectifier was scanned over a total axial distance of 18 µm with a total measurement time of less than 20 seconds. The acquired binary image file was subsequently analysed for characterisation of the nanostructured rectifier surface.

Following data analysis of the FF-OCT measurement, a surface height map of the two Al bars and the insulator of the rectifier was shown in Fig. 5.9 (a). The surface height in this figure is revealed by the colour level. A step between the top Al electrode and the insulator surface can be clearly distinguished in Fig. 5.9 (b). However, the bottom Al electrode is

shown to have almost the same electrode height as the insulator surface. There also exist surface lifts at both sides of the bottom electrode, as shown in Fig. 5.9.

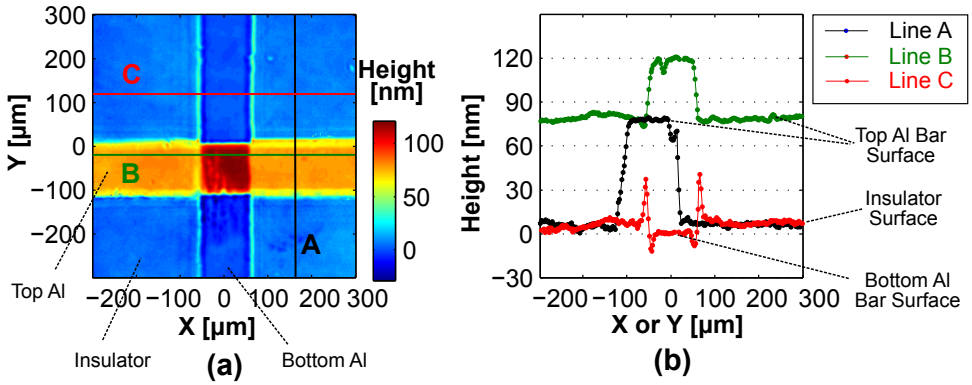

Fig. 5.9 (a) FF-OCT image of the overlapping Al electrodes of the rectifier and (b) the height profiles along lines A, B and C in (a).

As demonstrated by the height profiles in Fig. 5.9 (b), the insulator surface is about 70 nm lower than the height of the top Al electrode; and the bottom Al electrode is about 74 nm lower than the height of the top Al electrode. These values will be used in the calculation of the electrode thicknesses.

The faulty measured surface height is believed to be caused by the phase change upon reflections from the rectifier, because Al electrodes are metallic material and their reflections undergo a phase change of β (in Equation 5.1) that is different from a normal π phase change of an air/glass interface. The Al electrode contributes to most of the reflected intensity from the layered configurations at marked positions 2, 3 and 4, as shown in the 3-D schematic in Fig. 5.8 (a). These positions correspond to the bottom electrode, the top electrode and their joint on the rectifier. It is hence required to analyse the phase change at these areas in order to correct the faulty surface heights in the FF-OCT measurement. It is also noted that, there is no phase change for light propagating from the insulator Ta_2O_5 to the substrate SiO_2 in the layered configuration at marked position 1, as identified in Fig. 5.8 (a), because the refractive index of the insulator is higher than the substrate material. These factors should be considered in the analysis of phase changes taking place at surfaces and interfaces before correcting the faulty surface map.

5.4.2.3 Nanostructured Surface Characterisation

The MIIM rectifier has been mentioned as having four layered configurations, in which the top Al electrode and the joint exhibit the same phase change at the Al surface in the FF-OCT

measurement. Therefore, three cases, including configurations of air/Al, insulators/Al and insulators/SiO_2 are investigated in the following part.

Case I: Air/Al

In the FF-OCT measurement, the reference mirror surface (air/window interface) interfered with the top Al electrode (air/Al interface). While the two arms were matched, the reflection from the mirror had an additional OPL of $\frac{\lambda_0}{4}$ as a result of a π phase change at the mirror; the reflection from the Al electrode had an addition OPL of $\frac{\lambda_0}{4} \cdot \frac{\beta_1}{\pi}$, where β_1 equals to 0.93π according to Equation 5.1. The relationship of the OPLs of the reference mirror and the Al electrode can be expressed as in Equation 5.6 and illustrated in Fig. 5.10 (a):

$$\mathrm{OPL_{ref}} + \frac{\lambda_0}{4} = \mathrm{OPL_{Al}} + \frac{\lambda_0}{4} \cdot \frac{\beta_1}{\pi} \tag{5.6}$$

Hence, s_1 of Fig. 5.10 (a) is computed as 13 nm by $\frac{\lambda_0}{4} \cdot \frac{\pi - \beta_1}{\pi}$.

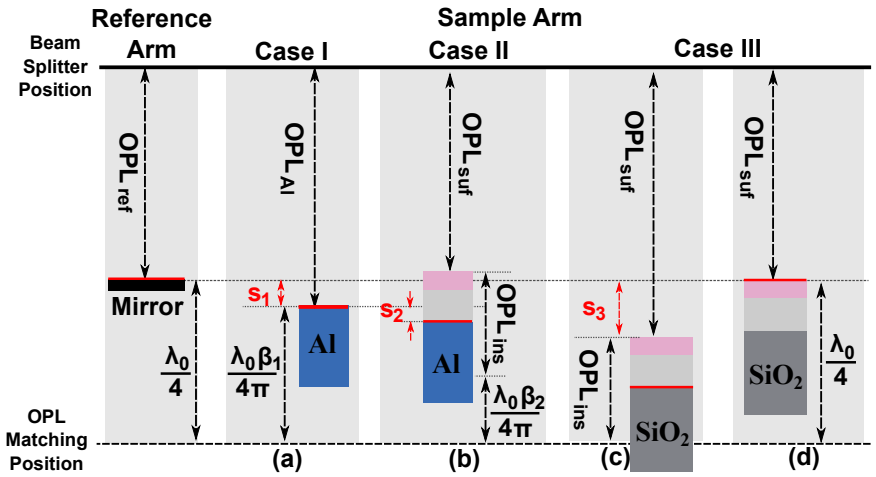

Fig. 5.10 Schematics of OPL relationships when the reference mirror was interfering with the Al surface of Case I in (a), the Ta_2O_5/Al interface of Case II in (b), the Ta_2O_5/SiO_2 interface and Al_2O_3 surface of Case III in (c) and (d).

Case II: Air/Al_2O_3/Ta_2O_5/Al

For the layer configuration of insulator films deposited upon the bottom Al, the propagation of FF-OCT light inside the configuration is illustrated in Fig. 5.11 (a). Along with the transmission of the light, reflections took place at the Al_2O_3 surface, Al_2O_3/Ta_2O_5 interface and Ta_2O_5/Al interface. The reflectance at a surface or interface is calculated

according to Equation 5.7, assuming normal incidence is regarded for all reflections and transmissions and no light was absorbed by the insulators.

$$r = \left(\frac{n_1 - n_2}{n_1 + n_2}\right)^2 \tag{5.7}$$

where n_1 and n_2 are the refractive indices of the light incident medium and the reflecting medium. The reflectance at the air/Al_2O_3, Al_2O_3/Ta_2O_5, and Ta_2O_5/Al interfaces are calculated as 7.5 %, 0.8 % and 91.8 %, respectively. The reflection from the Ta_2O_5/Al interface dominates the total reflected light. The remaining reflections represent less than 10 % of the total reflected intensity, hence they can be omitted.

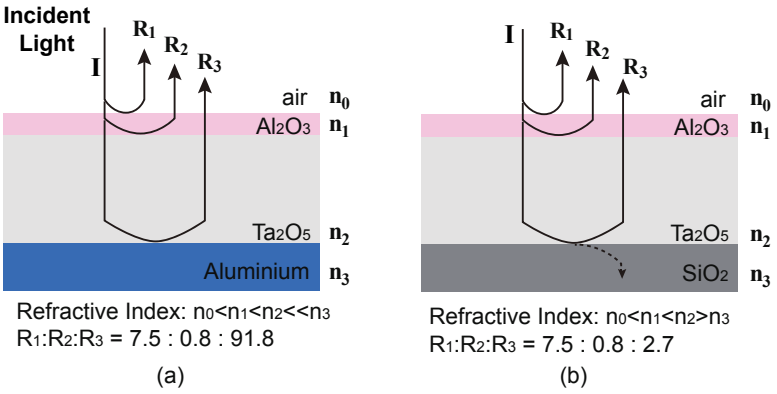

Fig. 5.11 Light transmission and reflection inside the layered configuration of Case II in (a) and Case III in (b). R_1, R_2 and R_3 represent the reflectance of corresponding surface and interfaces; n_0, n_1, n_2 and n_3 represent reflective indices of corresponding media.

The OPL for the light to travel inside the insulators OPL_{ins} can be calculated by the refractive indices and thicknesses of the two insulator films via the expression:

$$OPL_{ins} = n_{Al_2O_3} d_{Al_2O_3} + n_{Ta_2O_5} d_{Ta_2O_5} \tag{5.8}$$

OPL_{ins} is obtained as 19 nm by substituting the values supplied in Table 5.2 into Equation 5.8. The OPL of the reference mirror should be matched with that of the Ta_2O_5/Al interface at the occurrence of FF-OCT interference. The OPL relationship can be expressed in Equation 5.9 and illustrated in Fig. 5.10 (b).

$$OPL_{ref} + \frac{\lambda_0}{4} = OPL_{suf} + OPL_{ins} + \frac{\lambda_0}{4} \cdot \frac{\beta_2}{\pi} \tag{5.9}$$

where OPL_{suf} is the OPL of the air/Al_2O_3 surface; β_2 is the phase changes induced by the Ta_2O_5/Al interface and is calculated as 0.85π by applying Equation 5.1. Hence, s_2 of Fig. 5.10 (b) can be computed as 5 nm by $d_{Ta_2O_5} + d_{Al_2O_3} - OPL_{ins} + \frac{\lambda_0}{4} \cdot \frac{\beta_1 - \beta_2}{\pi}$.

Case III: Air/Al_2O_3/Ta_2O_5/SiO_2

For the layer configuration of insulator films deposited upon the substrate SiO_2, the propagation of FF-OCT light is illustrated in Fig. 5.11 (b). Along with the transmission of the light, reflections took place at the Al_2O_3 surface, Al_2O_3/Ta_2O_5 and Ta_2O_5/SiO_2 interfaces. The corresponding reflectance is calculated according to Equation 5.7 as 7.5 %, 0.8 % and 2.7 %, respectively. The reflectance of the Al_2O_3 surface is about three times that of the Ta_2O_5/SiO_2 interface. They contribute about 93 % of the total reflected intensity. Therefore the detected FF-OCT signal obtained from this layered configuration is a combination of FF-OCT signals of the Al_2O_3 surface and the Ta_2O_5/SiO_2 interface, which are separated by a small axial displacement of s_3 and have a signal intensity ratio of about 3:1. As shown in Fig. 5.10 (c), this small axial displacement is represented by s_3, i.e. the OPL variation of the Al_2O_3 surface.

In the FF-OCT measurement, the reference surface interfered twice with the Al_2O_3 surface and the Ta_2O_5/SiO_2 interface, respectively. While the two arms were matched, the relationship of the OPLs of the reference mirror, the Ta_2O_5/SiO_2 interface and the Al_2O_3 surface are expressed as in Equations 5.10 and 5.11 and illustrated in Fig. 5.10 (c) and (d).

$$OPL_{ref} + \frac{\lambda_0}{4} = OPL_{suf} + OPL_{ins}, \tag{5.10}$$

$$OPL_{ref} + \frac{\lambda_0}{4} = OPL_{suf} + \frac{\lambda_0}{4}. \tag{5.11}$$

Note that for the interference event at the Al_2O_3 surface, both reference and sample arms undergo a phase change of π with light transmitting a further OPL of $\frac{\lambda_0}{4}$; for the interference event at the Ta_2O_5/SiO_2 interface, the reference undergoes a phase change of π as normal, but there is no phase change for the reflection from the Ta_2O_5/SiO_2 interface, because the refractive index decreases along the light propagation from Ta_2O_5 to SiO_2. Hence, s_3 of Fig. 5.10 (c) is calculated as 201 nm by $\frac{\lambda_0}{4} - OPL_{ins}$.

Therefore, the Ta_2O_5/SiO_2 interface was first detected as an interference signal; after the sample arm was moved over a further distance of 201 nm, the Al_2O_3 surface was detected as a subsequent interference signal. The simple FF-OCT system only detected a single

interference signal as a result of the superposition of the two interference signals. Fig. 5.12 (a) simulates two FF-OCT interference signals, of which their maximum peaks are separated by 201 nm. The blue line represents the signal from the Al_2O_3 surface centred at a height of 0 and the red line represents the signal from the Ta_2O_5/SiO_2 interface centred at a height of 201 nm. Their maximum intensities are adjusted to have a ratio of about 7.5:2.7, which is the theoretical reflectance ratio.

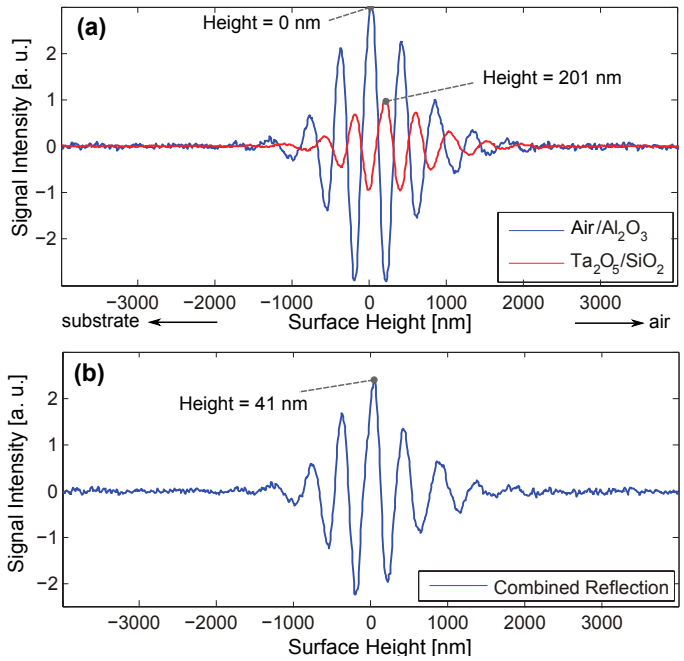

Fig. 5.12 (a) Two FF-OCT interference signals separated by 201 nm with a defined intensity ratio close to 7.5 : 2.7, and (b) the combination of the two interference signals, with a maximum peak position identified at a height of 41 nm.

The combination interference signal, as shown in Fig. 5.12 (b) has a central peak at a height of 41 nm. It means that the measured surface height of this layer configuration (insulators/SiO_2) is 41 nm higher than the actual height of the Al_2O_3 surface. In other words, the actual insulator surface is beneath the measured surface height of 41 nm.

5.4.2.4 Determination of Electrode Thickness

The measured FF-OCT map shows a faulty surface height variation, where the Al_2O_3 surface is higher than that of the bottom electrode. Based on the phase change analysis of all layered configurations, the thickness of the top electrode is obtained as 98 nm (70 nm + 41 nm - s_1), the thickness of the bottom electrode is obtained as 28 nm (70 nm + 41 nm + 9 nm - 74 nm

-s_1 - s_2). The corrected surface map clearly illustrates the sandwich structure, as shown in Fig. 5.13.

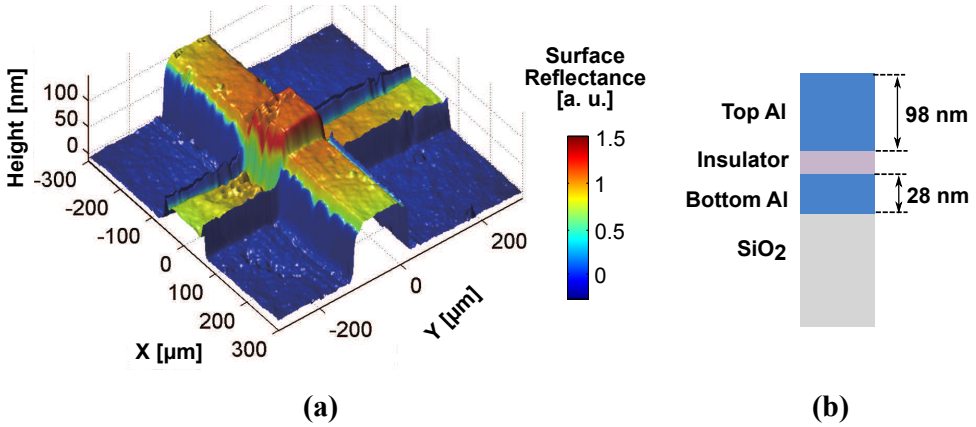

Fig. 5.13 (a) 3-D representation of the corrected rectifier surface. The facecolour represents the surface reflectance in FF-OCT measurement, and (b) cross-sectional schematic of the sandwich structure with identified electrode thickness.

5.5 Analysis of Refractive Power

Refractive surgery is any eye surgery used to correct ocular diseases, such as cataract surgery and keratoconus surgery. The most widely performed refractive surgery is LASIK, which uses excimer lasers to reshape the curvature and refractive power of the cornea in order to correct the refractive error and to improve the clarity of vision [379]. LASIK surgery involves the creation of a thin flap in the cornea, the ablation of the corneal tissue and the reposition of the flap [380].

During tissue ablation, an exact amount of corneal tissue underneath the flap is vaporised in a finely controlled manner. The ablation zone and depth are set according to the corneal thickness and pupil size of the patient [381, 382]; the ablation of corneal tissue is guided based on the nomogram customised for the patient. Developed nomograms by the surgeon during surgery planning are predictors of surgical outcomes [383]. Optimised nomograms aim at correcting not only defocus and astigmatism, but also high order aberrations, which significantly improve refractive and visual outcome [384–386].

The refractive outcome is usually studied in terms of the curvature and refractive power by using topographic techniques after laser refractive surgery. Corneal power is commonly measured by manual keratometry or simulated keratometry output from computerised corneal topography systems [387]. However, corneal power is measured on the assumption that the

corneal surface has a uniform curvature and hence power. A deviated estimation of corneal power could be caused by a limited number of data points measured on the cornea and the direct use of the empirical corneal refractive index. The keratometric equation commonly used to calculate corneal power is given by [388]:

$$P_k = \frac{n_k - n_0}{r_a}, \tag{5.12}$$

where P_k is the refractive power of the cornea expressed in dioptres (i.e. 1/metres); n_k is the keratometric refractive index usually given as 1.3375 [389], n_0 is the refractive index of air, and r_a is the radius of curvature of the anterior corneal surface in metres.

In this study, flat polymethyl-methacrylate (PMMA) surfaces were ablated with a refractive surgery (excimer) laser system. The spherical aberration produced by refractive surgery is investigated by measuring the surface curvature and refractive power of the ablated PMMA surfaces by using the simple FF-OCT system. The capability of surface characterisation of the system is explored and evaluated based on the FF-OCT measurement.

5.5.1 PMMA Models

Laser ablation was performed onto flat PMMA surfaces. On each PMMA panel, five laser refractive surgery ablations were conducted. The photo of the PMMA models ablated on the panel under test is shown in Fig. 5.14. Models A, B and E are ablated surfaces for the correction of refractive errors: myopia, astigmatism and hyperopia, respectively. Models C and D are to test optical homogeneity. Table 5.3 lists the refractive error that was intended to be corrected, the ablated zone diameter and the power of correction used in the refractive surgery ablation performed for Models A, B and E.

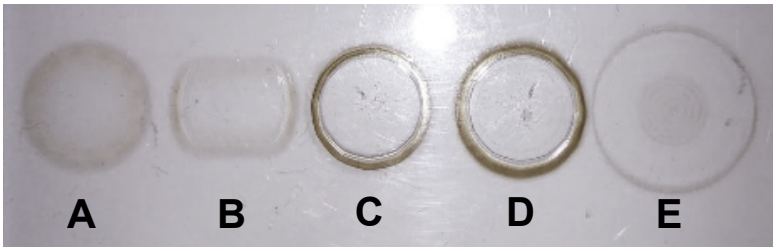

Fig. 5.14 Photo of the laser ablated PMMA models A to E (from left to right). Models A, B and E are ablated surfaces to correct myopia, astigmatism and hyperopia refractive errors, respectively; models C and D are ablated surfaces for the test of optical homogeneity.

To determine the refractive outcome of these laser-ablated PMMA surfaces for the correction of refractive error, the surface topography of Models A, B and E needs to be

Table 5.3 Description of the parameters used in each refractive surgery ablation performed for the creation of Models A, B and E on the PMMA panel. D is for dioptre; Sph stands for the correction of spherical error, e.g. myopia and hyperopia; Cyl stands for the correction of cylindrical error, e.g. astigmatism and presbyopia.

	Model A	Model B	Model E
Refractive Correction	Myopia	Astigmatism	Hyperopia
Optical Zone Diameter (mm)	6	6	9
Correction Power (D)	-4 Sph	-4 Cyl	+2 Sph

measured. The simple FF-OCT system was used for the profilometric measurements of the actual surface of Models A, B and E after laser ablation. The refractive power can be evaluated and compared to the intended power of correction of laser refractive surgery. The surface topography of Models C and D was also measured for the study of optical homogeneity.

5.5.2 Surface Characterisation by FF-OCT

5.5.2.1 FF-OCT Measurement

The surface topography of Models A, B, C, D and E was investigated by using the simple FF-OCT system. The FF-OCT measurement was carried out for Models A and B by focusing onto an FOV of $(5.7 \times 5.7)\,\mathrm{mm}^2$, which was enough to cover their optical zone. A larger FOV of $(5.7 \times 7.0)\,\mathrm{mm}^2$ was used for the measurement of Model E. Similar experimental procedures were employed for all PMMA models with a steady movement of the sample arm under $1\,\mu\mathrm{m\,s}^{-1}$ and a fixed rate image acquisition under 120 fps. The PMMA models were scanned over a total axial distance of 35 µm with a total measurement time of less than 40 seconds. The acquired binary image files of Models A, B, C, D and E were subsequently analysed for the characterisation of the laser-ablated surface.

5.5.2.2 PMMA Models for Refractive Correction

Following data analysis of the surface topography of FF-OCT measurement, the 3-D surface representation of the ablated surfaces of Models A, B and E were shown in Fig. 5.15. A spherical concave surface of Model A is shown in Fig. 5.15 (a); a spherical convex surface of Model E is shown in Fig. 5.15 (c); a cylindrical concave surface of Model B is shown in Fig.

5.15 (b). The height of a point on the surface is revealed by both the corresponding position of the axial surface height axes line and the colour level. The surface map defines the highest position with dark red and deepest position with dark blue. The ablation depths of Models A, B and E are identified by the surface maps to be approximately 30 µm, 17 µm and 17 µm, respectively.

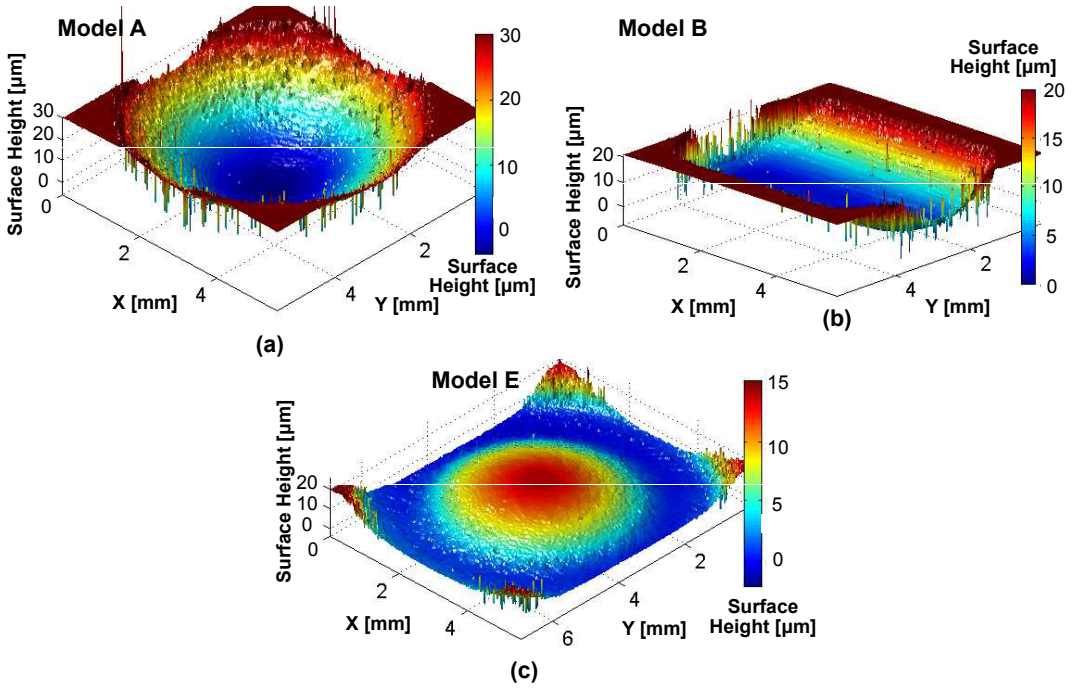

Fig. 5.15 3-D surface representation of the ablated surfaces of Model A in (a), Model E in (c) and Model B in (b).

These surface maps are found to be correlated with the purpose of refractive corrections. The ablated spherical concave surface of Model A forms a concave lens on the PMMA panel, which is commonly used for myopia correction. The spherical convex surface of Model E forms a convex lens, which is commonly used for hyperopia correction. The cylindrical concave surface of Model B forms a cylindrical concave lens, which is commonly used for astigmatism correction. Note that there are also surface errors (outliers) at some points in these surface maps, of which the surface heights have not been resolved. This could be due to the surfaces of these models after laser ablation not exhibiting a smooth surface profile under FF-OCT imaging. Moreover, the models could suffer from steeply sloped surfaces, which is one of the challenges for optical interferometric techniques to characterise surface topography and the main cause of creating artefact or errors in the surface measurement [390].

5.5.2.3 PMMA Models for Optical Homogeneity Testing

Following similar data analysis to that for Models A, B and E, the 3-D surface representation of the ablated surfaces of Models C and D are shown in Fig. 5.16. The complicated surface shapes of Models C and D could indicate the modified corneal shape after laser refractive surgery due to the high-order aberration [391], which is mathematically classified by using the Zernike polynomials for the description of specific aberration components [392, 393]. The ablation depth of Models C and D are identified by the surface maps to be approximately 7 µm and 6 µm, respectively.

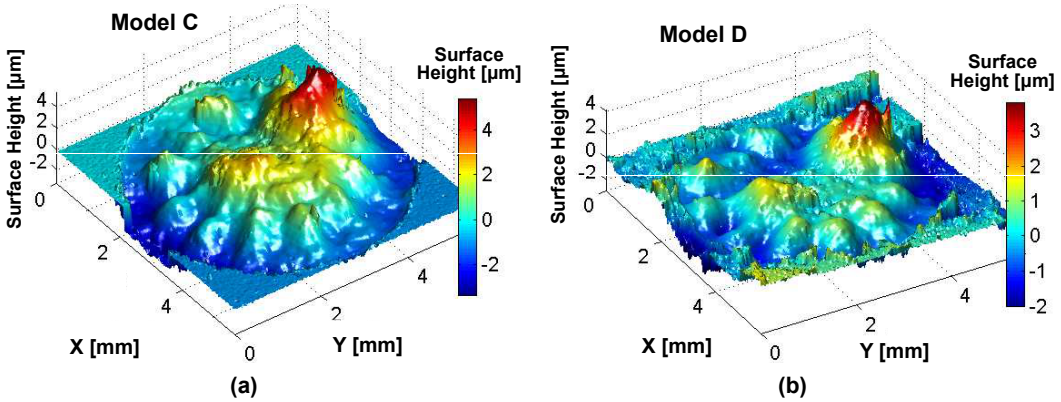

Fig. 5.16 3-D surface representation of the ablated surfaces of Model C in (a) and Model D in (b).

The peak-like surface structure could be the steep central island, which is a type of irregular astigmatism that can appear on corneal topography after laser refractive surgery. A desirable corneal surface contour after laser refractive surgery would be smooth and optically homogeneous, with a well-centred, uniform, aspheric profile [394]. The central island is clinically significant because it is known to result in optical inhomogeneity; that is, multifocality in the cornea [395]. The central islands are found to be about 3 µm in height for both models. The presence of the central island on the ablated PMMA models could give an indication of laser ablation in actual laser refractive surgery.

5.5.3 Determination of Refractive Powers

The corneal refractive power in dioptre is inversely proportional to the radius of curvature in meter, as illustrated in Equation 5.12. To evaluate the radius of curvature, some data analysis techniques were applied to the acquired surface maps of Models A, B and E in FF-OCT measurements.

5.5.3.1 Refractive Power

The surface maps of Models A, B and E all exhibit approximate spherical or cylindrical surfaces. The radius of curvature of the central meridian should resemble that of the measured surface. The surface height profile of the central meridian should also be statistically approaching a circle function, which has a fixed radius of curvature (i.e. the radius of the circle function).

A nonlinear least square circle fit algorithm was programmed and applied to the extracted central meridian surface height profiles to find their radii of the best fit circle functions. A single refractive power and radius value can be obtained for each model as an initial assessment of refractive outcomes. The measured central meridian surface height profiles of Models A, B and E and the corresponding best fit circle functions are shown in Fig. 5.17.

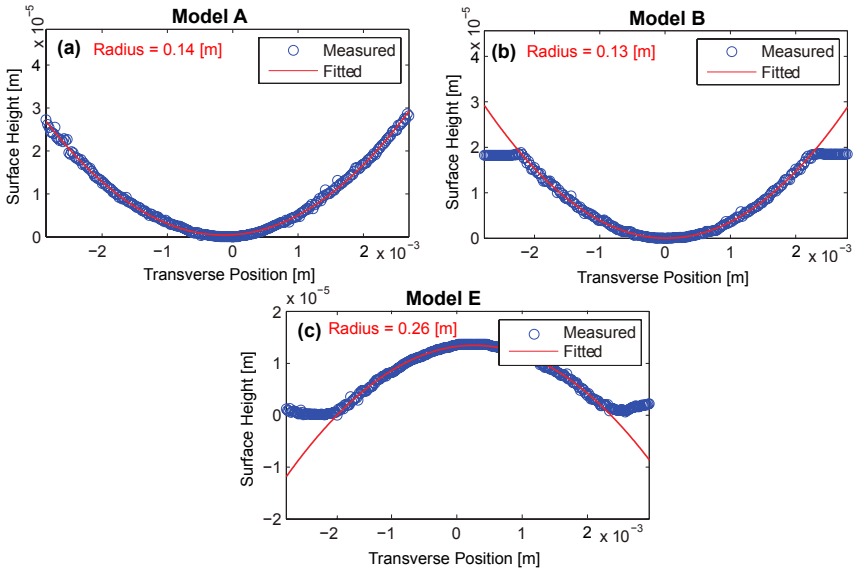

Fig. 5.17 Measured central meridian surface height profiles in blue circle markers and best fit circle functions in red lines of Model A in (a), Model E in (b) and Model B in (c). The radii of the best fit functions are labelled in red.

The best fit circles are shown to be in accordance with the shape of the measured central meridian surface profile. The radius of the best fit circles were obtained as 0.14 m, 0.13 m and 0.26 m for Models A, B and E, respectively. The refractive power can be subsequently calculated as -3.6 D, -3.9 D and 1.9 D, according to Equation 5.12, in which the obtained radius of the best fit circles are taken as the radius of curvature; the refractive index of the PMMA of 1.5 is taken as n_k and that of the air of 1.0 is taken as n_0. The sign of the refractive power depends on the refractive corrections. The obtained refractive power values of Model A, B and E are very close to that of surgery parameters listed in Table 5.3.

5.5.3.2 Areal Refractive Power

A single refractive power may not be sufficient for the evaluation of the refractive outcome of a PMMA model. In this section, the areal refractive power is studied by computing the 2-D curvature at each point of the FF-OCT measured surface map.

Prior to the calculation of the 2-D curvature, the FF-OCT surface maps of Models A, B, and E were smoothed against the height defects caused by surface artefact or errors. Here, a local regression algorithm using weighted linear least squares and a second degree polynomial model was used to eliminate any outliers and smooth out surface fluctuations.

To compute the 2-D curvature, the surface map can be expressed by:

$$z = h(x,y), \tag{5.13}$$

where the pair x, y locates a point on the surface map and z returns the surface height of the point. The curvature of a point at (x,y) can be calculated via the expression:

$$H = \frac{\left(1+h_x^2\right)h_{yy} - 2h_x h_y h_{xy} + (1+h_y^2)h_{xx}}{2(1+h_x^2+h_y^2)^2}, \tag{5.14}$$

where h_x and h_y denote the partial differentiations with respect to x and y; and h_{xx}, h_{yy}, and h_{xy} denote the second partial differentiations [396]. As the curvature H is defined as the reciprocal of the radius r_a in meter, the refractive power P_k in Equation 5.12 can be evaluated by:

$$P_k = (n_k - n_0)\cdot H, \tag{5.15}$$

To determine the refractive power of the ablated PMMA models, the refractive index of the PMMA of 1.5 is used for n_k and that of the air of 1.0 is used for n_0.

The resultant refractive power maps of Models A, B and E are shown in Fig. 5.18. The mean and STD values were quantified over the dashed line enclosed regions (of about 14 mm^2, 10 mm^2 and 8 mm^2) of the refractive power map for Models A, B and E. Both Models A and E show refractive power values (-3.6 D and 2.0 D) that are very close to the fitted ones (-3.6 D and 1.9 D) and the surgery parameters (-4 D and 2 D) listed in Table 5.3. However, the mean refractive power of -1.8 D of Model B exhibits a 50 % deviation from the fitted value (-3.9 D) and the surgery parameter (-4 D). It indicates that the laser refractive surgery might not be able to correct the astigmatism efficiently with the presence of surface irregularities. In addition, the STD values identify the variation of the refractive

power over 3 to 4 dioptres, which may require further assessment of the effect of the ablated surface roughness to the refractive outcomes.

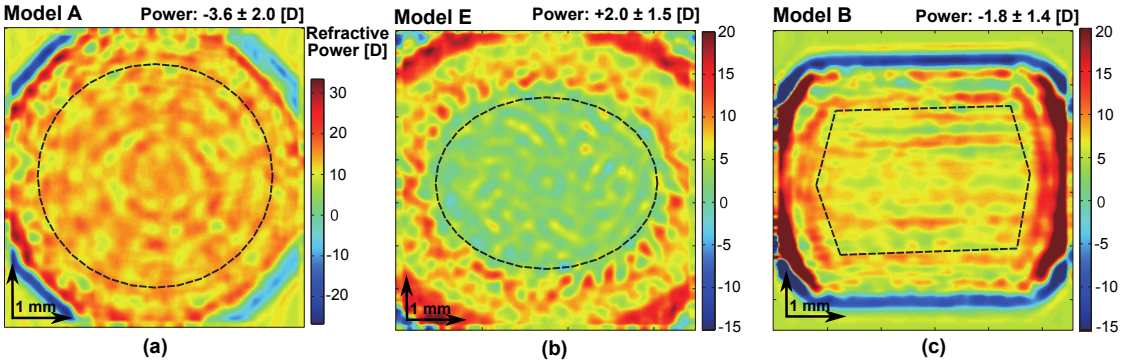

Fig. 5.18 2-D refractive power maps of Model A in (a), Model E in (b) and Model B in (c).

5.5.4 Discussion

The simple FF-OCT system has been used for the surface characterisation of the laser ablated surface and the determination of their refractive powers. Imaging has also detected uneven surface shapes, which are likely to be caused by laser ablation. The presence of the uneven surface shapes could potentially result in a refractive power variation of above 3 D, as illustrated in the refractive power maps. Although their effect on the final refractive outcome of spherical refractive errors is unknown, surface irregularities lead to inefficiency for the correction of the cylindrical refractive error. On the other hand, the central islands on the ablated surface of Models C and D show optical inhomogeneity after laser ablation. These two aspects may suggest a requirement for improvement of laser ablation.

5.6 Summary

In this chapter, the simple FF-OCT system has been validated by AFM for the use of measuring the surface topography of the nanostructured step-like surface. The FF-OCT measured thickness has a less than 10 nm deviation from the standard AFM measurement. The capability of the simple system has been first demonstrated in the determination of the electrode thickness of semiconductor microelectronics. It is shown that the step-like structure and the sandwich configuration can be investigated with the measured FF-OCT surface maps. The simple system has also been used to generate a surface map for the study of surface curvature and areal refractive power. It has been demonstrated to be effective for

the determination of refractive power, but also useful in identifying surface irregularity which might influence laser-ablation efficiency.

Chapter 6

Conclusion

OCT has been a powerful analytical technique in 3-D imaging and the characterisation of the surface topography for application in many disciplines. Technological improvements, such as scanning speed, sensitivity and resolution, have increased the use of OCT in academia and industry and boosted the development of OCT variants. FF-OCT is prevalent for its high efficiency to immediately produce high resolution tomographic images in the *en-face* orientation during measurement using a camera. It is also advantageous for its simplicity and straightforward operation. Current FF-OCT systems can perform 3-D imaging with high resolution and high sensitivity; at the same time, they demand high performance system components as well as complex measuring processes. An FF-OCT system with simplified measurement procedures is considered to be easier to implement and more efficient to promote a wide range of applications, in terms of both cost and complexity.

This thesis first described the development of a simple FF-OCT system and identified its performance attributes, then highlighted the potential of the simple system with respect to imaging and surface topography.

The simple FF-OCT system has been developed to have a simple hardware configuration and a powerful data analysis for both tomographic imaging and surface topography studies. The measurement requires only a longitudinal scan of the sample and image acquisition by the camera. The presented system is advantageous with fast measurement (taking less than two minutes for a 100 µm depth scan) and data analysis of 3-D volumetric data. Effective data processing allows for the accomplishment of a micrometre-scale spatial resolution of $(3.6 \times 10.3)\,\mu m^2$ and a good sensitivity of 74 dB for tomographic imaging, and sub-micrometre precision for surface topography with the simple FF-OCT system. The simplicity and ease of use allows the system to be easily adapted for a wide variety of applications.

The characterisation of pharmaceutical pellet coatings, corneas and automotive paints has been used as typical applications to illustrate the capability of the simple FF-OCT system in tomographic imaging.

First of all, pharmaceutical pellets of up to 1 mm in diameter with three different coating structures have been investigated by using the simple FF-OCT system. The coating layer boundaries and internal morphology features at more than 100 µm beneath the pellet surfaces have been revealed with micrometre-scale precision. Coating characteristics such as layer thickness, uniformity and porosity have been evaluated by analysing the acquired B-scan images and A-scan signals. Consistency has been found between FF-OCT and XµCT measurements, indicating the reliability and accuracy of the simple system for the spatial evaluation of the pellet structure. The presented system also demonstrates its efficiency and convenience for the imaging of such small pellets, compared to single-point OCT schemes. The high spatial resolution, the quick measurement and the low-cost attributes make the simple system an attractive tool for the evaluation of similar pharmaceutical products.

Secondly, the simple FF-OCT system has also been demonstrated as an analytical tool for the characterisation of corneal structure. Several structural features have been detected. They are likely to be the corneal front and rear surfaces, the epithelium and the Bowman's membrane, because the central corneal thickness and the front two corneal layers have been found to be in accordance with previous works. Thus the simple system has the potential to provide useful information for the prediction of corneal oedematous state and the indication of epithelial erosions. Despite this, the imaging cannot discriminate other corneal layers and could result in a measurement artefact, which may limit the imaging potential for corneal structure and the possibility for analysing corneal disorders with the simple FF-OCT system.

Thirdly, various paint films coated on identical mirror surfaces have been characterised, in order to investigate the imaging potential of the simple system for these paint materials. The measurements have shown the resolve of the surface and the subsurface structure of the basecoat and clearcoat. The system has also been demonstrated to be capable of not only measuring single-point thickness but also obtaining the areal thickness map, which has been shown to be consistent with that of profilometry results. The characterisation of these paint samples using the simple FF-OCT system have provided a stepping stone for the future study of industrial automotive paints.

The profilometry of microelectronics and the refractive PMMA models has been used as a typical application to demonstrate the capability of the simple FF-OCT system in surface topography.

The simple FF-OCT system has been first validated by AFM for the profiling of a nanostructured step-like surface, and a less than 10 nm deviation of the FF-OCT measurement has been found from the standard AFM measurement. Surface topography of semiconductor microelectronics has been subsequently measured by the simple system, revealing the step-like surface nanometre-scale structures of the photoconductive antenna and the sandwich configuration of the rectifier. The electrode thickness has been determined by analysing the optical path length and the phase change upon reflections. Furthermore, surface maps of laser ablated PMMA models have been obtained, exposing their surface shapes and possible refractive corrections. Then the refractive power (map) has been evaluated by finding the best fit circle function or computing the 2-D curvature. In addition to refractive power, the simple FF-OCT system has also been demonstrated to be useful for identifing surface irregularity which could have an effect on the efficiency of laser ablation surgery.

To sum up, the main contributions of this thesis are as follows:

1. Development of the simple FF-OCT system

    - A high spatial resolution of $(3.6 \times 10.3)\,\mu m^2$ and a good sensitivity of 74 dB have been achieved for tomographic imaging and a sub-micrometre precision has been achieved for surface topography measurement.
    - It is advantageous to have a simple configuration, a fast image acquisition speed, simple experimental operations, a low cost and ease of use, allowing it to be easily adapted for a wide range of applications.

2. Tomographic imaging using the simple FF-OCT system

    - The coating layered structure and internal morphology features of small-size pharmaceutical pellets have been characterised with micrometre-scale imaging resolution. Coating characteristics such as layer thickness, uniformity and porosity have been evaluated by analysing the acquired B-scan images and A-scan signals.
    - The corneal surfaces and the front two corneal layers have been measured in accordance with previous works. A potential for the simple FF-OCT system has been suggested for the prediction of oedematous state and epithelial erosions.
    - The surface and the subsurface of basecoat and clearcoat paint films have been measured in accordance with profilometry results. Both the single-point thickness and the areal thickness map have been obtained by analysing the FF-OCT results.

3. Surface topography using the simple FF-OCT system

    - The simple FF-OCT system has been validated to have a less than 10 nm deviation from the standard AFM measurement.
    - The electrode thickness of semiconductor microelectronics has been determined by analysing the optical path length and the phase change upon reflections.
    - The refractive power (map) has been evaluated by finding the best fit circle function or computing the 2-D curvature.

References

[1] D. Huang, E. A. Swanson, C. P. Lin, J. S. Schuman, W. G. Stinson, W. Chang, M. R. Hee, T. Flotte, K. Gregory, C. A. Puliafito, and Al Et. Optical coherence tomography. *Science*, 254(5035):1178–1181, Nov 1991.

[2] James G. Fujimoto, Costas Pitris, Stephen A. Boppart, and Mark E. Brezinski. Optical Coherence Tomography: An Emerging Technology for Biomedical Imaging and Optical Biopsy. *Neoplasia*, 2(1–2):9–25, Jan 2000.

[3] A. F. Fercher, W. Drexler, C. K. Hitzenberger, and T. Lasser. Optical coherence tomography - principles and applications. *Reports on Progress in Physics*, 66(2):239, Feb 2003.

[4] Adolf Friedrich Fercher. Optical coherence tomography - development, principles, applications. *Zeitschrift für Medizinische Physik*, 20(4):251–276, 2010.

[5] Haida Liang, Marta Cid, R. Cucu, G. Dobre, A. Podoleanu, Justin Pedro, and David Saunders. En-face optical coherence tomography - a novel application of non-invasive imaging to art conservation. *Optics Express*, 13(16):6133–6144, Aug 2005.

[6] Jakub Czajkowski, Tuukka Prykäri, Erkki Alarousu, Jaakko Palosaari, and Risto Myllylä. Optical coherence tomography as a method of quality inspection for printed electronics products. *Optical Review*, 17(3):257–262, Jun 2010.

[7] Jakob M. A. Mauritz, Richard S. Morrisby, Roger S. Hutton, Coulton H. Legge, and Clemens F. Kaminski. Imaging pharmaceutical tablets with optical coherence tomography. *Journal of Pharmaceutical Sciences*, 99(1):385–391, Jan 2010.

[8] E. Beaurepaire, A. C. Boccara, M. Lebec, L. Blanchot, and H. Saint-Jalmes. Full-field optical coherence microscopy. *Optics Letters*, 23(4):244–246, Feb 1998.

[9] R. Langer. Drug delivery and targeting. *Nature*, 392(6679 Suppl):5–10, Apr 1998.

[10] J. D. Kirsch and J. K. Drennen. Determination of film-coated tablet parameters by near-infrared spectroscopy. *Journal of Pharmaceutical and Biomedical Analysis*, 13(10):1273–1281, Sep 1995.

[11] Amar Agarwal. *Handbook of Ophthalmology*. SLACK Incorporated, Jan 2006.

[12] Hiroshi Ishikawa and Joel S. Schuman. Anterior segment imaging: ultrasound biomicroscopy. *Ophthalmology clinics of North America*, 17(1):7–20, Mar 2004.

[13] Eric S Tam and David S Rootman. Comparison of central corneal thickness measurements by specular microscopy, ultrasound pachymetry, and ultrasound biomicroscopy. *Journal of Cataract & Refractive Surgery*, 29(6):1179–1184, Jun 2003.

[14] Wolfgang Drexler, Uwe Morgner, Ravi K. Ghanta, Franz X. Kartner, Joel S. Schuman, and James G. Fujimoto. Ultrahigh-resolution ophthalmic optical coherence tomography. *Nature medicine*, 7(4):502–507, Apr 2001.

[15] R. Lambourne and T. A. Strivens. *Paint and Surface Coatings: Theory and Practice*, chapter Automotive paints, pages 411–491. Elsevier, Aug 1999.

[16] Howard J. Humecki. *Practical Guide to Infrared Microspectroscopy*, chapter Infrared microspectroscopy of forensic paint evidence, pages 163–286. CRC Press, Jan 1995.

[17] David J. Whitehouse. *Handbook of Surface Metrology*. CRC Press, Jan 1994.

[18] Sergei N. Magonov and Myung-Hwan Whangbo. *Surface Analysis with STM and AFM: Experimental and Theoretical Aspects of Image Analysis*. John Wiley & Sons, Sep 2008.

[19] Richard Leach. *Optical Measurement of Surface Topography*. Springer Science & Business Media, Mar 2011.

[20] Fred H. Albee. Studies in Bone Growth. *Annals of Surgery*, 71(1):32–39, Jan 1920.

[21] D. M. Peyce. Lower accessory pulmonary artery with intralobar sequestration of lung: A report of seven cases. *The Journal of Pathology and Bacteriology*, 58(3):457–467, Jul 1946.

[22] I. George Zubal, Charles R. Harrell, Eileen O. Smith, Zachary Rattner, Gene Gindi, and Paul B. Hoffer. Computerized three dimensional segmented human anatomy. *Medical Physics*, 21(2):299–302, Feb 1994.

[23] Douglass H. Howry, Gerald Posakony, C. Richard Cushman, and Joseph H. Holmes. Three-Dimensional and Stereoscopic Observation of Body Structures by Ultrasound. *Journal of Applied Physiology*, 9(2):304–306, Sep 1956.

[24] Jeró, nima M. A. Teixeira, Nicholas M. Fisk, and Vivette Glover. Association between maternal anxiety in pregnancy and increased uterine artery resistance index: cohort based study. *BMJ*, 318(7177):153–157, Jan 1999.

[25] Peter D. Gatehouse, Jennifer Keegan, Lindsey A. Crowe, Sharmeen Masood, Raad H. Mohiaddin, Karl-Friedrich Kreitner, and David N. Firmin. Applications of phase-contrast flow and velocity imaging in cardiovascular MRI. *European Radiology*, 15(10):2172–2184, jul 2005.

[26] A. Carrillo, J.L. Duerk, J.S. Lewin, and D.L. Wilson. Semiautomatic 3-D image registration as applied to interventional MRI liver cancer treatment. *IEEE Transactions on Medical Imaging*, 19(3):175–185, Mar 2000.

[27] Kumaresan Sandrasegaran, Arumugam Rajesh, Daniel A. Rushing, Jonas Rydberg, Fatih M. Akisik, and John D. Henley. Gastrointestinal stromal tumors: CT and MRI findings. *European Radiology*, 15(7):1407–1414, Mar 2005.

[28] Tara C. Noone, Jason Hosey, Zeynep Firat, and Richard C. Semelka. Imaging and localization of islet-cell tumours of the pancreas on CT and MRI. *Best Practice & Research Clinical Endocrinology & Metabolism*, 19(2):195–211, Jun 2005.

[29] U. Bühring, U. Herrlinger, T. Krings, R. Thiex, M. Weller, and W. Küker. MRI features of primary central nervous system lymphomas at presentation. *Neurology*, 57(3):393–396, Aug 2001.

[30] D. T. Delpy and M. Cope. Quantification in tissue near-infrared spectroscopy. *Philosophical Transactions of the Royal Society of London B: Biological Sciences*, 352(1354):649–659, Jun 1997.

[31] Ruth M. Woodward, Bryan E. Cole, Vincent P. Wallace, Richard J. Pye, Donald D. Arnone, Edmund H. Linfield, and Michael Pepper. Terahertz pulse imaging in reflection geometry of human skin cancer and skin tissue. *Physics in Medicine and Biology*, 47(21):3853, Nov 2002.

[32] J. G. Fujimoto, M. E. Brezinski, G. J. Tearney, S. A. Boppart, B. Bouma, M. R. Hee, J. F. Southern, and E. A. Swanson. Optical biopsy and imaging using optical coherence tomography. *Nature Medicine*, 1(9):970–972, Sep 1995.

[33] S. Ito, S. M. Zakeeruddin, R. Humphry-Baker, P. Liska, R. Charvet, P. Comte, M. K. Nazeeruddin, P. Péchy, M. Takata, H. Miura, S. Uchida, and M. Grätzel. High-Efficiency Organic-Dye- Sensitized Solar Cells Controlled by Nanocrystalline-TiO2 Electrode Thickness. *Advanced Materials*, 18(9):1202–1205, May 2006.

[34] D. J. Whitehouse. Surface metrology. *Measurement Science and Technology*, 8(9):955, Sep 1997.

[35] Jacob Beutel, J Michael Fitzpatrick, Steven C Horii, Yongmin Kim, Harold L Kundel, Milan Sonka, and Richard L Van Metter. *Handbook of Medical Imaging, Volume 1. Physics and Psychophysics*. SPIE, 1000 20th Street, Bellingham, WA 98227-0010 USA, Feb 2000.

[36] James B. Pawley. *Handbook of Biological Confocal Microscopy*. Springer US, Boston, MA, 3rd edition, 2006.

[37] David Boas and Maria Franceschini. Near infrared imaging. *Scholarpedia*, 4(4):6997, 2009.

[38] Yao-Chun Shen. Terahertz pulsed spectroscopy and imaging for pharmaceutical applications: A review. *International Journal of Pharmaceutics*, 417(1–2):48–60, Sep 2011.

[39] Richard Leach. Introduction to Surface Texture Measurement. In Richard Leach, editor, *Optical Measurement of Surface Topography*, pages 1–14. Springer Berlin Heidelberg, 2011.

[40] G. Binnig and H. Rohrer. Scanning Tunneling Microscopy. *IBM J. Res. Dev.*, 44(1-2):279–293, January 2000.

[41] Roger Artigas. Imaging Confocal Microscopy. In Richard Leach, editor, *Optical Measurement of Surface Topography*, pages 237–286. Springer Berlin Heidelberg, 2011.

[42] Peter de Groot. Phase Shifting Interferometry. In Richard Leach, editor, *Optical Measurement of Surface Topography*, pages 167–186. Springer Berlin Heidelberg, 2011.

[43] Paul J. Caber, Stephen J. Martinek, and Robert J. Niemann. New interferometric profiler for smooth and rough surfaces. In J. Michael Downs, editor, *Laser Dimensional Metrology: Recent Advances for Industrial Application*, volume 2088, pages 195–203, Brighton, UK, Oct 1993.

[44] H.H. Gilgen, R.P. Novàk, R.P. Salathé, W. Hodel, and P. Beaud. Submillimeter optical reflectometry. *Journal of Lightwave Technology*, 7(8):1225–1233, Aug 1989.

[45] A. F. Fercher, K. Mengedoht, and W. Werner. Eye-length measurement by interferometry with partially coherent light. *Optics Letters*, 13(3):186–188, Mar 1988.

[46] Gordon S. Kino and Stanley S. C. Chim. Mirau correlation microscope. *Applied Optics*, 29(26):3775–3783, September 1990.

[47] Mark E. Brezinski, Guillermo J. Tearney, Brett E. Bouma, Joseph A. Izatt, Michael R. Hee, Eric A. Swanson, James F. Southern, and James G. Fujimoto. Optical Coherence Tomography for Optical Biopsy Properties and Demonstration of Vascular Pathology. *Circulation*, 93(6):1206–1213, Mar 1996.

[48] F. Lexer, C. K. Hitzenberger, W. Drexler, S. Molebny, H. Sattmann, M. Sticker, and A. F. Fercher. Dynamic coherent focus OCT with depth-independent transversal resolution. *Journal of Modern Optics*, 46(3):541–553, Mar 1999.

[49] W. Drexler, U. Morgner, F. X. Kärtner, C. Pitris, S. A. Boppart, X. D. Li, E. P. Ippen, and J. G. Fujimoto. In vivo ultrahigh-resolution optical coherence tomography. *Optics Letters*, 24(17):1221–1223, Sep 1999.

[50] A. F. Fercher, C. K. Hitzenberger, G. Kamp, and S. Y. El-Zaiat. Measurement of intraocular distances by backscattering spectral interferometry. *Optics Communications*, 117(1–2):43–48, May 1995.

[51] S. R. Chinn, E. A. Swanson, and J. G. Fujimoto. Optical coherence tomography using a frequency-tunable optical source. *Optics Letters*, 22(5):340–342, Mar 1997.

[52] U. H. P. Haberland, V. Blazek, and H. J. Schmitt. Chirp Optical Coherence Tomography of Layered Scattering Media. *Journal of Biomedical Optics*, 3(3):259–266, 1998.

[53] Gerd Häusler and Michael Walter Lindner. "Coherence Radar" and "Spectral Radar" – New Tools for Dermatological Diagnosis. *Journal of Biomedical Optics*, 3(1):21–31, 1998.

[54] Adolf F. Fercher. Optical coherence tomography. *Journal of Biomedical Optics*, 1(2):157–173, 1996.

[55] Andrés F. Zuluaga and Rebecca Richards-Kortum. Spatially resolved spectral interferometry for determination of subsurface structure. *Optics Letters*, 24(8):519–521, Apr 1999.

[56] Maciej Wojtkowski, Rainer Leitgeb, Andrzej Kowalczyk, Tomasz Bajraszewski, and Adolf F. Fercher. In vivo human retinal imaging by Fourier domain optical coherence tomography. *Journal of Biomedical Optics*, 7(3):457–463, 2002.

[57] R. Leitgeb, W. Drexler, A. Unterhuber, B. Hermann, T. Bajraszewski, T. Le, A. Stingl, and A. Fercher. Ultrahigh resolution Fourier domain optical coherence tomography. *Optics Express*, 12(10):2156–2165, May 2004.

[58] S. Yun, G. Tearney, Johannes de Boer, N. Iftimia, and B. Bouma. High-speed optical frequency-domain imaging. *Optics Express*, 11(22):2953–2963, Nov 2003.

[59] Nader Nassif, Barry Cense, B. Hyle Park, Seok H. Yun, Teresa C. Chen, Brett E. Bouma, Guillermo J. Tearney, and Johannes F. de Boer. In vivo human retinal imaging by ultrahigh-speed spectral domain optical coherence tomography. *Optics Letters*, 29(5):480–482, Mar 2004.

[60] Michael Choma, Marinko Sarunic, Changhuei Yang, and Joseph Izatt. Sensitivity advantage of swept source and Fourier domain optical coherence tomography. *Optics Express*, 11(18):2183–2189, Sep 2003.

[61] Arnaud Dubois, Laurent Vabre, Albert-Claude Boccara, and Emmanuel Beaurepaire. High-resolution full-field optical coherence tomography with a linnik microscope. *Applied Optics*, 41(4):805–812, Feb 2002.

[62] Arnaud Dubois. Effects of phase change on reflection in phase-measuring interference microscopy. *Applied Optics*, 43(7):1503–1507, Mar 2004.

[63] A. Dubois, G. Moneron, K. Grieve, and A. C. Boccara. Three-dimensional cellular-level imaging using full-field optical coherence tomography. *Physics in Medicine and Biology*, 49(7):1227, Apr 2004.

[64] Arnaud Dubois, Kate Grieve, Gael Moneron, Romain Lecaque, Laurent Vabre, and Claude Boccara. Ultrahigh-resolution full-field optical coherence tomography. *Applied Optics*, 43(14):2874–2883, May 2004.

[65] L. Vabre, A. Dubois, and A. C. Boccara. Thermal-light full-field optical coherence tomography. *Optics Letters*, 27(7):530–532, Apr 2002.

[66] A. Dubois and A. C. Boccara. Full-field optical coherence tomography. In Professor Dr Wolfgang Drexler and Professor Dr James G. Fujimoto, editors, *Optical Coherence Tomography*, Biological and Medical Physics, Biomedical Engineering, pages 565–591. Springer Berlin Heidelberg, Jan 2008.

[67] E. A. Swanson, J. A. Izatt, C. P. Lin, J. G. Fujimoto, J. S. Schuman, M. R. Hee, D. Huang, and C. A. Puliafito. In vivo retinal imaging by optical coherence tomography. *Optics Letters*, 18(21):1864–1866, Nov 1993.

[68] Adolf F. Fercher, Christoph K. Hitzenberger, Wolfgang Drexler, Gerhard Kamp, and Harald Sattmann. In Vivo Optical Coherence Tomography. *American Journal of Ophthalmology*, 116(1):113–114, Jul 1993.

[69] A. F. Fercher and C. K. Hitzenberger. Chapter 4 optical coherence tomography. In E. Wolf, editor, *Progress in Optics*, volume 44, pages 215–302. Elsevier, 2002.

[70] M. R. Hee, J. A. Izatt, E. A. Swanson, D. Huang, J. S. Schuman, C. P. Lin, C. A. Puliafito, and J. G. Fujimoto. Optical coherence tomography of the human retina. *Archives of Ophthalmology*, 113(3):325–332, Mar 1995.

[71] Michael R. Hee, Caroline R. Baumal, Carmen A. Puliafito, Jay S. Duker, Elias Reichel, Jason R. Wilkins, Jeffery G. Coker, Joel S. Schuman, Eric A. Swanson, and James G. Fujimoto. Optical Coherence Tomography of Age-related Macular Degeneration and Choroidal Neovascularization. *Ophthalmology*, 103(8):1260–1270, Aug 1996.

[72] Wolfgang Drexler, Harald Sattmann, Boris Hermann, Tony H. Ko, Michael Stur, Angelika Unterhuber, Christoph Scholda, Oliver Findl, Matthias Wirtitsch, James G. Fujimoto, and Adolf F. Fercher. Enhanced visualization of macular pathology with the use of ultrahigh-resolution optical coherence tomography. *Archives of Ophthalmology*, 121(5):695–706, May 2003.

[73] Philip J. Rosenfeld, Andrew A. Moshfeghi, and Carmen A. Puliafito. Optical coherence tomography findings after an intravitreal injection of bevacizumab (avastin) for neovascular age-related macular degeneration. *Ophthalmic Surgery, Lasers & Imaging: The Official Journal of the International Society for Imaging in the Eye*, 36(4):331–335, Aug 2005.

[74] Anne E. Fung, Geeta A. Lalwani, Philip J. Rosenfeld, Sander R. Dubovy, Stephan Michels, William J. Feuer, Carmen A. Puliafito, Janet L. Davis, Harry W. Flynn Jr, and Maria Esquiabro. An Optical Coherence Tomography-Guided, Variable Dosing Regimen with Intravitreal Ranibizumab (Lucentis) for Neovascular Age-related Macular Degeneration. *American Journal of Ophthalmology*, 143(4):566–583.e2, Apr 2007.

[75] M. R. Hee, C. A. Puliafito, C. Wong, J. S. Duker, E. Reichel, B. Rutledge, J. S. Schuman, E. A. Swanson, and J. G. Fujimoto. Quantitative assessment of macular edema with optical coherence tomography. *Archives of Ophthalmology*, 113(8):1019–1029, Aug 1995.

[76] Carmen A. Puliafito, Michael R. Hee, Charles P. Lin, Elias Reichel, Joel S. Schuman, Jay S. Duker, Joseph A. Izatt, Eric A. Swanson, and James G. Fujimoto. Imaging of Macular Diseases with Optical Coherence Tomography. *Ophthalmology*, 102(2):217–229, Feb 1995.

[77] Michael R. Hee, Carmen A. Puliafito, Jay S. Duker, Elias Reichel, Jeffrey G. Coker, Jason R. Wilkins, Joel S. Schuman, Eric A. Swanson, and James G. Fujimoto. Topography of diabetic macular edema with optical coherence tomography. *Ophthalmology*, 105(2):360–370, Feb 1998.

[78] Tomohiro Otani, Shoji Kishi, and Yasuhiro Maruyama. Patterns of diabetic macular edema with optical coherence tomography. *American Journal of Ophthalmology*, 127(6):688–693, Jun 1999.

[79] Philip J. Rosenfeld, Anne E. Fung, and Carmen A. Puliafito. Optical coherence tomography findings after an intravitreal injection of bevacizumab (avastin) for macular edema from central retinal vein occlusion. *Ophthalmic Surgery, Lasers & Imaging: The Official Journal of the International Society for Imaging in the Eye*, 36(4):336–339, Aug 2005.

[80] J. S. Schuman, M. R. Hee, C. A. Puliafito, C. Wong, T. Pedut-Kloizman, C. P. Lin, E. Hertzmark, J. A. Izatt, E. A. Swanson, and J. G. Fujimoto. Quantification of nerve fiber layer thickness in normal and glaucomatous eyes using optical coherence tomography. *Archives of Ophthalmology*, 113(5):586–596, May 1995.

[81] J. S. Schuman, T. Pedut-Kloizman, E. Hertzmark, M. R. Hee, J. R. Wilkins, J. G. Coker, C. A. Puliafito, J. G. Fujimoto, and E. A. Swanson. Reproducibility of nerve fiber layer thickness measurements using optical coherence tomography. *Ophthalmology*, 103(11):1889–1898, Nov 1996.

[82] Viviane Guedes, Joel S Schuman, Ellen Hertzmark, Gadi Wollstein, Anthony Correnti, Ronald Mancini, David Lederer, Serineh Voskanian, Leonardo Velazquez, Helena M Pakter, Tamar Pedut-Kloizman, James G Fujimoto, and Cynthia Mattox. Optical coherence tomography measurement of macular and nerve fiber layer thickness in normal and glaucomatous human eyes. *Ophthalmology*, 110(1):177–189, Jan 2003.

[83] Felipe A. Medeiros, Linda M. Zangwill, Christopher Bowd, Roberto M. Vessani, Remo Susanna Jr, and Robert N. Weinreb. Evaluation of retinal nerve fiber layer, optic nerve head, and macular thickness measurements for glaucoma detection using optical coherence tomography. *American Journal of Ophthalmology*, 139(1):44–55, Jan 2005.

[84] Ou Tan, Vikas Chopra, Ake Tzu-Hui Lu, Joel S. Schuman, Hiroshi Ishikawa, Gadi Wollstein, Rohit Varma, and David Huang. Detection of Macular Ganglion Cell Loss in Glaucoma by Fourier-Domain Optical Coherence Tomography. *Ophthalmology*, 116(12):2305–2314.e2, Dec 2009.

[85] Angelika Unterhuber, B. Povazay, B. Hermann, H. Sattmann, A. Chavez-Pirson, and W. Drexler. In vivo retinal optical coherence tomography at 1040 nm - enhanced penetration into the choroid. *Optics Express*, 13(9):3252–3258, May 2005.

[86] Wolfgang Drexler and James G. Fujimoto. State-of-the-art retinal optical coherence tomography. *Progress in Retinal and Eye Research*, 27(1):45–88, Jan 2008.

[87] Richard F. Spaide, Hideki Koizumi, and Maria C. Pozonni. Enhanced Depth Imaging Spectral-Domain Optical Coherence Tomography. *American Journal of Ophthalmology*, 146(4):496–500, Oct 2008.

[88] Ron Margolis and Richard F. Spaide. A Pilot Study of Enhanced Depth Imaging Optical Coherence Tomography of the Choroid in Normal Eyes. *American Journal of Ophthalmology*, 147(5):811–815, May 2009.

[89] Varsha Manjunath, Mohammad Taha, James G. Fujimoto, and Jay S. Duker. Choroidal Thickness in Normal Eyes Measured Using Cirrus HD Optical Coherence Tomography. *American Journal of Ophthalmology*, 150(3):325–329.e1, Sep 2010.

[90] Colin S. Tan, Yanling Ouyang, Humberto Ruiz, and SriniVas R. Sadda. Diurnal Variation of Choroidal Thickness in Normal, Healthy Subjects Measured by Spectral Domain Optical Coherence Tomography. *Investigative Ophthalmology & Visual Science*, 53(1):261–266, Jan 2012.

[91] J. A. Izatt, M. R. Hee, E. A. Swanson, C. P. Lin, D. Huang, J. S. Schuman, C. A. Puliafito, and J. G. Fujimoto. Micrometer-scale resolution imaging of the anterior eye in vivo with optical coherence tomography. *Archives of Ophthalmology*, 112(12):1584–1589, Dec 1994.

[92] S. Radhakrishnan, A. M. Rollins, J. E. Roth, S. Yazdanfar, V. Westphal, D. S. Bardenstein, and J. A. Izatt. Real-time optical coherence tomography of the anterior segment at 1310 nm. *Archives of Ophthalmology*, 119(8):1179–1185, Aug 2001.

[93] Sunita Radhakrishnan, Jason Goldsmith, David Huang, Volker Westphal, David K. Dueker, Andrew M. Rollins, Joseph A. Izatt, and Scott D. Smith. Comparison of optical coherence tomography and ultrasound biomicroscopy for detection of narrow anterior chamber angles. *Archives of Ophthalmology*, 123(8):1053–1059, Aug 2005.

[94] Tanuj Dada, Ramanjit Sihota, Ritu Gadia, Anand Aggarwal, Subrata Mandal, and Viney Gupta. Comparison of anterior segment optical coherence tomography and ultrasound biomicroscopy for assessment of the anterior segment. *Journal of Cataract & Refractive Surgery*, 33(5):837–840, May 2007.

[95] Sergey N. Bagayev, Valentin M. Gelikonov, Grigory V. Gelikonov, Evgeny S. Kargapoltsev, Roman V. Kuranov, Alexander M. Razhev, Ilya V. Turchin, and Andrey A. Zhupikov. Optical coherence tomography for in situ monitoring of laser corneal ablation. *Journal of Biomedical Optics*, 7(4):633–642, 2002.

[96] Christopher Wirbelauer and Duy Thoai Pham. Monitoring corneal structures with slitlamp-adapted optical coherence tomography in laser in situ keratomileusis. *Journal of Cataract & Refractive Surgery*, 30(9):1851–1860, Sep 2004.

[97] Daniel V. Palanker, Mark S. Blumenkranz, Dan Andersen, Michael Wiltberger, George Marcellino, Phillip Gooding, David Angeley, Georg Schuele, Bruce Woodley, Michael Simoneau, Neil J. Friedman, Barry Seibel, Juan Batlle, Rafael Feliz, Jonathan Talamo, and William Culbertson. Femtosecond laser-assisted cataract surgery with integrated optical coherence tomography. *Science Translational Medicine*, 2(58):58ra85, Nov 2010.

[98] G. J. Tearney, I.-K. Jang, and B. E. Bouma. Imaging Coronary Atherosclerosis and Vulnerable Plaques with Optical Coherence Tomography. In Professor Dr Wolfgang Drexler and Professor Dr James G. Fujimoto, editors, *Optical Coherence Tomography*,

Biological and Medical Physics, Biomedical Engineering, pages 1083–1101. Springer Berlin Heidelberg, 2008.

[99] Ik-Kyung Jang, Brett E. Bouma, Dong-Heon Kang, Seung-Jung Park, Seong-Wook Park, Ki-Bae Seung, Kyu-Bo Choi, Milen Shishkov, Kelly Schlendorf, Eugene Pomerantsev, Stuart L. Houser, H. Thomas Aretz, and Guillermo J. Tearney. Visualization of coronary atherosclerotic plaques in patients using optical coherence tomography: comparison with intravascular ultrasound. *Journal of the American College of Cardiology*, 39(4):604–609, Feb 2002.

[100] Hiroshi Yabushita, Brett E. Bouma, Stuart L. Houser, H. Thomas Aretz, Ik-Kyung Jang, Kelly H. Schlendorf, Christopher R. Kauffman, Milen Shishkov, Dong-Heon Kang, Elkan F. Halpern, and Guillermo J. Tearney. Characterization of human atherosclerosis by optical coherence tomography. *Circulation*, 106(13):1640–1645, Sep 2002.

[101] Guillermo J. Tearney, Hiroshi Yabushita, Stuart L. Houser, H. Thomas Aretz, Ik-Kyung Jang, Kelly H. Schlendorf, Christopher R. Kauffman, Milen Shishkov, Elkan F. Halpern, and Brett E. Bouma. Quantification of Macrophage Content in Atherosclerotic Plaques by Optical Coherence Tomography. *Circulation*, 107(1):113–119, Jan 2003.

[102] Francesco Prati, Evelyn Regar, Gary S. Mintz, Eloisa Arbustini, Carlo Di Mario, Ik-Kyung Jang, Takashi Akasaka, Marco Costa, Giulio Guagliumi, Eberhard Grube, Yukio Ozaki, Fausto Pinto, Patrick W. J. Serruys, and for the Expert's OCT Review Document. Expert review document on methodology, terminology, and clinical applications of optical coherence tomography: physical principles, methodology of image acquisition, and clinical application for assessment of coronary arteries and atherosclerosis. *European Heart Journal*, 31(4):401–415, Feb 2010.

[103] Takashi Kubo, Toshio Imanishi, Shigeho Takarada, Akio Kuroi, Satoshi Ueno, Takashi Yamano, Takashi Tanimoto, Yoshiki Matsuo, Takashi Masho, Hironori Kitabata, Kazushi Tsuda, Yoshiaki Tomobuchi, and Takashi Akasaka. Assessment of culprit lesion morphology in acute myocardial infarction: ability of optical coherence tomography compared with intravascular ultrasound and coronary angioscopy. *Journal of the American College of Cardiology*, 50(10):933–939, Sep 2007.

[104] Ik-Kyung Jang, Guillermo J. Tearney, Briain MacNeill, Masamichi Takano, Fabian Moselewski, Nicusor Iftima, Milen Shishkov, Stuart Houser, H. Thomas Aretz, Elkan F. Halpern, and Brett E. Bouma. In Vivo Characterization of Coronary Atherosclerotic Plaque by Use of Optical Coherence Tomography. *Circulation*, 111(12):1551–1555, Mar 2005.

[105] M. E. Brezinski, G. J. Tearney, N. J. Weissman, S. A. Boppart, B. E. Bouma, M. R. Hee, A. E. Weyman, E. A. Swanson, J. F. Southern, and J. G. Fujimoto. Assessing atherosclerotic plaque morphology: comparison of optical coherence tomography and high frequency intravascular ultrasound. *Heart*, 77(5):397–403, May 1997.

[106] Parth Patwari, Neil J Weissman, Stephen A Boppart, Christine Jesser, Debra Stamper, James G Fujimoto, and Mark E Brezinski. Assessment of coronary plaque with optical coherence tomography and high-frequency ultrasound. *The American Journal of Cardiology*, 85(5):641–644, Mar 2000.

[107] Nirlep A. Patel, Debra L. Stamper, and Mark E. Brezinski. Review of the Ability of Optical Coherence Tomography to Characterize Plaque, Including a Comparison with Intravascular Ultrasound. *CardioVascular and Interventional Radiology*, 28(1):1–9, Oct 2004.

[108] Tearney Gj, Brezinski Me, Southern Jf, Bouma Be, Boppart Sa, and Fujimoto Jg. Optical biopsy in human gastrointestinal tissue using optical coherence tomography. *The American journal of gastroenterology*, 92(10):1800–1804, Oct 1997.

[109] Michael V. Sivak Jr., Kenji Kobayashi, Joseph A. Izatt, Andrew M. Rollins, R. Ungrunyawee, Amitabh Chak, Richard C. K. Wong, Gerard A. Isenberg, and Joseph Willis. High-resolution endoscopic imaging of the GI tract using optical coherence tomography. *Gastrointestinal Endoscopy*, 51(4, Part 1):474–479, Apr 2000.

[110] Patrick R. Pfau, Michael V. Sivak Jr., Amitabh Chak, Margaret Kinnard, Richard C. K. Wong, Gerard A. Isenberg, Joseph A. Izatt, Andrew Rollins, and Volker Westphal. Criteria for the diagnosis of dysplasia by endoscopic optical coherence tomography. *Gastrointestinal Endoscopy*, 58(2):196–202, Aug 2003.

[111] Gerard Isenberg, Michael V. Sivak Jr., Amitabh Chak, Richard C. K. Wong, Joseph E. Willis, Brian Wolf, Douglas Y. Rowland, Ananya Das, and Andrew Rollins. Accuracy of endoscopic optical coherence tomography in the detection of dysplasia in Barrett's esophagus: a prospective, double-blinded study. *Gastrointestinal Endoscopy*, 62(6):825–831, Dec 2005.

[112] John A. Evans, John M. Poneros, Brett E. Bouma, Jason Bressner, Elkan F. Halpern, Milen Shishkov, Gregory Y. Lauwers, Mari Mino– Kenudson, Norman S. Nishioka, and Guillermo J. Tearney. Optical Coherence Tomography to Identify Intramucosal Carcinoma and High-Grade Dysplasia in Barrett's Esophagus. *Clinical Gastroenterology and Hepatology*, 4(1):38–43, Jan 2006.

[113] Pier Alberto Testoni and Benedetto Mangiavillano. Optical coherence tomography in detection of dysplasia and cancer of the gastrointestinal tract and bilio-pancreatic ductal system. *World Journal of Gastroenterology : WJG*, 14(42):6444–6452, Nov 2008.

[114] Petra Wilder-Smith, Kenneth Lee, Shuguang Guo, Jun Zhang, Kathryn Osann, Zhongping Chen, and Diana Messadi. In vivo diagnosis of oral dysplasia and malignancy using optical coherence tomography: Preliminary studies in 50 patients. *Lasers in Surgery and Medicine*, 41(5):353–357, Jul 2009.

[115] John M. Poneros, Stephan Brand, Brett E. Bouma, Guillermo J. Tearney, Carolyn C. Compton, and Norman S. Nishioka. Diagnosis of specialized intestinal metaplasia by optical coherence tomography. *Gastroenterology*, 120(1):7–12, Jan 2001.

[116] John A. Evans, Brett E. Bouma, Jason Bressner, Milen Shishkov, Gregory Y. Lauwers, Mari Mino-Kenudson, Norman S. Nishioka, and Guillermo J. Tearney. Identifying intestinal metaplasia at the squamocolumnar junction by using optical coherence tomography. *Gastrointestinal Endoscopy*, 65(1):50–56, Jan 2007.

[117] S. Jäckle, N. Gladkova, F. Feldchtein, A. Terentieva, B. Brand, G. Gelikonov, V. Gelikonov, A. Sergeev, A. Fritscher-Ravens, J. Freund, U. Seitz, S. Schröder, and N. Soehendra. In vivo endoscopic optical coherence tomography of esophagitis, Barrett's esophagus, and adenocarcinoma of the esophagus. *Endoscopy*, 32(10):750–755, Oct 2000.

[118] G Zuccaro, N Gladkova, J Vargo, F Feldchtein, E Zagaynova, D Conwell, G Falk, J Goldblum, J Dumot, J Ponsky, G Gelikonov, B Davros, E Donchenko, and J Richter. Optical coherence tomography of the esophagus and proximal stomach in health and disease. *The American Journal of Gastroenterology*, 96(9):2633–2639, Sep 2001.

[119] Costas Pitris, Christine Jesser, Stephen A. Boppart, Debra Stamper, Mark E. Brezinski, and James G. Fujimoto. Feasibility of optical coherence tomography for high-resolution imaging of human gastrointestinal tract malignancies. *Journal of Gastroenterology*, 35(2):87–92, Feb 2000.

[120] Petra Wilder-Smith, Woong-Gyu Jung, Matthew Brenner, Kathryn Osann, Hamza Beydoun, Diana Messadi, and Zhongping Chen. In vivo optical coherence tomography for the diagnosis of oral malignancy. *Lasers in Surgery and Medicine*, 35(4):269–275, Oct 2004.

[121] Ananya Das, Michael V. Sivak Jr., Amitabh Chak, Richard C. K. Wong, Volker Westphal, Andrew M. Rollins, Joseph Willis, Gerard Isenberg, and Joseph A. Izatt. High-resolution endoscopic imaging of the GI tract: A comparative study of optical coherence tomography versus high-frequency catheter probe EUS. *Gastrointestinal Endoscopy*, 54(2):219–224, Aug 2001.

[122] Brett E. Bouma and Guillermo J. Tearney. *Handbook of Optical Coherence Tomography*. CRC Press, Nov 2001.

[123] Mark E. Brezinski. *Optical Coherence Tomography: Principles and Applications*. Academic Press, Aug 2006.

[124] Wolfgang Drexler and James G. Fujimoto, editors. *Optical Coherence Tomography*. Springer Berlin Heidelberg, 2008.

[125] Guillermo J. Tearney, Mark E. Brezinski, Brett E. Bouma, Stephen A. Boppart, Costas Pitris, James F. Southern, and James G. Fujimoto. In Vivo Endoscopic Optical Biopsy with Optical Coherence Tomography. *Science*, 276(5321):2037–2039, Jun 1997.

[126] THOMAS D. WANG and JACQUES VAN DAM. Optical Biopsy: A New Frontier in Endoscopic Detection and Diagnosis. *Clinical gastroenterology and hepatology : the official clinical practice journal of the American Gastroenterological Association*, 2(9):744–753, Sep 2004.

[127] Alexandra Nemeth, Gunther Hannesschlager, Elisabeth Leiss, Karin Wiesauer, and Michael Leitner. Optical Coherence Tomography –Applications in Non –Destructive Testing and Evaluation. In Masanori Kawasaki, editor, *Optical Coherence Tomography*. InTech, Mar 2013.

[128] D. Stifter. Beyond biomedicine: a review of alternative applications and developments for optical coherence tomography. *Applied Physics B*, 88(3):337–357, Aug 2007.

[129] Piotr Targowski, Michalina Góra, and Maciej Wojtkowski. Optical Coherence Tomography for Artwork Diagnostics. *Laser Chemistry*, 2006:1–11, 2006.

[130] Bogumiła J. Rouba, Paweł Karaszkiewicz, Ludmiła Tymińska-widmer, Michalina Góra, Ewa Kwiatkowska, and Piotr Targowski. Optical Coherence Tomography for Non-Destructive Investigations of Structure of Objects of Art. In *9th International Conference on NDT of Art*, Jerusalem, Israel, May 2008.

[131] A. Hannesschläger, G.and Nemeth, C. Hofer, C. Goetzloff, J. Reussner, K. Wiesauer, and M. Leitner. Optical coherence tomography as a tool for non destructive quality control of multi-layered foils. In *6th NDT in Progress 2011, International Workshop of NDT Experts*, Prag, September 2011.

[132] Shuncong Zhong, Yao-Chun Shen, Louise Ho, Robert K. May, J. Axel Zeitler, Mike Evans, Philip F. Taday, Michael Pepper, Thomas Rades, Keith C. Gordon, Ronny Müller, and Peter Kleinebudde. Non-destructive quantification of pharmaceutical tablet coatings using terahertz pulsed imaging and optical coherence tomography. *Optics and Lasers in Engineering*, 49(3):361–365, Mar 2011.

[133] D. M. Koller, G. Hannesschläger, M. Leitner, and J. G. Khinast. Non-destructive analysis of tablet coatings with optical coherence tomography. *European Journal of Pharmaceutical Sciences*, 44(1–2):142–148, Sep 2011.

[134] Erkki Alarousu, Leszek Krehut, Tuukka Prykäri, and Risto Myllylä. Study on the use of optical coherence tomography in measurements of paper properties. *Measurement Science and Technology*, 16(5):1131, May 2005.

[135] Tuukka Prykäri, Jakub Czajkowski, Erkki Alarousu, and Risto Myllylä. Optical coherence tomography as an accurate inspection and quality evaluation technique in paper industry. *Optical Review*, 17(3):218–222, Jun 2010.

[136] Paul J. L. Webster, Joe X. Z. Yu, Ben Y. C. Leung, Mitchell D. Anderson, Victor X. D. Yang, and James M. Fraser. In situ 24 kHz coherent imaging of morphology change in laser percussion drilling. *Optics Letters*, 35(5):646–648, Mar 2010.

[137] Lars Thrane, Thomas M. Jø rgensen, Mikkel Jø rgensen, and Frederik C. Krebs. Application of optical coherence tomography (OCT) as a 3-dimensional imaging technique for roll-to-roll coated polymer solar cells. *Solar Energy Materials and Solar Cells*, 97:181–185, Feb 2012.

[138] Ping Liu, Roger M. Groves, and Rinze Benedictus. Quality assessment of aerospace materials with optical coherence tomography. In *Proc. SPIE Optical Micro- and Nanometrology IV*, volume 8430, pages 84300I–84300I–7, May 2012.

[139] Anderson Freitas, Marcello Amaral, and Marcus Raele. Optical Coherence Tomography: Development and Applications. In F. J. Duarte, editor, *Laser Pulse Phenomena and Applications*. InTech, Nov 2010.

[140] P. A. Flournoy, R. W. McClure, and G. Wyntjes. White-Light Interferometric Thickness Gauge. *Applied Optics*, 11(9):1907, Sep 1972.

[141] Tianchu Li, Anbo Wang, Kent Murphy, and Richard Claus. White-light scanning fiber Michelson interferometer for absolute position distance measurement. *Optics Letters*, 20(7):785–787, Apr 1995.

[142] Hideki Maruyama, Shogo Inoue, Teruki Mitsuyama, Masato Ohmi, and Masamitsu Haruna. Low-coherence interferometer system for the simultaneous measurement of refractive index and thickness. *Applied Optics*, 41(7):1315–1322, Mar 2002.

[143] Peter de Groot, Xavier Colonna de Lega, Jim Kramer, and Michael Turzhitsky. High precision surface inspection on the microscale by broadband interferometry. In Wolfgang Osten and Werner Jüptner, editors, *Procedings of the 4th International Workshop on Automatic Processing of Fringe Patterns*, pages 333–340. Elsevier, 2001.

[144] Peter de Groot. Coherence Scanning Interferometry. In Richard Leach, editor, *Optical Measurement of Surface Topography*, pages 187–208. Springer Berlin Heidelberg, 2011.

[145] Scott Diddams and Jean-Claude Diels. Dispersion measurements with white-light interferometry. *Journal of the Optical Society of America B*, 13(6):1120, Jun 1996.

[146] James C. Wyant. White light interferometry. In *Proc. SPIE 4737, Holography: A Tribute to Yuri Denisyuk and Emmett Leith*, volume 4737, pages 98–107, 2002.

[147] Akiko Harasaki, Joanna Schmit, and James C. Wyant. Improved vertical-scanning interferometry. *Applied Optics*, 39(13):2107–2115, May 2000.

[148] Christoph K. Hitzenberger. Measurement of corneal thickness by low-coherence interferometry. *Applied Optics*, 31(31):6637–6642, nov 1992.

[149] Michal Lucki, Leos Bohac, and Richard Zeleny. Fiber Optic and Free Space Michelson Interferometer - Principle and Practice. In Moh. Yasin, editor, *Optical Sensors - New Developments and Practical Applications*. InTech, Mar 2014.

[150] D. F. Swinehart. The Beer - Lambert Law. *Journal of Chemical Education*, 39(7):333, Jul 1962.

[151] Steven L. Jacques. Optical properties of biological tissues: a review. *Physics in Medicine and Biology*, 58(11):R37, Jun 2013.

[152] I. Hartl, X. D. Li, C. Chudoba, R. K. Ghanta, T. H. Ko, J. G. Fujimoto, J. K. Ranka, and R. S. Windeler. Ultrahigh-resolution optical coherence tomography using continuum generation in an air silica microstructure optical fiber. *Optics Letters*, 26(9):608–610, May 2001.

[153] B. Povazay, K. Bizheva, A. Unterhuber, B. Hermann, H. Sattmann, A. F. Fercher, W. Drexler, A. Apolonski, W. J. Wadsworth, J. C. Knight, P. St. J. Russell, M. Vetterlein, and E. Scherzer. Submicrometer axial resolution optical coherence tomography. *Optics Letters*, 27(20):1800–1802, Oct 2002.

[154] A. F. Fercher, C. K. Hitzenberger, M. Sticker, E. Moreno-Barriuso, R. Leitgeb, W. Drexler, and H. Sattmann. A thermal light source technique for optical coherence tomography. *Optics Communications*, 185(1–3):57–64, Nov 2000.

[155] J.M. Schmitt. Optical coherence tomography (OCT): a review. *IEEE Journal of Selected Topics in Quantum Electronics*, 5(4):1205–1215, Jul 1999.

[156] Maciej Wojtkowski. High-speed optical coherence tomography: basics and applications. *Applied Optics*, 49(16):D30–D61, Jun 2010.

[157] Maciej Wojtkowski, Tomasz Bajraszewski, Piotr Targowski, and Andrzej Kowalczyk. Real-time in vivo imaging by high-speed spectral optical coherence tomography. *Optics Letters*, 28(19):1745–1747, Oct 2003.

[158] P. H. Tomlins and R. K. Wang. Theory, developments and applications of optical coherence tomography. *Journal of Physics D: Applied Physics*, 38(15):2519, Aug 2005.

[159] Rüdiger Paschotta. *Fiber Optics*, chapter Fibers and other waveguides. Wiley-VCH, 1st edition, Oct 2008.

[160] Wojtek J. Walecki and Fanny Szondy. Fiber optics low-coherence IR interferometry for defense sensors manufacturing. In *Proc. SPIE 7322, Photonic Microdevices/Microstructures for Sensing*, volume 73220K, 2009.

[161] Marc Dufour. Inspection of hard-to-reach industrial parts using small-diameter probes. *SPIE Newsroom*, 2006.

[162] M L Dufour, G Lamouche, V Detalle, B Gauthier, and P Sammut. Low-coherence interferometry –an advanced technique for optical metrology in industry. *Insight - Non-Destructive Testing and Condition Monitoring*, 47(4):216–219, Apr 2005.

[163] A F. Fercher and E Roth. Ophthalmic Laser Interferometry. In *Proc. SPIE 0658, Optical Instrumentation for Biomedical Laser Applications*, volume 0658, pages 48–51, 1986.

[164] William Howard Steel. *Interferometry*. CUP Archive, 1983.

[165] A. F. Fercher, C. Hitzenberger, and M. Juchem. Measurement of Intraocular Optical Distances Using Partially Coherent Laser Light. *Journal of Modern Optics*, 38(7):1327–1333, Jul 1991.

[166] H. D. Ford, R. Beddows, P. Casaubieilh, and R. P. Tatam *. Comparative signal-to-noise analysis of fibre-optic based optical coherence tomography systems. *Journal of Modern Optics*, 52(14):1965–1979, Sep 2005.

[167] Joseph A. Izatt, Michael R. Hee, Gabrielle M. Owen, Eric A. Swanson, and James G. Fujimoto. Optical coherence microscopy in scattering media. *Optics Letters*, 19(8):590, Apr 1994.

[168] Zahid Yaqoob, Jigang Wu, Emily J. McDowell, Xin Heng, and Changhuei Yang. Methods and application areas of endoscopic optical coherence tomography. *Journal of Biomedical Optics*, 11(6):063001–063001–19, 2006.

[169] B. L. Danielson and C. D. Whittenberg. Guided-wave reflectometry with micrometer resolution. *Applied Optics*, 26(14):2836–2842, Jul 1987.

[170] Rüdiger Paschotta. *Optical Heterodyne Detection*, chapter Optical Metrology. Wiley-VCH, 1st edition, Oct 2008.

[171] J. Fred Holmes and Badih J. Rask. Optimum optical local oscillator power levels in coherent detection systems. In *Proc. SPIE 1982, Photoelectronic Detection and Imaging: Technology and Applications*, volume 1982, pages 157–163, 1993.

[172] J. Fred Holmes and Badih J. Rask. Optimum optical local-oscillator power levels for coherent detection with photodiodes. *Applied Optics*, 34(6):927, Feb 1995.

[173] Wolfgang Drexler, Oliver Findl, Rupert Menapace, Andreas Kruger, Andreas Wedrich, Georg Rainer, Angela Baumgartner, Christoph K. Hitzenberger, and Adolf F. Fercher. Dual Beam Optical Coherence Tomography: Signal Identification for Ophthalmologic Diagnosis. *Journal of Biomedical Optics*, 3(1):55–65, 1998.

[174] Leonard Mandel and Emil Wolf. *Optical Coherence and Quantum Optics*. Cambridge University Press, Sep 1995.

[175] Max Born and Emil Wolf. *Principles of Optics: Electromagnetic Theory of Propagation, Interference and Diffraction of Light*. Cambridge University Press, Oct 1999.

[176] Adolf Friedrich Fercher, Christoph K. Hitzenberger, Wolfgang Drexler, G. Kamp, I. Strasser, and Haicang Li. In-vivo optical coherence tomography in ophthalmology. In G. et al Müller, editor, *Proc. SPIE IS11, Medical Optical Tomography: Functional Imaging and Monitoring*, volume IS11, pages 355–370, Bellingham, August 1993. SPIE Press.

[177] J. A. Izatt and M. A. Choma. Theory of Optical Coherence Tomography. In Professor Dr Wolfgang Drexler and Professor Dr James G. Fujimoto, editors, *Optical Coherence Tomography*, Biological and Medical Physics, Biomedical Engineering, pages 47–72. Springer Berlin Heidelberg, 2008.

[178] F. Lexer, C. K. Hitzenberger, A. F. Fercher, and M. Kulhavy. Wavelength-tuning interferometry of intraocular distances. *Applied Optics*, 36(25):6548–6553, Sep 1997.

[179] B. Golubovic, B. E. Bouma, G. J. Tearney, and J. G. Fujimoto. Optical frequency-domain reflectometry using rapid wavelength tuning of a Cr^{4+}:forsterite laser. *Optics Letters*, 22(22):1704–1706, Nov 1997.

[180] S. H. Yun, G. J. Tearney, J. F. de Boer, and B. E. Bouma. Motion artifacts in optical coherence tomography with frequency-domain ranging. *Optics Express*, 12(13):2977, 2004.

[181] R. Leitgeb, C. Hitzenberger, and Adolf Fercher. Performance of fourier domain vs. time domain optical coherence tomography. *Optics Express*, 11(8):889–894, Apr 2003.

[182] Johannes F. de Boer, Barry Cense, B. Hyle Park, Mark C. Pierce, Guillermo J. Tearney, and Brett E. Bouma. Improved signal-to-noise ratio in spectral-domain compared with time-domain optical coherence tomography. *Optics Letters*, 28(21):2067, nov 2003.

[183] Stephan A. Boppart, Brett E. Bouma, Costas Pitris, James F. Southern, Mark E. Brezinski, and James G. Fujimoto. In vivo cellular optical coherence tomography imaging. *Nature Medicine*, 4(7):861–865, Jul 1998.

[184] Joseph M. Schmitt and Gitesh Kumar. Optical scattering properties of soft tissue: a discrete particle model. *Applied Optics*, 37(13):2788–2797, May 1998.

[185] Orazio Svelto. *Principles of Lasers*. Springer Science & Business Media, Mar 2010.

[186] Professor Dr J. Fujimoto and Professor Dr W. Drexler. Introduction to Optical Coherence Tomography. In Professor Dr Wolfgang Drexler and Professor Dr James G. Fujimoto, editors, *Optical Coherence Tomography*, Biological and Medical Physics, Biomedical Engineering, pages 1–45. Springer Berlin Heidelberg, 2008.

[187] Professor Dr W. Drexler, Y. Chen, A. Aguirre, B. Považay, A. Unterhuber, and Professor Dr J. G. Fujimoto. Ultrahigh Resolution Optical Coherence Tomography. In Professor Dr Wolfgang Drexler and Professor Dr James G. Fujimoto, editors, *Optical Coherence Tomography*, Biological and Medical Physics, Biomedical Engineering, pages 239–279. Springer Berlin Heidelberg, 2008.

[188] J. M. Schmitt, S. L. Lee, and K. M. Yung. An optical coherence microscope with enhanced resolving power in thick tissue. *Optics Communications*, 142(4–6):203–207, Oct 1997.

[189] H. Hodara. Statistics of thermal and laser radiation. *Proceedings of the IEEE*, 53(7):696–704, Jul 1965.

[190] E. A. Swanson, D. Huang, M. R. Hee, J. G. Fujimoto, C. P. Lin, and C. A. Puliafito. High-speed optical coherence domain reflectometry. *Optics Letters*, 17(2):151, Jan 1992.

[191] J. F. de Boer. Spectral/Fourier Domain Optical Coherence Tomography. In Professor Dr Wolfgang Drexler and Professor Dr James G. Fujimoto, editors, *Optical Coherence Tomography*, Biological and Medical Physics, Biomedical Engineering, pages 147–175. Springer Berlin Heidelberg, 2008.

[192] V. J. Srinivasan, R. Huber, I. Gorczynska, J. G. Fujimoto, J. Y. Jiang, P. Reisen, and A. E. Cable. High-speed, high-resolution optical coherence tomography retinal imaging with a frequency-swept laser at 850 nm. *Optics Letters*, 32(4):361, 2007.

[193] Bharat Bhushan, James C. Wyant, and Chris L. Koliopoulos. Measurement of surface topography of magnetic tapes by Mirau interferometry. *Applied Optics*, 24(10):1489, May 1985.

[194] J. C. Wyant. Use of an ac heterodyne lateral shear interferometer with real-time wavefront correction systems. *Applied Optics*, 14(11):2622, Nov 1975.

[195] O. Sasaki and H. Okazaki. Sinusoidal phase modulating interferometry for surface profile measurement. *Applied Optics*, 25(18):3137, Sep 1986.

[196] O. Sasaki and H. Okazaki. Analysis of measurement accuracy in sinusoidal phase modulating interferometry. *Applied Optics*, 25(18):3152, Sep 1986.

[197] O. Sasaki, H. Okazaki, and M. Sakai. Sinusoidal phase modulating interferometer using the integrating-bucket method. *Applied Optics*, 26(6):1089–1093, Mar 1987.

[198] Woo-June Choi, Ji-Hoon Na, Seon-Young Ryu, Byeong-Ha Lee, and Dong-Seob Ko. Realization of 3-d topographic and tomograpic images with ultrahigh-resolution full-field optical coherence tomography. *Journal of the Optical Society of Korea*, 11(1):18–25, Mar 2007.

[199] Blandine Laude, Antonello De Martino, Bernard Drévillon, Laurence Benattar, and Laurent Schwartz. Full-Field Optical Coherence Tomography with Thermal Light. *Applied Optics*, 41(31):6637, Nov 2002.

[200] Kate Grieve, Michel Paques, Arnaud Dubois, José Sahel, Claude Boccara, and Jean-François Le Gargasson. Ocular tissue imaging using ultrahigh-resolution, full-field optical coherence tomography. *Investigative Ophthalmology & Visual Science*, 45(11):4126–4131, Nov 2004.

[201] A. D. Aguirre and Professor Dr J. G. Fujimoto. Optical Coherence Microscopy. In Professor Dr Wolfgang Drexler and Professor Dr James G. Fujimoto, editors, *Optical Coherence Tomography*, Biological and Medical Physics, Biomedical Engineering, pages 505–542. Springer Berlin Heidelberg, 2008.

[202] René Däendliker. Concept of modes in optics and photonics. In *Proc. SPIE 3831, Sixth International Conference on Education and Training in Optics and Photonics*, volume 3831, pages 193–198, 2000.

[203] J. M. Schmitt, S. H. Xiang, and K. M. Yung. Speckle in Optical Coherence Tomography. *Journal of Biomedical Optics*, 4(1):95–105, 1999.

[204] Jeehyun Kim, Donald T. Miller, Eunha Kim, Sanghoon Oh, Junghwan Oh, and Thomas E. Milner. Optical coherence tomography speckle reduction by a partially spatially coherent source. *Journal of Biomedical Optics*, 10(6):064034–064034–9, 2005.

[205] B. Karamata, P. Lambelet, M. Laubscher, R. P. Salathé, and T. Lasser. Spatially incoherent illumination as a mechanism for cross-talk suppression in wide-field optical coherence tomography. *Optics Letters*, 29(7):736, 2004.

[206] Kieran G. Larkin. Efficient nonlinear algorithm for envelope detection in white light interferometry. *Journal of the Optical Society of America A*, 13(4):832–843, Apr 1996.

[207] Abraham. Savitzky and M. J. E. Golay. Smoothing and Differentiation of Data by Simplified Least Squares Procedures. *Analytical Chemistry*, 36(8):1627–1639, Jul 1964.

[208] R.W. Schafer. What Is a Savitzky-Golay Filter [Lecture Notes]. *IEEE Signal Processing Magazine*, 28(4):111–117, Jul 2011.

[209] Stanley S. C. Chim and Gordon S. Kino. Phase measurements using the Mirau correlation microscope. *Applied Optics*, 30(16):2197, Jun 1991.

[210] Peter de Groot. Principles of interference microscopy for the measurement of surface topography. *Advances in Optics and Photonics*, 7(1):1, Mar 2015.

[211] Byeong Ha Lee, Woo June Choi, and Jihoon Na. Full-field optical coherence tomography based on hilbert transform. *The Review of Laser Engineering*, 36(APLS):1347–1350, 2008.

[212] David A. Zweig and Robert E. Hufnagel. Hilbert transform algorithm for fringe-pattern analysis. In *Proc. SPIE 1333, Advanced Optical Manufacturing and Testing*, volume 1333, pages 295–302, 1990.

[213] Jihoon Na, Woo June Choi, Eun Seo Choi, Seon Young Ryu, and Byeong Ha Lee. Image restoration method based on hilbert transform for full-field optical coherence tomography. *Applied Optics*, 47(3):459–466, Jan 2008.

[214] Yi-Wen Liu. Hilbert Transform and Applications. In Salih Salih, editor, *Fourier Transform Applications*. InTech, Apr 2012.

[215] A. D. Poularikas. The Hilbert Transform. In A. D. Poularikas, editor, *Handbook of Formulas and Tables for Signal Processing*, Electrical Engineering Handbook. CRC Press, Sep 1998.

[216] J. Lagarias, J. Reeds, M. Wright, and P. Wright. Convergence Properties of the Nelder–Mead Simplex Method in Low Dimensions. *SIAM Journal on Optimization*, 9(1):112–147, Jan 1998.

[217] Alberto de Castro, Sergio Barbero, Sergio Ortiz, and Susana Marcos. Accuracy of the reconstruction of the crystalline lens gradient index with optimization methods from Ray Tracing and Optical Coherence Tomography data. *Optics Express*, 19(20):19265, Sep 2011.

[218] Yeou-Yen Cheng and James C. Wyant. Multiple-wavelength phase-shifting interferometry. *Applied Optics*, 24(6):804, Mar 1985.

[219] Miguel Arevallilo Herráez, David R. Burton, Michael J. Lalor, and Munther A. Gdeisat. Fast two-dimensional phase-unwrapping algorithm based on sorting by reliability following a noncontinuous path. *Applied Optics*, 41(35):7437, Dec 2002.

[220] Miguel Arevallilo Herráez, Munther A. Gdeisat, David R. Burton, and Michael J. Lalor. Robust, Fast, and Effective Two-Dimensional Automatic Phase Unwrapping Algorithm Based on Image Decomposition. *Applied Optics*, 41(35):7445, Dec 2002.

[221] Joseph W. Goodman. *Introduction to Fourier Optics*. Roberts and Company Publishers, 2005.

[222] Harry C. Andrews, AG. Tescher, and R.P. Kruger. Image processing by digital computer. *IEEE Spectrum*, 9(7):20–32, Jul 1972.

[223] D. W. Phillion. General methods for generating phase-shifting interferometry algorithms. *Applied Optics*, 36(31):8098–8115, Nov 1997.

[224] Y. Surrel. Phase stepping: a new self-calibrating algorithm. *Applied Optics*, 32(19):3598–3600, Jul 1993.

[225] Johannes Schwider, Oliver R. Falkenstoerfer, Horst Schreiber, Andreas Zoeller, and Norbert Streibl. New compensating four-phase algorithm for phase-shift interferometry. *Optical Engineering*, 32(8):1883–1885, 1993.

[226] Bing Zhao and Yves Surrel. Phase shifting: six-sample self-calibrating algorithm insensitive to the second harmonic in the fringe signal. *Optical Engineering*, 34(9):2821–2822, 1995.

[227] J. Schmit and K. Creath. Extended averaging technique for derivation of error-compensating algorithms in phase-shifting interferometry. *Applied Optics*, 34(19):3610–3619, Jul 1995.

[228] Y. Surrel. Design of algorithms for phase measurements by the use of phase stepping. *Applied Optics*, 35(1):51–60, Jan 1996.

[229] A. Dubois. Phase-map measurements by interferometry with sinusoidal phase modulation and four integrating buckets. *Journal of the Optical Society of America. A, Optics, Image Science, and Vision*, 18(8):1972–1979, Aug 2001.

[230] J. C. Wyant. Phase-Shifting Interferometry. on-line publication, 2011.

[231] Howard Wolinsky. Disease mongering and drug marketing. *EMBO Reports*, 6(7):612–614, Jul 2005.

[232] Jiben Roy. *An Introduction to Pharmaceutical Sciences: Production, Chemistry, Techniques and Technology*. Elsevier, Jul 2011.

[233] Kathlyn Stone. What is an Active Pharmaceutical Ingredient? http://pharma.about.com/od/A/g/Api-Active-Pharmaceutical-Ingredient.htm, Jun 2014.

[234] Alison Haywood and Beverley D Glass. Pharmaceutical excipients - where do we begin? *Australian Prescriber*, 34(4), Aug 2011.

[235] Gaurav Tiwari, Ruchi Tiwari, Birendra Sriwastawa, L Bhati, S Pandey, P Pandey, and Saurabh K Bannerjee. Drug delivery systems: An updated review. *International Journal of Pharmaceutical Investigation*, 2(1):2–11, 2012.

[236] Wikipedia. Route of administration. https://en.wikipedia.org/wiki/Route_of_administration, Jun 2015. Page Version ID: 669283125.

[237] Abdul W. Basit, Fridrun Podczeck, J. Michael Newton, Wendy A. Waddington, Peter J. Ell, and Larry F. Lacey. The use of formulation technology to assess regional gastrointestinal drug absorption in humans. *European Journal of Pharmaceutical Sciences: Official Journal of the European Federation for Pharmaceutical Sciences*, 21(2–3):179–189, Feb 2004.

[238] M. Andersson, S. Folestad, J. Gottfries, M. O. Johansson, M. Josefson, and K. G. Wahlund. Quantitative analysis of film coating in a fluidized bed process by in-line NIR spectrometry and multivariate batch calibration. *Analytical Chemistry*, 72(9):2099–2108, May 2000.

[239] Ab Hawthorne, Yr Mahida, At Cole, and Cj Hawkey. Aspirin-induced gastric mucosal damage: prevention by enteric-coating and relation to prostaglandin synthesis. *British Journal of Clinical Pharmacology*, 32(1):77–83, Jul 1991.

[240] Donald L. Wise. *Handbook of Pharmaceutical Controlled Release Technology*. CRC Press, Aug 2000.

[241] Nahor Haddish-Berhane, Seong Hoon Jeong, Kamyar Haghighi, and Kinam Park. Modeling film-coat non-uniformity in polymer coated pellets: a stochastic approach. *International Journal of Pharmaceutics*, 323(1–2):64–71, Oct 2006.

[242] P. Avalle, M. J. Pollitt, K. Bradley, B. Cooper, G. Pearce, A. Djemai, and S. Fitzpatrick. Development of Process Analytical Technology (PAT) methods for controlled release pellet coating. *European Journal of Pharmaceutics and Biopharmaceutics*, 87(2):244–251, Jul 2014.

[243] Louise Ho, Yvonne Cuppok, Susanne Muschert, Keith C. Gordon, Michael Pepper, Yaochun Shen, Florence Siepmann, Juergen Siepmann, Philip F. Taday, and Thomas Rades. Effects of film coating thickness and drug layer uniformity on in vitro drug release from sustained-release coated pellets: a case study using terahertz pulsed imaging. *International Journal of Pharmaceutics*, 382(1–2):151–159, Dec 2009.

[244] Philip Denton and Chris Rostron. *Pharmaceutics: The Science of Medicine Design*. OUP Oxford, Jul 2013.

[245] B. J. Lee, S. G. Ryu, and J. H. Cui. Controlled release of dual drug-loaded hydroxypropyl methylcellulose matrix tablet using drug-containing polymeric coatings. *International Journal of Pharmaceutics*, 188(1):71–80, Oct 1999.

[246] Padmaja Shivanand and Omar L. Sprockel. A controlled porosity drug delivery system. *International Journal of Pharmaceutics*, 167(1–2):83–96, Jun 1998.

[247] M. P. Wagh, Y. H. Sonawane, and O. U. Joshi. Terahertz Technology: A Boon to Tablet Analysis. *Indian Journal of Pharmaceutical Sciences*, 71(3):235–241, 2009.

[248] Ann Ringqvist, Lynne S Taylor, Katarina Ekelund, Gert Ragnarsson, Sven Engström, and Anders Axelsson. Atomic force microscopy analysis and confocal Raman microimaging of coated pellets. *International Journal of Pharmaceutics*, 267(1–2):35–47, Nov 2003.

[249] Louise Ho, Ronny Müller, Keith C. Gordon, Peter Kleinebudde, Michael Pepper, Thomas Rades, Yaochun Shen, Philip F. Taday, and J. Axel Zeitler. Applications of terahertz pulsed imaging to sustained-release tablet film coating quality assessment and dissolution performance. *Journal of Controlled Release: Official Journal of the Controlled Release Society*, 127(1):79–87, Apr 2008.

[250] M. Andersson, B. Holmquist, J. Lindquist, O. Nilsson, and K. G. Wahlund. Analysis of film coating thickness and surface area of pharmaceutical pellets using fluorescence microscopy and image analysis. *Journal of Pharmaceutical and Biomedical Analysis*, 22(2):325–339, Mar 2000.

[251] L. Ho, R. Müller, M. Römer, K. C. Gordon, J. Heinämäki, P. Kleinebudde, M. Pepper, T. Rades, Y. C. Shen, C. J. Strachan, P. F. Taday, and J. A. Zeitler. Analysis of sustained-release tablet film coats using terahertz pulsed imaging. *Journal of Controlled Release*, 119(3):253–261, Jun 2007.

[252] Mark D. Mowery, Robert Sing, John Kirsch, Amir Razaghi, Simon Béchard, and Robert A. Reed. Rapid at-line analysis of coating thickness and uniformity on tablets using laser induced breakdown spectroscopy. *Journal of Pharmaceutical and Biomedical Analysis*, 28(5):935–943, Jun 2002.

[253] D. Brock, J. A. Zeitler, A. Funke, K. Knop, and P. Kleinebudde. A comparison of quality control methods for active coating processes. *International Journal of Pharmaceutics*, 439(1–2):289–295, Dec 2012.

[254] J. Luypaert, D. L. Massart, and Y. Vander Heyden. Near-infrared spectroscopy applications in pharmaceutical analysis. *Talanta*, 72(3):865–883, May 2007.

[255] Gabriele Reich. Near-infrared spectroscopy and imaging: Basic principles and pharmaceutical applications. *Advanced Drug Delivery Reviews*, 57(8):1109–1143, Jun 2005.

[256] M. Andersson, M. Josefson, F. W. Langkilde, and K. G. Wahlund. Monitoring of a film coating process for tablets using near infrared reflectance spectrometry. *Journal of Pharmaceutical and Biomedical Analysis*, 20(1–2):27–37, Jun 1999.

[257] Jukka Rantanen, Sakari Lehtola, Pirjo Rämet, Jukka-Pekka Mannermaa, and Jouko Yliruusi. On-line monitoring of moisture content in an instrumented fluidized bed granulator with a multi-channel NIR moisture sensor. *Powder Technology*, 99(2):163–170, Sep 1998.

[258] Jose D. Perez-Ramos, W. Paul Findlay, Garnet Peck, and Kenneth R. Morris. Quantitative analysis of film coating in a pan coater based on in-line sensor measurements. *AAPS PharmSciTech*, 6(1):E127–E136, Sep 2005.

[259] Meike Römer, Jyrki Heinämäki, Clare Strachan, Niklas Sandler, and Jouko Yliruusi. Prediction of Tablet Film-coating Thickness Using a Rotating Plate Coating System and NIR Spectroscopy. *AAPS PharmSciTech*, 9(4):1047–1053, Oct 2008.

[260] John F. Kauffman, Marybeth Dellibovi, and Charles R. Cunningham. Raman spectroscopy of coated pharmaceutical tablets and physical models for multivariate calibration to tablet coating thickness. *Journal of Pharmaceutical and Biomedical Analysis*, 43(1):39–48, Jan 2007.

[261] Simon Ensslin, Klaus Peter Moll, Hendrik Metz, Markus Otz, and Karsten Mäder. Modulating pH-independent release from coated pellets: effect of coating composition on solubilization processes and drug release. *European Journal of Pharmaceutics and Biopharmaceutics*, 72(1):111–118, May 2009.

[262] J. Craig Richardson, Richard W. Bowtell, Karsten Mäder, and Colin D. Melia. Pharmaceutical applications of magnetic resonance imaging (MRI). *Advanced Drug Delivery Reviews*, 57(8):1191–1209, Jun 2005.

[263] Simon Ensslin, Klaus Peter Moll, Kurt Paulus, and Karsten Mäder. New insight into modified release pellets - internal structure and drug release mechanism. *Journal of Controlled Release: Official Journal of the Controlled Release Society*, 128(2):149–156, Jun 2008.

[264] Samuel R. Pygall, Joanne Whetstone, Peter Timmins, and Colin D. Melia. Pharmaceutical applications of confocal laser scanning microscopy: The physical characterisation of pharmaceutical systems. *Advanced Drug Delivery Reviews*, 59(14):1434–1452, Dec 2007.

[265] F. L. Laksmana, L. J. Van Vliet, P. J. A. Hartman Kok, H. Vromans, H. W. Frijlink, and K. Van der Voort Maarschalk. Quantitative Image Analysis for Evaluating the Coating Thickness and Pore Distribution in Coated Small Particles. *Pharmaceutical Research*, 26(4):965–976, Dec 2008.

[266] P. F. Taday, I. V. Bradley, D. D. Arnone, and M. Pepper. Using Terahertz pulse spectroscopy to study the crystalline structure of a drug: a case study of the polymorphs of ranitidine hydrochloride. *Journal of Pharmaceutical Sciences*, 92(4):831–838, Apr 2003.

[267] J. Axel Zeitler, Karin Kogermann, Jukka Rantanen, Thomas Rades, Philip F. Taday, Michael Pepper, Jaakko Aaltonen, and Clare J. Strachan. Drug hydrate systems and dehydration processes studied by terahertz pulsed spectroscopy. *International Journal of Pharmaceutics*, 334(1–2):78–84, Apr 2007.

[268] Anthony J. Fitzgerald, Bryan E. Cole, and Philip F. Taday. Nondestructive analysis of tablet coating thicknesses using terahertz pulsed imaging. *Journal of Pharmaceutical Sciences*, 94(1):177–183, Jan 2005.

[269] Yao-Chun Shen and P.F. Taday. Development and application of terahertz pulsed imaging for nondestructive inspection of pharmaceutical tablet. *IEEE Journal of Selected Topics in Quantum Electronics*, 14(2):407–415, Mar 2008.

[270] M. Haaser, Y. Karrout, C. Velghe, Y. Cuppok, K. C. Gordon, M. Pepper, J. Siepmann, T. Rades, P. F. Taday, and C. J. Strachan. Application of terahertz pulsed imaging to analyse film coating characteristics of sustained-release coated pellets. *International Journal of Pharmaceutics*, 457(2):521–526, Dec 2013.

[271] Robert K. May, Michael J. Evans, Shuncong Zhong, Ian Warr, Lynn F. Gladden, Yaochun Shen, and J. Axel Zeitler. Terahertz in-line sensor for direct coating thickness measurement of individual tablets during film coating in real-time. *Journal of Pharmaceutical Sciences*, 100(4):1535–1544, Apr 2011.

[272] Daniel Markl, Günther Hannesschläger, Stephan Sacher, Michael Leitner, and Johannes G. Khinast. Optical coherence tomography as a novel tool for in-line monitoring of a pharmaceutical film-coating process. *European Journal of Pharmaceutical Sciences: Official Journal of the European Federation for Pharmaceutical Sciences*, 55:58–67, May 2014.

[273] Hong Wen and Kinam Park. *Oral Controlled Release Formulation Design and Drug Delivery: Theory to Practice*. John Wiley & Sons, Jan 2011.

[274] Chen Li, J. Axel Zeitler, Yue Dong, and Yao-Chun Shen. Non-destructive evaluation of polymer coating structures on pharmaceutical pellets using full-field optical coherence tomography. *Journal of Pharmaceutical Sciences*, 103(1):161–166, Jan 2014.

[275] R.J. Lewis, editor. *Hawley's Condensed Chemical Dictionary*. John Wiley & Sons, Inc., New York, 13th edition, 1997. p.464.

[276] Limin Zhu, Randal A. Seburg, and Eric W. Tsai. Determination of surface-bound hydroxypropylcellulose (HPC) on drug particles in colloidal dispersions using size exclusion chromatography: A comparison of ELS and RI detection. *Journal of Pharmaceutical and Biomedical Analysis*, 40(5):1089–1096, Mar 2006.

[277] Yoseme. Hydroxypropyl cellulose. http://www.yoseme.com/products/375015.html. Accessed: 2015-07-15.

[278] Jaime Curtis-Fisk, Paul Sheskey, Karen Balwinski, Karen Coppens, Carol Mohler, and Jin Zhao. Effect of Formulation Conditions on Hypromellose Performance Properties in Films Used for Capsules and Tablet Coatings. *AAPS PharmSciTech*, 13(4):1170–1178, Sep 2012.

[279] ChemicalBook. Cellulose microcrystalline. http://www.chemicalbook.com/ChemicalProductProperty_EN_CB4217972.htm. Accessed: 2015-07-15.

[280] J. Axel Zeitler, Philip F. Taday, David A. Newnham, Michael Pepper, Keith C. Gordon, and Thomas Rades. Terahertz pulsed spectroscopy and imaging in the pharmaceutical setting–a review. *The Journal of Pharmacy and Pharmacology*, 59(2):209–223, Feb 2007.

[281] Bruker. Skyscan 1172 technical details. https://www.bruker.com/products/x-ray-diffraction-and-elemental-analysis/x-ray-micro-ct/skyscan-1172/technical-details.html, 2015.

[282] C. Robert Bagnell. Chapter 13 confocal laser scanning microscopy. Pathology 464 Light Microscopy, 2012.

[283] Kyle Quinn. Pushing the limits of imaging resolution and penetration depth. http://discover.osa.org/optical-society-blog/bid/337759/Pushing-the-limits-of-imaging-resolution-and-penetration-depth, Feb 2014.

[284] Bing Qin, Shihao Chen, Robert Brass, Yan Li, Maolong Tang, Xinbo Zhang, Xiaoyu Wang, Qinmei Wang, and David Huang. Keratoconus diagnosis with optical coherence tomography based pachymetric scoring system. *Journal of Cataract and Refractive Surgery*, 39(12):1864–1871, Dec 2013.

[285] Mohamed Abou Shousha, Carol L. Karp, Victor L. Perez, Rodrigo Hoffmann, Roberta Ventura, Victoria Chang, Sander R. Dubovy, and Jianhua Wang. Diagnosis and management of conjunctival and corneal intraepithelial neoplasia using ultra high-resolution optical coherence tomography. *Ophthalmology*, 118(8):1531–1537, Aug 2011.

[286] Sonia H. Yoo and Volkan Hurmeric. Femtosecond laser-assisted keratoplasty. *American Journal of Ophthalmology*, 151(2):189–191, Feb 2011.

[287] Burkhard von Jagow and Thomas Kohnen. Corneal architecture of femtosecond laser and microkeratome flaps imaged by anterior segment optical coherence tomography. *Journal of Cataract and Refractive Surgery*, 35(1):35–41, Jan 2009.

[288] Laurence S. Lim, Han T. Aung, Tin Aung, and Donald T. H. Tan. Corneal imaging with anterior segment optical coherence tomography for lamellar keratoplasty procedures. *American Journal of Ophthalmology*, 145(1):81–90, Jan 2008.

[289] M. Bechmann, M. Thiel, B. Roesen, S. Ullrich, M. Ulbig, and K. Ludwig. Central corneal thickness determined with optical coherence tomography in various types of glaucoma. *The British Journal of Ophthalmology*, 84(11):1233–1237, Nov 2000.

[290] Ronald H. Silverman, Monica S. Patel, Omer Gal, Aman Sarup, Avnish Deobhakta, Haitham Dababneh, Dan Z. Reinstein, Ernest J. Feleppa, and D. Jackson Coleman. Effect of Corneal Hydration on Ultrasound Velocity and Backscatter. *Ultrasound in medicine & biology*, 35(5):839–846, May 2009.

[291] N. Ritter, R. Owens, J. Cooper, and P.P. Van Saarloos. Location of the pupil-iris border in slit-lamp images of the cornea. In *International Conference on Image Analysis and Processing, 1999. Proceedings*, pages 740–745, 1999.

[292] B. R. Masters and A. A. Thaer. Real-time scanning slit confocal microscopy of the in vivo human cornea. *Applied Optics*, 33(4):695–701, Feb 1994.

[293] R. Bovelle, SC. Kaufman, H.W. Thompson, and H. Hamano. Corneal thickness measurements with the topcon sp-2000p specular microscope and an ultrasound pachymeter. *Archives of Ophthalmology*, 117(7):868–870, Jul 1999.

[294] Winifred Nolan. Anterior segment imaging: ultrasound biomicroscopy and anterior segment optical coherence tomography:. *Current Opinion in Ophthalmology*, 19(2):115–121, Mar 2008.

[295] C. J. Pavlin, J. A. McWhae, H. D. McGowan, and F. S. Foster. Ultrasound biomicroscopy of anterior segment tumors. *Ophthalmology*, 99(8):1220–1228, Aug 1992.

[296] Mingtao Zhao, Anthony N. Kuo, and Joseph A. Izatt. 3d refraction correction and extraction of clinical parameters from spectral domain optical coherence tomography of the cornea. *Optics Express*, 18(9):8923–8936, Apr 2010.

[297] M. Bechmann, M. J. Thiel, A. S. Neubauer, S. Ullrich, K. Ludwig, K. R. Kenyon, and M. W. Ulbig. Central corneal thickness measurement with a retinal optical coherence tomography device versus standard ultrasonic pachymetry. *Cornea*, 20(1):50–54, Jan 2001.

[298] Trefford Simpson and Desmond Fonn. Optical coherence tomography of the anterior segment. *The Ocular Surface*, 6(3):117–127, Jul 2008.

[299] Lori Vollmer, Joseph Sowka, Joseph Pizzimenti, and Xinha Yu. Central corneal thickness measurements obtained with anterior segment spectral domain optical coherence tomography compared to ultrasound pachymetry in healthy subjects. *Optometry (St. Louis, Mo.)*, 83(5):167–172, May 2012.

[300] T. Nishida. Cornea: anatomy and physiology. In J. H. Krachmer, M. J. Mannis, and E. J. Holland, editors, *Cornea: Fundamentals, Diagnosis and Management*. Elsevier, 2nd edition, 2005.

[301] Mission for Vision. Anatomy of the human eye: Cornea Histology. http://www.images.missionforvisionusa.org/anatomy/2005/10/cornea-histology.html, Oct 2005.

[302] Yan Li, Ou Tan, Robert Brass, Jack L. Weiss, and David Huang. Corneal Epithelial Thickness Mapping by Fourier-domain Optical Coherence Tomography in Normal and Keratoconic Eyes. *Ophthalmology*, 119(12):2425–2433, Dec 2012.

[303] Frank Joseph Goes. Anatomy of the human eye. In *The Eye in History*. JP Medical Ltd, Jan 2013.

[304] Olivier Casadessus, Ga´elle Georges, Laure Siozade Lamoine, Carole Deumié, and Louis Hoffart. Light scattering from edematous human corneal grafts' microstructure: experimental study and electromagnetic modelization. *Biomedical Optics Express*, 3(8):1793, Aug 2012.

[305] D. M. Maurice. The structure and transparency of the cornea. *The Journal of Physiology*, 136(2):263–286.1, Apr 1957.

[306] Sushmita Kaushik and Surinder Singh Pandav. Ultrasound biomicroscopy in glaucoma. *Journal of Current Glaucoma Practice*, 4(2):77–82, May 2010.

[307] S. Patel, J. Marshall, and F. W. Fitzke. Refractive index of the human corneal epithelium and stroma. *Journal of Refractive Surgery (Thorofare, N.J.: 1995)*, 11(2):100–105, Apr 1995.

[308] National Eye Institute. Facts About the Cornea and Corneal Disease. https://nei.nih.gov/health/cornealdisease, May 2013.

[309] Anthony P. Adamis, Vadim Filatov, Brenda J. Tripathi, and R. A. mesh C. Tripathi. Fuchs' endothelial dystrophy of the cornea. *Survey of Ophthalmology*, 38(2):149–168, Sep 1993.

[310] Wilson MC and Shields M. A comparison of the clinical variations of the iridocorneal endothelial syndrome. *Archives of Ophthalmology*, 107(10):1465–1468, Oct 1989.

[311] Ashok Sharma, Jennifer Marie Nottage, Kanish Mirchia, Rajan Sharma, Kanwar Mohan, and Verinder Singh Nirankari. Persistent Corneal Edema after Collagen Cross-Linking for Keratoconus. *American Journal of Ophthalmology*, 154(6):922–926.e1, Dec 2012.

[312] D.L. Van Horn, D.J. Doughman, J.E. Harris, G.E. Miller, R. Lindstrom, and R.A. Good. Ultrastructure of human organ-cultured cornea: Ii. stroma and epithelium. *Archives of Ophthalmology*, 93(4):275–277, Apr 1975.

[313] K. M. Meek, D. W. Leonard, C. J. Connon, S. Dennis, and S. Khan. Transparency, swelling and scarring in the corneal stroma. *Eye*, 17(8):927–936, 2003.

[314] A. J. Quantock, K. M. Meek, P. Brittain, A. E. Ridgway, and E. J. Thonar. Alteration of the stromal architecture and depletion of keratan sulphate proteoglycans in oedematous human corneas: histological, immunochemical and X-ray diffraction evidence. *Tissue & Cell*, 23(5):593–606, 1991.

[315] S. N. Griffiths, N. Drasdo, D. A. Barnes, and A. G. Sabell. Effect of epithelial and stromal edema on the light scattering properties of the cornea. *American Journal of Optometry and Physiological Optics*, 63(11):888–894, Nov 1986.

[316] Jianhua Wang, Trefford L. Simpson, and Desmond Fonn. Objective Measurements of Corneal Light-Backscatter during Corneal Swelling, by Optical Coherence Tomography. *Investigative Opthalmology & Visual Science*, 45(10):3493, Oct 2004.

[317] Wikipedia. Recurrent corneal erosion. https://en.wikipedia.org/wiki/Recurrent_corneal_erosion, May 2015. Page Version ID: 662405476.

[318] Mohamed El Sanharawi, Otman Sandali, Elena Basli, Nacim Bouheraoua, Barbara Ameline, Isabelle Goemaere, Cristina Georgeon, Taous Hamiche, Vincent Borderie, and Laurent Laroche. Fourier-Domain Optical Coherence Tomography Imaging in Corneal Epithelial Basement Membrane Dystrophy: A Structural Analysis. *American Journal of Ophthalmology*, 159(4):755–763.e1, Apr 2015.

[319] Lee Eye Center. Map - dot - fingerprint dystrophy. http://www.leeeyecenter.com/map-dot-fingerprint-dystrophy.htm, Aug 2015.

[320] M. Hammer, A. Roggan, D. Schweitzer, and G. Ḿuller. Optical properties of ocular fundus tissues–an in vitro study using the double-integrating-sphere technique and inverse Monte Carlo simulation. *Physics in Medicine and Biology*, 40(6):963–978, Jun 1995.

[321] Dhiraj K. Sardar, Guang-Yin Swanland, Raylon M. Yow, Robert J. Thomas, and Andrew T. C. Tsin. Optical properties of ocular tissues in the near infrared region. *Lasers in Medical Science*, 22(1):46–52, Mar 2007.

[322] Thomas J. T. P. van den Berg and Henk Spekreijse. Near infrared light absorption in the human eye media. *Vision Research*, 37(2):249–253, Jan 1997.

[323] J. J. Vos, A. A. Munnik, and J. Boogaard. Absolute Spectral Reflectance of the Fundus Oculi. *Journal of the Optical Society of America*, 55(5):573, May 1965.

[324] E.F. Maher. Transmission and absorption coefficients for ocular media of the rhesus monkey. In *Report SAM-TR-78-32*. USAF School of Aerospace Med Brooks AF Base, Dec 1978.

[325] Balamurali Vasudevan, Trefford L. Simpson, and Jacob G. Sivak. Regional variation in the refractive-index of the bovine and human cornea. *Optometry and Vision Science: Official Publication of the American Academy of Optometry*, 85(10):977–981, Oct 2008.

[326] Michael J. Doughty, Stavros Petrou, and Heather Macmillan. Anatomy and morphology of the cornea of bovine eyes from a slaughterhouse. *Canadian Journal of Zoology*, 73(11):2159–2165, Nov 1995.

[327] D. A. Hoeltzel, P. Altman, K. Buzard, and K. Choe. Strip extensiometry for comparison of the mechanical response of bovine, rabbit, and human corneas. *Journal of Biomechanical Engineering*, 114(2):202–215, May 1992.

[328] Ga´el Latour, Ga´elle Georges, Laure Siozade Lamoine, Carole Deumié, John Conrath, and Louis Hoffart. Human graft cornea and laser incisions imaging with micrometer scale resolution full-field optical coherence tomography. *Journal of Biomedical Optics*, 15(5):056006–056006–9, 2010.

[329] ASTM D7091-13. *Standard Practice for Nondestructive Measurement of Dry Film Thickness of Nonmagnetic Coatings Applied to Ferrous Metals and Nonmagnetic, Nonconductive Coatings Applied to Non-Ferrous Metals*, volume 06.01 of *D01.23*. American Society for Testing and Materials, 2013.

[330] ISO 2808:2007. *Paints and varnishes - Determination of film thickness*, volume TC35 SC9. International Organization for Standardization, 4th edition, Feb 2007.

[331] ISO 2360:2003. *Non-conductive coatings on non-magnetic electrically conductive basis materials - Measurement of coating thickness - Amplitude-sensitive eddy-current method*, volume TC107. International Organization for Standardization, 3rd edition, Nov 2003.

[332] D.C. Conner, A. Greenfield, P.N. Atkar, A.A. Rizzi, and H. Choset. Paint deposition modeling for trajectory planning on automotive surfaces. *IEEE Transactions on Automation Science and Engineering*, 2(4):381–392, Oct 2005.

[333] ASTM D6132-13. *Standard Test Method for Nondestructive Measurement of Dry Film Thickness of Applied Organic Coatings Using an Ultrasonic Coating Thickness Gage*, volume 06.01 of *D01.23*. American Society for Testing and Materials, 2013.

[334] Ke Su, Yao-chun Shen, and J.A. Zeitler. Terahertz Sensor for Non-Contact Thickness and Quality Measurement of Automobile Paints of Varying Complexity. *IEEE Transactions on Terahertz Science and Technology*, 4(4):432–439, Jul 2014.

[335] Frederick J. Trulson, August F. Scarpelli, and George L. Sarosy. Ultrasonic multilayer paint thickness measurement. Patent, Aug 1991. U.S. Classification 73/597, 73/602, 367/100, 73/620, 73/627; International Classification G01B17/02; Cooperative Classification G01B17/025; European Classification G01B17/02C.

[336] Keith R. Carduner, Roscoe O. Carter III, Dennis Schuetzle, and Michael J. Decello. Method and apparatus for measuring the thickness of a layer on a substrate, Feb 1992. U.S. Classification 250/339.09, 250/340, 250/341.5, 250/339.11; International Classification G01B11/06; Cooperative Classification G01B11/0625; European Classification G01B11/06C2.

[337] J. Ying, F. Liu, P. P. Ho, and R. R. Alfano. Nondestructive evaluation of incipient corrosion in a metal beneath paint by second-harmonic tomography. *Optics Letters*, 25(16):1189–1191, Aug 2000.

[338] Joke De Gelder, Peter Vandenabeele, Filip Govaert, and Luc Moens. Forensic analysis of automotive paints by Raman spectroscopy. *Journal of Raman Spectroscopy*, 36(11):1059–1067, Nov 2005.

[339] Takeshi Yasui, Takashi Yasuda, Ken-ichi Sawanaka, and Tsutomu Araki. Terahertz paintmeter for noncontact monitoring of thickness and drying progress in paint film. *Applied Optics*, 44(32):6849–6856, Nov 2005.

[340] Haida Liang. Optical coherence tomography: a non-invasive technique applied to painting conservation. *SPIE Newsroom*, 2006.

[341] Piotr Targowski and Michalina Gora. Optical coherence tomography holds promise for conserving art. *SPIE Newsroom*, 2009.

[342] Haida Liang, Kafing Keita, and Tom Vajzovic. PRISMS: a portable multispectral imaging system for remote in situ examination of wall paintings. In *Proceedings of SPIE - The International Society for Optical Engineering*, volume 6618, pages 661815–661818, 2007.

[343] Rebecca Lange, Haida Liang, Helen Howard, and Jane Spooner. Optical coherence tomography and spectral imaging of a wall painting. *SPIE Newsroom*, Aug 2011.

[344] Hans-Joachim Streitberger and Karl-Friedrich Dössel, editors. *Automotive Paints and Coatings*. Wiley-VCH Verlag GmbH & Co. KGaA, 2nd edition, May 2008.

[345] Wikipedia. Automotive paint. https://en.wikipedia.org/wiki/Automotive_paint, May 2015. Page Version ID: 664067472.

[346] Daniel Marks, P. Scott Carney, and Stephen A. Boppart. Adaptive spectral apodization for sidelobe reduction in optical coherence tomography images. *Journal of Biomedical Optics*, 9(6):1281–1287, Dec 2004.

[347] Yingli Wang, Yanmei Liang, and Kuanhong Xu. Signal processing for sidelobe suppression in optical coherence tomography images. *Journal of the Optical Society of America A*, 27(3):415, Mar 2010.

[348] Xiaojun Yu, Xinyu Liu, Jun Gu, Dongyao Cui, Junying Wu, and Linbo Liu. Depth extension and sidelobe suppression in optical coherence tomography using pupil filters. *Optics Express*, 22(22):26956–26966, Nov 2014.

[349] Takuma Doi, Kouji Toyoda, and Yoshihisa Tanimura. Effects of phase changes on reflection and their wavelength dependence in optical profilometry. *Applied Optics*, 36(28):7157, Oct 1997.

[350] G. Binnig, C. F. Quate, and Ch. Gerber. Atomic Force Microscope. *Physical Review Letters*, 56(9):930–933, Mar 1986.

[351] Dieter K. Schroder. *Semiconductor Material and Device Characterization*. John Wiley & Sons, 3rd edition, Feb 2006.

[352] ISO 13095:2014. *Surface Chemical Analysis - Atomic force microscopy - Procedure for in situ characterization of AFM probe shank profile used for nanostructure measurement*, volume TC201 SC9. International Organization for Standardization, 1st edition, Aug 2014.

[353] Lihong Gao, Fabien Lemarchand, and Michel Lequime. Comparison of different dispersion models for single layer optical thin film index determination. *Thin Solid Films*, 520(1):501–509, Oct 2011.

[354] Peter J. King, Naser Sedghi, Steve Hall, Ivona Z. Mitrovic, Paul R. Chalker, Matthew Werner, and Sarah Hindley. Physical and electrical characterization of Ce-HfO2 thin films deposited by thermal atomic layer deposition. *Journal of Vacuum Science & Technology B*, 32(3):03D103, May 2014.

[355] R. Kuroda, T. Suwa, Akinobu Teramoto, R. Hasebe, S. Sugawa, and T. Ohmi. Atomically Flat Silicon Surface and Silicon/Insulator Interface Formation Technologies for (100) Surface Orientation Large-Diameter Wafers Introducing High Performance and Low-Noise Metal #x2013;Insulator #x2013;Silicon FETs. *IEEE Transactions on Electron Devices*, 56(2):291–298, Feb 2009.

[356] Chien-Liang Chen and Ya-Chin King. TiN Metal Gate Electrode Thickness Effect on BTI and Dielectric Breakdown in HfSiON-Based MOSFETs. *IEEE Transactions on Electron Devices*, 58(11):3736–3742, Nov 2011.

[357] Ngoc-Long Do, Enric Garcia-Caurel, Nicolas Bérerd, Nathalie Moncoffre, and Dominique Gorse Pomonti. Determination of thicknesses of oxide films grown on titanium under argon irradiation by spectroscopic ellipsometry. *Journal of Nuclear Materials*, 447(1–3):197–207, Apr 2014.

[358] Woo-Ri Do and Jin-Ha Hwang. Physical or chemical characterization and device applications of transparent zinc-tin-oxide thin films deposited using RF sputtering. *Ceramics International*, 40(7, Part A):9809–9816, Aug 2014.

[359] Magdalena Szymańska, Sylwia Gierałltowska, łLukasz Wachnicki, Marcin Grobelny, Katarzyna Makowska, and Robert Mroczyński. Effect of reactive magnetron sputtering parameters on structural and electrical properties of hafnium oxide thin films. *Applied Surface Science*, 301:28–33, May 2014.

[360] X. Colonna de Lega and Peter J. de Groot. Characterization of materials and film stacks for accurate surface topography measurement using a white-light optical profiler. In *Proc. SPIE 6995, Optical Micro- and Nanometrology in Microsystems Technology II*, volume 6995, pages 69950P–69950P–9, 2008.

[361] P.R. Smith, D.H. Auston, and M.C. Nuss. Subpicosecond photoconducting dipole antennas. *IEEE Journal of Quantum Electronics*, 24(2):255–260, Feb 1988.

[362] M. Venkatesh, K. S. Rao, T. S. Abhilash, S. P. Tewari, and A. K. Chaudhary. Optical characterization of GaAs photoconductive antennas for efficient generation and detection of Terahertz radiation. *Optical Materials*, 36(3):596–601, Jan 2014.

[363] Masahiko Tani, Shuji Matsuura, Kiyomi Sakai, and Shin-ichi Nakashima. Emission characteristics of photoconductive antennas based on low-temperature-grown GaAs and semi-insulating GaAs. *Applied Optics*, 36(30):7853, Oct 1997.

[364] Michael R. Stone, Mira Naftaly, Robert E. Miles, J.R. Fletcher, and D.P. Steenson. Electrical and radiation characteristics of semilarge photoconductive terahertz emitters. *IEEE Transactions on Microwave Theory and Techniques*, 52(10):2420–2429, Oct 2004.

[365] J. Wahlstrand, T. Dekorsy, G. Klatt, and S. Cundiff. Terahertz Sources: Photoconductive emitters advance ultrafast terahertz sources. Laser Focus World, Jan 2011.

[366] Martin C. Nuss and Joseph Orenstein. Terahertz time-domain spectroscopy. In Professor Dr George Grüner, editor, *Millimeter and Submillimeter Wave Spectroscopy of Solids*, number 74 in Topics in Applied Physics, pages 7–50. Springer Berlin Heidelberg, 1998.

[367] Kunihiko Ishihara, Keishi Ohashi, Tomofumi Ikari, Hiroaki Minamide, Hiroyuki Yokoyama, Jun-ichi Shikata, and Hiromasa Ito. Terahertz-wave near-field imaging with subwavelength resolution using surface-wave-assisted bow-tie aperture. *Applied Physics Letters*, 89(20):201120, Nov 2006.

[368] Y. Cai, I. Brener, J. Lopata, J. Wynn, L. Pfeiffer, and J. Federici. Design and performance of singular electric field terahertz photoconducting antennas. *Applied Physics Letters*, 71(15):2076–2078, Oct 1997.

[369] Sachit Grover and Garret Moddel. Optical Frequency Rectification. In Garret Moddel and Sachit Grover, editors, *Rectenna Solar Cells*, pages 25–46. Springer New York, 2013.

[370] Phiar Corporation. A new technology for terahertz electronics. http://ecee.colorado.edu/~moddel/QEL/MIIM_Overview.pdf, Aug 2003. Version NP1.0.

[371] Subramanian Krishnan, Elias Stefanakos, and Shekhar Bhansali. Effects of dielectric thickness and contact area on current-voltage characteristics of thin film metal-insulator-metal diodes. *Thin Solid Films*, 516(8):2244–2250, Feb 2008.

[372] Sachit Grover and Garret Moddel. Metal Single-Insulator and Multi-Insulator Diodes for Rectenna Solar Cells. In Garret Moddel and Sachit Grover, editors, *Rectenna Solar Cells*, pages 89–109. Springer New York, 2013.

[373] A. D. Weerakkody, N. Sedghi, I. Z. Mitrovic, H. van Zalinge, I. Nemr Noureddine, S. Hall, J. S. Wrench, P. R. Chalker, L. J. Phillips, R. Treharne, and K. Durose. Enhanced low voltage nonlinearity in resonant tunneling metal-insulator-insulator-metal nanostructures. *Microelectronic Engineering*, 147:298–301, Nov 2015.

[374] M. N. Gadalla, M. Abdel-Rahman, and Atif Shamim. Design, Optimization and Fabrication of a 28.3 THz Nano-Rectenna for Infrared Detection and Rectification. *Scientific Reports*, 4, Mar 2014.

[375] B. Berland. Photovoltaic Technologies Beyond the Horizon - Optical Rectenna Solar Cell. 1 August 2001-30 September 2002. Final report, Feb 2003.

[376] Dale K. Kotter, Steven D. Novack, W. Dennis Slafer, and Patrick Pinhero. Solar nantenna electromagnetic collectors. In *Proceedings of the 2nd International Conference on Energy Sustainability*, Jacksonville, Florida, USA, Aug 2008.

[377] I. H. Malitson and M. J. Dodge. Refractive index and birefringence of synthetic sapphire. *Journal of the Optical Society of America*, 62:1405, 1972.

[378] Lihong Gao, Fabien Lemarchand, and Michel Lequime. Exploitation of multiple incidences spectrometric measurements for thin film reverse engineering. *Optics Express*, 20(14):15734, Jul 2012.

[379] W. N. Charman. Wavefront technology: past, present and future. *Contact Lens & Anterior Eye: The Journal of the British Contact Lens Association*, 28(2):75–92, Jun 2005.

[380] Wikipedia. LASIK. https://en.wikipedia.org/wiki/LASIK, Aug 2015. Page Version ID: 677984894.

[381] Murray McFadden. Determining the diameter of the optical zone, ablation depth, and minimum corneal thickness required for lasik. http://www.lasik1.com/LASIK_Envelope.html, Sep 2001. Copyright 1996-2005 Murray McFadden MD, Inc.

[382] Melania Cigales and Jairo E Hoyos, editors. *Dr. Hoyos' Step by Step Astig Ablation with Photo CD-ROM by Cigales*. Jaypee Brothers Medical Publishers (P) Ltd, 2006.

[383] Paolo Vinciguerra and Fabrizio I. Camesasca. *Refractive Surface Ablation: PRK, LASEK, Epi-LASIK, Custom, PTK, and Retreatment*. SLACK Incorporated, 2007.

[384] M. Mrochen, M. Kaemmerer, and T. Seiler. Wavefront-guided laser in situ keratomileusis: early results in three eyes. *Journal of Refractive Surgery (Thorofare, N.J.: 1995)*, 16(2):116–121, Apr 2000.

[385] Roger F. Steinert, Ann Z. McColgin, and Sumit Garg. Laser in situ Keratomileusis (LASIK). American Academy of Ophthalmology, Dec 2013.

[386] Lara C. Pullen. Wavefront-Guided LASIK Nomogram Improves Myopia Outcomes. In *American Academy of Ophthalmology (AAO) 2012 Annual Meeting*. American Academy of Ophthalmology, Nov 2012.

[387] M. Leyland. Validation of Orbscan II posterior corneal curvature measurement for intraocular lens power calculation. *Eye (London, England)*, 18(4):357–360, Apr 2004.

[388] Maolong Tang, Yan Li, Mariana Avila, and David Huang. Measuring total corneal power before and after laser in situ keratomileusis with high-speed optical coherence tomography. *Journal of Cataract and Refractive Surgery*, 32(11):1843–1850, Nov 2006.

[389] American National Standards Institute (ANSI). Corneal topography system: Standard terminology, requirements. http://webstore.ansi.org/RecordDetail.aspx?sku=ANSI+Z80.23-2008+(R2013), 2008. Washington, DC.

[390] Martin F. Fay, Xavier Colonna de Lega, and Peter de Groot. Measuring High-Slope and Super-Smooth Optics with High-Dynamic-Range Coherence Scanning Interferometry. In *OSA Technical Digest (online)*, Classical Optics 2014, page OW1B.3. OSA, 2014. Optical Fabrication and Testing 2014.

[391] Gregory J. McCormick, Jason Porter, Ian G. Cox, and Scott MacRae. Higher-Order Aberrations in Eyes with Irregular Corneas after Laser Refractive Surgery. *Ophthalmology*, 112(10):1699–1709, Oct 2005.

[392] Michael K. Smolek and Stephen D. Klyce. Goodness-of-prediction of Zernike polynomial fitting to corneal surfaces. *Journal of Cataract and Refractive Surgery*, 31(12):2350–2355, Dec 2005.

[393] Michael K. Smolek. Method for Expressing Clinical and Statistical Significance of Ocular and Corneal Wavefront Error Aberrations. *Cornea*, 31(3):212–221, Mar 2012.

[394] R. R. Krueger, N. F. Saedy, and P. J. McDonnell. Clinical analysis of steep central islands after excimer laser photorefractive keratectomy. *Archives of Ophthalmology*, 114(4):377–381, Apr 1996.

[395] Shin-Wook Kang, Eui-Sang Chung, and Woo-Jung Kim. Clinical analysis of central islands after laser in situ keratomileusis. *Journal of Cataract & Refractive Surgery*, 26(4):536–542, Apr 2000.

[396] Nicholas M. Patrikalakis and Takashi Maekawa. Differential Geometry of Surfaces. In *Shape Interrogation for Computer Aided Design and Manufacturing*, pages 49–72. Springer Berlin Heidelberg, 2002.

Appendix A

List of Abbreviations and Symbols

1-D	One-Dimensional
2-D	Two-Dimensional
3-D	Three-Dimensional
AC	Alternating Current
AFM	Atomic Force Microscopy
API	Active Pharmaceutical Ingredient
CCD	Charged-Coupled Device
CCT	Central Corneal Thickness
CLSM	Confocal Laser Scanning Microscopy
CMOS	Complementary Metal-Oxide-Semiconductor
CPEUS	Catheter-probe Endoscopic Ultrasonography
CSI	Coherence Scanning Interferometry
CSM	Confocal Scanning Microscopy
CT	Computed Tomography
DC	Direct Current
DOF	Depth of Field
DR	Dynamic Range
EBMD	Epithelial Basement Membrane Dystrophy
EPRS	Electron Paramagnetic Resonance Spectroscopy
EC	Ethyl Cellulose
FF-OCT	Full-Field Optical Coherence Tomography
FOV	Field of View
FT	Fourier Transform
FWHM	Full Width at Half Maximum

FWC	Full Well Capacity
GaAs	Gallium Arsenide
GI	Gastrointestinal
GUI	Graphic User Interface
HPC	Hydroxypropyl Cellulose
HPMC	Hydroxypropyl Methylcellulose
ICE	Iridocorneal Endothelial
IVUS	Intravascular Ultrasound
HT	Hilbert Transform
LASIK	Laser Assisted in Situ Keratomileusis
LCI	Low Coherence Interferometry
MCC	Microcrystalline Cellulose
MIM	Metal-insulator-metal
MIIM	Mental-Insulator-Insulator-Mental
MOSFET	Metal-Oxide-Semiconductor Field-Effect Transistor
MRI	Magnetic Resonance Imaging
NA	Numeric Aperture
ND	Neutral Density
NDT	Non-destructive Testing
NIR	Near-Infrared
NIRSI	Near-Infrared Spectroscopy and Imaging
OCM	Optical Coherence Microscopy
OCT	Optical Coherence Tomography
OPD	Optical Path Difference
OPL	Optical Path Length
PET	Positron Emission Tomography
PMMA	Polymethyl-Methacrylate
PSF	Point Spread Function
PSI	Phase-shifting Interferometry
PT	Piezoelectric Transducer
ROI	Region of Interest
SE	Spectroscopic Ellipsometry
SEM	Scanning Electron Microscopy
SNR	Signal-to-Noise Ratio
STD	Standard Deviation

STM	Scanning Tunnelling Microscopy
THz	Terahertz
TPI	Terahertz Pulsed Imaging
UBM	Ultrasound Biomicroscopy
UMOT	Ultrasound-modulated Optical Tomography
VSI	Vertical Scanning Interferometry
WLI	White Light Interferometry
XRD	X-ray Diffraction
XμCT	X-rays Micro Computed Tomography